



**MATERIAL
AND MECHANICAL
ENGINEERING
TECHNOLOGY**

Editorial board of the journal

Gulnara Zhetessova (Abylkas Saginov Karaganda Technical University, Kazakhstan)
Alexander Korsunsky (University of Oxford, England)
Olegas Cernasejus (Vilnius Gediminas Technical University, Lithuania)
Jaroslav Jerz (Institute of Materials & Machine Mechanics SAS, Slovakia)
Boris Moyzes (Tomsk Polytechnic University, Russia)
Nikolai Belov (National Research Technological University «Moscow Institute of Steel and Alloys», Russia)
Georgi Popov (Technical University of Sofia, Bulgaria)
Sergiy Antonyuk (University of Kaiserslautern, Germany)
Zharkynay Christian (University of Texas at Dallas Institute of Nanotechnology, USA)
Katica Simunovic (University of Slavonski Brod, Croatia)
Lesley D.Frame (School of Engineering University of Connecticut, USA)
Łukasz Gierz (Poznan University of Technology, Poland)
Łukasz Warguła (Poznan University of Technology, Poland)
Olga Zharkevich (Abylkas Saginov Karaganda Technical University, Kazakhstan)

Content

Pak Yu., Pak D., Tebayeva A., Aitkaliyev A. Instrumental Testing of Quasi-Binary Ore Materials by the Gamma-Albedo Method	3
Gowthaman A.M., Dr. P. Nallasamy, Mr. Shanmuga Sundaram D, Mr. S. Yashwanth Kumar Investigation on Tribological Characteristics of Bio-Nanolubricants For Textile Ring Frame Spindles.....	11
Zhetessova G.S., Beisembayev K.M., Abdugaliyeva G.B., Orazbekov D.E., Levshanov R.V. Structural and Parameter Analysis and Study of Mechanized Supports for Their Robotization.....	22
Mustafin A., Sadykov N. Reducing Vibration of Elastically Supported Rolling Bearings on a Centrifugal Pump.....	31
Issagulov A.Z., Sharaya O.A., Vodolazskaya N.V., Arinova S.K., Tugambaeva A.A. Mechanisms for Forming the Surface Structure of Steel Products During Heat Hardening.....	38
Al-Aloosi W., Alaiwi Y., Al-Khafaji Z. Advancements in Concentrated Solar Power: A Review of Heat Transfer and Parabolic Trough Technologies.....	45
Gurpreet Singh, Gyanendra Singh, Harish Kumar H Internal Surface Finish Analysis of Inconel 625 Tube Using MAF and CMAF Processes.....	58
Ospanov B.S., Tatkeeva G.G., Kelesbek N.K. Efficient Power Voltage Management of SiC MOSFET at Low Frequencies.....	66
Tursunov T.M., Tursunov N.Q., Kren A.P., Urazbaev T.T., Ziyamukhamedova U. A Selection of Geometric Parameters of Indenters that Provide Sufficient Sensitivity to Changes in Characteristics in the Volume of Material.....	72
Yurchenko V.V., Smagulov A.S., Reshetnikova O.S., Zharkevich O.M., Mussayev M.M. Investigation of Strength of Belt Conveyor Roller Bearing Shells.....	80
Rakhmatov M., Riskulov A., Nurmetov K. Composite Materials with Enhanced Abrasion Resistance and Certain Functional Characteristics Based on Thermoplastics.....	86
Kim A.S., Mateshov A.K., Savchenko N.K., Shakirova Y.K. Overview of Monitoring Methods for Metalworking Fluids.....	94
Zhumasheva Zh., Nurakhmetov B. Designing a Robot-Manipulator of the Structure of a Human Upper Limb.....	102

Instrumental Testing of Quasi-Binary Ore Materials by the Gamma-Albedo Method

Pak Yu., Pak D.*, Tebayeva A., Aitkaliyev A.

Abylkas Saginov Karaganda Technical University, Karaganda, Kazakhstan

*corresponding author

Abstract. It is noted that the traditional (standard) method of testing ore materials, due to its high labor intensity and low representativeness, cannot serve as the basis for controlling the quality of ores during their extraction and processing. The proposed spectrometric modification of the gamma-albedo method allows eliminating labor-intensive operations of ore grinding, preparing analytical samples (~0.1 mm) and direct chemical analysis for iron. Studies of the spectral distribution of scattered gamma radiation from the Se-75 radioisotope source (~220 keV) on ores with different iron content revealed critical energies and zones of their displacement depending on the ore quality and the energy of scattered gamma radiation. The critical energies found in the spectral distribution of gamma radiation albedo allowed selecting the optimal energy intervals in the hard (above the critical energy) and soft (below the critical energy) regions of the spectrum from the point of view of the maximum contrast of the ratio Ψ value of the scattered gamma radiation intensities measured in the selected energy intervals, with changing the iron concentration. In the course of testing the proposed modification of the method of monitoring the iron content in partially prepared samples weighing ~ 60 kg, with the size of 40 mm, there was achieved the mean square error of 1.32% abs. Reliability of the achieved accuracy is confirmed by the comparative value of the relative mean square deviation of the ratio Ψ value of intensities calculated on the basis of multiple measurements of a partially prepared sample.

Keywords: instrumental testing, gamma radiation albedo, critical energies, standard testing method, ore heterogeneity error, method sensitivity, partially prepared samples

Introduction

The accuracy and reliability of instrumental testing are usually assessed by comparing its data with the results of traditional (standard) testing, the final stage of which is most often the chemical analysis of iron ore material for iron content. With this approach, the results of standard testing are usually accepted as true. Hence, the actions of researchers are aimed at minimizing random discrepancies between the instrumental method and the data of chemical analysis, taking into account the tolerances adopted by the relevant standards [1-2]. However, these tolerances apply only to the final stage of testing.

The standard testing method is characterized by high labor intensity and relatively low representativeness. This is due to the fact that the testing process involves performing lengthy operations: selection of primary (spot) samples from the sampled batch of ore; crushing the combined sample to the size of 40 mm, averaging, reducing and crushing to 10 mm and 3 mm; averaging, reducing and crushing to the size of 0.16 mm; direct chemical analysis of analytical samples for iron content.

The ore heterogeneity creates the problem of its representativeness, i.e. correspondence of the iron concentration in the selected sample and the batch being tested. The error in representativeness of testing (the ore heterogeneity) is the error caused by the fact that the iron content in the sample subjected to direct analysis can differ from its content in the batch being tested.

A significant contribution to the error in determining the iron content in the existing iron ore testing regulated by the Interstate Standard is made by the error of representativeness, which is formed when selecting primary samples from the controlled batch of material [1]. This error is caused by segregation phenomena and statistical fluctuations in the number of iron-containing mineral inclusions in the primary sample. To minimize the effect of segregation, it is envisaged to form a combined sample from the number of selected primary samples. To minimize the effect of statistical fluctuation, it is envisaged to select point samples with the mass selected depending on the size.

Studies have shown that the greatest contribution to the overall [3] error of standard testing is made by the selection of primary samples. The selection error σ_0 characterizes the difference between the iron content in the controlled lot and the combined sample.

In the process of crushing the initial combined sample and subsequent preparation of a sample with the size of up to 40 mm, an error σ_{Π} occurs, which characterizes the difference between the iron content in the combined sample and the prepared sample with the size of up to 40 mm.

At subsequent stages of testing (grinding, averaging, reduction and preparation of samples of analytical size, an error σ_{Π} occurs, which characterizes the difference between the iron content in the sample prepared up to 40 mm and samples of the analytical size.

At the final stage of standard testing, the error σ_X occurs, which characterizes the difference between the results of chemical analysis of analytical samples for iron content.

Considering the independence of errors at each stage of testing and the additivity of variances of individual components, the total testing error σ can be represented in the form:

$$\sigma = \sqrt{\sigma_S^2 + \sigma_P^2 + \sigma_G^2 + \sigma_C^2}, \quad (1)$$

where σ_S^2 is the variance that characterizes the sampling error;

σ_P^2 is the variance that characterizes the error of preparing a sample at the stage of crushing;

σ_G^2 is the variance that characterizes the error at the stage of grinding, reducing and preparing analytical samples;

σ_C^2 is the variance that characterizes the error of chemical analysis.

Thus, the algorithm for selecting primary samples and subsequent stages of sample preparation should ensure that the concentration of iron C_{Fe} in the combined sample corresponds to its value in the sampled ore batch with an error not exceeding the error permitted by the standard.

The standard sampling method according to SS [1] regulates the minimum mass of the selected primary samples and their number depending on the mass of the sampled ore batch, its size and the magnitude of the variation in the quality of the ore by iron content. An important point is the selection of primary samples. Experience shows that, in general, the sampling error depends to a greater extent not on the mass of the selected primary sample, but on the number of samples that make up the combined sample. In general, the iron content in the combined sample will differ from the true iron content in the sampled ore batch.

The standard deviation of the iron concentration in point samples from the iron concentration in the sampled batch of ore can be taken as the parameter characterizing the sampling error σ_S due to heterogeneity. The sampling error was experimentally determined based on the magnitude of the variation in quality (iron concentration) in the selected point samples:

$$\sigma_0 = \sqrt{\frac{\sum_{i=1}^n \bar{C} - C_i}{n-1}}, \quad (2)$$

where \bar{C} is the mean value of C_{Fe} in point samples;

n is the number of point samples.

For sufficiently large values of n , the value of \bar{C} will approach the true concentration of iron in the analyzed batch of ore. The value of quality variation for iron ores of the Lisakovsk deposit (Kazakhstan) estimated according to SS [4], was 2.42%. Hence, the number of point samples n , depending on the specified sampling error, is found using the formula:

$$n = (k \cdot \sigma / \beta_0)^2, \quad (3)$$

where k is the coefficient equal to 2 with 95% -th probability;

σ is the standard deviation of the iron content in primary samples;

β_0 is the specified sampling error, %.

The specified sampling error β_0 changing within the range of (0.90-0.37) depending on the mass of the sampled ore batch, means that on average in 95% of cases the iron content in the combined sample will not differ from its content in the sampled batch by more than β_0 percent.

When sampling an ore batch weighing up to 500 tons and the quality variation value equal to 2.42%, the optimal sampling parameters were found: the minimum mass of spot samples 8 kg; the minimum number of spot samples 29; the mass of the combined sample 232 kg.

In the process of sample preparation, along with crushing and grinding, mixing and reducing the sample is a mandatory operation. SS [1] regulates the minimum required sample mass m after reduction depending on the size and quality variation of the ore

$$m = k_1 \cdot d_{max}^2, \quad (4)$$

where k_1 is the coefficient that depends on the quality variation;

d_{max} is the size of the maximum piece, mm. The size of the maximum piece is taken as the size of the sieve opening on which no more than 5% of the material remains after sifting.

With the selected $k_1 = 0.1$ (ore of the great quality variation) and the size to 40 mm, the needed sample mass made 160 kg.

The standard deviation of C_{Fe} in samples crushed to 40 mm from the iron concentration in the combined sample characterizes the error of ore heterogeneity at this stage of sample preparation. This error σ_{II} estimated by the discrepancy in the iron concentration in samples of this size class, was 1.26%.

A similar approach was used to estimate the heterogeneity at the subsequent stage of testing (grinding, mixing, reducing and preparing samples of analytical size (~0.16 mm)). The error at this stage of sample preparation σ_{III} was 0.84%.

The error of the final stage of testing that characterizes the discrepancy in the results of chemical analysis of analytical samples, was 0.5%.

Thus, the total error of the standard sampling method, estimated according to expression (1) taking into account individual components ($\sigma_o = 2.42\%$, $\sigma_{II} = 1.26\%$, $\sigma_{III} = 0.84\%$, $\sigma_X = 0.5\%$), made 2.9% abs.

2. Research methods

The problems of ensuring the necessary accuracy and reliability of traditional testing methods are especially relevant in connection with the intense development of instrumental nuclear-physical methods of quality control of various raw materials [5-8]. In this case, the metrological characteristics of instrumental methods are usually assessed by a simple comparison of the results of instrumental and chemical analyses, unreasonably neglecting significant errors at the labor-intensive stages of traditional testing. In this regard, the error of the standard testing method should be considered as an acceptable limit of the accuracy of instrumental methods. Therefore, the accuracy and reliability of nuclear testing methods cannot be assessed by direct comparing their data with the results of chemical analysis.

At present, standard testing is mainly used at Kazakhstan mining and metallurgical enterprises, the final stage of which is chemical analysis. In some cases, chemical analysis is successfully replaced by nuclear-physical methods.

The X-ray fluorescence method that consists in measuring the X-ray fluorescence of the elements being determined is widely used for the analysis of quasi-binary materials [9-10].

Various modifications of this method are characterized by relatively high sensitivity and sufficient accuracy of quantitative analysis of finely ground material of analytical size (~0.1 mm). X-ray fluorescence of iron is used to determine the pyrite content in coals.

The fundamental feature of the new modification of the method is selection of optimal energy parameters in the area of analytical lines of sulfur, iron and scattered gamma radiation. The capabilities of the X-ray fluorescence method are limited to the analysis of finely ground samples. Labor-intensive sample preparation processes and low representativeness of analytical samples are retained.

The value of the gamma radiation albedo is widely used in the practice of studying various metals and quasi-binary materials [8-11]. Depending on the energy of the primary and registered scattered gamma radiation and the probe parameters, enhanced metrological characteristics of the gamma-albedo method are achieved. The novelty of the two-probe study of complex substances consists in measuring the energy spectra of scattered gamma radiation at different probe lengths, finding critical energies corresponding to the maximum in the albedo spectra of gamma radiation and optimal energy intervals that ensure maximum sensitivity to the effective atomic number of the substance being studied.

A distinctive feature of the gamma annihilation method is registration of annihilation radiation arising from the effect of electron-positron pair formation. The proportionality of the macro cross-section of pair formation from the atomic number (effective atomic number for substances) is the basis for the analysis of quasi-binary materials, in particular coals [12]. To increase sensitivity, an improved technique has been developed that is distinguished by the choice of the optimal probe length for annihilation gamma radiation and the optimal energy range for scattered gamma radiation. The gamma annihilation method can be successfully applied in the analysis of quasi-binary materials containing heavy elements.

The neutron activation method is widely used for elemental analysis in materials science and mining and geological studies due to its high sensitivity and selectivity of the analysis due to the possibility of taking into account competing nuclear reactions, the choice of time and energy parameters [13]. The high labor intensity of the multi-stage activation method and the low representativeness of the analysis (activation sample 1-2 grams) serve as constraints.

Modifications of the neutron-gamma method of inelastic scattering of fast neutrons and radiative capture of thermal neutrons are used for elemental analysis of various materials [14]. A method for instrumental quality control of solid fuel has been developed, based on spectrometry of neutron-gamma radiation of inelastic scattering of fast neutrons by carbon and radiative capture of thermal neutrons by mineral components (ash-forming elements) [15]. An inversion alternating nature of the dependence of sensitivity to the heat of combustion of fuel on the layer thickness has been established. Optimized selection of boundary values of the layer thickness and instrumental signals allows achieving satisfactory accuracy of quality control of coarse-dispersed fuel.

The advantage of the method is the relatively high depth of research, which allows for non-destructive analysis of solid bulk materials in large masses with the ability to compensate for the disturbing influence of neutron-moderating and absorbing properties of the analyzed materials.

The aim of the study is to improve the existing system of standard testing of iron ores in terms of reducing labor intensity, increasing the efficiency and accuracy of obtaining representative information of the quality of iron ores in large masses. Labor intensity is reduced by eliminating a number of standard testing operations (crushing, grinding, reducing, and preparing analytical-size samples). Increased accuracy and representativeness are achieved by determining the iron concentration in partially prepared large-mass samples using the deep gamma-albedo method that provides the increased sensitivity to iron due to optimization of the scattered gamma-radiation spectrometry principle.

Due to its relative simplicity, the gamma-albedo method is widely used in geological and geophysical studies and in the mining and metallurgical industry. The intensity of scattered gamma radiation, which is the main metrological characteristic of this method, generally depends on the effective atomic number of the medium, the energy of the primary gamma radiation, and the geometric conditions of measurement. The choice of primary gamma radiation energy is made depending on the task at hand and the object of testing (powder sample, broken rock mass, natural occurrence conditions) from the point of view of ensuring maximum sensitivity to iron, maximum depth (representativeness) of the study and minimum effect of the granulometric composition.

Depending on the material and granulometric composition of the ores being sampled, stability of the relationship between the effective atomic number and the iron content, the range of its variation and the density of the ore, various methodological approaches and modifications of the gamma-albedo method are used, taking into account the features of inversion dependences and multiple scattering of polyenergetic gamma radiation, angular and linear characteristics of probe devices.

There are examples of determining C_{Fe} in prepared samples of the 3 mm class by the gamma-albedo method. The error does not exceed 0.5% with the sample mass of about 1 kg. Gamma-albedo testing of railcars using hard gamma radiation Cs-137 (661 keV) is ineffective due to its low sensitivity to iron and low representativeness of testing. Considering the dimensions of the railcar, a significant mass of the ore being sampled is outside the effective control zone. Any instrumental testing method should be considered effective if its results apply to the entire volume of the ore being monitored.

The variety of factors influencing the metrological characteristics of testing actualizes the choice of the optimal energy of primary gamma radiation in terms of the maximum sensitivity to iron and the minimum sensitivity to interference. In this case, the interference is the size of the ore, the dispersion of which causes heterogeneity.

3. Results and discussion

Studies of the gamma radiation albedo have established that the dependence of the relative sensitivity of the method to the effective atomic number S_Z on the value of Z has an inversion character [8]. Moreover, the inversion region (maximum S_Z) shifts to the region of increased values of the effective atomic number with an increase in the energy of primary gamma radiation. The error due to the heterogeneity of the sampled ore (size) depends in a complex way on the particle diameter (size variation), ore composition and the depth of the method [3]. In the general case, the error due to size variation has an inversion character from the energy of primary gamma radiation for a specific particle diameter. The maximum error is observed when the depth of the method (energy of gamma radiation, Z of the ore) is commensurate with the particle size.

Uncontrolled fluctuations in particle size introduce an error into the results of the method, which can be estimated from the expression:

$$\sigma = \left[\left(\frac{S_d}{S_{Fe}} \right)^2 \cdot D \right]^{1/2} \quad (5)$$

where S_d is the method sensitivity to the size;

S_{Fe} is the method sensitivity to iron;

D is the size variance.

Thus, to achieve the minimum error due to heterogeneity (size), the optimal energy of primary gamma radiation should be selected based on the minimum S_d/S_{Fe} ratio. These recommendations predetermined the possibility of express testing of iron ores in large masses using the gamma-albedo method.

The spectrum of scattered gamma radiation depends in a complex way on many parameters: the energy of the primary gamma radiation, the density and material composition of the sample object, and the linear-angular characteristics

of the probe. A spectrometric version of the gamma-albedo method is known, which consists in measuring the intensity of scattered gamma radiation in two energy ranges of the spectrum and determining the value of Z or the concentration of the heavy component (ash content in coals, iron content in ores) based on the value of the ratio of the measured intensities in the selected spectrum ranges. The method, having sufficient noise immunity to density variations, is characterized by a relatively low sensitivity to iron. How to achieve an increased sensitivity of the method to Z (iron content) and the minimal effect of the size (dispersity) of the analyzed ore?

To minimize the disturbing effect of particle size, the energy of primary gamma radiation is selected, at which the depth of the method significantly exceeds the maximum particle size. The gamma-albedo method, implemented using a ^{75}Se radioisotope source (~ 220 keV), provides a research depth of about 14 cm, which is more than 3 times greater than the maximum particle size in the prepared samples.

A relatively low sensitivity of the spectrometric modification of the gamma-albedo method is explained by the choice of non-optimal measurement parameters, at which the same qualitative nature of the intensity change in the normalized spectral regions is observed with a change in the iron concentration in the ore.

There were studied the features of the spectral distribution of the albedo of polyenergetic ^{75}Se gamma radiation depending on the probe parameters and the iron concentration in the ore.

From the probe device, the collimated gamma-radiation flow is directed perpendicularly to the ore surface. Scattered gamma radiation is recorded using a 40×30 mm NaJ(Tl) scintillation detector and an AI-1024 multichannel analyzer. The objects of control are partially prepared iron ore samples of the 40 mm class, weighing ~ 60 kg, placed in a measuring cuvette measuring $50 \times 30 \times 16$ cm, ensuring the absence of edge effects. The spectral distribution of scattered gamma radiation was studied on control and reference samples with an iron content of 29.7% and 49.3% at different values of the probe length L and the distance H from the probe to the ore surface.

Figure 1 shows the instrumental spectra of scattered gamma radiation from reference samples with different iron concentrations. The spectra were obtained with the parameters L and H , providing an inversion character in the behavior of the intensities of scattered gamma radiation in different energy ranges of the spectrum. The hard peak in the spectrum is mainly caused by single scattering of gamma quanta with the energy of 265 keV. The shift in the critical energy depending on the iron concentration in the ore is caused by changing the average scattering angle of the primary gamma radiation and intense photoelectric absorption of lower-energy gamma radiation with increasing the iron concentration. In the region above the critical energy, the increased intensity of scattered gamma radiation is due to increasing the electron density.

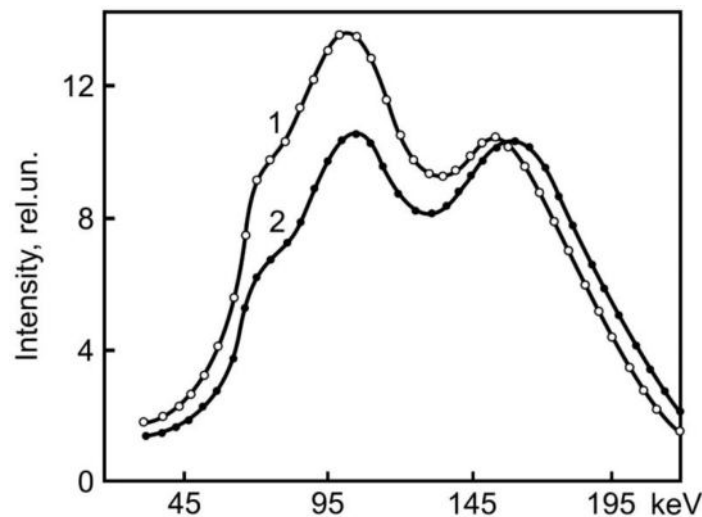


Fig.1. Spectra of gamma radiation albedo: 1 - $C_{\text{Fe}} = 30\%$; 2 - $C_{\text{Fe}} = 50\%$

The inversion character in the behavior of the soft and hard components of the spectrum with changing the iron concentration is observed with the characteristics of the L and H probes (the average scattering angle changes), at which the critical energies, the maxima in the spectrum are in the energy intervals of (90-110) keV and (145-160) keV. This is explained by the predominant role of photoelectric absorption of gamma radiation with the energy less than ~ 100 keV for iron and the predominant role of Compton scattering for gamma radiation with the energy above ~ 150 keV.

By successive changing the parameters of the H , L probe, the energy spectra of the gamma radiation scattered from the reference samples were measured. By the machine processing of the measured spectra, the dependences of the

relative sensitivity of S_{Fe} to iron on energy were constructed (Figure 2). The energy quantization step and the width of the energy window were chosen equal to 25 keV. The relative sensitivity S_{Fe} is estimated as the relative increment of the measured intensity for a single change in the iron content.

The dependence of the relative sensitivity to iron S_{Fe} on energy has an inversion alternating character. The maximum sensitivity is observed in the region of maximum intensity (critical energy). At energies above ~ 140 keV (depending on H) the sensitivity changes its sign. With increasing the iron content, the intensity of scattered gamma radiation increases. Moreover, with decreasing the air gap H, the region of zero sensitivity occurs at high values of the energy of scattered gamma radiation.

Based on the established patterns, the control parameters (probe parameters L and H, energy ranges of the recorded gamma radiation) were optimized, which made it possible to increase the sensitivity of the spectrometric modification of the gamma-albedo method of monitoring the iron content in ores [8].

The optimal energy intervals in the soft region of the spectrum (75-110) keV and the hard region of the spectrum (180-215) keV provide the maximum contrast of the ratio values of the intensities of scattered gamma radiation measured in the selected energy intervals of the spectrum to the change in C_{Fe} .

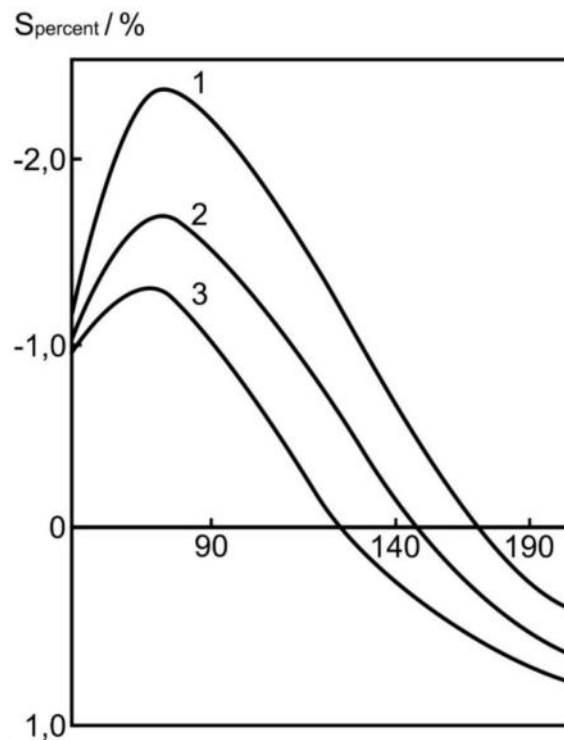


Fig.2. Sensitivity to iron dependence on the energy of gamma radiation registered: 1 – H=2 cm; 2 – H=4 cm; 3 – H=7 cm

The sensitivity to iron of the spectrometric gamma-albedo method depending on the probe parameters L and H is shown in Figure 3. The optimal measurement parameters were selected: L=18 cm and H=2 cm. With the selected probe parameters and optimal energy intervals, the relative sensitivity of the proposed method to iron was 2.86%.

A relatively high sensitivity allowed providing the satisfactory accuracy of ore quality assessment by spectrometry of scattered gamma radiation with Se-75 source.

When testing and analyzing 18 partially prepared samples of iron ores of the 40 mm class and weighing about 60 kg in the range of iron concentration variation of 32-49%, the mean square error of iron determination of 1.32% abs. was achieved. The relative statistical error at the selected time of 7 minutes was less than 1%.

To assess reliability of the proposed instrumental testing method, additional studies of the heterogeneity of the sampled ore were carried out at the stage of sample preparation of the 40 mm class. For this purpose, the averaged partially prepared sample was divided into 4 parts by quartering. Each second part was placed in the measuring cuvette as a point sample and the method reading was measured: the ratio Ψ value of the intensities of scattered gamma radiation in the selected energy ranges of the spectrum. After each measurement, the sample was unloaded and reloaded. Multiple measurements were performed under identical conditions. The standard deviation of the measured intensity ratio Ψ can be taken as the parameter characterizing the error due to heterogeneity at a given stage of testing. The relative standard deviation of the ratio Ψ value for 20 control measurements was 4.12%, which is adequate to the standard error of 1.44%

abs. for iron. These results are in satisfactory agreement with the previously obtained error of 1.26% abs. at this stage of standard testing.

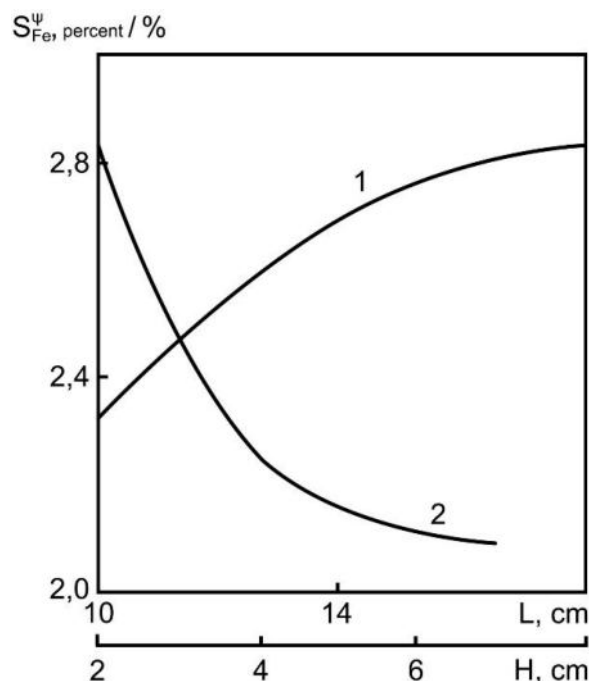


Fig. 3. - Spectrometric method sensitivity to iron dependence on geometrical parameters: 1 – on the probe length ($H=2$ cm); 2 – on H ($L=18$ cm)

Conclusion

A new spectrometric modification of the gamma-albedo method of monitoring the iron content in partially prepared samples weighing about 60 kg is proposed. It allows eliminating labor-intensive stages of grinding, preparation of analytical samples and direct chemical analysis. The established inversion, alternating-sign nature of sensitivity to iron from the energy of scattered gamma radiation allows optimizing the control parameters (energy intervals and probe characteristics), providing the maximum sensitivity to iron of the proposed modification of the method. In the process of laboratory testing the developed modification of the method of testing iron ores of the 40 mm class in the range of iron concentration variation of 32-49%, the mean square error in determining the iron concentration was 1.32% abs. Reliability of the obtained data on the accuracy of testing is confirmed by the results of an additional study of ore heterogeneity at the recommended stage of testing partially prepared samples. The proposed modification of the gamma-albedo method allows improving the standard testing system in terms of increasing reliability, representativeness and efficiency of the obtained information of the ore quality and reducing labor intensity by eliminating a number of testing stages.

Acknowledgment. This research has been/was/is funded by the Science Committee of the Ministry of Science and Higher Education of the Republic of Kazakhstan (Grant No. AP23485184).

References

- [1] Interstate standard SS 15054-80. Iron ores, concentrates, agglomerates and pellets. Methods of sampling and preparing samples for chemical analysis. IPC Publishing House of Standards. 1999.
- [2] SS 53657-2009. Iron ores, concentrates, agglomerates and pellets. Method of determining iron in terms of oxide. Moscow: Standartinform, 2010.
- [3] Pak Y.N., Vdovkin A.V. Borodachyov A.D. The effect of heterogeneity in gamma-ray albedo analysis of mineral raw materials. Applied Radiation and Isotopes 54 (2001), 509-517.
- [4] SS 25470-82 (ST SEV 2845-81). Iron ores, concentrates, agglomerates and pellets. Method of determining the degree of homogeneity by chemical and granulometric composition. M. Publishing House of Standards, 1983.
- [5] Bolshakov A.Yu. Nuclear-physical testing systems for ore quality management. L.: Nedra, 1979, 188 p.
- [6] Shestakov V.V. Nuclear-geophysical express analysis of transported ores and resource-saving technologies. Sverdlovsk, 1987, 112 p.
- [7] Pak Yu.N., Vdovkin A.V. Calculation of the sensitivity of determining the effective atomic number of complex media by the albedo of gamma radiation. Atomic energy. Vol. 74, issue 6, 1993.
- [8] Pak Yu., Pak D., Imanov M. et al. Method of analyzing a multicomponent substance. Eurasian patent 034998, 2020.
- [9] M. Tiwari, S. K. Sahu, R. C. Bhangare, P. Y. Ajmal, G. G. Pandit. Elemental characterization of coal, fly ash, and bottom ash using an energy dispersive X-ray fluorescence technique. Applied Radiation and Isotopes. 2014. 90. P.53-57.

- [10] Cherkashina T.Yu., Panteeva S.V., Pashkova G.V. Applicability of direct total reflection X-ray fluorescence spectrometry for multielement analysis of geological and environmental objects. *Spectrochimica Acta Part B: Atomic Spectroscopy*. Volume 99, 2014, P. 59-66.
- [11] Pazirandeh, A., Sobhkhiz, N.V. Theoretical and Experimental Investigation on Backscattered Low Energy Gamma Radiation from Different Metals. *Iran. Int. J. Sci.* 2000, 1 (2), 147–147.
- [12] Pak Yu., Vdovkin A.. The gamma annihilation method of controlling ash-content in coals // *Nuclear Geoph.* – 1991. - №3. P. 345-351.
- [13] Blideanu V., Besnard-Vauterin C., Khouri K. A., Rapp B., Bennaceur W., Skukan N. New measurements on neutron-induced activation towards an innovative approach for controlled interferences in neutron activation analysis // *Radiation Physics and Chemistry*, Volume 234, 2025.
- [14] Hosamani M.M., Vinayak A., Hiremath G.B., Prashant N., Pati Nl, Badiger N.M. . Determination of neutron moderation parameters through neutron captured gamma ray emission – A novel method // *Annals of Nuclear Energy*. Volume 171, 2022.
- [15] Pak Yu. N., Kolesova S.B., Pak D. Yu. Instrumental Solid Fuel Quality Control by a Neutron Method // *Solid Fuel Chemistry*, Vol. 55, No 6, 2021. pp. 414-419.

Information of the author

Pak Yuri Nikolayevich, Dr. eng., professor, Abylkas Saginov Karaganda Technical University
e-mail: pak_gos@mail.ru

Pak Dmitri Yuryevich, cand. tech. sci., associate professor, Abylkas Saginov Karaganda Technical University
e-mail: pak_kargtu@mail.ru

Tebayeva Anar Yulayevna, master, lecturer, Abylkas Saginov Karaganda Technical University
e-mail: anara.tebaeva@gmail.com

Aitkaliyev Ardak **Kuandykovich**, doctoral student, Abylkas Saginov Karaganda Technical University
e-mail: aitkaliyev86@gmail.com

Investigation on Tribological Characteristics of Bio-Nanolubricants For Textile Ring Frame Spindles

Gowthaman A.M. ^{1*}, Dr. P. Nallasamy², Mr. Shanmuga Sundaram D³, Mr. S. Yashwanth Kumar⁴

¹Research scholar, Department of Mechanical Engineering, PSG college of technology, Coimbatore, India.

²Assistant Professor, Department of Mechanical Engineering, PSG College of Technology, Coimbatore, India.

³Assistant Professor, Department of Mechanical Engineering, PSG College of Technology, Coimbatore, India.

⁴PG Scholar, Department of Engineering Design, PSG College of Technology, Coimbatore, India

*corresponding author

Abstract. Energy loss due to friction is one of the most prominent problems in the industry. Most of the textile industries have this prominent problem and uses lubrication to minimize it. Mineral oil-based lubrication has been widely used but there seen no such significant improvement in performance of the system. This investigation aims to provide the solution of efficient and eco-friendly bio-nanolubricants. An optimum level of nanoparticles with biodegradable oil as base oil with a surfactant combination, with its physical and tribological properties could replace the conventional oil with improvement in performance. The nanoparticles and base oils which are taken for the investigation are titanium dioxide (TiO₂), graphene, copper oxide (CuO), sesame oil, coconut oil and pongamia oil. The physical characterization reveals that all the developed bio-nanolubricants show higher viscosity, flash and fire points and cloud and pour points and in tribological characterization sesame + CuO nanolubricant has shown 79% less friction than the conventional lubricant. Based on conclusion of characterization sesame + CuO nanolubricant, pongamia + graphene nanolubricant and pongamia + TiO₂ nanolubricant are the most suitable for textile ring frame spindles. Additionally, dispersion stability, thermal conductivity and anti-corrosion test of the developed nanolubricants are also favorable. In the field test, pongamia + TiO₂ nanolubricant has shown more heat transfer which in turn less heat generation due to its low coefficient of friction (COF) than the conventional lubricant Servospin EE10 and in the power consumption test, pongamia + TiO₂ nanolubricant has shown 5.5% less energy loss than the conventional lubricant and it is evident that pongamia + TiO₂ nanolubricant is suitable for this application. Furthermore, this study highlights the potential of utilizing the biodegradable oils as environmentally friendly and sustainable alternatives to mineral oil.

Keywords: Bio-nanolubricants, ring frame spindles, friction mechanisms, power consumption, heat generation.

Introduction

Energy losses due to friction are incredibly high. Energy losses in any mechanical part due to friction result in heating and promote the wear on the surfaces of moving part. Energy losses due to the friction can be reduced by a few technologies such as the design of tyres and bearings, tribology, and additives. [1] Further, in order to overcome the energy losses, the lubricant which imparts the best lubrication is essential. [4]

The lubrication of the ring frame spindle, an indispensable component within the textile industry, plays a paramount role in ensuring seamless operation and optimal yarn production. This intricate cylindrical apparatus, comprising various elements like bearings, shafts, and gears, necessitates meticulous lubrication to minimize friction and wear. Adequate lubrication guarantees the smooth rotation of the spindle, reducing mechanical strain and extending its lifespan.

1 Preliminary field study

1.1.1 Energy study of a textile industry

Energy study was performed at Supertex mills Pvt ltd, India. The primary focus is to identify the areas of high-power consumption.

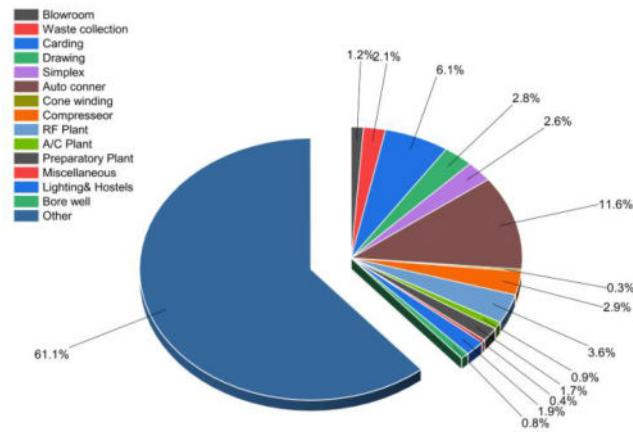


Fig.1. - Power distribution of textile mill

The figure 1 shows that 61.1% of total power consumption is in the ring frame machines. Around 58% of power consumption in a single ring frame machine is because of spindles. From the energy study it is evident focusing on the spindles with consideration of different factors can lead to efficient energy saving.

1.1.2 Effect of lubrication on spindle power consumption

As there are many factors influencing the power consumption in the textile ring frame spindle, it is important to study all of it. Lubrication which is used for reduction of friction, and by optimizing the lubricant can further reduce friction and the power consumption too. An energy study was carried out by considering the factor as lubricant and the results are shown in table 1.

Table 1. Power consumption comparison

Power consumption comparison		
Description	EE10 (Old)	EE10 (New)
Number of spindles per machine	1008	
Spindle wharve diameter (mm)	19	
Ringframe speed (rpm)	18020	
Study duration (hrs)	2	
Units consumed for 2 hrs (kW)	25.76	25.4
Units consumed per hour (kW)	12.88	12.7
Power saving for new oil per hour (kW)	0.18	

The study was carried out in LMW LR6 machine where lubricant used in ring frame spindle was Servospin EE10. The machine consists of 1008 spindle and runs at idle condition for the energy study. Study was carried out for two hours. The study shows that over a period, the power consumption increases and may be due to degradation of lubricant. This study is evident that the lubricant also influences the energy losses.

2 Literature review

P. Nallasamy et al., 2015 [6] studied the performance of PAO (Polyalphaolefin) + 1wt% MoS₂ nanolubricant and found it was better than standard slideway lubricant ISO VG 32. Reduction of 24% in COF was observed. P. Nallasamy et al., 2018 [5] studied on the tribological properties of 0.1% wt. of CuO based nanolubricants for machine tool slideway. Eswaraiyah. V et al., 2011 [8] prepared graphene based engine oil nanofluids and performed their frictional characteristics (FC), antiwear (AW), and extreme pressure (EP) properties and determined that 0.025 mg/mL of graphene in engine oil, COF and WSD were reduced by 80 and 33%, respectively. Wu, H et al., [9] determined that 0.8 wt.% TiO₂ water-based lubricant leads to the lowest COF and the best anti-wear ability under all the lubrication conditions at room temperature.

Zulkifli et al., 2013 [10] studied that the nanoparticle also improved WSD of the TMP esters especially at low load (40kg) by creating an additional protective layer. Koshy C P et al., 2015 [13] focuses on the tribological performance of coconut oil with MoS₂ nanoparticles and observed enhanced thermal and tribological properties. Shafi W K et al., 2018 [15] studies highlight the use of bio-degradable nanolubricants and provides the reason for replacement of mineral oils.

Kiu, S. S. K. et al., [7] studied the tribological behaviors of graphene nanoparticles as lubricant additive in vegetable oil were investigated as a function of nanoparticle concentration. The results showed that 50 ppm is the optimum

concentration that recorded the lowest wear scar diameter and friction coefficient as compared to control sample. Shaari et al., [11] studied that nanoparticle TiO_2 as additive has slightly improved the lubricating properties of palm oil biolubricant.

Azman et al., 2018 [12] observed that the presence of copper (II) oxide nanoparticles of 0.34 wt.% in PKO has improved the tribological properties by reducing the COF and WSD by 56 and 48% respectively. Virwal Harsh Rajubhai et al., [14] studied minimum friction coefficient and wear was observed at 0.075% concentration which gets further increased at 0.1% concentration of CuO with pongamia oil.

Mohamed Kamal Ahmed Ali et al., [2] performed analysis with 5W30 engine oil and Al_2O_3 and TiO_2 nanoparticles with oleic acid as surfactant. Uflyand et al., [3] the tribological properties was evaluated using different test experiments under different operating conditions. The results showed a decrease in the friction coefficient and wear. It was also found that the better performance of the nanolubricant was due to formation of tribo films on the surface.

It is to be noted that no studies have been carried out so far for the application of textile ring frame spindle using biodegradable oil based nanolubricants. This research work thrives to bridge the gap to develop the high-performance biodegradable based nanolubricant for the textile spindle with comparison to the conventional lubricant.

2 Experimental investigations

2.1 Preparation of nanolubricants

The biodegradable oils selected were sesame oil, coconut oil and pongamia oil. The nanoparticles choose were TiO_2 at 0.8wt%, CuO at 0.34%, graphene at 0.0025% and surfactant was oleic acid. The nanoparticles, base oil and surfactant mixture was stirred manually for 10 minutes and to obtain good dispersion stability the mixture was subjected to ultrasonication for 4 hours. The conventional ring frame spindle lubricants Servospin EE 10 and Servospin EE 22 were chosen for comparing the tribological performance of nanolubricants.

2.2 Physical properties

2.2.1 Viscosity testing

The kinematic viscosity was measured for all the developed nanolubricants using Redwood viscometer. The testing was performed at three different temperatures which are 26°C (room temperature), 40°C and 80°C. The results are plotted in form of graph as shown in Figure 2.

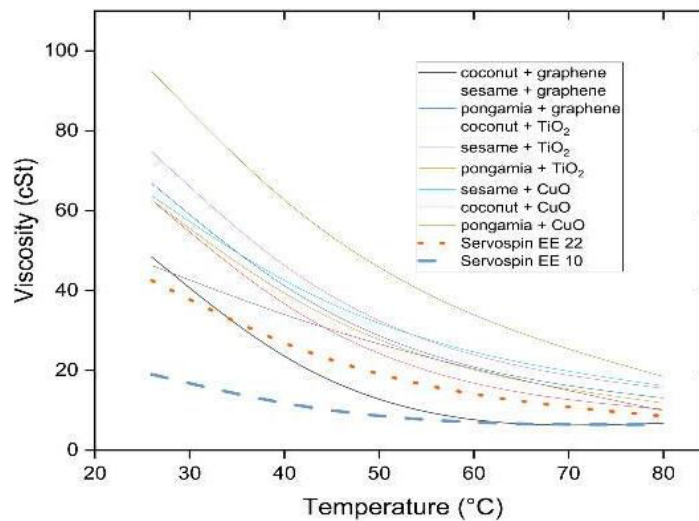


Fig.2. - Viscosity of nanolubricants

It is found that the kinematic viscosity of the developed nanolubricants is higher than the conventional lubricants, which shows a significant improvement in the viscosity. From literature study, for high-speed applications viscosity of 30 cSt to 50 cSt is considered as optimal value. The nanolubricants such as sesame + graphene, pongamia + graphene, sesame + TiO_2 , pongamia + TiO_2 , sesame + CuO, pongamia + CuO are considered to have most suitable viscosity for the application. The viscosity of all the nanolubricants decrease with increase in the temperature.

2.2.2 Flash point and fire point test

The flash point and the fire point of all the developed nanolubricants shown in figure 3 are higher than the conventional lubricant. The flash point and fire point of all developed lubricants lies above 200°C. Coconut + TiO_2 nanolubricant shows 50% higher flash point than conventional lubricant. And sesame + TiO_2 nanolubricant shows 51% higher fire point than conventional lubricant.

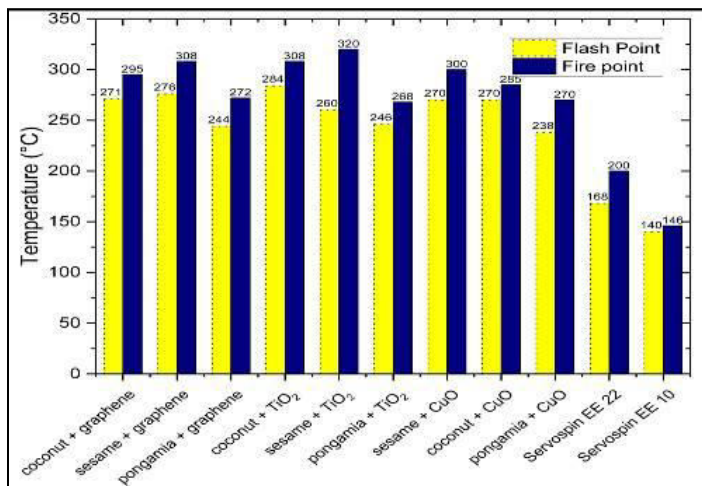


Fig.3. - Flash point and fire point

2.2.3 Cloud point and pour point

The cloud point of all the developed nanolubricants is closer to the room temperature and it will not affect the efficiency in the application. And the pour point of the all the nanolubricants lies below 0°C as shown in figure 4 which is considered for colder conditions too.

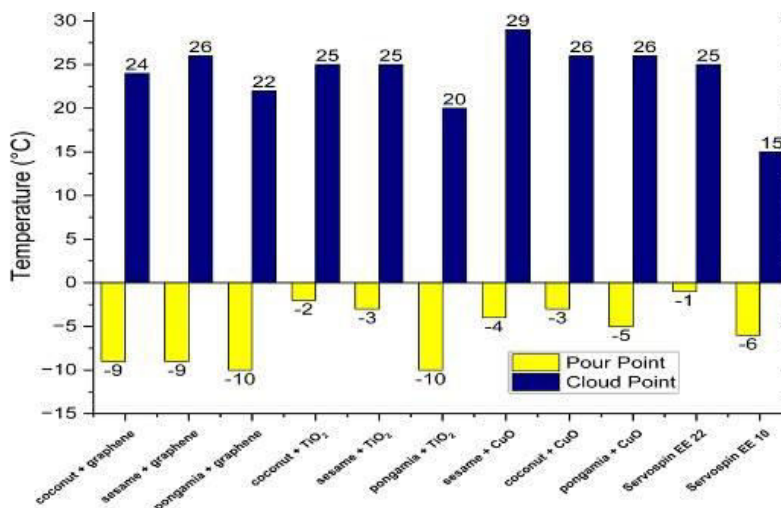


Fig.4. - Cloud point and pour point

2.3 Tribology property test

2.3.1 Determination of friction and wear

The pin on disc wear test rig (DUCOM) is used study the friction characteristics of the lubricant as per ASTM G99-05 standard is shown in figure 5. The experiments were carried out with the following conditions:

- Speed: 1500 rpm
- Applied Load: 5 N
- Time duration: 5 minutes
- Track diameter: 80 mm
- Pin material: Aluminum alloy
- Track material: EN31



Fig.5. - Pin on disc wear test rig

This tester is used to determine the friction and wear characteristics of the specimen under lubrication. It is interfaced with the computer through WinDucom software for viewing the results. The specifications of the pin on disc equipment are listed in the Table 2.

Table 2. Specifications of pin on disc wear test rig

S.No	Parameters	Description	Remarks
1	Normal Load (N)	5-200	Dead weights 0.5,1&2Kg
2	Frictional Force (N)	Up to 200	Button or Beam type sensor
3	Wear measurement (microns)	5000	LVDT sensor
4	Disc Speed (rpm)	100±2000	Variable
5	Motor and drive	AC motor with drive	2 kW
6	Test duration	Pre set Timer	99 Hr:59 Min:59 Sec
7	Machine dimensions (feet)	3 x 2.5 x 3	

3.4 Field test

3.4.1 Heat generation test

A) Test after a week of time

The heat generation test was performed at Supertex mills India private limited, Coimbatore. The spindle used for testing heat generation is HD spindle of LR6 machine of LMW make shown in figure 6. The instrument used for measurement is FLIR E4 infrared thermal camera, specification given in table 3, which is an industrial instrument for the measurement of heat generation. In this test, the developed nanolubricants are filled inside the spindle and after a week of run, the temperature was measured continuously at an interval of one hour for 12 readings. The neck region of the bolster was taken for the heat generation as it has high heat generation than any other region. Each lubricant was filled with two spindles of the machine.

Table 3. FLIR E4 Specification

Measurement	Description
Object temperature range (°C)	-20 to +250
Accuracy (°C)	±1 of reading, for ambient temperature 10°C to 35°C (+50°F to 95°F) and object temperature above +0°C (+32°F)

B) Test after a month of time

In this test, the developed lubricants are left unchanged at the textile ring frame spindles for a month with continuous run at production. Same procedure was followed and the measurement of heat generation was taken.

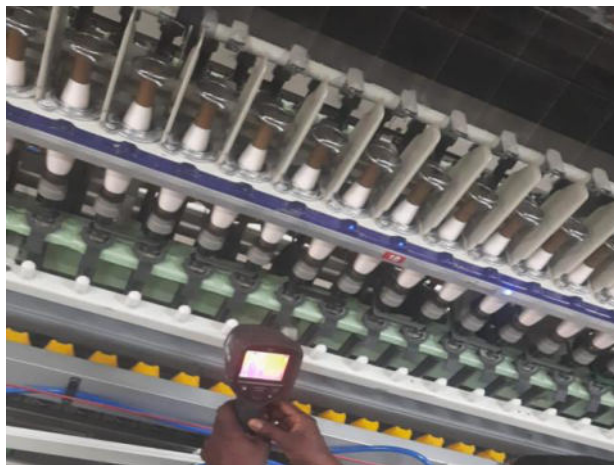


Fig. 6. - FLIR E4 measuring Spindle heat

3.4.2 Volumetric change test

The volumetric change test is the observation of volume of the developed nanolubricants after a month of run using dip stick shown in figure 7. This test is also known as dip stick analysis. Due to degradation or evaporation, the volume of bio-oils may change and it is necessary to monitor the volume of the lubricant in the spindles.



Fig.7. - Dip stick analysis

3.4.3 Power consumption test

The power consumption test was performed at Supertex mills India private limited, Coimbatore. The machine used for power consumption test was LR6 machine of 144 spindles shown in figure 8. The spindles of the machine are manually filled with the developed nanolubricants.



Fig. 8. LR6 Machine

The power consumption always varies with speed of spindles and it necessary to test at various speed, so the test was taken at speed of 18000 rpm for 4 hours and 14000 rpm and for 2 hours.

3 Results and discussion

3.1 Results of friction and wear test

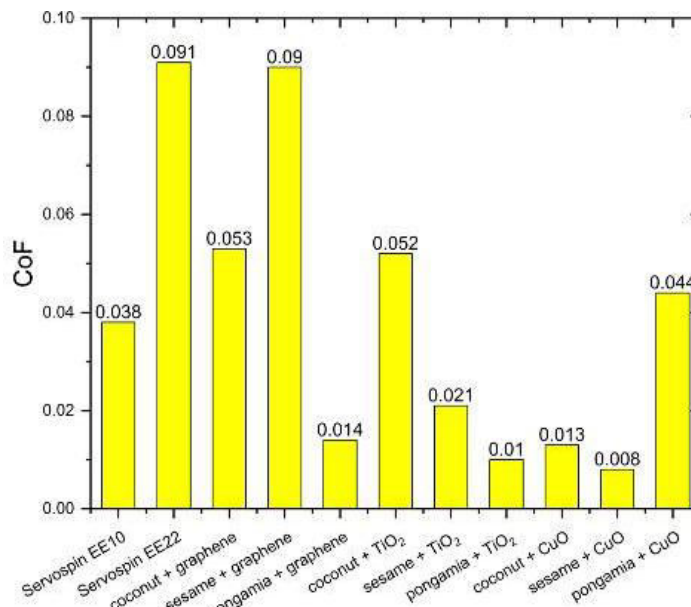


Fig. 9. - CoF of nanolubricants

From the graph 9, it is evident that nanolubricants such as pongamia + graphene, sesame + TiO₂, pongamia + TiO₂, coconut + CuO, sesame + CuO have shown lesser COF than the conventional lubricants. The mechanism behind for the reduction in friction of pongamia + graphene is the protective film formation [18], for pongamia + TiO₂ is rolling effect [16] and for sesame + CuO is the self-repairing effect called as mending effect [17]. Sesame + CuO has shown 79% less COF than the conventional lubricant.

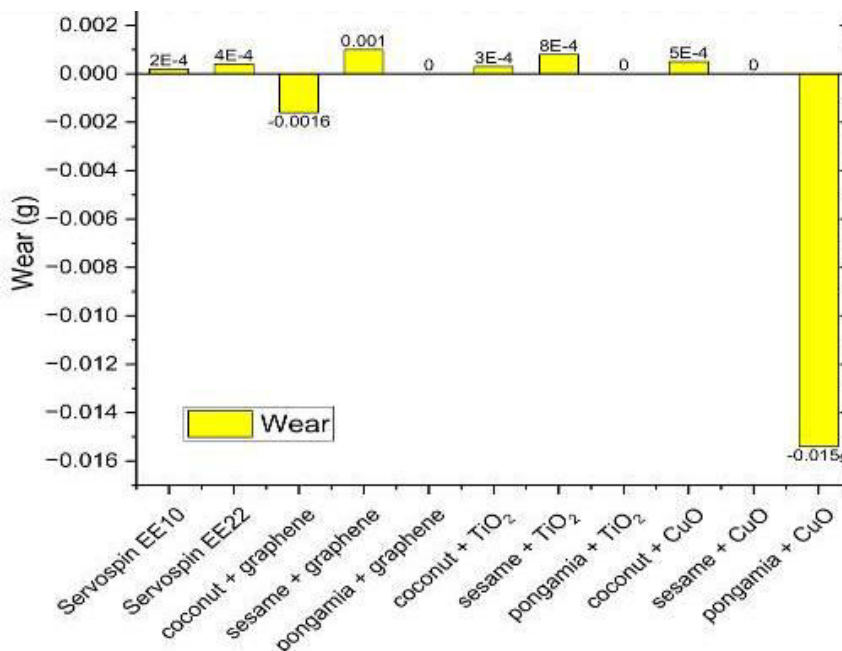


Fig. 10. - Wear

The wear of the pin materials due to friction in wet lubrication condition is shown in figure 10. Results show that pongamia + graphene, pongamia + TiO₂ and sesame + CuO nanolubricants have zero wear.

From the test results of viscosity, flash point and fire points, cloud point and pour points, friction and wear, the following bio-nanolubricants are found to be more suitable for the application:

- Sesame + CuO nanolubricant;
- Pongamia + graphene nanolubricant;
- Pongamia + TiO₂ nanolubricant.

3.2 Results of thermal conductivity test

The thermal conductivity of the nanolubricants is found to be higher than the conventional lubricant Servospin EE10 as shown in figure 11.

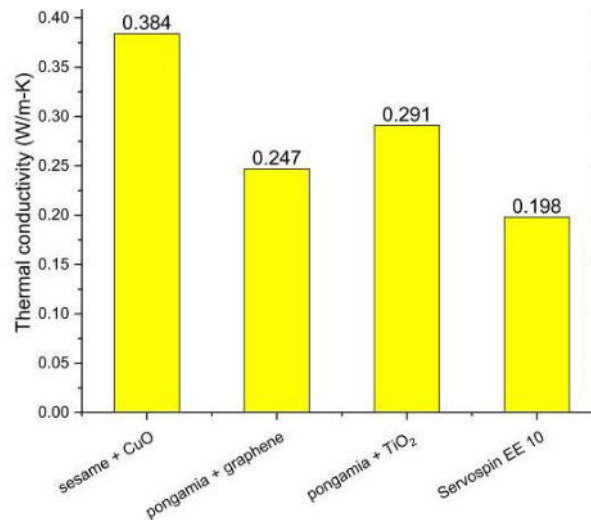


Fig. 11. - Thermal conductivity of nanolubricants

The sesame + CuO nanolubricant shows 48% higher thermal conductivity than the conventional lubricant Servospin EE10. Therefore, implementation of these nanolubricants would enhance the carrying away of heat from the application.

3.3 Results of anti-rust test

The nanolubricants are tested for pH level to determine the nature of the lubricant. The pH level of all the selected nanolubricants lies between 6 to 8 pH which is neutral. The neutral pH is more satisfactory for the anti-rust property. Synthesis chemical laboratory, Coimbatore certified that the nanolubricants have anti-corrosive property through salt spray analysis.

3.4 Results of dispersion stability

For better dispersion stability of nanoparticles in nanolubricants, the zeta potential value should not lie between -25 mV to +25 mV and from the figure 12 it is clear that zeta potential value of all the nanolubricants lie well outside the limit.

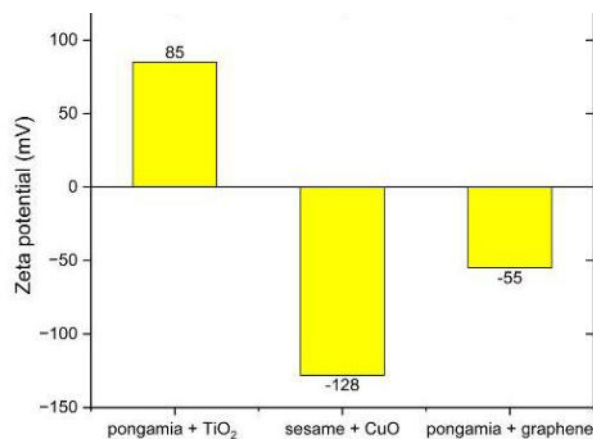


Fig. 12. - Dispersion stability of nanolubricants

3.5 Results of field test

3.5.1 Heat generation test results

The heat generation test results of the ring frame spindle after a week (figure 13) shows that pongamia + TiO₂ nanolubricant has better heat transfer capacity than the conventional lubricant due to its high thermal conductivity and less

coefficient of friction. Sesame + CuO and pongamia + graphene nanolubricants show equivalent heat transfer as of the conventional lubricant Servospin EE10.

The heat generation test results of the ring frame spindle after a month (figure 14) shows that that pongamia + TiO₂ and sesame + CuO nanolubricants have more heat transfer capacity due to its higher thermal conductivity than the conventional lubricant. Pongamia + graphene nanolubricant shows equivalent heat transfer capacity as of the conventional lubricant Servospin EE10.

Sample A, B, C are pongamia + TiO₂, sesame + CuO, Pongamia + graphene and the Serco spin EE 10 is mentioned as regular.

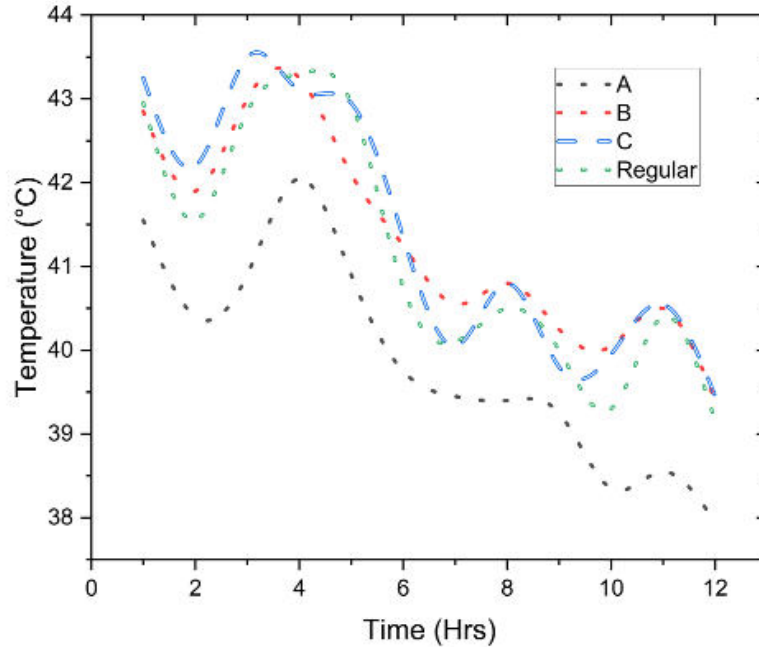


Fig. 13. - Heat generation after a week of time

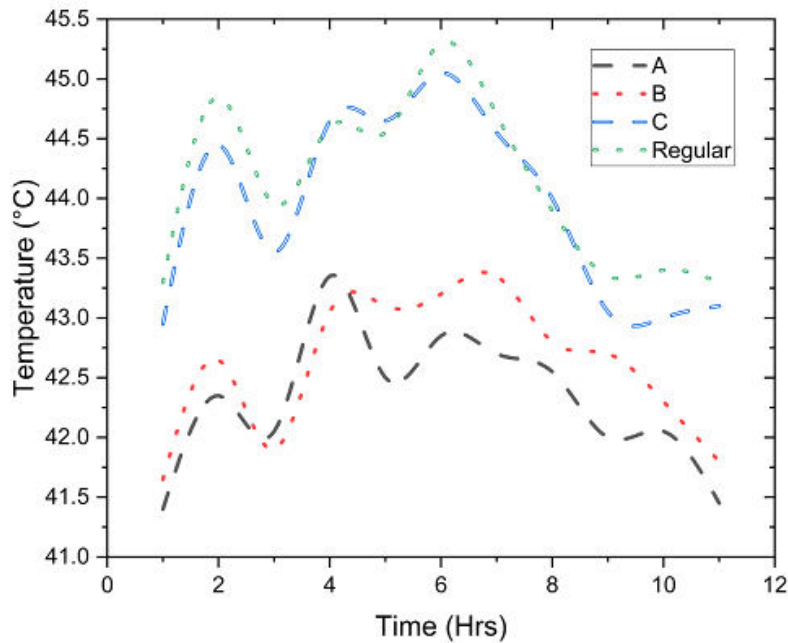


Fig.14. - Heat generation after a month of time

3.5.2 Volumetric change test

The volumetric change test of the nanolubricants after a month of run using dip stick shows that there is no volumetric change for the selected nanolubricants such as pongamia + graphene, pongamia + TiO₂ and sesame + CuO.

3.5.3 Power consumption test

Power consumption test results at 18000 rpm is tabulated in table 4 and the result shows that pongamia + TiO₂ nanolubricant has 3.39% reduction in the power consumption per hour due to less friction [16] than the conventional oil.

Table 4. Power consumption at 18000 rpm

Parameters	Servospin EE 10	Pongamia + TiO ₂	Sesame + CuO	Pongamia + graphene
No of spindles per machine	144	144	144	144
Main motor capacity - kW	7.5	7.5	7.5	7.5
Spindle type	HS	HS	HS	HS
Spindle wharve dia - mm	18.5	18.5	18.5	18.5
Spindle speed – rpm	18020	18020	18020	18020
Study duration - hours	4	4	4	4
Units consumed during study – kW	7.36	7.11	7.23	7.42
Units consumed per hour - kW	1.84	1.78	1.81	1.86

Power consumption test results at 14000 rpm is tabulated in table 5 and the result shows that pongamia + TiO₂ nanolubricant has 2.92% reduction in the power consumption per hour due to less friction [16] than the conventional oil.

Table 5. Power consumption at 14000 rpm

Parameters	Servospin EE 10	Pongamia + TiO ₂	Sesame + CuO	Pongamia + graphene
No of spindles per machine	144	144	144	144
Main motor capacity (kW)	7.5	7.5	7.5	7.5
Spindle type	HS	HS	HS	HS
Spindle wharve diameter (mm)	18.5	18.5	18.5	18.5
Spindle speed (rpm)	14000	14000	14000	14000
Study duration (hours)	2	2	2	2
Units consumed during study (kW)	3.42	3.32	3.37	3.39
Units consumed per hour (kW)	1.71	1.66	1.69	1.70

Conclusion

Based on the preliminary studies and literature review it was found that there exist excessive heat generation in the ring frame spindles due to degradation of lubricant over a period and causes energy losses.

Biodegradable base oils such as sesame oil, coconut oil and pongamia oil were selected for the research due to their excellent tribological properties. Nanoparticles such as TiO₂, CuO and graphene, surfactant such as oleic acid were selected for the research.

In order to study the performance of the nanolubricants, various tests have been carried out such as viscosity test, flash point and fire point tests, cloud point and pour point tests, friction test and wear test. The test results show that all the nanolubricants show 52-82% higher in the viscosity than the conventional nanolubricant servo spin EE 10. Coconut + TiO₂ nanolubricant shows 50% higher flash point than conventional lubricant. And sesame + TiO₂ nanolubricant shows 51% higher fire point than conventional lubricant. The cloud point and pour point of our nanolubricants are most suitable for this application. Sesame + CuO nanolubricant has shown 79% less COF than the conventional lubricant.

Overall, from the results of viscosity, flash and fire points, cloud and pour points, friction and wear test the following samples are found to be more suitable for the application:

- Sesame + CuO nanolubricant;
- Pongamia + graphene nanolubricant;
- Pongamia + TiO₂ nanolubricant.

The nanolubricant sesame + CuO shows 48% higher thermal conductivity than the conventional lubricant Servospin EE10. The pH level of all the selected nanolubricants lies between 6 to 8 pH which is neutral. The neutral pH is more satisfactory for the anti-rust property.

The final field tests such as heat generation test after a week and after a month of time, power consumption test at 18000 rpm for 4 hours and 14000 rpm for 2 hours and volumetric change observation after a month of run are performed at supertax mills Coimbatore. Based on the results of all the tests, pongamia + TiO₂ nanolubricant is selected as the most suitable lubricant for the textile ring frame spindle application.

References

- [1] Holmberg K., Andersson P., Erdemir A. Global energy consumption due to friction in passenger cars. *Tribol. Int.* 2012, 47, 221–234.
- [2] Mohamed Kamal Ahmed Ali, Peng Fuming, Hussein A. Younus, Mohamed A.A. Abdelkareem, F.A. Essa, Ahmed Elagouz, Hou Xianjun, Fuel economy in gasoline engines using Al₂O₃/TiO₂ nanomaterials as nanolubricant additives, *Applied Energy*, Volume 211, 2018, Pages 461-478, ISSN 0306-2619, <https://doi.org/10.1016/j.apenergy.2017.11.013>.
- [3] Uflyand, I.E.; Zhinzhiro, V.A.; Burlakova, V.E. Metal-containing nanomaterials as lubricant additives: State-of-the-art and future development. *Friction* 2019, 7, 93–116.
- [4] Shahnazar, S.; Bagheri, S.; Hamid, S.B.A. Enhancing lubricant properties by nanoparticle additives. *Int. J. Hydrog. Energy* 2016, 41, 3153–3170.
- [5] Nallasamy P., Saravanakumar N., Gukan Rajaram and R.K. Rishwin Kumar. Experimental study on the tribological properties of CuO-based biodegradable nanolubricants for machine tool slideways //International Journal of Surface Science and Engineering Published Online: September 16, 2018pp 194-206 <https://doi.org/10.1504/IJSURFSE.2018.094771>
- [6] Nallasamy P, Saravanakumar N, Nagendran S, Suriya E, Yashwant D. “Tribological investigations on MoS₂-based nanolubricant for machine tool slideways. Proceedings of the Institution of Mechanical Engineers” Part J: Journal of Engineering Tribology. 2015;229(5):559-567. doi:10.1177/1350650114556394
- [7] Kiu, S. S. K. et al. (2017). Tribological investigation of graphene as lubricant additive in vegetable oil. *Journal of physical science.*, 28(Supp. 1), 257–267, <https://doi.org/10.21315/jps2017.28.s1.17>
- [8] Eswaraiyah, V.; Sankaranarayanan, V.; Ramaprabhu, S. “Graphene-Based Engine Oil Nanofluids for Tribological Applications. *ACS Appl. Mater. Interfaces* 2011, 3, 4221–4227.
- [9] Wu, H.; Zhao, J.; Xia, W.; Cheng, X.; He, A.; Yun, J.-H.; Wang, L.; Huang, H.; Jiao, S.; Huang, L.; et al.” A study of the tribological behavior of TiO₂ nano-additive water-based lubricants”. *ELSEVIER* 2017, 109, 398–408.
- [10] Zulkifli, N.; Kalam, M.; Masjuki, H.; Yunus, R. “Experimental Analysis of Tribological Properties of Biolubricant with Nanoparticle Additive.” *Procedia Eng.* 2013, 68, 152–157.
- [11] Shaari, M.Z.; Roselina, N.R.N.; Kasolang, S.; Hyie, K.M.; Murad, M.C.; Abu Bakar, M.A. “Investigation of Tribological Properties of Palm Oil Biolubricant Modified Nanoparticles.” *ELSEVIER J. Teknol.* 2015, 76, 69–73.
- [12] Azman, N.F.; Samion, S.; Sot, M.N.H.M. “Investigation of tribological properties of CuO/palm oil nanolubricant using pin-on-disc tribotester.” *Institution of Civil Engineers.* 2018, 6, 30–37.
- [13] Koshy, C.P.; Rajendrakumar, P.K.; Thottackkad, M.V. “Evaluation of the tribological and thermo-physical properties of coconut oil added with MoS₂ nanoparticles at elevated temperatures.” *Wear* 2015, 330–331, 288–308.
- [14] Rajubhai, V.H.; Singh, Y.; Suthar, K.; Surana, A.R. “Friction and wear behavior of Al-7% Si alloy pin under pongamia oil with copper nanoparticles as additives.” *Mater. Today Proc.* 2019, 25, 695–698.
- [15] Shafi, W.K.; Raina, A.; Haq, M.I.U. Friction and wear characteristics of vegetable oils using nanoparticles for sustainable lubrication. *Tribol. Mater. Surf. Interfaces* **2018**, 12, 27–43.
- [16] Peng, D.; Kang, Y.; Hwang, R.; Shyr, S.; Chang, Y. Tribological properties of diamond and SiO₂ nanoparticles added in para_n. *Tribol. Int.* **2009**, 42, 911–917.
- [17] Wang, L.; Gong, P.; Li, W.; Luo, T.; Cao, B. Mono-dispersed Ag/Graphene nanocomposite as lubricant additive to reduce friction and wear. *Tribol. Int.* **2020**, 146, 106228.
- [18] Gulzar, M.; Masjuki, H.; Kalam, M.A.; Varman, M.; Zulkifli, N.W.M.; Mufti, R.A.; Zahid, R. Tribological performance of nanoparticles as lubricating oil additives. *J. Nanoparticle Res.* **2016**, 18, 1–25.

Information of the authors

Gowthaman A. M., research scholar, Department of Mechanical Engineering, PSG college of technology
e-mail: journalizone@gmail.com

Dr. P. Nallasamy, assistant professor, Department of Mechanical Engineering, PSG College of Technology
e-mail: journalizone@gmail.com

Mr. Shanmuga Sundaram, assistant professor, Department of Mechanical Engineering, PSG College of Technology
e-mail: journalizone@gmail.com

Mr. S. Yashwanth Kumar, PG Scholar, Department of Engineering Design, PSG College of Technology
e-mail: journalizone@gmail.com

Structural and Parameter Analysis and Study of Mechanized Supports for Their Robotization

Zhetessova G.S., Beisembayev K.M.*, Abdugaliyeva G.B., Orazbekov D.E., Levshanov R.V.

Abylkas Saginov Karaganda Technical University, Karaganda, Kazakhstan

*corresponding author

Abstract. Ensuring the wear resistance of the main components of mining machines and their long-term operation in an abnormal working environment of the subsurface, where elements are dynamically loaded with pressures exceeding 130 MPa, raises research challenges. Solutions to these challenges can be based on software packages with advanced intelligent functions and mechatronics, with the development of programs in the form of code for rapidly changing conditions. The study of the structure of support sections shows that the formation of loads on the basic elements, which are most susceptible to wear, is determined by the kinematics of the design, the types of connections at the joints, the accuracy of manufacturing, and assembly procedures. Structural formation through models of kinetostatics, circuit engineering, and mechatronics is a promising tool for obtaining efficient designs. They are easily converted into a control database of multidimensional classifications with processors at the database nodes that correspond to the software implementation of the structures, and their digital models include modes of operation in the working environment. For the KNC 70 support technology developed by the Coal Institute in Kemerovo, uneven loads in the joints of the rotating arms have been identified during roof displacement. This causes deviations in the loads of the control jacks from their axes and creates wear zones. The calculation takes into account the friction coefficients of the sliding parts. Such zones are particularly pronounced during the accelerated movement of the piston while transporting massive structures. Data on their distribution allows for the identification of solutions to reduce this effect. A method has been developed for the computer-based accounting of the interaction of cantilevered canopies, controlled by a jack, with the rough surfaces of rock to determine the distribution of load along their interaction line. The selection of control systems is based on applications that provide results in the form of data and text-based programs in the languages that form the foundation of robotic control systems, which will allow for the safe use of artificial intelligence, which is controlled by the operator through easy-to-read and understand commands.

Keywords: unevenness; structure formation; wear; digital model; interaction lines; Artificial Intelligence

Introduction

Modern longwall mining technologies are based on the use of a wide range of bulky and expensive equipment. Therefore, significant capital investments are required to create a new section in the mine. However, earlier experience has been presented in the application of technologies with much lower capital intensity. These are chamber technologies. They are successfully applied for the extraction of complexly deposited minerals in the USA, India, Australia, and Russia. The work zone in chamber technology is such that it can be easily isolated from other sections, and therefore harmful gases do not enter the atmosphere.

The efficiency of chamber technologies is particularly high in the extraction of potash salts in Russia, which brings significant income to the country. This has been achieved by mining chambers with the efficient Ural 20 KS type combine harvester, which was developed with the involvement of Karaganda engineers. Currently, manufacturing enterprises in Kazakhstan do not produce such combines, and mainly imported mechanized complexes are used in the mines. The problem of restoring such plants or separate workshops is compounded by the fact that Kazakhstan is still focused on creating assembly plants that generate quick income, such as the assembly of cars and components based on rubber technical products. At the same time, it has been characteristic for the engineering enterprises in the region to manufacture mechanized supports of a new technical level, where the processing of their hydraulic equipment (movement jacks, lateral leveling jacks, supports) was carried out using numerical control machines and software for processing rods and cylinders with a radius of 0.025 to 0.3 m for operation under pressure up to 360 MPa.

The Karaganda complex M-130 demonstrated effective operation even in panels no longer than 120 meters, achieving a daily extraction of 3000 to 4000 tons. The use of the OKP-70 support made it possible to achieve a record monthly extraction that still stands today [1], [2]. The operational efficiency and longevity of machines depend on the quality of their component manufacturing and the kinematic design of the machine, which should reduce dynamics and ensure minimal reaction forces in hinged connections. This will determine the necessary wear resistance, especially of surface components that move relative to each other. This applies to the canopy of the support that moves along the roof, the rod and piston in the cylinder, and the cylindrical pins in the eyes as well as the spherical supports of the posts [4] – [6].

The aim of the work is to analyze and study the structure formation of sections of mechanized supports for their transformation into a robotic complex for chamber mining of complex coal seams, using methods of linearization of dynamic equations to simulate three-dimensional maneuvering of sections, including asymmetric loads from rock pressure.

1. Methods and experiment

Structural analysis, as a research tool, improves as it is applied. Along with its use for established technologies, it also serves as a means for creating and introducing innovations in mechanics, as well as in the processes of changing the

structure of machines and manufacturing materials. This is carried out in software packages that produce results in the form of data and program models expressed in text code, which can be easily modified in editors and used in other packages, allowing for the construction of a well-founded digital model of the machine, as shown in Figure 1. For the analysis of structural diagrams, Figure 2 utilizes the technology of linearizing dynamic equations (LDE), which offers a relatively simple representation of motion based on kinetostatics. This allows, based on 3D models, to obtain comprehensive information about the design and kinematic capabilities of the section, the structure of its hinge system and interaction with other machines in the unit.

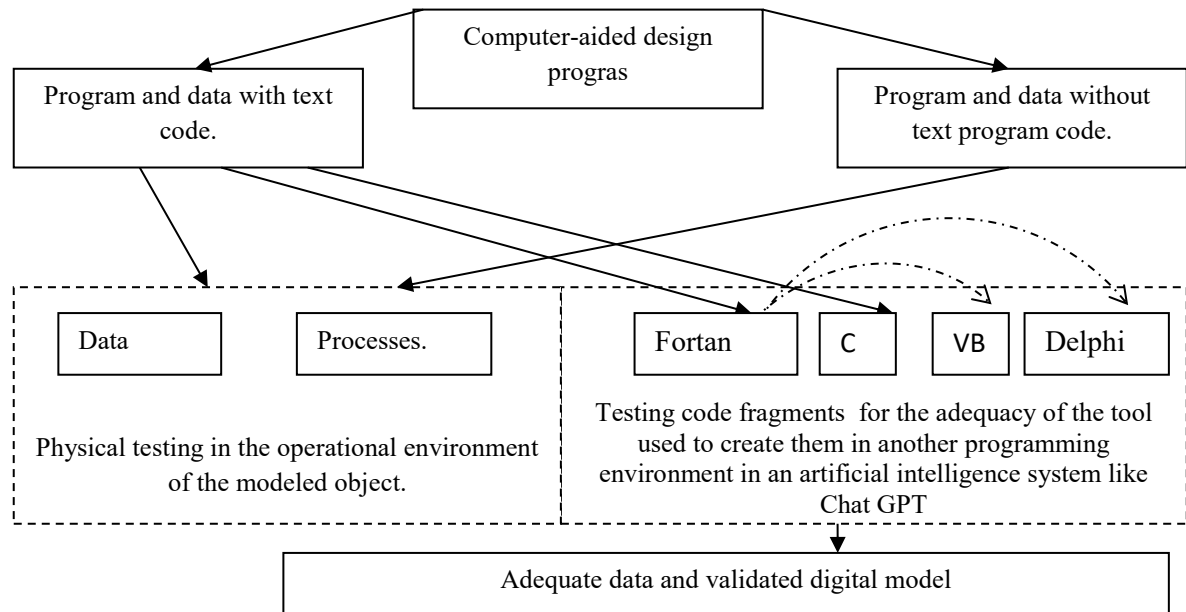


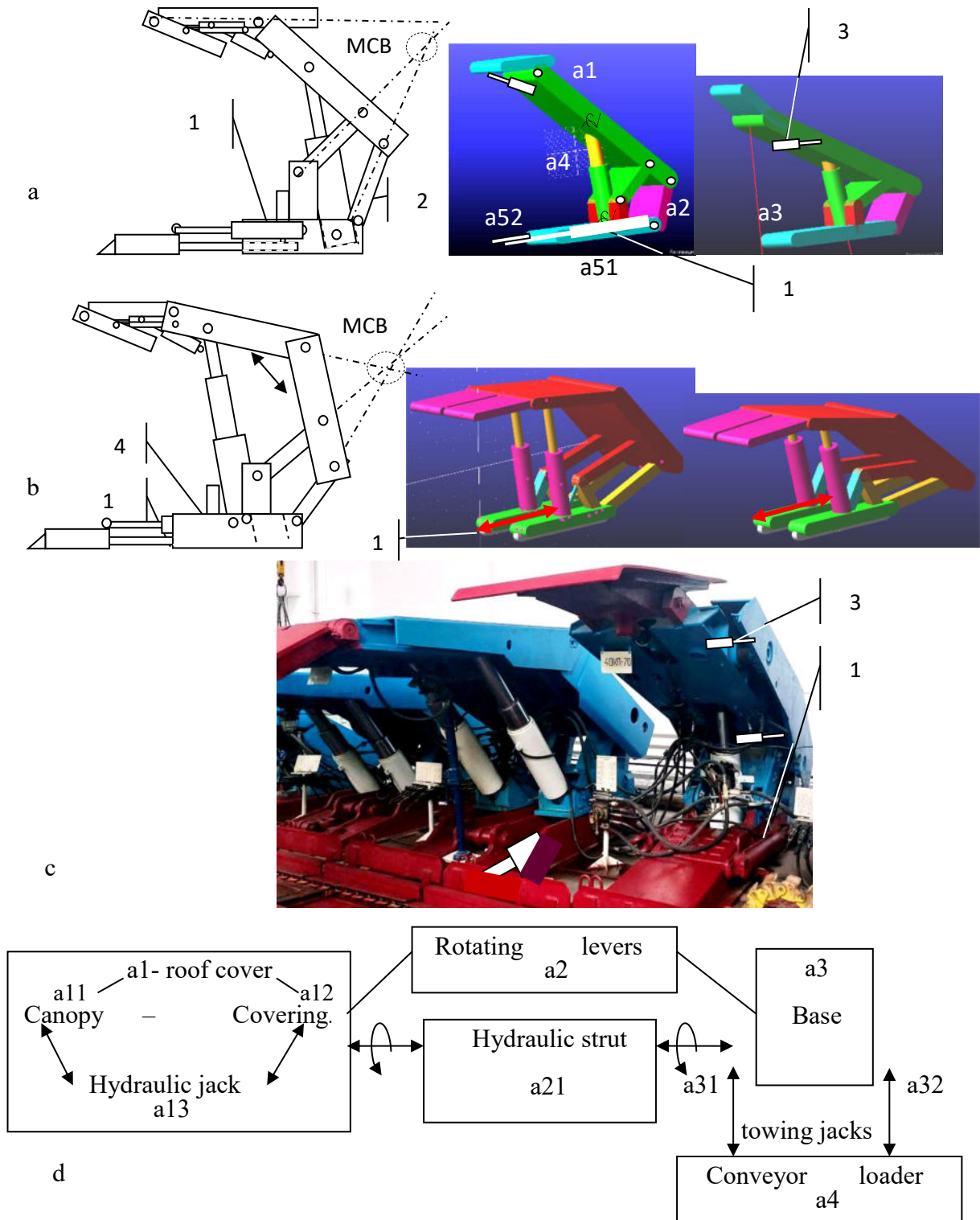
Fig. 1.- Algorithm for testing the product developed using artificial intelligence design software packages.

As the conducted experiments show, for the analysis of the machine structure, the proposed method for creating a kinematic-static model is the most acceptable due to the use of standard elements. In this case, the structure of the machine is simplified, but all dynamic characteristics are performed with sufficient accuracy, which can be easily established by the displacement speed of real samples and the model. There is no need to execute a complete constructive implementation of the model; it is enough to consider the masses and axial moments of inertia of the parts, using two primitives (Linck, Box) and three constraints (Revolute, Zylindrical, Translate).

Please note that packages for working with mechanized supports and their robotic systems contain functions and structures oriented towards the finite element method, therefore text programs created in these packages (for example, Ansys APDL) should be verified in Fortran-type languages, and individual fragments of them (without FEM functions) should be verified in VB or Delphi languages, which are usually available to a large contingent of users. At the same time, to improve the program (usually these are lines for determining the current state of the face when moving support sections), which you offer to execute AI, you should specify operator options that are well known to you, which will significantly reduce the number of errors in the resulting code.

The proposed schemes and programs represent dangerous operating modes, and, in particular, for the lemniscate mechanism, where the intersection of its instantaneous center of rotation (ICR) with the axial lines of the visor or the overlap causes an increase in the loads in the hinges of the four-link levers. The control program should consider preventing such positions. The diagram was created based on a textual description of the structure. Using circuit engineering, it fully represents the design and kinematics of the section, including its connection with the loader-conveyor. Diagrams a to b primarily express a research variant of the structure and do not significantly lag behind photographs of the real design due to their mobility. Diagram c, despite the main textual description, fully represents the data and processes. Moreover, it allows the construction description to be integrated into traditional databases with special indexing of design elements. Previously, we presented the structure of a multidimensional database for the sections of the support [2] in the form of a window for an infological model, the content of which is enhanced by the introduction of models of type a and b.

The data base contains references to modeling packages in its nodes, and for this reason, the diagrams of types "a" and "b" represent the capabilities for dynamic description of loading and displacement of the section. The database for the sections is structured such that the main element of its design is the support, as it provides the primary function for the safety of personnel during operation.



a – shield (protective-supporting) section of the support; b – supporting-protective support; c - Section of the OKP-70 support in the machine room of the KarTU, on the left Glinic: 1 - travel jack (a51, a52), 2 - rotary levers of the lemniscate mechanism (a2), 3 - side jacks, 4 - conveyor control jack.

Fig. 2.- Structuring of support sections to form a robotic system

Currently, two types of constructive implementations of sections are mainly used (see Fig. 2), which we categorize as: protective-supporting and supporting-protective.

In the figure, using schematic techniques, the structures and connections of support sections are presented, highlighting their potential for automation when working in the challenging conditions of mines and quarries. Mechanized support operates under pressures that no other machine experiences. This is due to the vast height of the rock column (up to 700 meters) acting on the section, creating hanging rock in the mined space that periodically collapses onto the moving support with spans of 20-25 meters. The pressure in the supports can reach values of 25 to 130 MPa. Moreover, the optimal technology for working with it should minimize, but ensure, the presence of a person in the mining

face. The weight of a section can reach 12 tons, and having 150 to 200 sections in a face requires significant capital investment and operational costs.

The complex of these factors necessitates for the enterprise to recover the cost of the equipment through continuous operation, which is possible only under ideal mining and geological conditions. At the same time, support sections of the OKP 70 type have been operating in the Karaganda basin for over 40 years. Its design, featuring a powerful support embedded in the rear part of the section, provides ample space for worker passage and ventilation in the face, given the super-category gas factors of the Karaganda coal seams, as shown in Figure 2.

The proposed representation of the structure and kinematics for sections of both types, unlike the photographs of such sections, as shown in Figure 2c, allows for modifications and improvements to the design, enabling the synthesis of their force parameters. This has been made possible through their creation in LUD packages, under simplified kinetostatics, in conjunction with established standard means of visualization that are easily separable from the computational part, which is important for effective testing.

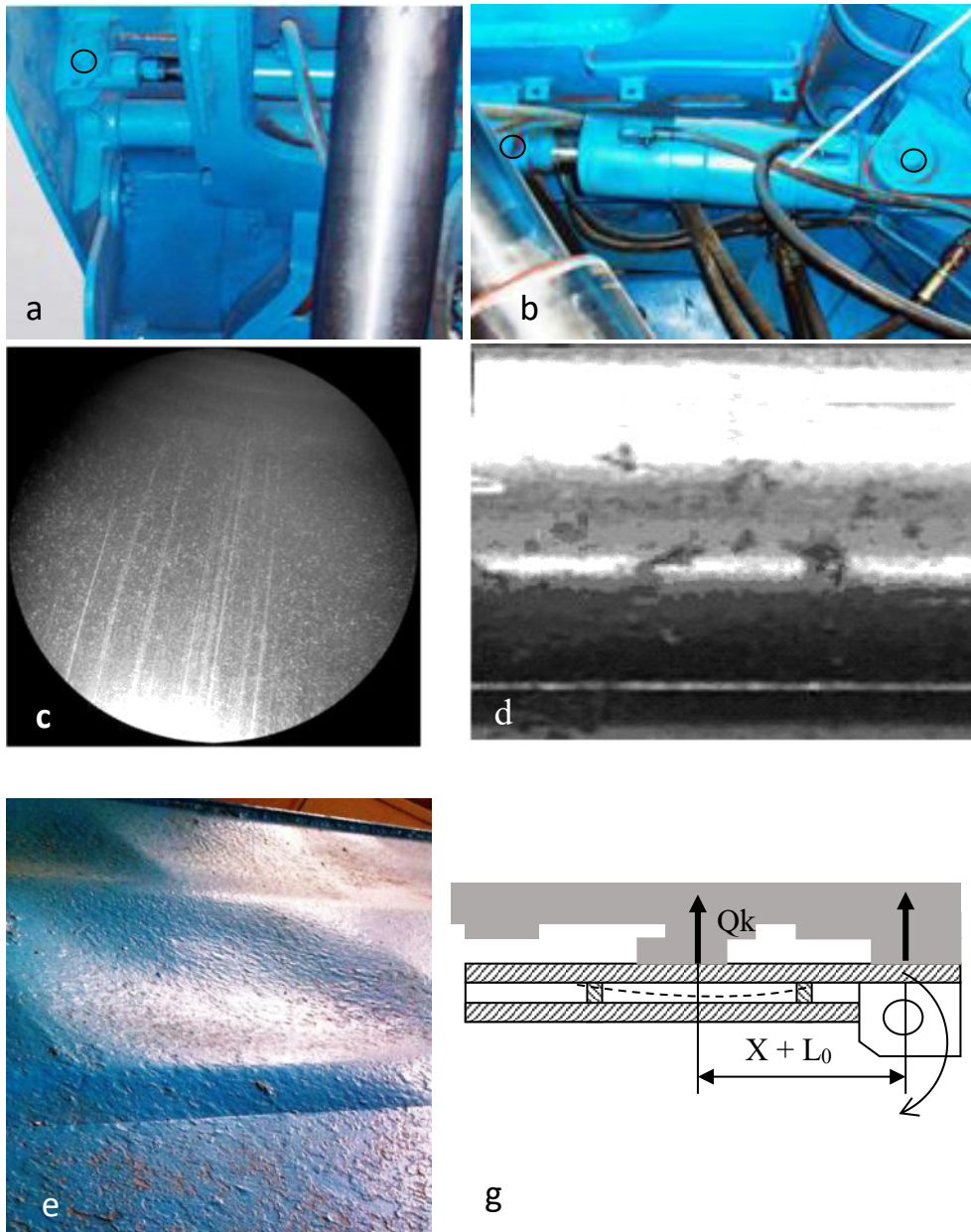
2. Results and discussion

Assistance in creating such tools is provided by artificial intelligence (AI) packages, specifically: DQN (Deep Q-Network) - for feedback-based learning, PPO (Proximal Policy Optimization) - for reinforcement learning in complex environments; CNN (Convolutional Neural Networks) - for processing visual data. They also address issues related to robotics. However, effective dynamic analysis is still carried out using packages such as MATLAB/Simulink - tools for modeling and analyzing dynamic systems; ADAMS (MSC Software) - specialized software for the dynamic analysis of mechanical systems and mechanisms with robotics processors; and the SolidWorks Motion module, for the dynamic analysis of moving mechanisms.

In recent years, the interviewing of AI systems has been developing, which, when questions are structured correctly, allows for the identification of the best systems, as well as, by analyzing the responses, uncovering fundamental flaws in AI, including instances of obtaining inadequate information. The developers of these systems do not impose restrictions on their use in a resident mode, and in a paid mode, they are still inexpensive, thus providing opportunities for support in programming. The effectiveness of AI in design has already been proven, but even now, there are known cases of obtaining unreliable data. Therefore, the creation and expansion of testing methodologies is the best way to address such situations, and it is greatly simplified when there is a result not only in data but also in the form of source code that corresponds to the capabilities of interpreters of popular object-oriented languages such as Fortran, C++, Delphi, and VB.

Therefore, the use of CAE packages, such as ADAMS (MSC Software) or Ansys APDL, where the testing technologies from Figure 1 can be easily applied, will allow for a safer transition to and expansion of the use of AI. Thus, the necessity to verify the obtained results through alternative means is an important point for accelerating development. This is where the continuity of technologies and their tools comes into play. We note that the use of packages that do not generate text code is quite justified in well-studied areas of engineering and processes based on proven kinematic schemes, designs, materials used, and levels of their loading. Clarity of the structural scheme is especially important in the processes of interaction between the machine and the working environment, and in the presented example with roofing, accounting for its roughness will allow for a more accurate synthesis of its parameters. As can be seen from the diagram in Figure 1, a single section of the support can contain up to 8 hydraulic cylinders, and servicing them in automatic mode will require 24 sensors (16 pressure sensors and 8 position sensors). Therefore, the application of mechatronic solutions is an important aspect of structural analysis. In this case, the sections in Figure 2 have up to 11 main nodes, considering the supports and the jacks controlling them, as well as over 20 articulated systems for their connections. The sections of OKP 70 can rotate left and right by 180 degrees within these systems, with the turning radius being such that, for the structure described in the Eurasian patent application by the authors N 202391679, it does not result in losses of useful minerals. They can also move upward and downward along an inclined surface of no less than 25 degrees. The presented system allows for the simulation of these movements, conducting process and parametric analysis, and calculating the duration of their execution [5]. The hydraulic cylinders have easily vulnerable parts - namely, the rods and cylinders - that require special precision treatment for smooth operation. Wear on these components leads to leakage of working fluid and equipment failures. Suboptimal connections between the units of the support section can exacerbate wear. Thus, Figure 3a, b, c, d examines the causes of wear related to the joints of hydraulic cylinders with other components of the support section. Wear at the lugs causes load misalignment from the rod axis, for instance, in the movement jacks located at the base of the section. Rock and coal debris accumulates in the inter-sectional gaps, entering the lugs, which leads to wear and deformation of their openings. Dynamic analysis of the movement of the piston and rod in the hydraulic cylinder shows that, in this case, the wear zones in the sliding systems are intensified and can concentrate in areas of stress concentration, such as those located at the Grundbushing—the zone of the rod's exit from the cylinder during accelerated rod movement, as shown in Figure 4. The relevance of such issues is highlighted by data [4], which indicates that failure rates of support columns in longwall faces reached 31%, and for jacks, 23%. The reasons include impacts during the collapse of roof blocks (37%) and loss of longitudinal stability (28%). Load

misalignment on one of the jack lugs also causes bending moments on the rod. Such situations are common in longwall operations due to sharp irregularities in mining pressure.



a, b - mounting of hydraulic cylinders with the possibility of non-axial loading; c, d - wear of the rod in the presence of bending moments and corrosive factors; e - scheme of random interaction and deformation of supporting elements for the real rock environment

Fig. 3 - Irrational mounting of hydraulic cylinders and selection of the calculation scheme.

Thus, structural models of types a and b, when using the LUD processor, allow for the simulation of unilateral rock displacement, which leads to tilting of the support section and uneven loads on the lugs. For this situation, a model of the support section has been developed for coal release from the upper coal seam onto the face conveyor, designed by the Coal Institute of the Russian Academy of Sciences (Kemerovo), as shown in Figure 4c, with a bearing capacity of support columns up to 900,000 Pa. The graphs depict a case where the load was concentrated on one side of the canopy, leading to a sharp redistribution of reaction force magnitudes at the joints to the left and right of the section, causing it to tilt laterally. In this case, the movement of the side edges of the section using type 4 jacks, as shown in Figures 2a and 2d, will result in non-axial loading on the jacks, as illustrated in Figure 3b. However, for a support that has spherical joints, this situation is not dangerous.

However, for a support that has spherical joints, this situation is not dangerous. The most heavily loaded areas of the sections are their supporting parts: canopies and bases. The issue of crushing sheets between the supporting ribs has been successfully addressed by thickening the outer sheets in contact with the rock, as shown in Figures 2e and 2g. As a result,

the durability of the metal structure has significantly increased (for example, the supports of OKP 70 have been in operation for over 40 years!). The kinematics of the section, as the analysis showed, will provide operational modes compatible with those of the robots [5], [6], and it is sufficient to replace hydraulic equipment with electro-hydraulic equipment, for instance, based on systems from the Marco company (KarTU has a memorandum for joint work). The wear of the surfaces of the coverings, canopies, and bases should be considered proportional to the distribution of average loads along their contact lines with the rock.

In addition to the deformation of the crushed surface of the canopy and the cover, the sliding of rock blocks on them is also taken into account, causing, due to friction, additional abrasive wear.

When analyzing the interaction of the covering with the rock, the influence of the cantilevered canopy, operated by the jack, is also taken into account. The canopy, pivotally connected to the covering at point O, has a single support zone with the rock, and its position along the length of the canopy is considered uniformly probable. The first contact point is the hinge at point O; therefore, for the scheme shown in Figure 5, we have three contact zones. After the movement of the section and the bracing of the support, we have two contacts located on the covering on both sides of the resultant force. The determination of loads along the contact line for Figure 3g corresponds to simple equations of equilibrium.

$$Q_i + Q_j + Q_k = \sum P_i; \quad Q_i l_{ci} - Q_j l_{cj} - Q_k l_{ck} = 0, \quad (1)$$

For a uniformly probable contact scheme, we obtain:

$$Q_{jcp} = \frac{1}{(mk * m\lambda)} * \sum_{k=1}^{k=mk} \dots \sum_{i=1}^{i=m\lambda} \frac{\sum P(2i-1)(2k-1)l_{kk} - 4Mom_k(i+mn)}{2l_{kk}(i+j+k-1)(2k-1)}, \quad (2)$$

$$Q_{icp} = \frac{1}{(mk * m\lambda)} * \sum_{k=1}^{k=mk} \dots \sum_{j=1}^{j=m\lambda} \frac{\sum P(2j-1)(2k-1)l_{kk} - 4Mom_k(i+mn)}{2l_{kk}(i+j+k-1)(2k-1)}, \quad (3)$$

$$Q_{kcp} = \frac{2Mom_k}{l_{kk}(2k-1)}, \quad (4)$$

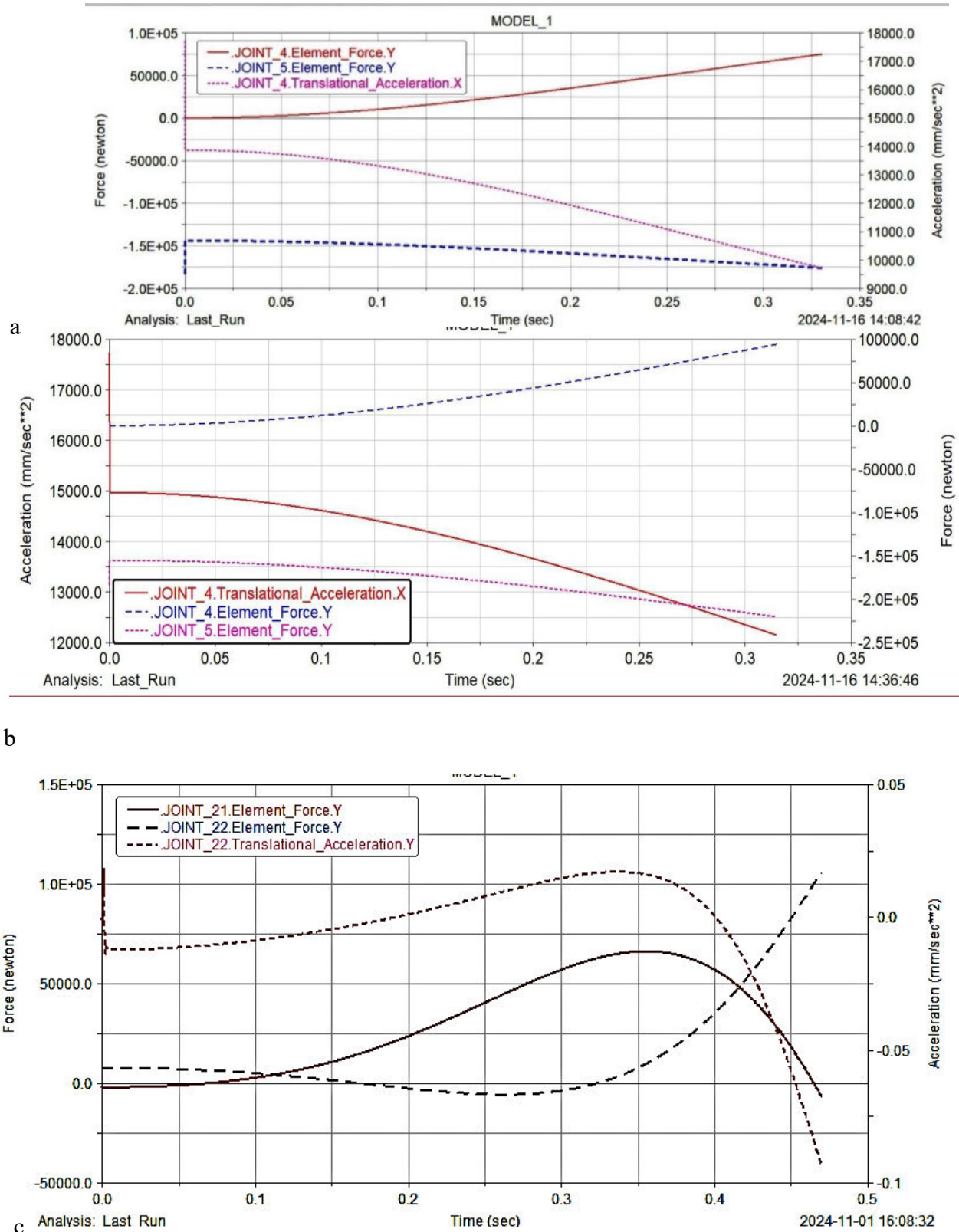
where l_{kk} is the length of the cantilever awning.

From the condition of interaction under which the moment M will be minimal, ensuring contact across all sections, we obtain:

$$M_O = \frac{Pl_{kk}(2k-1)(2i-1)}{4m_k(i+m_n+k-1)}, \quad (5)$$

The calculation program takes into account the factor of increased interaction frequency at the edge of the eave. Adjustments to the distributions consideration is given to the influence of the equality:

$$\sum_{n=(Lk/A)}^{n=1} Pk(Lk/A - k)(Lk/A), \quad (6)$$



a - static and dynamic friction coefficients of 0.7 and 0.4; b - static and dynamic friction coefficients of 0.4 and 0.2; c - reactions in the pivot arms on the left and right under uneven loading of the section.

Fig. 4 - Normal reaction forces on the surfaces of the piston and in the area of the guide and bushings, as well as the load on the joints of the pivot arms for the volumetric model.

Where P_k is the coefficient of load non-uniformity along the contact line; Q is equal to the total resistance of the supports; Q_i is the pressure to the left of x_c ; Q_j is the pressure to the right of x_c ; Q_k is the pressure on the roof from the eave side for the zone at the k -th section. The load distribution for such a ceiling is not entirely optimal. There are two peaks in the zone of the resultant supports and above the hinge of the eaves. At the same time, there is a noticeable reduction in loads on the rock between these zones, which, in the case of a roof model with cyclic cracks, could lead to the possibility of significant settling and the formation of rock blocks in this area [8]. It is also clear that the depth of this "pit" can be managed through active support using jacks on the eave. Based on the analysis, the use of eaves with a hinge in their middle part would be more effective for this scheme, as achieving a uniform load distribution in this case would be much easier. Taking into account the influence of the factor presented in expression (6) leads to an increase in the load at the end of the eave by almost 30%.

Thus, the structural approach to the analysis of mechanisms allows us to present effective technologies of chamber mining, which have a universal set of robotic equipment for the extraction of seams in difficult conditions, fundamentally different in terms of the factors complicating the work (fractures, changes in the angles of incidence of seams, steeply inclined and steep seams, the presence of weakened zones in the roof and soil), which also allows us to reduce the range of equipment and technologies of the type [11], [12], significantly simplify the volumes of necessary research due to the use of already tested equipment, assembled into new structures, and the use of programs based on modeling packages, the forecasting efficiency of which has been proven [13]-[16], and the adequacy of the work has been confirmed by Artificial Intelligence.

Conclusions

The analysis of the structures of the mechanisms can be conducted by creating simple models in dynamic programming packages based on kinetostatics. These models can easily be converted into a control database built on the principle of multidimensional classifications, with processors located in the nodes of the database, logically corresponding to their software content. The structures can then be expanded into complete digital models with device functionality in the working environment and applied in parametric analysis. This made it possible to identify wear zones in the piston rods and cylinders of hydraulic jacks, taking into account the friction coefficients of sliding parts during their accelerated movement during transportation of massive structures, as well as possible structural designs for the connections to reduce this effect.

Expressions have been obtained for the computer accounting of the interaction between the cantilevered jack-controlled canopy and the rough surface of the roof, for determining the load distribution along the interaction line, which allows for consideration of the zones of their intense wear. It has been established that the increase in load at the end of the cantilevered canopy reaches 30%, which must be taken into account during their fabrication, especially during the operation modes of the working areas with ceiling-reserved shapes, when the upper ledge is knocked down during the movement of the canopy. An important element of the automated design packages for robotic systems is the presence of tools that display the source code, which can be used in the logical blocks of automated execution of basic functions, as well as for testing the obtained results in an alternative programming language environment. This is particularly important when using packages where access to the internal workings of the solvers is restricted by the manufacturer, allowing for the safe use of artificial intelligence in design.

Structural analysis of the formation of design and kinematic schemes of sections of mechanized support is an important element of the analysis of their suitability for robotization. It has been established that the support section of the OKP 70 type complies with the principles of robotization when replacing its hydraulic system with electrohydraulic equipment with processors. At the same time, a step-by-step modernization of its metal structure should also be carried out.

References

- [1] The head of the government congratulated the miners of JSC "Ispat-Karmet" on setting a world record for monthly coal production. // <https://www.caravan.kz/news/glava-pravitelstva-pozdravil-shakhterov-oao-ispatkarmet-s-ustanovleniem-mirovogo-rekordamesyachnojj-dobychi-uglya-178208/>. View date 21.11.2024
- [2] Asmagambet D.K., Buyalich G.D., Zhettesova G.S., Beisembayev K.M., Akizhanova Zh.T Investigation of the rotary system for removing chambers // *Ugol*, № 6, 2023, pp.50-55.
- [3] LI Dexing, Wang Enyuan, Yue Jianhua, et al. A weak current technique for coal and rock dynamic disaster prediction and its application. // *Chinese Journal of Rock Mechanics and Engineering*, 41(4), 2022. - p.764-774.
- [4] Sinkov V.G., Nemtsev E.N., Miroshnichenko S.V., Khorolsky A.A. Increasing the load-bearing capacity of hydraulic props in mechanized supports // *Geotechnical Mechanics* 2015. №125
- [5] Nikonova T.Yu., Zhetesova G.S.; Beisembaev K.M., Abdugaliyeva, G.B., Zharkevich, O.M., Skaskevich A. Chamber extraction of minerals in complex mining and geological conditions without carbon emissions // *Ugol*, № 11, 2024. - p. 57 – 63.
- [6] Govorukhin Yu.M., Rib S.V. Modeling of detailed methods of process coverage of the krovli river. // *Gorny magazine*, No. 4, 2019. - p. 23-26
- [7] Yub B., Peng M., Tai Y. Assessment and control of the mine tremor disaster induced by the energy accumulation and dispersion of thick-hard roofs // *International Journal of Mining Science and Technology*, Volume 34, Issue 7, 2024. - p. 925-941
- [8] Mena A., Wollstein R., Baus J., Yang J. Finite Element Modeling of the Human Wrist: A Review // *Journal of Wrist Surgery*, Vol. 12 No. 6, 2023. - p. 478 – 487. <https://www.thieme-connect.com/products/ejournals/pdf/10.1055/s-0043-1768930.pdf>.
- [9] Beysembayev K.M., Reshetnikova O.S., Nokina Z.N., Teliman, I.V., Asmagambet D.K. New technologies of mining stratal minerals and their computation // *New technologies of mining stratal minerals and their computation // IOP Conference Series: Materials Science and Engineering* 2018, 327(2), 022012

- [10] Isabek T.K., Khuangan N., Altpayeva A.R., Shalmerdenova R.T. Modeling The Outburst State of an Arrau With Disjunctive disruption and Mining using the Finite Element Method //Ugol, № 6, 2020.- p. 55-60.
- [11] Nevzorov D.N., Trufanova I.S. Improving the efficiency of a conveyor train: a study of the influence of drive station parameters on the adhesion force //Mining Industry. № 1, 2025. – p. 184–191
- [12] Garashchenko Zh.M., Teremetskaya V.A., Gabov V.V. Mining of coal pillars with unified extraction modules and local faces //Mining industry, № 58, 2024. – p. 151–157
- [13] Rojter M., Krah M., Kisling U., Veksler Ju.A. Razrabotka metoda sejsmoakusticheskogo monitoringa dinamicheskikh javlenij v ochistnyh zabojah ugol'nyh shaht //FTPRPI, 1, 2021. – p. 28-35.
- [14] Yu B., Mingxian Peng M., Tai Ya., Guo Sh. Assessment and control of the mine tremor disaster induced by the energy accumulation and dispersion of thick-hard roofs //International Journal of Mining Science and Technology, Vol.34, Issue 7, 2024.- p. 925-941
- [15] Plykin M. Parallel Computing in Ansys. URL: //https://www.ansysadvantage.ru /parallel-estimates-in-ansys.(Date of access. 23/04/2025)
- [16] Nabiullin R., Teliman I., Khoroshavin S. The interaction of the main actuators of hydraulic excavators //E3S Web of Conferences: 18, Ekaterinburg, 02–11 april 2020. – Ekaterinburg, 2020. – P. 03013. – DOI 10.1051/e3sconf/202017703013.

Information of the authors

Zhetessova Gulnara Santayevna, d.t.s., professor, Abylkas Saginov Karaganda Technical University

e-mail: zhetessova@mail.ru

Beissembayev Kakim Manapovich, d.t.s., docent, Abylkas Saginov Karaganda Technical University

e-mail: kakim08@mail.ru

Abdugaliyeva Gulnur Baimurzayevna, c.t.s, associate professor, Abylkas Saginov Karaganda Technical University

e-mail: gulnura84@mail.ru

Orazbekov Darkhan, master student, Abylkas Saginov Karaganda Technical University

e-mail: kakim08@mail.ru

Levshanov Ruslan, master student, Abylkas Saginov Karaganda Technical University

e-mail: kakim08@mail.ru

Reducing Vibration of Elastically Supported Rolling Bearings on a Centrifugal Pump

Mustafin A., Sadykov N.*

Toraighyrov University, Pavlodar, Kazakhstan

*corresponding author

Abstract. In this work, the vibration of the pump rotor supports from centrifugal force is studied. For this purpose, it is proposed to install a flooring made of vibration-insulating material under the pump casing. When fitting the outer rings of the rolling bearing into the pump casing through an elastic bushing, it is possible to increase the compliance of the supports while maintaining sufficient strength and wear resistance of the surfaces. It is proposed to use such a complex support of the pump rotor, consisting of a rolling bearing and a polyurethane bushing, which allows, in case of rotor imbalance caused by the radial displacement of the axes of the pump and the engine, to reduce vibrations at the main oscillation frequency by several times. On the casing supports, when using vibration-insulating material as a flooring, it is significantly reduced by 5.87 times. And the use of elastic elements made of elastomer as a flooring for the pump casing and the installation of a damper made of a polyurethane bushing under the outer ring of the rolling bearing reduce vibration loads perceived by the foundation and rolling bearings by tens of times.

Keywords: elastically supported bearing, vibration, pump, elastomer, rotor.

Introduction

The article uses the experience of foreign sources, in particular, the author Jerry Hallam published the results [1] of a large-scale study of the reliability of 480 pumps over a five-year period at the Amoco Texas City oil refinery. The author's National Instrument Lab VIEW system [2] allows you to evaluate the tested machine based on the signals generated by the machine, and polyurethane-based damping materials developed by the Austrian company Getzner Werkstoffe GmbH [3] allow you to absorb vibrations in a wide range of frequencies and loads. Vibration and process data were collected on individual single-stage centrifugal pumps from a number of industrial enterprises in the Perth area [4]. Considering the main causes of vibration of the pumping unit, we determined the frequency spectrum by which it is necessary to select the amplitude-frequency characteristics of the damping devices and optimize their parameters. Unbalance of the rotor (imbalance) during its rotation causes variable loads on the rotor supports and shaft bending. This is the most common of the frequently encountered causes of vibration. The maximum amplitude of vibration during imbalance has a radial direction. The vibration frequency (in Hz) typical of imbalance is: $f = n/60$, where n is the rotor speed per minute. Rolling bearing defects are characterized by a high-frequency component, for most possible defects with a frequency equal to f and multiples of it by the number of rolling elements. The operation of technological and chemical plants at reduced capacity led to the fact that highly efficient or large-sized pumps were operated in a wide range of performance, including long-term operation at flows significantly below capacity [5]. Shock-free throughput without vibration is considered the most important indicator of the best operating conditions [6]. According to authoritative sources who examined several dozen pumping station sites of main oil pipelines, about 38-45% of all failures occur due to increased vibrations [7]. They cause bearing failure, dynamic loading of the pump-to-foundation connections, rotor displacement and beating. In this regard, the operating conditions of the end and slot seals deteriorate, accompanied by an increase in fluid leaks and overlapping of gaps in the casing and impeller connections. The main causes of vibration problems in a single-stage and multi-stage centrifugal pump are synchronous vibrations, mechanical imbalance, etc. It is known that a pump unit on a frame with elastic damper supports experiences 50 times less vibration loads. However, these shock absorbers primarily solve the problem of reducing vibration transmitted to the foundation, and also require significant time and money to perform repairs and replace them. In the work [8] it is shown that the study of vibrations occurring on the pump rotor shaft supports and in the pump casing fastenings on the frame can be considered as vibrations of two separate masses with elastic supports. In particular, it was found that vibrations excited by the imbalance of the pump rotor are compensated to a greater extent by using damping on the supports themselves. In particular, these conclusions are confirmed by research by Getzner Werkstoffe (Austria) [3].

The purpose of this work is to study the vibration of the rotor supports from the centrifugal force caused by the displacement of the rotor relative to the central axis of the 2D630-125 Pump. Pumps 2D630-125 and units based on them are used at pumping stations of urban, industrial and rural water supply, as well as in the petrochemical industry.

1. Methods and experiment

Frequency of vibrations during shaft rotation

$$f = k \cdot \varphi / 2\pi, \quad (1)$$

where $k = 1, 2, 3$ – harmonic number.

At $k = 1$ for the fundamental frequency $f = 308,7/6,28 = 49,15 \text{ Hz}$, the maximum permissible parallel displacement of the axes is $0,10 \text{ mm}$. The centrifugal force acting on the rotor supports, with a rotor mass of $m_r = 120 \text{ kg}$ is

$$F_a = 120 \cdot 308,7^2 \cdot 0,1 \cdot 10^{-3} = 1145 \text{ N}$$

The main load in the existing formulae for calculating the rigidity coefficient for assembled rolling bearings is taken to be their load-carrying capacity, i. e. the actual load and the pattern of its distribution on the rolling elements are not taken into account. However, the greatest force falls on the ball [2], located opposite the line of action of the load. Its value is approximately equal to

$$F_0 = 5F/z, \quad (2)$$

where z – number of rolling elements for a bearing;

F – the radial force supported by one bearing, equal to half the sum of the rotor gravity and centrifugal forces

For a centrifugal pump 2D630-125 with a two-way supply of liquid to the impeller, the radial force on the bearing

$$F = (120 \cdot 9,8 + 1145)/2 = 1172,5 \text{ N}$$

then according to the formula for calculating the greatest pressure force with the number of rolling elements for bearings №313 – $z = 5$

$$F_0 = 5 \cdot \frac{1172,5}{8} = 732,5 \text{ N}$$

The load distribution depends to a large extent on the size of the bearing clearance and on the accuracy of the geometric shape. The convergence of the axes of two spheres contacting along concave surfaces according to Hertz's theory [2]

$$\delta = 1,55^3 \sqrt{(F_0/E)^2 (R_1 - R_2)/2R_1R_2}, \quad (3)$$

where R_1 – radius of curvature of the surface of the inner ring along the racetrack

$$R_1 = ((D - d)/2 - d_b)/2 + 0,5d = ((140 - 65)/2 - 23,8)/2 + 0,5 \cdot 65 = 46,2 \text{ mm}$$

$R_2 = 12 \text{ mm}$ – radius of curvature of the ball. Then, according to the formula, the convergence of the axes of the two spheres during deformation of the rolling elements

$$\delta = 1,55^3 \sqrt{(732,5/2 \cdot 10^5)^2 (46,2 - 12)/2 \cdot 46,2 \cdot 12} = 0,011 \text{ mm}$$

Rolling bearing rigidity

$$c_{r.b.} = F_0/\delta = 732,5/0,011 \cdot 10^{-3} = 66,59 \cdot 10^6 \text{ N/m}$$

Natural frequency of an oscillatory system ω_a

$$\dot{\omega}_a = \sqrt{2c_{r.b.}/m_r},$$

where m_r – rotor mass;

$c_{r.b.}$ – rigidity of rolling bearings on both sides of the rotor.

$$\dot{\omega}_a = \sqrt{2 \cdot 66,59 \cdot 10^6 / 120} = 1053 \text{ s}^{-1}$$

The transfer coefficient [3] at low damping can be approximately determined by the formula

$$\mu_t = |1/1 - (\omega/\omega_a)^2|, \quad (4)$$

The amplitude of the force transmitted in the direction of the vertical axis is determined by the formula

$$F = F_a \cdot |1 - (\omega/\omega_a)^2|, \quad (5)$$

where F_a – amplitude of the disturbing force;

F – amplitude of force transmitted to the support

The ratio of the frequencies of the oscillations of the disturbing force and the natural oscillations of the system $308,7/1053 = 0,292$. Expression $|1 - (\omega/\omega_a)^2| = 1 - 0,292^2 = 0,914$.

The transfer coefficient at low damping can be approximately determined by the formula:

$$\mu_t = |1/1 - (\omega/\omega_a)^2|, \quad (6)$$

Good vibration isolation is achieved with $\mu_t = 1/8 - 1/15 = 0,125 - 0,066$.

The transmission coefficient $1/0,914 = 1,094$ is not included in the recommended range, which characterizes low vibration isolation of bearings. The force transmitted to the support without taking into account the damping of the system $F = 1145 \cdot 1,094 = 1252$ N slightly exceeds the value of $1252/1145 = 1,09$ times that exciting from centrifugal forces. To ensure vibration isolation of rolling bearings, it is necessary to increase the compliance of the support and reduce the frequency of natural oscillations of the system. It is proposed to install a polyurethane bushing in the hole of the 2D630-125 pump housing, instead of the bearing cup. In this case, all technical requirements and dimensions adopted for assembling the bearing in the housing are preserved.

Polyurethane bushings are currently used in cars, for example, polyurethane shock absorber bushings are widely used by motorists for vehicles. The main advantages of polyurethane bushings compared to rubber are the following:

- wear resistance;
- elasticity;
- low friction;
- resistance to oils, fuel and petroleum;
- operation at high pressure.

The wall thickness of a polyurethane bushing is determined from the strength condition of thick-walled cylinders loaded with external pressure

$$h = \frac{D}{2} \left(\sqrt{\frac{[\sigma_s] + 0.4P_Z}{[\sigma_s] - 1.3P_Z}} - 1 \right), \quad (7)$$

where σ_s – permissible tensile stress for elastomer grade SR55 according to the data of the company «Getzner Werkstoff» [3], [11] is taken as 0,061 MPa;

$P_Z = p_1$ – pressure on the walls of the bushing.

The radial deformation of the bushings from uniformly distributed pressure p_1 can be determined using the Lamé formula [9]:

$$\delta_1 = \frac{r_1 \cdot p_1}{E} \left(\frac{r_2^2 + r_1^2}{r_2^2 - r_1^2} + \frac{1}{m} \right), \quad (8)$$

where $\frac{1}{m}$ – the ratio of Poisson's ratios of the materials of the bushing and pump body;

r_1 – bushing hole radius;

$r_2 = r_1 + h$ – outer radius of the bushing circle;

E – elastomer elasticity modulus grade SR55.

Rigidity coefficient of polyurethane bushing

$$c_{el} = p_1 \cdot A / \delta_1 = F_0 / \delta_1$$

The stiffness coefficient according to the above formula

$$c_{el} = 732,5/0,00137 = 0,535 \cdot 10^6 \text{ N/m}$$

When the elements of the system are connected in series, the reduced rigidity

$$c_r = c_r \cdot c_{el} / (c_r + c_{el}). \quad (9)$$

After substituting the data

$$c_r = 0535 \cdot 66,59 \cdot 10^{12} / (0,535 + 66,59)10^6 = 0,364 \cdot 10^6 \text{ N/m}$$

Natural frequency of the system

$$\dot{\omega}_a = \sqrt{2c_r/m} = \sqrt{2 \cdot 0,364 \cdot 10^6/120} = 77,8 \text{ s}^{-1}$$

The ratio of frequencies of forced and natural oscillations of the system is $308,7/77 = 4$, which corresponds to the recommendations for reducing resonance oscillations. Isolation of oscillations by shock absorbers achieves the goal when the ratio of frequencies of forced and natural oscillations, $\dot{\omega}_a/\omega_a > \sqrt{2}$. In practice, the ratio of these frequencies is taken to be 2,5-5. The expression $|1/1 - (\omega/\omega_a)^2| = |1 - 4^2| = 15$, the transmission coefficient $1/15 = 0,066$ is included in the recommended range, which characterizes sufficient vibration isolation of the bearings. The force transmitted to the support, taking into account the damping of the system $F = 2345 \cdot 0,066 = 15,47 \text{ N}$, i. e. $2345/15,47 = 151,5$ times less than the force disturbing the oscillations. The reciprocal of the transmission coefficient, expressed in logarithmic units, will determine the vibration isolation (dB) of the shock-absorbing mount.

$$VI = 20 \cdot \lg 1/\mu_t. \quad (10)$$

According to calculations

$$VI = 20 \cdot \lg 1/0,066 = 23,6 \text{ Hz},$$

which corresponds to the permissible vibration level.

To simulate the vibrations of the 2D630-125 pump body on the foundation, it is necessary to determine the elastic and damping properties of the elements included in this model. To build a foundation for a 2D630-125 pump unit, the class of concrete being laid must be at least 10 (compressive strength in MPa). Concrete of class B25 is accepted, the rigidity of the foundation for the pumping unit according to formula (11)

$$c_f = E_f \cdot A_f/h, \quad (11)$$

where $E_f = 30 \cdot 10^3 \text{ Mpa}$ – modulus of elasticity of concrete under compression;

A_f – the area of the foundation base is taken to be greater than the area of the horizontal projection of the pump;

h – the depth of the underground part of the foundation, for heated rooms the minimum is 0,5 m

$$c_f = 30 \cdot 10^9 \cdot 0,33/0,5 = 20 \cdot 10^9 \text{ N/m}.$$

Natural frequency of the system

$$\omega_a = \sqrt{20 \cdot 10^9/625} = 5656 \text{ s}^{-1}.$$

It is much higher than the frequency of disturbing vibrations, which characterizes the low vibration isolation of the system $|1/1 - (\omega/\omega_a)^2| = |1 - (308,7/5656)^2| = 1$. Transfer coefficient $\mu_t \sim 1$. Therefore, the support reaction is equal to the disturbing force.

For the elastomer material grade SR55, the dynamic modulus of elasticity is $0,753 \cdot 10^6 \text{ MPa}$ [12]. Rigidity of the flooring under the pump sole

$$c_{el} = 0,753 \cdot 10^6 \cdot 0,33/0,03 = 8,74 \cdot 10^6 \text{ N/m}$$

Reduced rigidity of the foundation and elastomer deck

$$c_{r1} = 8,74 \cdot 20000 \cdot 10^6 / (8,74 + 20000) \cdot 10^6 \sim 8,74 \cdot 10^6 \text{ N/m}$$

Natural frequency of the system

$$\omega_a = \sqrt{8,74 \cdot 10^6/625} = 118,25 \text{ s}^{-1},$$

below the frequency of disturbing oscillations in $308,7/118,25 = 2,61$, what characterizes sufficient vibration isolation of the system $|1/1 - (\omega/\omega_a)^2| = |1 - (308,7/118,25)^2| = 5,81$ Load transferred to the support $2345/5,81 = 403,6 \text{ N}$.

One of the common methods for assessing the dynamic parameters of mechanical equipment is modelling the movement of the masses of its individual elements [12]. The movement or their kinematic and force interaction are described by systems of differential equations. Mathematical modelling allows us to assess the calculations performed and supplement them with studies that are difficult to conduct without taking into account the dynamics of the process [13]. As shown in Figure 1, the mathematical model of the pump unit consists of two moving masses connected to each other by

elastic connections in the form of stiffness coefficients. The mass of the pump casing without the rotor, m_1 , and the mass of the rotor, i. e. the shaft with supports and the impeller assembly, m_2 . For ease of analysis, the location of the masses and the coordinate of their movement X in Figure 1 and further in the text are assumed to be horizontal, although in reality the oscillations of the system elements occur in the radial, i. e. vertical direction.

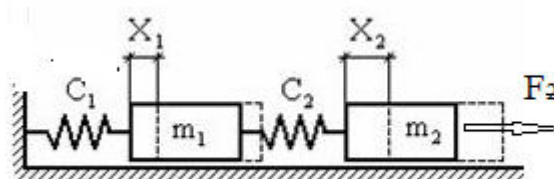


Fig. 1. - Two-mass forced oscillation system

The differential equations of free oscillations of masses have the form:

$$\begin{cases} m_1 \ddot{X}_1 + c_1 X_1 - c_2 (X_2 - X_1) = 0; \\ m_2 \ddot{X}_2 + c_2 (X_2 - X_1) = 0, \end{cases} \quad (11)$$

frequency equation of a system of two masses:

$$\omega^4 - \left(\frac{c_1 + c_2}{m_1} + \frac{c_2}{m_2} \right) \omega^2 + \frac{c_1 c_2}{m_1 m_2} = 0 \quad (12)$$

This frequency equation always has two real and positive solutions, i. e. a system with two degrees of freedom has two natural frequencies, which are found from the solution of the quadratic frequency equation [14]:

$$\omega_{1,2} = \frac{0.5(c_1 + c_2)}{m_1} + \frac{0.5c_2}{m_2} \mp \sqrt{\left(\frac{0.25(c_1 + c_2)}{m_1} + \frac{c_2}{m_2} \right)^2 - \frac{c_1 c_2}{m_1 m_2}} \quad (13)$$

2. Results and discussion

For the pump 2D630-125, the calculation of equations (12) of free oscillations of the system gives the values of natural frequencies $\omega_1 = 749 \text{ s}^{-1}$; $\omega_2 = 5666 \text{ s}^{-1}$. The frequency of forced oscillations of the pump rotor on rolling bearings at harmonic $k = 3$ is $\omega = 308,7 \cdot 3 = 926 \text{ s}^{-1}$. It is close to the natural frequency of the system. $\omega_2 = 749 \text{ s}^{-1}$, $926/749 = 1,23$ frequency ratio, which promotes excitation of near-resonant oscillations of the rotor. The main rotor frequency $\omega = 308,7 \text{ s}^{-1}$ is below the range of natural frequencies of the bearing support and is not sufficient to excite resonant vibrations. The parameters of the mathematical model presented in Table 1.

Table 1. Parameters of the mathematical model

Parameters	m_1 , kg	m_2 , kg	c_1 , N/m	c_2 , N/m	c_{r1} , N/m	c_{r2} , N/m	ω_1 , s^{-1}	ω_2 , s^{-1}
2D630-125	625	120	$20 \cdot 10^9$	$1331 \cdot 10^6$	$8,74 \cdot 10^6$	$364 \cdot 10^3$	0	308,7

After calculating the free oscillations of the system and determining the natural frequencies, the calculation of forced oscillations is carried out.

For an independent study of oscillations caused by one external source, a solution is made to the system of two equations from the second force $F_2(\omega)$, arising from the violation of the shaft alignment. This method has shown its effectiveness and sufficient accuracy in work [15].

When calculating the disturbance from the centrifugal force on the second mass, the first force is taken equal to zero, and the second force $F_2(\omega_2)$, applied to the rotor supports, is calculated under the condition that the disturbance frequency is equal to the rotor frequency ω_2

$$A_1 = F_2 c_2 / ((c_1 + c_2 - m_1 \omega_2^2)(c_2 - m_2 \omega_2^2) - c_2^2); \quad (14)$$

$$A_2 = F_2 (c_1 + c_2 - m_1 \omega_2^2) / ((c_1 + c_2 - m_1 \omega_2^2)(c_2 - m_2 \omega_2^2) - c_2^2) \quad (15)$$

The calculation of the expression using special programs for calculating algebraic equations on a computer [8] showed (Table 2) that when exciting oscillations with force $F_2(\omega)$ for a 2D630-125 pump without a damping device (DD) at the points where the casing is attached to the foundation, the elastic deformation force of the casing supports (14) on the foundation was $F_{01} = 20 \cdot 10^9 \cdot 1,288 \cdot 10^7 = 2576 \text{ N}$. Calculation of the amplitude of the second mass using expression (15) yielded a value of $A_2 = 0,965 \cdot 10^{-5} \text{ m}$, the elastic deformation force of the rotor supports without an

elastic element was $2F_{12} = 2 \cdot 0,965 \cdot 10^{-5} \cdot 133,1 \cdot 10^6 = 2513$ N, (the force per support is 1256 N). The force exciting vibrations for two supports is equal to 2345 N, the transfer of external load to both types of supports occurs approximately equally and this is due to the fact that the transfer coefficient, as shown above, is close in value to one. Calculation of the amplitude of the first mass with an elastic element in the form of a Vibro-damping Elastomeric Plate (VEP) flooring under the pump showed the value $A_1 = -0,402 \cdot 10^{-4}$ m, the elastic deformation force of the pump supports with the VEP was $F_{01} = -0,402 \cdot 10^{-4} \cdot 8,74 \cdot 10^6 = -351$ N. The deformation of the supports of two masses according to the calculation of the equation taking into account the sign is equal to the difference in amplitudes $A_1 - A_2 = (-0,402 + 0,247) \cdot 10^{-4} = -0,155 \cdot 10^{-4}$ m, the elastic deformation force of the rotor supports was $2F_{12} = -0,155 \cdot 10^{-4} \cdot 1,33 \cdot 10^6 = -2063$ N, (the force per support is 1031,5 N)

Table 2. Elastic deformation forces of supports without elastic elements and with them in pump 2D630-125

Pump 2D630-125			
Disturbing force, N	$F_2(\omega) = 2345\sin 308t$		
Force on rotor supports and foundation, N	without DD	VEP on the base	VEP on the foundation and elastic bushings on bearings
$2F_{12}$	2513	2063	18,3
F_{01}	2576	351	27,7
$2F_{12}^*$	2564		15,47
F_{01}^*	2345	403,6	

Thus, the presence of an elastic support under the base of the pump housing slightly reduces the load from vibration acting on the bearings (from 2513 N to 2063 N). While the reaction on the housing supports to vibration when using VEP is significantly reduced. While the reaction on the housing supports from vibration when using VEP is significantly reduced from 2063 N to 351 N, i. e. by 5.87 times, the use of elastic elements made of elastomer as a flooring for the pump housing and the installation of dampers made of polyurethane bushings under the outer ring of the rolling bearing reduce the vibration loads perceived by the foundation from 2576 N to 27.7 N, and on rolling bearings from 2513 N to 18.3 N.

Table 2 shows the elastic deformation forces of the supports F_{01} , F_{12} are presented based on the results of mathematical modelling and calculation using the transfer coefficient (shown in the table with an asterisk). The results are almost identical with a small error, which confirms the objectivity of the adopted methods and the reliability of the calculation results.

Conclusions

The following conclusions follow from the analysis of the results:

- the amplitude of the load oscillations depends on the ratio of the frequencies of forced and natural oscillations. Due to the high frequency of natural oscillations of the bearings and lower frequencies of oscillations of the centrifugal force, the efficiency of vibration isolation is reduced.

- it is shown that the use of elastic elements made of elastomer as a flooring for the pump casing slightly reduces the vibration loads acting on the rotor supports when oscillations are excited by the centrifugal force of the rotor. While the reaction on the body supports from vibration when using the VEP is significantly reduced

- it is shown that the use of elastic elements made of elastomer as a flooring for the pump casing and the installation of dampers made of polyurethane bushings under the outer ring of the rolling bearing reduce the vibration loads perceived by the foundation and bearings.

References

- [1] Schiavello B, Visser FC. Proceedings of the 24th International Pump Users Symposium. In: Pump Cavitation – Various NPSH r Criteria, NPSH a Margins, and Impeller Life Expectancy. 2008.
- [2] 48th conference in Timisoara. In: Vibration diagnostics of structures and equipment. Timisoara, Romania; 2020.
- [3] Elastic Decoupling of Pumps TB Pumps en Copyright by Getzner Werkstoffe GmbH : 11 – 2016.
- [4] Listewnik K, Grzeczka G, Kłaczyński M, Cioch W. Online application for machine vibration diagnostics in accordance with ISO 10816. Journal of Vibroengineering. 2015; 17(8):4248-4258.
- [5] Norton M.P., Hodkiewicz M. Alternative Energy Development Board Project B143; 2000, p.3-39
- [6] Goldsmith M. Suction specific speed and vibration performance. December 21, 2015.
- [7] Perevoshchikov S. I. Development of scientific bases of management of vibration of the hydro-dynamic origin in centrifugal pumps of main pipelines. – Tiumen': Alfabuild, 2019. – 347 p.
- [8] Mustafin A. Kh., Seytenova G. Zh., Kabylkaiyr D. N. Modelirovanie vibracii nasosnyh agregatov na oporah i metody ih snizheniya. Materialy10-j Mezhdunarodnoj nauchno-tekhnicheskoj konferencii [Modelling vibration of pump units on supports and methods for reducing them. Proceedings of the 10th International Scientific and Technical Conference]. – Omsk : 26-29 February 2020.
- [9] Birger I. A. Raschety na prochnost' detalej mashin. Spravochnik [Strength Calculations of Machine Parts. Handbook] / Birger I. A., Shorr B. F., Iosilevich G. V. – M. : Mashinostroenie, 1993. – 702 p.

- [10] Birger A. N. Prochnost'. Ustojchivost'. Kolebaniya. Spravochnik v 3 tomah [Strength. Stability. Oscillations. Handbook. In 3 volumes]. / Ed. Birger A. N., Panovko Ya. G. – M. : Mashinostroenie, 1968. – vol. 3. – 567 p.
- [11] Galihanova E. A., Bakaeva L. N., Dernakova A. V. Poliuretanovyy elastomer kak uprugij material v sejsmozashchite zdaniy i sooruzhenij [Polyurethane elastomer as an elastic material in seismic protection of buildings and structures] // Alfabuild, No 5, 2019.
- [12] Villar M. M., Pérez M. M. Conference: ASME 7th Biennial Conference on Engineering Systems Design and Analysis Elastic Analysis of Journal Bearings; 2004 January
- [13] Mustafin A. Kh. Populyarnaya mekhanika v inzhenerii [Popular Mechanics in Engineering]. – Pavlodar : Toraighyrov University, 2021. – 96 p.
- [14] Reshenie sistem linejnyh uravnenij. [Solution of systems of linear equations] Available at: <https://matrixcalc.org/ru/slu.html>.
- [15] Mustafin A. Kh., Sadykov N. S. Povyshenie nadezhnosti i effektivnosti mekhanicheskogo oborudovaniya v neftekhimicheskom proizvodstve [Improving the reliability and efficiency of mechanical equipment in petrochemical production]. Pavlodar: Toraighyrov University; 2024.

Information of the authors

Mustafin Adilbek, c.t.s., professor, Toraighyrov University

e-mail: mustafin-51@mail.ru

Sadykov Nursultan, master of science, senior lecturer, Toraighyrov University

e-mail: sadykov.n@teachers.tou.edu.kz

Mechanisms for Forming the Surface Structure of Steel Products During Heat Hardening

Issagulov A.Z.¹, Sharaya O.A.², Vodolazskaya N.V.³, Arinova S.K.¹, Tugambaeva A.A.^{1*}

¹Karaganda Technical University, Karaganda, Kazakhstan

²Russian Institute for Scientific and Technical Information, Moscow, Russia

³MIREA — Russian Technological University, Moscow, Russia

*corresponding author

Abstract. The paper considers the questions of strengthening of critical joints made from materials and working in complex power, temperature and high-speed operating conditions of friction parts. Production of hardened surface layers is achieved by purposeful formation of specified structural state of metal, i.e. by modification using low-temperature plasma. This method of heat treatment helps to solve the problem of increasing the wear resistance of metal products and materials for their manufacture. Particular attention is paid to the study of the conditions for the formation of the optimal microstructure and phase composition of steel in order to obtain satisfactory hardness and ductility. There are offered modes of hardening treatment, which can be used for plasma hardening of details under conditions of metallurgical production. The conducted thermophysical measurements allowed determining the heating rate of the product surface during plasma heat treatment, which was 2000 K/s. It was found that plasma hardening of a standard high-speed steel tool increases microhardness of its surface to 12000 MPa and creates a hardened layer 1-1.5 mm deep.

Keywords: low-temperature plasma, chemical-thermal treatment, hardening, microstructure.

Introduction

Improving the reliability of the equipment is one of the most important components of the product quality assurance system. It provides for reducing the number of failures due to wear of machine structural elements [1-3]. Depending on the current operating conditions, the wear process can be of a different nature: from the usual mechanical, including abrasive and fatigue, to molecular mechanical and corrosion-mechanical [4-6]. This problem requires increased attention to the possibility of creating fundamentally new materials with a given level of properties and to the development of strengthening technologies for the surface layer of products from known metal alloys. To solve it, an integrated approach is usually used. It combines the principles of forming the chemical composition of the material and then the structure by developing technological processes for its strengthening treatment during the production process or during the repair and restoration work.

In order to improve the strength characteristics and operational properties of machine parts, targeted formation of a given structural state of metal is usually carried out by chemical-thermal treatment methods, for example, nitro cementation, carbonitration, etc [7-10]. And also there are methods based on the use of highly concentrated energy sources such as ionic, plasma, laser, electro-spark, ultrasonic, high frequency induction and others [11-16]. A result of this effect is either structural changes in the original surface i.e. the modification process or the formation of a given coating on the surface.

The importance of continuing scientific investigation in the field of strengthening coatings of materials is evidenced by the analysis of recent scientific research and publications. The introduction and development of various methods of forming a given structural state of the metal leads to an increase in surface quality and service life, in particular steel parts of critical joints. Therefore, investigation of these methods and their features is an urgent task requiring continued research in the field.

At a present time it is considered perspective to use heat treatment with low-temperature plasma to strengthen the surfaces of materials. The plasma (the ionized gas) represents the directed flow of charges particles with a high concentration of energy in it. The principle of thermal treatment on the basis of plasma has its foundation in the rapid warming (=1000 Kelvin degrees per second) and the regulated cooling of the work surface, which cannot be reached by using the traditional ways of thermal treatment and which permits the creation of a specific structure with a set of specific characteristics. The plasma treatment (or the so-called surface modification) unlike the laser or ion implantation is characterized by a larger depth of the strengthened layer, the simplicity of the technological process and a high coefficient of efficiency [17-26].

This fact confirms the scientific significance regarding surface structure studying of steel pieces, which has a unique combination of mechanical, physical and chemical properties obtained using this thermal hardening method.

To realize the prospects of an innovative version of the development of production potential, it is necessary to consider and solve a number of tasks aimed at improving technologies and technical means to ensure the operable state of existing domestic and especially foreign equipment, taking into account the possibility of its import substitution. One of the main directions identified in the process of finding solutions is the development of various technologies that allow improving the operational properties of the working surfaces of the parts of critical joints based on methods of applying a layer of material, hardening and modification.

The object of the investigation is the technological process of structure formation and specific characteristics in the process of thermal strengthening of structural steel pieces by using plasma. Medium carbon steels were selected as the test material. As the material under study there was selected steel 65G, SS 14959-2016 (analogs: G15660 – USA, 66Mn4 –

Germany, 080A67 – GB, 65Mn - China) and twist drills with the diameter of 17-20 mm made of fast-cutting steels of R6M5, R6AM5 and 11R3AM3F2 grades according to SS 19265-73 (analogs: S6-5-2 - EN 1.3343, M2 - USA).

The aim of this work is to study chemical-thermal treatment with low-temperature plasma and to obtain its optimal technological mode, which contributes to increasing wear resistance of steel blanks and tools (drills) made of high-speed steel.

To achieve the goal, it is necessary to agree on the optimal regimes of heat treatment in order to create a new form of thermal treatment which would allow for the specific changes in the steel structure. This can be represented by the block decomposition, the birth of micro-tensions and the increase in thickness of the dislocations in the surface layer.

1. Research methodology

The experimental installation consisted of an indirect arc plasmatron 1 and a steel sample 2 (Fig.1). The EDP-104-like plasmatrone, the power of which was about 9 kilowatts with the 50 ampere current, was used for the surface modifications of the steel pieces. The nozzle diameter was of 8 mm. In the central part of the steel sample and on its surface a thermocouple was stuck, and at the time the piece was in movement that thermocouple passed just above the discharge jet of the plasmatrone. The measuring of temperature at the time of the warming and cooling was allowed by the fast-acting plotter. The speed of the relative movement of the piece changed from 2 to 30 mm per second, and the distance between the nozzle cut and the work surface was changing from 17 to 30 mm. The cooling of the piece was put into practice with the use of water which was sprayed with a pneumatic jet at the time the piece was pulled out of the plasma flow.

A typical heating curve of the sample surface layer is shown in Figure 2. The beginning of the temperature rise coincided with the moment of contact of the sample edge with the plasma jet. At the same time, the spread of luminous streams up to 30 mm long on the inner surface of the sample was noted.

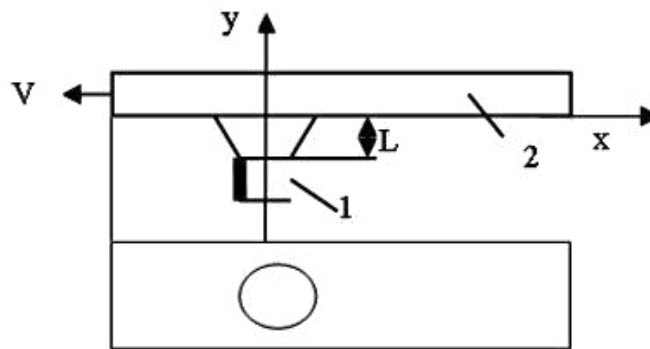


Fig.1 - Schematic diagram of the trial type: 1 – plasmatron, 2 - steel sample

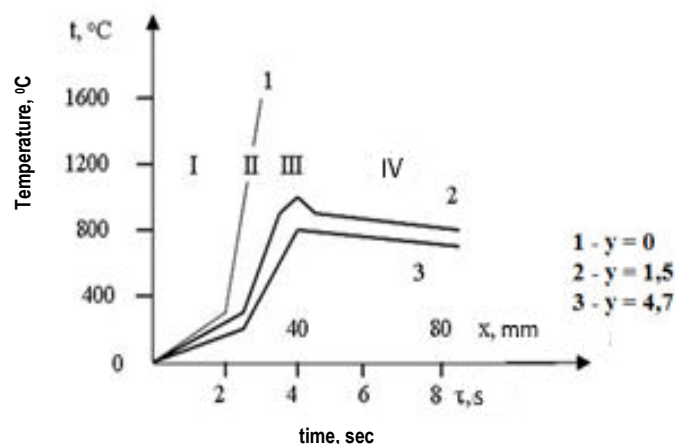


Fig.2. - Typical heating curves $V = 9$ mm/s, $L = 17$ mm

In region I, the rate of temperature elevation for curve 2 was 80 K/s, for curve 3 - 40 K/s. In the II-zone of the heating spot, the temperature rise occurred linearly at a rate of 1700, 450 and 250 K/s for curves 1, 2 and 3, respectively. In area III, for curves 1 and 2, a temperature drop at a rate of 700 and 100 K/s was observed, and for curve 3, the temperature was kept at 700 °C. In area IV, where the sample was already moving away from the action of the plasma jet, the temperature in all sections was equalized and it was cooled at a rate of 10-15 K/s.

The dependence of the maximum temperature of the sample on the processing distance and the speed of its movement is shown in Figure 3.

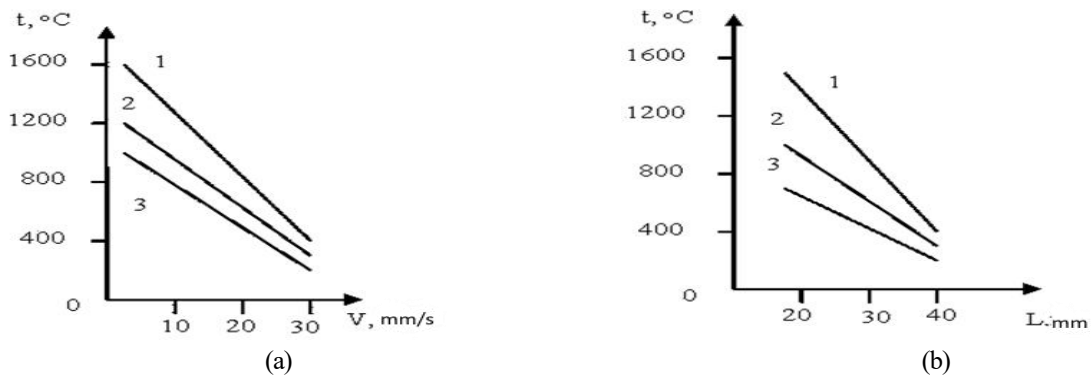


Fig.3. - Temperature of the sample - speed of its movement relationship where $L = 15$ mm (a) and $V = 8$ mm/s (b)

A special attention has been paid to research the conditions of the formation of the optimal microstructure and the phase composition of steel in order to get a satisfying hardness and plasticity. Studying the steel microstructure with regard to the sample profiles after the plasma treatment has shown that the surface layers had no cracks and were pure to a high extent. According to the metallographic analysis the structure of the surface coating under the initial conditions was ferrite-pearlite, and after the plasma treatment a conversion from the structure of fine-needled martensite close to the surface to the initial sorbitic pearlite-like core structure was established. The surface layer of the sample was monitored as a white 24 μm -thick layer which was immune to etching in the metallographic reagents. At the certain places the closest to the surface the subgrain boundaries could be seen (Fig.4).

The results of light microscopy were complemented by the electronic-microscopic analysis of the surface steel layers in the initial state and after the plasma treatment. It was necessary to prepare a few samples treated in the same conditions for getting full information about the microstructure characteristics and the change of quantity parameters subject to the distance changes between the plasmotrone nozzle and the work surface. In this case the sample's surface structure was looked into at the depth of $0.50 \mu\text{m}$.

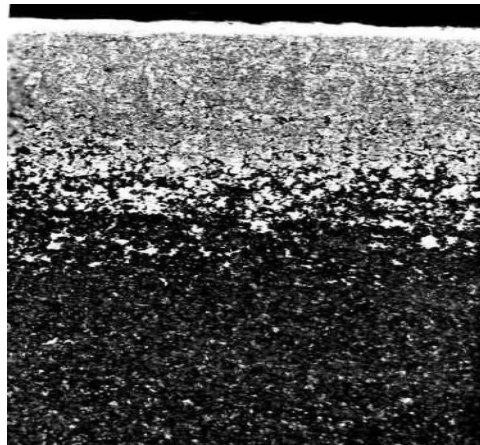


Fig.4. - Steel microstructure after surface modification, x 100 (light microscopy)

After the surface modification the foil paper was made from the sample for further electronic-microscopic analysis through the instrumentality of the electronic microscope "Tesla BS-540" (the accelerating voltage was 120 kV) with goniometric head. The dislocation thickness was measured by the means of the secant line with use of a proportion: $p=2 \text{ NM}/(\text{LT})$.

where N – is a number of intersections of the secant line with the image of dislocations on the microphotograph;

L – is the total length of the secant line;

T – is the foil's thickness;

M – is the total zoom of the microphotography.

In the initial state the steel microstructure was represented by ferrite and pearlite (Fig.5).

The pearlite component was seen in the form of lamellar and globular modifications. The medium thickness of the cementite plates turned up to be $0.077 \mu\text{m}$, the inter-plate distance was $0.2 \mu\text{m}$. Within one colony the cementite plates are oriented in the same direction. Inside the ferrite the dislocations were distributed chaotically, their scalar density did not surpass 10^8 cm^{-2} .

After the air plasma treatment in the surface layers of the samples the hardened zone was formed, the dispersibility of the microstructure increased significantly. The main structural component of the hardened near-surface region of the samples was the fine-dispersed martensite of mixed morphology (Fig.6).

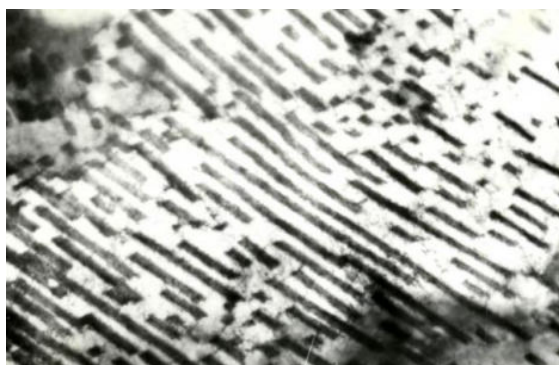


Fig.5. - Steel microstructure in initial state, x 10200



Fig.6. - Microstructure of steel surface after plasma treatment, x 10000

The quantity of residuary austenite situated between the martensite plates did not surpass 10 %. The dimensions of the martensite plates changed with regard to the plasma treatment regime within $L = 1.09 - 3.15 \mu\text{m}$, $d = 0.25 - 0.74 \mu\text{m}$.

After the plasma thermal treatment the main structural components of the hardened zone were the fine-disperse martensite of mixed morphology and the residuary austenite (up to 10 %). The dimensions of the martensite plates changed within $L = 1.09 - 3.15 \mu\text{m}$ and $d = 0.25 - 0.74 \mu\text{m}$.

It has been determined that with regard to the thermal treatment regimes the zone of plasma treatment upon the surface of the steel sample was up to 1.5-2.4 mm in size. The analysis of the microhardness distribution profiles throughout the depth of the hardened layer has shown that the depth of the layer with the 12640 – 13650 MPa microhardness did go up to 150 - 200 μm (Fig. 7).

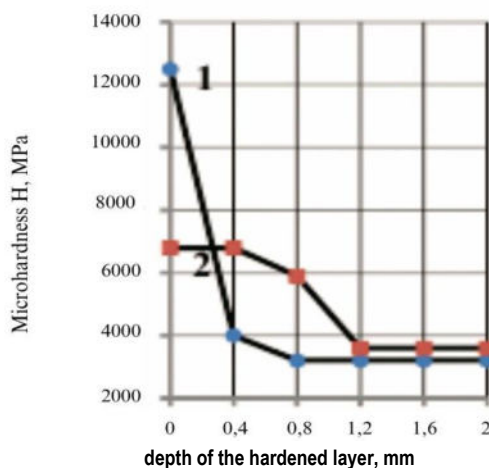


Fig. 7. - Microhardness distribution profiles by the depth of the hardened layer

2. Results and discussion

Twist drills are among the most common types of cutting tools. Currently, the use of traditional methods of heat treatment of tools made of high-speed steel grades to increase their wear resistance has been almost exhausted.

According to literature data, the use of highly concentrated energy sources, such as lasers and low-temperature plasma, can significantly increase hardness and wear resistance of products made of high-speed steels.

Plasma hardening was used for industrial cutting tools that had already undergone heat treatment (quenching and triple tempering) using a standard technology. Twist drills with the diameter of 17–20 mm made of high-speed R6M5, R6AM5, and 11R3AM3F2 steel grades, were subjected to plasma hardening for subsequent heat strengthening.

The plasma drill was fed into the heating zone with the rotation speed of 2–10 rpm. The plasma torch was positioned at the angle of 60 degrees relative to the drill axis and at the distance of 30–40 mm. The heating time varied from 2 to 25 seconds. The product was cooled with a water-air mixture under pressure. Rotation of the tool made it possible to increase the heating time and to ensure uniform heating of the drill working surface. The quality of the tool treatment was controlled indirectly by the color of the oxide film and the distribution of the microhardness numbers. This made it possible to establish the optimal parameters for plasma treatment of the products: the distance 30 mm, the rotation speed 10 rpm, the heating time 10 sec.

For all the variants of drill treating modes, it was possible to obtain a hardened layer 1–1.5 mm deep from the surface. According to the results of metallographic analysis, the microstructure of the hardened layer contained a white zone with high microhardness not etched in acids up to 12000 MPa, the depth of which reached 0.4 mm. Next, there was a structure representing martensite and residual austenite; the microhardness of this zone was 9000 MPa. The construction of microhardness profiles showed that with increasing the distance from the surface of the product into the depth, there was decreasing hardness numbers to their values in the original structure (core).

Testing drills for durability after plasma hardening. The drills made of P6M5 steel (the diameter 17.4 mm) were used to drill a steel plate (Steel 40) 30 mm thick on a vertical drilling machine of the 2A135 modification with the speed of 250 rpm and the feed rate of 0.2 mm/rev without cooling. When drilling the plate with a drill after plasma treatment, the chips were light, i.e. their temperature was not high. When drilling with a conventional drill, i.e. not treated with plasma, the chips were dark, i.e. their temperature was high. Temper colors were observed on the main cutting blade, which indicated higher wear of the control (not treated with plasma) drill. In further studies, plasma-hardened drills made of P6M5 steel were tested as a result of treatment (drilling) cast iron samples. Plasma-hardened drills made twice as many holes as the control ones. After sharpening, the test drills also drilled twice as many holes.

1. The thermophysical measurements made it possible to determine the surface heating rate of the product during plasma heat treatment, which was 2000 K/s.

2. It was found that plasma hardening of a standard high-speed steel tool increases microhardness of its surface to 12000 MPa and creates a hardened layer 1–1.5 mm deep.

3. Tests of the test drills conducted under factory conditions, showed increasing their durability by 2 times and the possibility of multiple resharping of the drills within the thickness of the hardened layer.

4. A technology was developed for plasma hardening (heat strengthening) of twist drills made of P6M5, P6AM5, and 11P3AM3F2 steel grades.

Conclusions

As a result of the study of the formation of the surface structure of steel pieces in the process of thermal strengthening, it was revealed that the main condition of steel strengthening under the plasma heat treatment is the formation of the fine-dispersed martensite structure in the near-surface zones. It was found that the depth of zone affected by the plasma thermal treatment reaches 1.5 – 2.4 mm and depends on the parameters of the plasma device and the heat treatment regimes. The medium-carbon steel strengthening occurs with the 12640–13650 MPa microhardness and the 150–200 mkm depth. Thus, the obtained results make it possible to recommend the different technological regimes of plasma thermal treatment, which help to solve the problem of increasing the wear resistance of the surface layer of critical steel parts.

The conducted thermophysical measurements allowed determining the heating rate of the product surface during plasma heat treatment, which was 2000 K/s.

It was found that plasma hardening of a standard high-speed steel tool increases microhardness of its surface to 12000 MPa and creates a hardened layer 1–1.5 mm deep.

The obtained optimal hardening treatment modes for model samples were used for plasma hardening of tools in metallurgical production conditions.

Tests of pilot drills conducted in factory conditions showed increasing their durability by 2 times and the possibility of multiple resharping of drills within the thickness of the hardened layer.

A technology for plasma hardening (heat strengthening) of twist drills made of R6M5, R6AM5, and 11R3AM3F2 steel grades was developed.

Acknowledgments: This research was funded by the Committee of Science of the Ministry of Science and Higher Education of the Republic of Kazakhstan, grant number BR24993020.

References

- [1] Kuxmin V.V., Kosov D.S., Novikov A.L., Ivashchenko A.V. Industrial Plant Equipment Failure Prediction System. Stamford: Reliab. Qual. Complex Syst., 2015. – 87–90 p.
- [2] Pavlyuk R.V., Lebedev A.T., Zhevora Y.I., Zubenko E.V. The reliability analysis of combined harvesters in the usual conditions of operation //Conf. Ser.: Earth Environ. Sci., Vol. 488, 2020. – p. 012033. doi:10.1088/1755-1315/488/1/012033.
- [3] Krasnov A.E., Sapogov A.A. Service quality assessment in IT projects based on aggregate indicators // Russ. Technol. J., Vol. 12, Issue 5, 2024. – p. 90–97. <https://doi.org/10.32362/2500-316X-2024-12-5-90-97>.
- [4] Petropoulos G., Marinkovic A., Vodolazskaya N., Korlos A. Ntziantzas. Another approach of surface texture in turning using motif and “Rk” parameters //J. Balkan Tribol. Assoc., Vol. 12, Issue 1, 2006. – p. 7–15.
- [5] Strebkov S., Bondarev A., Slobodyuk A., Vasilenko E. Tribological compensation for reduced properties of parts during operation. Eng. Rural Dev., Vol. 20, 2021. – p. 227–233. doi:10.22616/ERDev2021.20.TF024.
- [6] Alexandrov A.E., Borisov S.P., Bunina L.V., Bikovsky S.S., Stepanova I.V., Titov A.P. Statistical model for assessing the reliability of non-destructive testing systems by solving inverse problems // Russ. Technol. J., Vol. 11, Issue 3, 2023. – p. 56–69. <https://doi.org/10.32362/2500-316X-2023-11-3-56-69>.
- [7] Vodolazskaya N.V., Sharaya O.A. Research of alternative options for strengthening surface treatment of cast iron product //Defect Diffus. Forum., Vol. 410, 2021. – p. 9–14. doi:10.4028/www.scientific.net/ddf.410.9.
- [8] Pedram Samadian, Ryan George, Constantin Chiriac, Cyrus Yau, Clifford Butcher, Michael J. Worswick Non-isothermal forming limits of press-hardening steels during hot stamping //Journal of Materials Processing Technology, Volume 340, June 2025, 118857. <https://doi.org/10.1016/j.jmatprotec.2025.118857>
- [9] Kovalev P.V., Popova S.D., Issagulov A.Z., Kulikov V.Y., Kvon S.S. Investigation of the effect of high strength strips steel modification with rare-earth metal (REM) //Metalurgija., Vol. 3–4, 2017. – p. 393–395.
- [10] Sharaya O.A., Vodolazskaya N.V. Hardening by sulfocyanation of parts of essential compounds //Innov. Agric. Complex: Probl. Perspect., Vol. 3, Issue 31, 2021. – p. 37–46.
- [11] Grigor'yanc A.G., Shiganov I.N., Misyurov A.I. Laser surface processing. - Moscow: MG TU. AD. Bauman., 2006. – 320 p.
- [12] Kuznetsov V.A., Smirnov A.V., Buvakin D.I. The study of the characteristics of metallic powders after electroerosion dispersion //Solid State Phenom., Vol. 284, 2018. – p. 696–700. doi:10.4028/www.scientific.net/SSP.284.696.
- [13] Strebkov S., Slobodyuk A., Bondarev A. Technology of electrospark hardening of cutting surface of feed mixer knives //Eng. Rural Dev., Vol. 20, 2021. – p. 819–824. doi:10.22616/ERDev2021.20.TF024.
- [14] Galin R., Shaburova N., Zakharyevich D. Features of technological processes of nanogalvanizing //SSP., Vol. 316, 2021. – p. 803–808. doi:10.4028/www.scientific.net/ssp.316.803.
- [15] Castro Cerda F.M., Goulas C., Jones D., Kamyabi A., Hamre D., Méndez P. Wood Modelling the laser surface hardening process in a steel with a spheroidized initial microstructure //Journal of Manufacturing Processes. Volume 125, 15 September 2024, p. 364-373. <https://doi.org/10.1016/j.jmapro.2024.07.052>
- [16] Issagulov A.Z., Kim V.A., Kvon S.S., Kulikov V.Y., Tussupova, A.U. Production of technical silicon and silicon carbide from rice-husk //Metalurgija., Vol. 4, 2014. – p. 685–688.
- [17] Selvabharathi R., Rajarajan P.C. Influence of laser surface hardening on low cycle fatigue performance of homogeneous-structure super austenitic stainless sheets by laser beam welding //Optik. Volume 252, February 2022, 168572. <https://doi.org/10.1016/j.ijleo.2022.168572>.
- [18] Shakhov V., Ivanovs S., Uchkin P., Ushakov Y. Studies in coatings for working bodies of deep-rippers recovered by plasma surfacing //Eng. Rural Dev., 2019. – p. 44–49.
- [19] Mikołajczak D., Kulka M., Makuch N., Dziarski P. Laser borided composite layer produced on austenitic 316L steel. Arch. Mech. Tech. Mater., Vol. 36, 2016. – p. 35–39. doi:10.1515/amtm-2016-0007.
- [20] Yadav S., Syed B., Ghosh S. Strengthening, strain hardening and fracture of heat-treated interstitial-free steel with massive ferrite conceptualizing the interface controlled reaction phenomena // Materialia. Volume 36, August 2024, 102158. <https://doi.org/10.1016/j.mtla.2024.102158>
- [21] Balanovsky A.E., Nguyen V.T. Increasing hardness of surface layer of low-carbon steel by account of plasma treatment of coating modification //Solid State Phenom., Vol. 316, 2021. – p. 794–802. doi:10.4028/www.scientific.net/ssp.316.794.
- [22] Joseph R. Surface Hardening of Steels: Understanding the Basics. ASM Int., 2002. – 412 p.
- [23] Tang L., Kang J., He P. Effects of spraying conditions on the microstructure and properties of NiCrBSi coatings prepared by internal rotating plasma spraying. Surf. Coatings Technol., Vol. 374, 2019. – p. 625–633. doi:10.1016/j.surfcoat.2019.06.056.
- [24] Levterov A., Nechitailo J., Plugina T., Volkov O. Application of thermo-frictional and chemical-thermal methods treatments for surface strengthening of materials //Mater. Sci. Forum., Vol. 1038, 2021. – p. 93–99. doi:10.4028/www.scientific.net/msf.1038.93.
- [25] Park Y.H., Abolhasani D., Moon Y.H. Graphene-based hardening agent modified using Ni and Cu nanoparticles in laser surface hardening of ferritic stainless steel //Applied Surface Science, Volume 700, 15 August 2025, 163151. <https://doi.org/10.1016/j.apsusc.2025.163151>
- [26] Sarsembaeva T.E., Kanaev A.T., Taimanova G.K. Differential heat treatment of one-piece freight-car wheels //Steel in Translation, 2017, 47(5), p. 345–348.

Information of the authors

Issagulov Aristotel Zeinullinovich, d.t.s., professor, Abylkas Saginov Karaganda Technical University
e-mail: aristotel@kstu.kz

Sharaya Olga Aleksandrovna, c.t.s., professor, Russian Institute for Scientific and Technical Information
e-mail: sharay61@mail.ru

Vodolazskaya Nataliia Vladimirovna, PhD, professor, MIREA — Russian Technological University
e-mail: vnv26@bk.ru

Arinova Sania Kaskataevna, PhD, senior lecturer, Abylkas Saginov Karaganda Technical University
e-mail: sanya_kazah@mail.ru

Tugambaeva Assem Adilkhanovna, doctoral student, Abylkas Saginov Karaganda Technical University
e-mail: dicosia0789@gmail.com

Advancements in Concentrated Solar Power: A Review of Heat Transfer and Parabolic Trough Technologies

Al-Aloosi W.¹, Alaiwi Y.², Al-Khafaji Z.^{2,3,4*}

¹University of Al Maarif, Al Anbar, Iraq.

²Altinbas University, Istanbul, Turkey;

³Universiti Kebangsaan Malaysia, Selangor, Malaysia

⁴Scientific Research Center, Al-Ayen University, Thi-Qar, Iraq

*corresponding author

Abstract: This review examines the advancements in concentrated solar power (CSP) technologies, focusing on their potential to meet energy demands sustainably while mitigating global warming. CSP systems, which harness solar energy through mirrors and lenses to generate high-temperature heat, offer a reliable alternative to fossil fuels. Key CSP technologies include Linear Fresnel Reflectors, Parabolic Dishes, Solar Towers, and Parabolic Trough Collectors (PTCs). Each system is assessed for its design, efficiency, and suitability in regions with high direct solar irradiance. Among these, PTCs are highlighted for their cost-effectiveness and thermal efficiency, with applications reaching temperatures up to 550°C, making them suitable for both small and large-scale implementations. The review also explores various heat transfer enhancement techniques, categorized into active, passive, and compound methods. Passive techniques, such as inserts, surface modifications, and nanofluids, are examined for their ability to increase heat transfer efficiency without external energy sources. Active methods like pumps, fans, and compound approaches are discussed for maximizing thermal performance. Advances in receiver design, including twisted tapes, wire coils, fins, and porous materials, are evaluated for their impact on heat transfer rates, thermal losses, and overall system efficiency. Additionally, the potential of nanofluids to improve thermal conductivity is explored. This comprehensive review underscores the importance of optimizing CSP systems to maximize efficiency, offering insights into innovations that could further enhance the adoption of solar thermal energy worldwide.

Keywords: solar thermal efficiency; parabolic trough collectors (ptcs); mitigating global warming.

Introduction

Global warming is the most essential concern nowadays, with repercussions like decreasing the amount of food that could be produced, rising sea levels, and changing weather patterns [1–4]. To combat global warming, it is necessary to discover clean, renewable, and sustainable energy sources to reduce carbon dioxide emissions. Solar thermal energy has been considered a practical solution for reducing our reliance on fossil fuels, reducing emissions that contribute to global warming, and providing human societies with electric power and systems of water heating, in addition to other industrial processes they require [5–8]. Concentrated solar power plants depend upon the direct normal irradiance representing the solar energy amount received for each unit area [9–11]. CSP plants can be designed to operate on a small or large scale, depending on the users' needs. They are particularly well-suited for use in sunny, dry regions. They can provide a reliable source of electricity if there is no sunshine, thanks to thermal energy storage systems [12].

This review aims to comprehensively analyze advancements in concentrated solar power (CSP) technologies, focusing on heat transfer enhancements for Parabolic Trough Collectors (PTCs) to improve thermal efficiency and promote sustainable energy. Objectives include evaluating major CSP systems—Linear Fresnel Reflectors, Parabolic Dishes, Solar Towers, and PTCs—for their design, efficiency, and suitability across applications. Additionally, the review investigates heat transfer techniques [13, 14], categorizing passive, active, and compound methods, and examines innovations in receiver design, such as twisted tapes, fins, and porous materials, for their impact on heat transfer. The potential of nanofluids to improve thermal conductivity in CSP systems is also assessed. This review addresses challenges and future directions in CSP scalability and cost-effectiveness, supporting clean energy goals and contributing to carbon reduction efforts worldwide.

1. Technologies for Concentrating Solar Power (CSP)

All approaches for CSP involve using mirrors or lenses to concentrate sunlight and convert it into electricity. These technologies have similar components, including a concentrator, a receiver, a heat transport medium or storage, and a power conversion unit. The main difference between the various CSP technologies is the shape and configuration of these components. Based on techniques that have been used in order to gather and concentrate solar radiation energy, the technology employed in CSP plants can be divided into four primary groups [15].

1.1. Linear Fresnel Reflectors

In concentrated solar power systems, individual reflectors are placed parallel to the ground so that every one of the reflectors is flat. It has a different focal length than its receiver. The spacing between reflectors is close to minimizing discontinuity in the reflective area or aperture. The reflectors' width has been optimized to allow access to reflectors for

maintenance while being manageable to complicate a support or tracking structure. as shown in Fig. 1. In contrast, a reflector could be placed to be related to more than one.

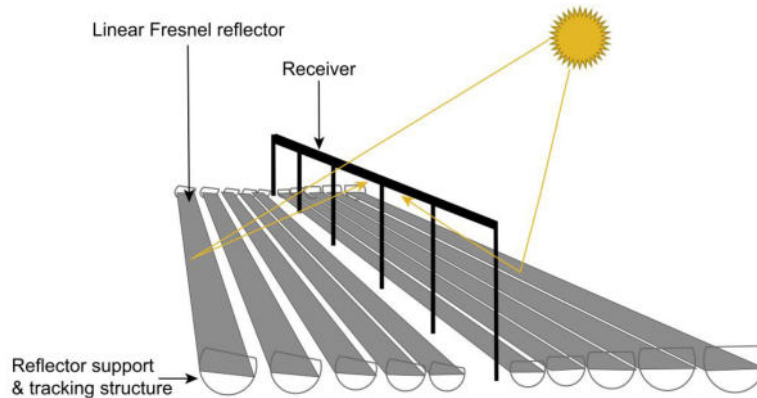


Fig. 1. - Linear Fresnel collector [15].

1.2. Parabolic dish

A parabolic dish collector is a solar thermal energy collector that uses a parabolic-shaped reflector to focus sunlight onto a central absorber tube. The reflector's parabolic shape allows it to focus sunlight onto a tiny area. The dish must follow the sun's movement to direct sun rays onto the receiver. These receivers can reach temperatures above 1,500°C, have concentrations between 600 and 2,000, and are the most efficient among all concentrated solar power (CSP) technologies [16].

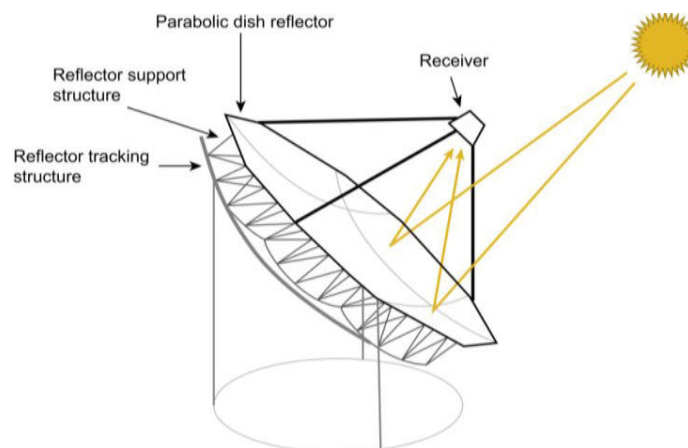


Fig. 2. - Parabolic dish collector [15].

1.3. Solar Tower

Solar towers are thermal power plants that use reflectors to focus sunlight on a central receiver at the top of the tower [17]. Concentrated sunlight makes electricity by heating a fluid, like water, to make steam that turns a turbine generator. The receiver absorbs a large amount of heat, reaching temperatures above 1,500°C [18]. The configuration of a solar tower is depicted in Fig. 3.

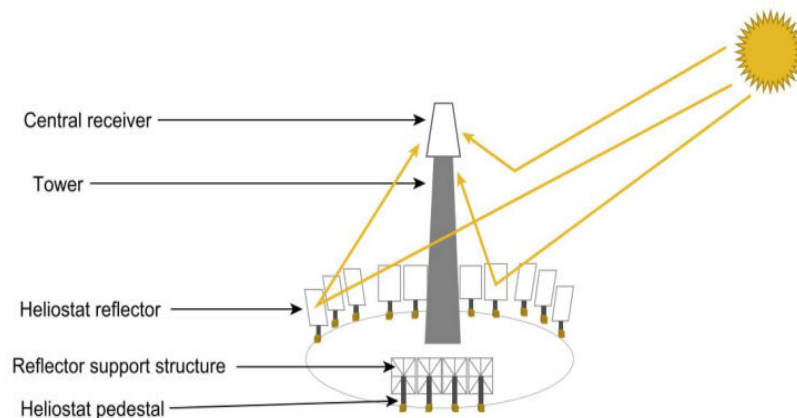


Fig. 3. - Solar tower [15].

2. Parabolic Trough Solar Collector (PTC)

PTC represents the oldest technology utilized in a broad range of applications. Particularly for levels of temperature that are as high as 400°C, PTCs can supply proper heat with high thermal efficiency with reasonable investment costs and are identified as mature and cost-effective technologies [19]. Therefore, this study will focus on this topic. Overall, CSP plants can effectively generate electricity using renewable energy and provide a reliable power source for various applications. However, they require a large amount of land and are typically only practical in areas with high levels of direct normal irradiance.

2.1. Fundamentals of PTCs

PTCs are line-focus concentrators producing high-temperature heat from concentrated solar energy. These systems can reach temperatures up to 550 degrees Celsius, though the exact maximum depends on the application. Figure 4 illustrated parabolic trough collector (PTC) system, the Heat Collection Element (HCE) is positioned precisely along the focal line of the reflective mirrors, serving as the central component responsible for thermal energy absorption. This element comprises a metallic absorber tube—typically constructed from stainless steel or a similar high-thermal-conductivity material—encapsulated within a vacuum-sealed borosilicate glass envelope to minimize convective and conductive heat losses. The absorber tube is designed to carry a heat transfer fluid (HTF), such as synthetic oil or molten salt, which facilitates the efficient transport of absorbed solar energy to downstream thermal conversion systems. Strategically mounted on the collector's structural supports, the HCE plays a critical role in maximizing optical-to-thermal energy conversion, and its precise alignment within the optical axis ensures optimal intercept of concentrated solar flux reflected by the parabolic mirrors.

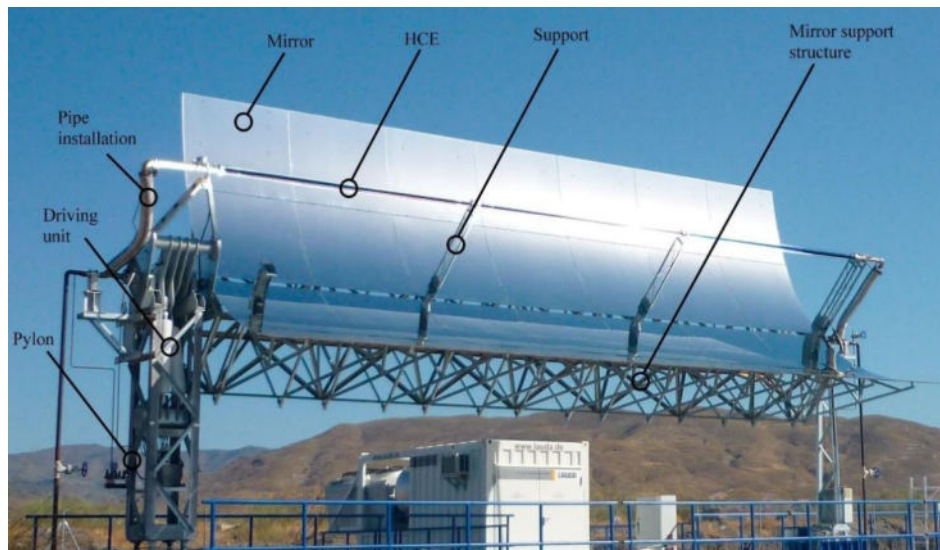


Fig. 4. - Parabolic trough collector system [20].

2.2. Reflector

This element includes high specular reflectance (over 88%) mirrors and structural components that reflect solar energy onto the receiver. The mirrors are typically made from low-iron float glass (about 4mm thick) of the large solar transmittance. They are silvered from the back and coated by selective coatings to maximize their durability and solar reflectance ($SR = 0.930$). Besides mounting structures, installation significantly affects overall plant performance [21]. In the previous articles, an analysis of reflecting coatings (for mirrors) and the general qualities of various materials was conducted, including an examination of techniques for applying reflective and selective coatings (SCs; for receivers) [22].

2.3. Receiver tube

The solar receiver tube represents a primary component of the solar thermal production systems; the PTC receiver tube is positioned at a point where the focal line of the parabolic mirror lies. In most cases, stainless steel is used for the tube material. A selective coating is applied to the outside of the tube. This coating has high absorptivity but low emissivity. Fig. 5 illustrates the absorber tube with a glass cover over it [23], which makes the outer layer transparent and anti-reflective to solar radiation, contributing to increased tube functionality. It is also capable of reducing convection and radiation losses [24].

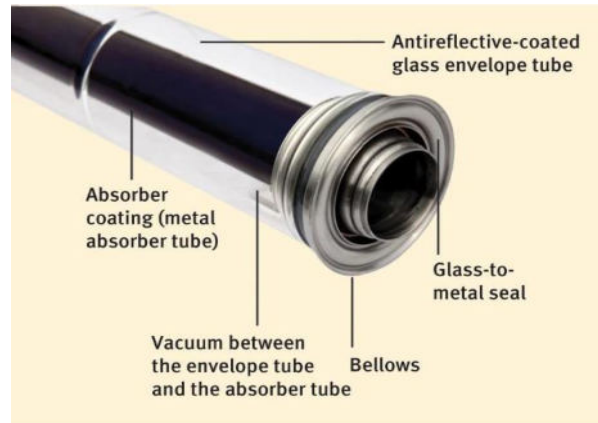


Fig. 5. - Typical receiver tube regarding the PTC [23].

2.4. Heat transfer fluid

The heat energy is relocated from the receiver to the storage system through a transmission fluid. Depending on the operating conditions and design. The choice of this fluid is essential. This fluid must have high thermal conductivity and capacity, low viscosity, low thermal expansion, low toxicity, minimum corrosive activity, and thermal and chemical stability throughout its entire operating temperature range and be environmentally friendly [25,26]. PTCs function at temperatures ranging from low to moderate, with the working fluid achieving temperatures of 50 to 400 degrees Celsius. This temperature range is one in which various industrial activities are carried out [18].

2.5. Solar tracking system

The device also includes one-axis solar tracking to align the trough with the sun's light and ensure that the maximal amounts of radiation are reflected on the focal line [27]. The parabolic troughs have been rotated to follow the sun's day-to-day path across the sky and optimize solar heat uptake.

2.6. Supporting structure

The primary purpose of the supporting structure is to fix the components of the complex, providing rigidity and stability to the entire system. The structure is generally made of structural materials such as steel or aluminum. From a structural perspective, the PTC supporting structure consists of three parts: the primary support (columns, piles, and box), the frame, and the receiver brackets, as shown in Fig. 6 [28].

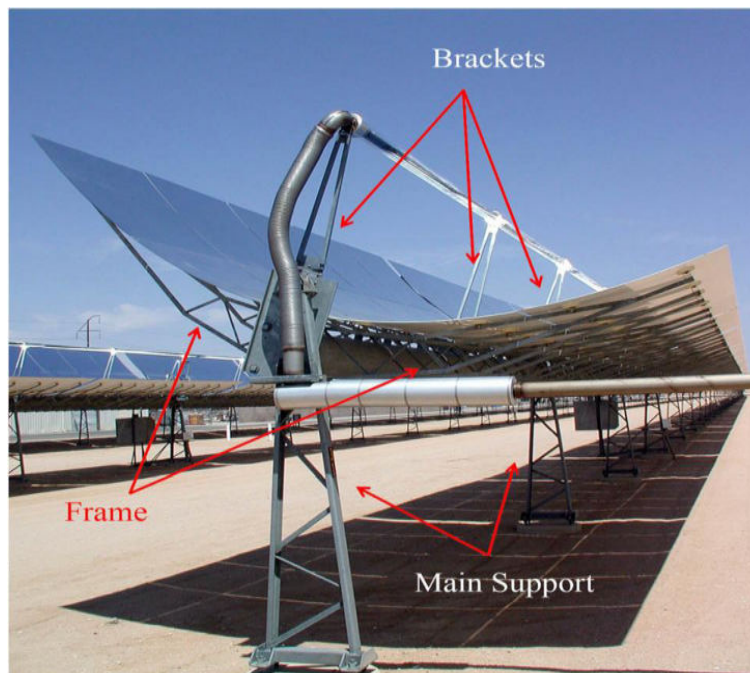


Fig. 6. - Structural division of the PTC.

The parabola's shape must be preserved, and the receiver must be moved to lie on the parabola's focal line. The structure's design is of the utmost importance because bending and torsion imbalances significantly impact the entire system's performance.

3. Heat Transfer Enhancement Techniques

The economic viability of solar thermal systems dramatically depends on the processing and use of input solar heat. The heat losses from the receiver of PTC primarily affect the system's overall performance [29]. Different strategies for improving heat transmission have been discovered and classified as one of three types [30],[31].

3.1. Active methods

External forces such as surface vibration and magnetic fields are applied in this method for heat transfer enhancement, such as:

- Pumps: Circulating a heat transfer fluid (HTF) with a pump can help raise the rate of heat transfer by moving the fluid through the system more quickly, which can be particularly effective in systems where the heat transfer fluid is not naturally circulated, such as in a closed-loop system;
- Fans: Blowing air over a heat exchanger can help to increase the heat transfer rate through convection, which can be achieved using a fan or other mechanical means to move the air;
- Electrical heating elements: Directly heating a substance using an electrical heating element can also increase the heat transfer rate, which could be accomplished using a variety of heat elements, including resistance and induction heat elements.

Overall, active heat transfer enhancement methods rely on external energy sources, such as mechanical or electrical devices, to increase the heat transfer rate. These methods can be effective in certain situations but may also increase the system's complexity and cost.

3.2. Passive method

This method does not require any external power input, and the additional power needed to enhance the heat transfer is taken from the available energy in the system, which ultimately leads to a fluid pressure drop. A good heat exchanger design should have efficient thermodynamic performance. Here are some examples of passive approaches to heat transfer enhancements:

- Materials with high thermal conductivity: Using materials with high thermal conductivity could help enhance the heat transfer rate by allowing heat to be more efficiently conducted through the material. For example, metals such as copper and aluminum have high thermal conductivity, making them good choices for heat exchangers and other heat transfer devices;
- Enhanced surface area: Another strategy for improving heat transmission efficiency is to raise the area of the heat exchanger. Fins or other surface modifications that increase the surface area in touch with heat transfer fluid can be utilized to accomplish this goal;
- Insulation: Insulating a system can help to decrease heat loss and optimize heat transfer efficiency. For example, insulating a pipe can prevent heat from being lost to the surrounding environment, transferring more heat to the desired location.

Overall, passive methods of heat transfer enhancement depend on the natural properties of the materials and system to improve heat transfer efficiency rather than requiring external energy sources. They are generally more straightforward and cost-effective than active methods but may be less effective in certain situations.

3.3. Compound Method

This method uses passive and active methods to enhance heat transfer. These methods can be particularly effective in situations where more than one method is needed to achieve the desired level of heat transfer efficiency. Compound methods of heat transfer enhancements involve using materials with high thermal conductivity and surface enhancements, such as fins, to increase the surface area in touch with heat transfer fluid. Other compound methods involve using insulation to reduce heat loss and a pump to circulate the heat transfer fluid more quickly.

Compound approaches of heat transfer enhancements combine the advantages of active and passive approaches in a single system, allowing for more efficient heat transfer and particularly useful in situations where a single method alone is insufficient.

4. Uses of Inserts in the Receivers

The usage of inserts in a concentrated solar power (CSP) system can improve heat transfer rates through enhancement of effective heat transfer area, creating swirling motion in the flow, and increasing turbulence with a lower in the thermal boundary layer thickness when metallic turbulators are inserted into the absorber system of the PTC system. Additionally, this method can lower the temperature of the outer absorption wall, reducing heat loss and improving thermal efficiency [18,19]. Increased effective heat transfer area: Inserts, such as turbulators or other surface enhancements, can increase the effective heat transfer area by presenting more surface areas to improve the system's efficiency by allowing more heat to be transferred from solar collectors to HTF. Swirl generation Inserts can also create swirling motion in heat transfer fluid flow, which can help increase the heat transfer rate by generating turbulence in the flow, which can help mix the fluid and enhance heat transfer by convection.

According to [34], heat transmission may increase by 17.5% compared to a smooth absorber by employing two different kinds of fins (longitudinal and porous). Researchers have conducted several computational studies on how inserts affect the rise in heat transfer. The numerical studies are built on codes for computational fluid dynamics (CFD), and other researchers utilize different software packages. There are four types of inserts: circular/porous inserts, fin-type inserts, twisted tape-type inserts, and others. These types will be covered in the second chapter of this study.

5. Literature Review

In past research, the focus was on the absorber tube to improve the device's thermal efficiency. The literature will also look up passive methods, such as changing the shape of the receiver tube or putting inserts inside the tube. In addition, nano-fluids as an HTF will be discussed, as will the impact on PTC's thermal performance.

5.1. Use Direct Inserts

Twisted Tapes Inserts

The first and second laws of thermodynamics and flow rate variety of 1 to 6L/min are used to calculate PTC thermal-hydraulic performance, which is done using twisting tape inserts, as shown in Fig. 7. The best thermal performance was achieved at the lowest torsion ratio (1 to 5). The enhancement is due to the increased flow of vortices that cause turbulence [35]. It has been considered how the twist ratio in the PTC receiver tube affects heat transmission and friction coefficients numerically. They noticed that louvered twisted tape had greater Nu and friction factor than the standard tube. The heat transfer coefficient improved by reducing Reynolds number and twist ratio, with the highest findings recorded for a 2.67 twist ratio and $Re = 5000$ [36]. Experiments and numerical simulations have been utilized to study pressure drop and heat transfer using regular twisted, perforated, U-shaped, and V-shaped tapes. The maximum Nu was found at the V-shaped bars with $dr = 0.03$, $w = 0.45$, which is 2.03 times the smooth tube and 2 times the tube with conventional twisted strips [37].

Research was done to determine the impact of the angle of incidence of the solar beam and the heat transfer rate when a helical screw-tape was inserted. The results showed that the transverse angle influences the energy flow more than the longitudinal angle. Also, the rate of heat loss in a smooth absorption tube is six times that of the tube's helical tape inside [38]. A tape with various nail-type twist ratios for a solar water heater concentrator has been utilized in the tube. The empirical findings indicate that the most significant overall thermal efficiency of 12.027 percent was reached with the shortest twist pitch ratio of 4.7870 [39]. An experiment was conducted with different flow rates and the idea of putting nail twist tape into the absorbent tube. The results were compared to see how smooth tube, tube with regular twist tape, and tube with nail twist tape had been used regarding thermal performance. Depending on the findings, the Nu improved by 10 to 15 percent when the smallest twist rate was 2, but it went up by 20 to 30 percent when nail twister tape was used [40]. Researchers studied a small-scale industrial PTC that used twisted tape in a receiver tube to improve performance. A genetic algorithm technique was used to analyze the efficiency of the first and second laws. It was discovered that increasing the flow rate causes thermal efficiency to increase. However, this rise is offset by a fall in the enhancement factor caused by the high-pressure drop [41]. Numerical studies showed that wall detached twisted tape increases the absorber's heat transmission performance. At the minimum torsion ratio, heat transmission and fluid friction increase due to mixing along the lengthy spiral route. The absorber's circumferential temperature differential was decreased by 4 to 68%, and the heat transmission was enhanced by 1.05 to 2.69 times [42]. They evaluated the influence of the twisting ratio and clearance ratio on the thermal performance of PTC utilizing molten salt as an HTF with turbulent flow from 5,000 to 25,000. Also, the temperature of the receiver wall could go down at the lowest clearance ratio of 0 to 1.

The higher Nu value has also been 2.9 times greater than a standard tube at a twisting ratio 2.5 [43]. Using standard or perforated twin twisted tapes could improve friction factor and heat transmission. The impact of altering the Reynolds number between 10,000 - 20,000 and the holes ($N = 0, 1, 2, \text{ and } 3$) Dual twisted tapes improved the Nu by 9%. On the other hand, perforating TTs significantly impacts the friction factor, decreasing it by up to 396 percent [44].

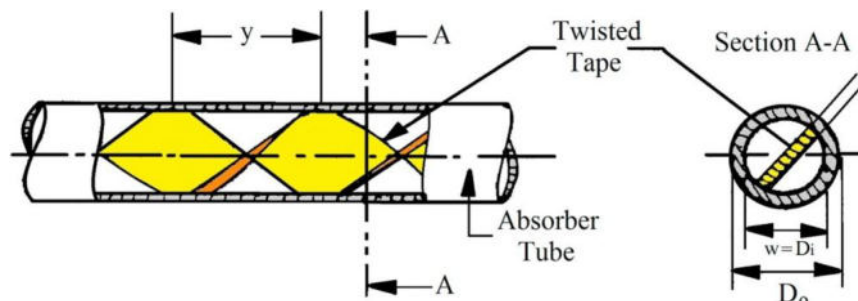


Fig. 7. - Schematic of the twisted tape insert [35].

The Indian Institute of Technology evaluated a cylindrical parabolic collector (CPC) system using a twisted tape and different flow rates, Reynolds numbers, and torsion ratios. The result showed that the value of $y = 5$ has the lowest skew ratio and the greatest Nu [45]. Using the twisted, curved tape increases heat transmission, as researchers discovered that at the height of 7 mm, the tape has a superior thermal performance of around 37% compared to the standard case [46].

Wire Coil

Due to the rise in heat transfer area and turbulence, wire coils improve thermal performance, but the wire pitch, distance between subsequent coils, and flow rate must be considered [14,47,48].

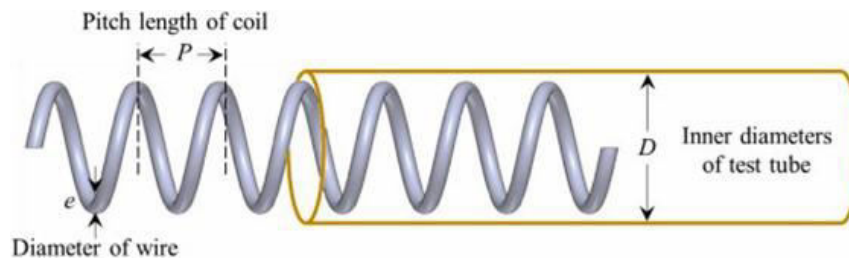


Fig. 8. - Wire coil insert.

Simulations using COMSOL Multiphysics with different flows for the absorbent tube of the PTC system with the insertion of wire coils with different pitches found that the coil increases flow turbulence and both Reynolds and Nu, with Nu increased by 104% - 330%, indicating a heat transfer coefficient improvement [49]. The friction coefficient and Nu for wire coils and twisted tape tubes have been analyzed experimentally and numerically. The Nu and f in twisted-tape tubes rose by 38–57% and 148–202% compared to regular tubes, whereas in wire-coiled tubes, they increased by 75–94% and 685–792%. Numerical research reveals that a twisted band or coil may increase tangential velocity [50]. Improved PTC efficiency was modeled with wire coil inserts inside the receiver 9-meter-wide parabolic trough collector with an 80-degree rim angle. When the flow rate decreases by 0.0036 m³/s, heat transfer efficiency increases by roughly 183%, while thermal effectiveness increases by 0.4% to 1.4% [51].

They were investigated using a coiled wire with an equilateral triangle cross-section and air as the transmission fluid. There was a 36% increase in efficiency when the pitch-to-diameter ratio was one, and the length-to-width ratio of the equilateral triangle to the tube's diameter (a/D) was 0.08920. The best system operation was found when the Reynolds number for all coiled wire inputs was smaller, resulting in a more compact heat exchanger [52]. Testing the inserts for coil wire turbulators was done experimentally and numerically. Seven pitch distances were simulated numerically. At pitch distances of 15, 30, and 45, the thermal increase was 2.28, 2.07, and 1.95 times that of a standard tube [53]. Experiments were performed using a serrated wire coil (DC) of 34.40, 41.20, and 47.90mm in diameter and pitch lengths (PC) of 10, 20, 30, and 40 mm to explore characteristics of the heat transfer and airflow friction in a pipe with the wire coils. With diameter ratio (DR)= 0.94 and pitch ratio (PR)= 0.1969, the optimum thermal fulfillment is achieved at $Re = 5112$ [54]. An experimental investigation involves wire coils with rectangular and circular cross-sections of varying pitches with air as the transmission fluid inside an elliptical tube. According to the findings, rectangular cross-section wire coils have a higher Nu value, friction coefficient, and thermal efficiency increase of 15%, 3%, and 14% than circular cross-section wire coils because the shape of a rectangular cross-section increases the strength of the air's turbulence [55].

Use Porous Materials

Solar energy systems may make use of porous materials for a variety of purposes. It is possible to increase heat transfer by using high-conductivity materials like metallic foams, metal porous metals, and other materials with high thermal conductivity, which work well to mix flow and have an acceptable pressure drop [56]. Employed the porous substance in the solar PTC absorber for its heat-conducting qualities. The results indicated that the incorporation of the porous medium enhances heat transmission capabilities, although the pressure decreased markedly. The domains of heat transport, thermal conductivity, and turbulence effects exhibit significant enhancement. The optimal heat transfer coefficient with a notable drag occurs under the parametric parameters of $w = d_i$, $H = 0.5d_i$ at $h = 30^\circ$. At a Reynolds number of 31.845 and a pressure loss of 0.0663 Psi, an enhancement of 64.2% in the tube-receiver Nusselt number is attained for the optimal recipient [57]. Three-dimensional simulations were used to investigate the impact of metallic foam on the PTC absorbent tube. The optimal thermo-hydraulic performance, accounting for increased flow resistance, is achieved when $H = 0.25$ with the insertion of metallic foam into the tube, resulting in an increase of approximately 5 to 10 times alongside a rise in f by 10 to 20 times, while the PEC ranges from 1.40 to 3.20 [58].

PTC was evaluated with six diverse receiver designs in an experiment test. The porous disc was optimized for all receivers to increase PTC efficiency and decrease receiver angular thermal gradients. The collector efficiency ranges from 63.9 % to 66.66 % [59]. On the solar air collector, an experiment was done with porous absorbent tubes made of corrugated iron, and another study was carried out with non-porous absorbent tubes made of aluminum mesh. According to the findings, the solar thermal efficiency was approximately 61 percent during the middle of the day, and the temperature that this collector could reach was 41 percent [60]. They utilized the porous medium of charcoal to improve the thermal efficiency of the solar air heater. As a result of these studies, the thermal increase was 30% greater than in the model that did not contain the porous medium [61].

This study used a 3D turbulent flow model to simulate employing (syltherm800) fluid to transmit heat in the PTC absorber tube. They numerically simulated an absorber tube with porous rings. A porous ring receiver tube's heat transfer and thermal efficiency are more significant than a smooth one. It was also noticed that the Nu enhanced with the size of the rings. The thermal performance factor was at its highest when H was equal to 0.8, Re was equal to 30,000, and the space between rings was double that of the inner ring [62]. Copper foam was used in the solar collector's receiver tube to assess

its performance within a range of flow rates from 0.0083 to 0.025 L/s. It was discovered that raising the flow rate improves efficiency and reduces the loss coefficient by 45 percent [63]. Three absorber tubes were used: porous, semi-porous, and nonporous. With an intake temperature ranging from 20C to 40C, a working fluid selection of 0.3 - 1.6 L/min was used. Thermal effectiveness improves with increased flow rate and reduced inlet temperature. Semi-insert and full-insert thermal efficiency increases were 119.6% and 171.2%, respectively. The most significant temperature differences were 12.2C, 8.8C, and 3.3C, namely porous, semi-porous, and nonporous [64].

Use Fin type inserts

Several researchers have investigated how the presence of fins influences thermal performance. They have examined fins that are wavy, pinched, porous, and longitudinally flat.

In a study using porous fin geometry on the tube's lower side, researchers found a slight rise in pressure drop as the coefficient of heat transfer augmented. Tee tubes have been observed under the various shapes of the inserts (circular, triangular, square, and trapezoidal). The researchers noticed a slight rise in pressure drop as the heat transfer coefficient increased. Results have shown that at 6.4 kg/s flow rate, trapezoidal inputs increased heat transfer by approximately 13.8% [65]. They put pin fin arrays on the absorber tube's bottom side to increase heat transfer and reduce circumferential temperature differences. Numerical results have shown that the average Nu has been increased by up to 9%, and the overall performance factor has been increased by up to 12% [66].

Simulated by Solid works using longitudinal fins of varying lengths (5, 10, and 15) in parabolic trough collectors and verified with carbon dioxide, air, and helium gas. The results showed that although fins increased pressure drop, they boosted thermal efficiency. A fin with a height of 10 is most suited for use, especially with helium as a transport fluid [67]. A new tube insert in the absorber tube with star-shaped geometric features was developed to enhance this insert's shape. The fin length ranged from 15–30 mm, while the fin thickness ranged from 3–5 mm in 16 instances. The Nu and heat transfer factor may be enhanced by 60%, and thanks to these improvements, thermal losses might be cut by 14%. For star inserts, a 5 mm fin thickness is ideal. The recommended fin length for the star insert is 20–30 mm [68].

To determine the optimal number and location of rectangular inner fins with thickness (2 mm) and length (10 mm). After that, they concluded that using three fins at the bottom of the tube was the optimal design because it increased the thermal efficiency by 0.51 percent [69]. It investigated how the inner longitudinal fin also has a flat and sinusoidal lateral surface of the PTC tube, affecting its thermal performance. The Nu, friction coefficient and thermal enhancement were determined using numerical analyses. This convective augmentation technique resulted in a consistent fluid temp distribution and decreased the absorber's ambient temperature. The Nu enhancement has been 25 % with flat fins and 78 % for fins with sinusoidal lateral surfaces. In addition, the maximum Nu enhancement increased from 57 to 210 percent when T_{in} dropped to 300 K because the fluid reaching the absorber at a low temperature can better utilize the energy of a source of heat (solar energy) [70].

An experimental investigation of three PTC receiver tubes, the smooth tube and two tubes with pin fins of varying heights and axial pitch, was conducted using air as heat transfer fluid. A finned inner tube's temperature and pressure drop were more significant than a smooth tube's. With a flow rate of 93 Nm³/h, the average air temperature was 266. According to the findings, the maximum exergy was obtained with a fin length of 3.50mm and an axial pitch of 1.8 mm [71]. Comprehensively investigated novel PTR performance with a star-shaped insert in an absorber tube. Results regarding exergy, thermal, and collector efficiency have been discussed. It has been shown that heat loss drop has been as high as 14%, and pumping work has still been deficient (16W), even though pressure drop has been obvious [72].

Other Types of Turbulator Inserts

The effects of the perforated plate inserts in a solar PTC with Syltherm800 as the heat transfer fluid revealed a rise in the percentage between 1.2 and 8 in the modified thermal efficiency when using perforated plate inserts [73]. In this analysis, researchers conducted a scientific experiment on an absorber tube equipped with hinged blades as the variable. The work aims to determine the energy transfer rate for various mass flow rates and intensities of sunlight. In this experiment, the working fluid that was used was distilled water. Under identical conditions, the researchers found that the efficiency of the new absorber tube ranged from 67.970 percent to 70.820 percent. In contrast, the efficiency of the smooth tube (which did not contain any inserts) was between 58.77 percent and 61.70 percent [74].

The insertion of a corrugated tape with a sinusoidal shape into the PTC tube has been simulated. A corrugated tape insertion increased the PEC and Nu by 2.11 and 3, respectively, and the heat loss was reduced by 33%, reducing heat stress in the absorber structure [75]. A PTC absorber tube with a conical strip insertion is examined numerically for its thermal-hydraulic and thermodynamic efficiency. This study investigates the influence of geometric characteristics on performance. Using four different fluid input temperatures, the conical strip inserts significantly increase heat transfer, increasing the Nu by 45 to 203 percent. The heat loss was reduced by up to 82.10%. The inserts create a significant increase in pressure drops, with a friction factor of 6.17–17.44 times that of a smooth PTC absorber [76]. In the presented work, the receiver tube regarding the PTC with internal toroidal rings has been investigated to improve heat transfer. Nine different receiver types were determined to affect the heat transfer rate considerably. In addition, at various input temperatures and fluid flow rates, the absorbed tube's fully turbulent heat transfer properties were numerically analyzed and confirmed. It was found that a thermally efficient ideal receiver has a diameter ratio of 0.88 as well as a pitch size (2d). Whereas the receive diameter ratio (0.92) and pitch size are the most energy-efficient, the improvement in efficiency for the thermally efficient and energy-efficient ideal cases is 3.74 and 1.88 percent, respectively, while the increase in Nu is 2.330 and 1.490 times higher when compared to smooth absorber tube [77].

5.2. Surface Modifications of The Tube

They looked at how turbulence flow, and heat transmission was altered with or without helical fins inside the tube and protrusions and dimples on the surface of Fig. 9 in terms of heat transfer, as tubes with dimples do better than tubes with protrusions or helical fins. When the Reynolds number increased from 1104 to 2104, Nu and coefficient of friction increased from 56% to 77% and 44% to 64%, respectively [78].

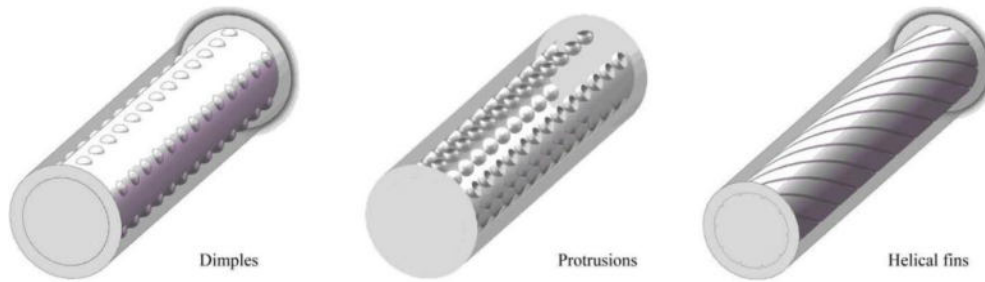


Fig. 9. - The schematic of dimples, protrusions, and helical fins [78].

Using a hollow V-shaped absorber with rectangular fins improved heat transmission. The heat transfer fluid was heated from 109.8 to 110.9, and the surface absorber was cooled from 136.2 to 121.5. It has been noted that the sunshine cannot escape since it may often be reflected in the triangle [79] developed an asymmetrical external convex corrugated tube absorber for PTC. Compared to the standard tube receiver, it was discovered that using the improved tube as the absorber could significantly minimize heat stress and improve heat transfer performance. In addition, the maximum von Mises thermal stress restriction has been 26.8%, while the maximal total heat transfer performance factor increase has been 148% [80]. Simulating the receiver tube with a dimpled surface and a constant Reynolds number while varying the Grashoff number from 109 to 3.2×10^{10} led to an increase in the performance assessment criterion to 1.3, which indicates that the reinforcement ratio rose as the Nu grew, at the expense of a 1.01–1.14 rise in friction coefficient [81].

The spiral corrugated suction tube was utilized to increase heat transfer, and research was carried out to determine how the degree of pitch and height to diameter influenced heat transfer. According to the research, a thermal efficiency of 65.8 percent could be achieved at the height of pitch ($DH = 0.12$) and at the height of ripple ($P/DH = 0.06$), where there was a reduction of 44 percent in the amount of heat lost in comparison to the standard tube [82]. They suggested using a hollow, arc-shaped receiver tube, where they studied the effects of the angle of inclination and the width of the aperture. Since the angle of inclination and the width of the opening have a significant effect on how much heat is lost by natural load, they found that 50–70 is a good range for the width of the opening for this type because manufacturing costs go up when the width of the opening gets smaller [83]. A numerical analysis of flow and heat transfer in the PTC with turbulence-inducing objects in the receiver tube was carried out. The pipe's elements feature a helical profile. The element cross-sections studied were rectangle, triangular, trapezoid, and quasi-triangular. According to the results, the case with a rectangle cross-section at $Veinlet = 0.2$ m/sec had the best thermal efficiency by 29% [84].

Use of Nanofluid

Researchers have studied the uses of Nanofluids as heat transfer fluids because traditional fluids like water, oil, and others have low heat conductivity, reducing the overall performance of systems due to the thinness of the thermal layer. Nanofluids in conventional liquids contain solid nanoparticles (1-100 nm) [85]. Nanofluids combine conventional liquids with metallic nanoparticles, such as copper, titanium dioxide, ammonia, silicon dioxide, and other standard nanoparticles [86].

Because an enormous number of studies have been conducted to investigate these fluids and the advantages that can be gained from utilizing them to achieve higher levels of thermal efficiency, we will focus on some of the studies conducted to provide a concise overview of their findings. An empirical study has been carried out to enhance the heat transfer and coefficient of friction by inserting a twisted tape into an absorbent tube and employing HTF, water, and silver Nanofluid. Results show increasing friction and Nu factor by 1.0-1.75 times and 1.25-2.10 times [87]. When three types of HTFs were tested in a converging-diverging tube, the researchers indicated that the Nanofluids improved thermal efficiency by 4.25 percent. However, the design's functional purpose improved thermal efficiency by 4.55 percent. According to the research, this application is recommended for high-temperature situations [88].

The use of mono- as well as hybrid Nano-fluids in PTC as a heat transfer fluid boosts thermal efficiency value by 1.8 percent for the hybrid Nanofluids and 0.7 percent for the mono Nanofluids at temperatures range of 300 K - 650 K [89]. When the vortex generator was used with and without Nanofluids, the researchers found that the use of the largest vortex generator (H30mm-30-N4) with 6 percent SiO_2 resulted in the most significant overall efficiency and thermal energy improvement, with 14.62 percent and 14.47 percent, respectively, compared to the other options [32]. Examined the effects of two Nanofluids, $CuO-H_2O$ and TiO_2-H_2O , as well as three pure fluids, which are ethylene glycol, water, and thermal oil, on an absorbed tube that has been equipped with a triangular cross-section in addition to forward perforated ring steps. Analysis was done on the working fluid effect, nanoparticle volume concentration, step inner diameter, and step spacing.

The maximal level of thermal efficiency ranged between 67% and 76.50% when 4% of $CuO-H_2O$ Nano fluid was used and flowed through a tube with inserts [90]. The influence of a hybrid Nanofluid ($Cu/SBA-15$) was examined to ascertain the energy and exergy efficacy of a PTSC absorber tube fitted with turbulators. According to CFD investigations,

heat transfer improvement is less for low Reynolds number values (less than 3500). Beyond this, average Nu rises in comparison to smooth absorber tubes. At noon, the highest energy and exergy efficiencies were 65% and 5%. These values were 2% and 1% higher than in the usual case [57].

Conclusion

This comprehensive review demonstrates that Concentrated Solar Power (CSP) systems represent a viable and sustainable solution to global energy challenges, particularly in reducing greenhouse gas emissions and dependence on fossil fuels. Among the various CSP technologies explored - Linear Fresnel Reflectors, Parabolic Dishes, Solar Towers, and Parabolic Trough Collectors (PTCs) - PTCs emerge as the most mature, cost-effective, and widely adopted for medium- to high-temperature thermal applications. The study emphasizes that enhancing the thermal performance of CSP systems relies heavily on advanced heat transfer strategies. Passive techniques such as surface modification, internal inserts, and nanofluids offer significant improvements in heat transfer without additional energy input. Active methods—such as forced circulation using pumps or fans - provide further enhancement but at the cost of increased complexity and energy consumption. Compound methods, which integrate passive and active approaches, yield the highest thermal efficiency gains. Notably, innovations in receiver design - such as the implementation of twisted tapes, wire coils, porous materials, and various fin configurations - contribute substantially to reducing thermal losses and increasing heat transfer rates. Furthermore, the integration of nanofluids with enhanced thermal conductivity has shown measurable gains in system performance, particularly at elevated temperatures. Overall, sustained innovation in heat transfer enhancement and system design is imperative for maximizing the efficiency and scalability of CSP technologies, thereby advancing the global transition toward clean, renewable energy systems.

References

- [1] Radhi S.S., Al-khafaji Z.S., Falah M.W. Sustainable heating system by infrared radiators 2022;4:42–52. <https://doi.org/10.37868/hsd.v4i1.82>.
- [2] Shubbar A., Nasr M., Falah M., Al-Khafaji Z. Towards net zero carbon economy: Improving the sustainability of existing industrial infrastructures in the UK. *Energies* 2021;14:5896. <https://doi.org/10.3390/en14185896>.
- [3] Jasim A.H., Radhi N.S. Review on Improvement the Turbine Oxidation and Hot Resistant against Corrosion by Nickel – Based Superalloy. *Mater Mech Eng Technol* 2024;2024:89–104. <https://doi.org/10.52209/2706-977X>.
- [4] Al-Khafaji Z., Kazem M.A., Radhi N.S., Falah M., Hadi Z.M. Reducing the Issues of Implements in the Human Body by Applying HAp: Review. *Mater Mech Eng Technol* 2024;64. <https://doi.org/10.52209/2706-977X>.
- [5] Al-Abboodi T., Yaser A., Al-Khafaji Z. Reducing vibration and noise in the oil sector using nanoparticle-reinforced polymers. *Acad J Manuf Eng* 2024;2024.
- [6] Jasim A., Yaser A, Al-Khafaji Z. An ansys simulation study on the effect of applying tita-nium alloy (ti-6al-4v) coating for wind turbine gear. *Acad J Manuf Eng* 2024;22.
- [7] Sattar S., Alaiwi Y., Radhi N.S., Al-khafaji Z. Numerical Simulation for Effect of Composite Coating (TiO₂ + SiO₂) Thickness on Steam Turbine Blades Thermal and Stress Distribution. *Acad J Manuf Eng* 2023;21.
- [8] Mohammed E., Al-khafaji Z. Effect of Surface Treatments by Ultrasonic on NiTi Biomaterials. *Acad J Manuf Eng* 2023;21:1–6.
- [9] Aljumaili A., Alaiwi Y., Al-Khafaji Z. A Review of Solar Panel Cooling Methods and Efficiencies. *Mater Mech Eng Technol* 2025;2025. https://doi.org/10.52209/2706-977X_2025_1_14.
- [10] Hasan AS, Kadhim MJH, Layla AY, Al-Khafaji Z. Exploring the NiPcTs-Si nanoheterojunction as a bilayer solar cell: theoretical and experimental analysis. *Opt Quantum Electron* 2024;56:1781. <https://doi.org/10.1007/s11082-024-07621-y>.
- [11] Kadhim MJH, Alradha RM, Jawad HK, Al-Dabbagh B, Al-Khafaji Z. Investigating the Effect of the Yellow Chlorophyll on the Characteristics of Liquid Polyethylene Glycol for Liquid Electrolyte Solar Cells. *Nat Eng Sci* 2024;9:244–56.
- [12] Abed N., Afgan I. An extensive review of various technologies for enhancing the thermal and optical performances of parabolic trough collectors. *Int J Energy Res* 2020;44:5117–64. <https://doi.org/10.1002/er.5271>.
- [13] Abdulkhudhur J.M., Yaser A., Zainab A.K. Investigation of Heat Transfer and Swirl Flow Between Concentric Cylinders. *Jordan J Mech Ind Eng* 2025;19:13–26.
- [14] Aljumaili A., Alaiwi Y., Al-Khafaji Z. Investigating back surface cooling system using phase change materials and heatsink on photovoltaic performance. *J Eng Sustain Dev* 2024;28:294–315.
- [15] Blanco M.J., Miller S. Introduction to concentrating solar thermal (CST) technologies. *Adv. Conc. Sol. Therm. Res. Technol.*, Elsevier; 2017, p. 3–25.
- [16] Aubrey C., Brakmann G AR. Solar thermal power. *ESTIA/Greenpeace* 2003:1–48.
- [17] Sharaf-eldin M.A., Yaseen Z.M., Elmetwalli A.H., Elsayed S., Scholz M., Al-khafaji Z., et al. Modifying Walk-In Tunnels through Solar Energy , Fogging , and Evaporative Cooling to Mitigate Heat Stress on Tomato 2023.
- [18] Kalogirou S.A. Solar thermal collectors and applications. *Prog Energy Combust Sci* 2004;30:231–95.
- [19] Bellos E., Tzivanidis C., Tsimpoukis D. Enhancing the performance of parabolic trough collectors using nanofluids and turbulators. *Renew Sustain Energy Rev* 2018;91:358–75. <https://doi.org/10.1016/J.RSER.2018.03.091>.
- [20] Yılmaz İ.H., Mwesigye A. Modeling, simulation and performance analysis of parabolic trough solar collectors: A comprehensive review // *Appl Energy* 2018;225:135–74.
- [21] Goswami D.Y., Kreith F. Handbook of energy efficiency and renewable energy. Crc Press; 2007.

- [22] Granqvist C.G. Preparation of thin films and nanostructured coatings for clean tech applications: A primer. *Sol Energy Mater Sol Cells* 2012;99:166–75.
- [23] Uygur S. Detailed simulations of parabolic trough collector for investigating enhancement of heat transfer to absorber tube flow 2021.
- [24] Qu M., Archer D.H., Yin H. A Linear Parabolic Trough Solar Collector Performance Model 2007:663–70. <https://doi.org/10.1115/ES2007-36052>.
- [25] Nahhas T. Materials and thermal storage systems by sensible heat for thermodynamic electro-solar plants 2017.
- [26] Khlewee A.S., Alaiwi Y., Jasim T.A., Mahdi M., Hussain A.J., Al-Khafaji Z. Numerical investigation of nanofluid-based flow behavior and convective heat transfer using helical screw 2024.
- [27] Olia H., Torabi M., Bahiraei M., Ahmadi M.H., Goodarzi M., Safaei M.R. Application of nanofluids in thermal performance enhancement of parabolic trough solar collector: State-of-the-art. *Appl Sci* 2019;9. <https://doi.org/10.3390/app9030463>.
- [28] Tagle-Salazar P.D., Nigam K., Rivera-Solorio CI. Parabolic trough solar collectors: A general overview of technology, industrial applications, energy market, modeling, and standards. *Green Process Synth* 2020;9:595–649. <https://doi.org/10.1515/gps-2020-0059>.
- [29] Ray S., Tripathy A.K., Sahoo S.S., Bindra H. Performance analysis of receiver of parabolic trough solar collector: Effect of selective coating, vacuum and semitransparent glass cover. *Int J Energy Res* 2018;42:4235–49.
- [30] Dewan A., Mahanta P., Raju K.S., Kumar P.S. Review of passive heat transfer augmentation techniques. *Proc Inst Mech Eng Part A J Power Energy* 2004;218:509–27.
- [31] Akbarzadeh S., Valipour M.S. Heat transfer enhancement in parabolic trough collectors: A comprehensive review. *Renew Sustain Energy Rev* 2018;92:198–218. <https://doi.org/10.1016/j.rser.2018.04.093>.
- [32] Abed N., Afgan I., Iacovides H., Cioncolini A., Khurshid I., Nasser A. Thermal-hydraulic analysis of parabolic trough collectors using straight conical strip inserts with nanofluids. *Nanomaterials* 2021;11. <https://doi.org/10.3390/nano11040853>.
- [33] Sandeep H.M., Arunachala U.C. Solar parabolic trough collectors: A review on heat transfer augmentation techniques. *Renew Sustain Energy Rev* 2017;69:1218–31. <https://doi.org/10.1016/J.RSER.2016.11.242>.
- [34] Reddy K.S., Kumar KR, Satyanarayana G V. Numerical Investigation of Energy-Efficient Receiver for Solar Parabolic Trough Concentrator. *Heat Transf Eng* 2008;29:961–72. <https://doi.org/10.1080/01457630802125757>.
- [35] Jaramillo O.A., Borunda M., Velazquez-Lucho KM, Robles M. Parabolic trough solar collector for low enthalpy processes: An analysis of the efficiency enhancement by using twisted tape inserts. *Renew Energy* 2016;93:125–41. <https://doi.org/10.1016/j.renene.2016.02.046>.
- [36] Ghadirijafarbeigloo S., Zamzamian A.H, Yaghoubi M. 3-D numerical simulation of heat transfer and turbulent flow in a receiver tube of solar parabolic trough concentrator with louvered twisted-tape inserts. *Energy Procedia*, vol. 49, Elsevier Ltd; 2014, p. 373–80. <https://doi.org/10.1016/j.egypro.2014.03.040>.
- [37] Hasanpour A, Farhadi M, Sedighi K. Intensification of heat exchangers performance by modified and optimized twisted tapes. *Chem Eng Process Process Intensif* 2017;120:276–85. <https://doi.org/10.1016/J.CEP.2017.07.026>.
- [38] Song X, Dong G, Gao F, Diao X, Zheng L, Zhou F. A numerical study of parabolic trough receiver with nonuniform heat flux and helical screw-tape inserts. *Energy* 2014;77:771–82. <https://doi.org/10.1016/j.energy.2014.09.049>.
- [39] Bhakta AK, Panday NK, Singh SN. Performance Study of a Cylindrical Parabolic Concentrating Solar Water Heater with Nail Type Twisted Tape Inserts in the Copper Absorber Tube. *Energies* 2018;11. <https://doi.org/10.3390/en11010204>.
- [40] Jafar KS, Sivaraman B. Performance characteristics of parabolic solar collector water heater system fitted with nail twisted tapes absorber. *J Eng Sci Technol* 2017;12:608–21.
- [41] Borunda M, Garduno-Ramirez R, Jaramillo OA. Optimal operation of a parabolic solar collector with twisted-tape insert by multi-objective genetic algorithms. *Renew Energy* 2019;143:540–50. <https://doi.org/10.1016/j.renene.2019.05.030>.
- [42] Mwesigye A, Bello-Ochende T, Meyer JP. Heat transfer and entropy generation in a parabolic trough receiver with wall-detached twisted tape inserts. *Int J Therm Sci* 2016;99:238–57. <https://doi.org/10.1016/J.IJTHERMALSCI.2015.08.015>.
- [43] Chang C, Xu C, Wu ZY, Li X, Zhang QQ, Wang ZF. Heat Transfer Enhancement and Performance of Solar Thermal Absorber Tubes with Circumferentially Non-uniform Heat Flux. *Energy Procedia* 2015;69:320–7. <https://doi.org/10.1016/j.egypro.2015.03.036>.
- [44] Afsharpanah F, Pakzad K, Amirsoleymani M, Delavar MA. Numerical study of heat transfer enhancement using perforated dual twisted tape inserts in converging-diverging tubes. *Heat Transf - Asian Res* 2018;47:754–67. <https://doi.org/10.1002/htj.21340>.
- [45] Kumar B, Nayak RK, Singh SN. Experimental Analysis of the Thermo-Hydraulic Performance on a Cylindrical Parabolic Concentrating Solar Water Heater with Twisted Tape Inserts in an Absorber Tube. *Zeitschrift Fur Naturforsch - Sect A J Phys Sci* 2018;73:431–9. <https://doi.org/10.1515/zna-2018-0023>.
- [46] Outokesh M, Ajarostaghi SSM, Bozorgzadeh A, Sedighi K. Numerical evaluation of the effect of utilizing twisted tape with curved profile as a turbulator on heat transfer enhancement in a pipe. *J Therm Anal Calorim* 2020;140:1537–53. <https://doi.org/10.1007/s10973-020-09336-0>.
- [47] Jasim MR, Alaiwi Y, Al-khafaji Z. Investigation Of The Effect Of Adding Nitrogen On The Torque Generated By A Four-Cylinder Engine. *Jordan J Mech Ind Eng* 2024:1–30.

- [48] Al-Abayechi Y, Alaiwi Y, Al-Khafaji Z. Exploration of key approaches to enhance evacuated tube solar collector efficiency. *J Adv Res Numer Heat Transf* 2024;19:1–14.
- [49] Diwan K, S. Soni M. Heat Transfer Enhancement in Absorber Tube of Parabolic Trough Concentrators Using Wire-Coils Inserts. *Univers J Mech Eng* 2015;3:107–12. <https://doi.org/10.13189/ujme.2015.030305>.
- [50] Wang S, Wang K, Lu K, Zhang Q. Experimental and numerical analysis for thermal-hydraulic characteristics in circular tubes with twisted tape and wire coil inserts. *E3S Web Conf* 2020;165. <https://doi.org/10.1051/e3sconf/202016506051>.
- [51] Yılmaz İH, Mwesigye A, Göksu TT. Enhancing the overall thermal performance of a large aperture parabolic trough solar collector using wire coil inserts. *Sustain Energy Technol Assessments* 2020;39. <https://doi.org/10.1016/J.SETA.2020.100696>.
- [52] Gunes S, Ozceyhan V, Buyukalaca O. Heat transfer enhancement in a tube with equilateral triangle cross sectioned coiled wire inserts. *Exp Therm Fluid Sci* 2010;34:684–91. <https://doi.org/10.1016/J.EXPTHERMFLUSCI.2009.12.010>.
- [53] Şahin HM, Baysal E, Dal AR, Şahin N. Investigation of heat transfer enhancement in a new type heat exchanger using solar parabolic trough systems. *Int J Hydrogen Energy* 2015;40:15254–66. <https://doi.org/10.1016/j.ijhydene.2015.03.009>.
- [54] Chompookham T, Chingtuaythong W, Chokphoemphun S. Influence of a novel serrated wire coil insert on thermal characteristics and air flow behavior in a tubular heat exchanger. *Int J Therm Sci* 2022;171. <https://doi.org/10.1016/J.IJTHERMALSCI.2021.107184>.
- [55] Omara MA, Abdelatif MA. Experimental study of heat transfer and friction factor inside elliptic tube fixed with helical coils. *Appl Therm Eng* 2018;134:407–18. <https://doi.org/10.1016/J.APPLTHERMALENG.2018.02.017>.
- [56] Rashidi S, Esfahani JA, Rashidi A. A review on the applications of porous materials in solar energy systems. *Renew Sustain Energy Rev* 2017;73:1198–210. <https://doi.org/10.1016/j.rser.2017.02.028>.
- [57] Rostami S, Shahsavari A, Kefayati G, Shahsavari Goldanlou A. Energy and exergy analysis of using turbulator in a parabolic trough solar collector filled with mesoporous silica modified with copper nanoparticles hybrid nanofluid. *Energies* 2020;13:2946.
- [58] Wang P, Liu DY, Xu C. Numerical study of heat transfer enhancement in the receiver tube of direct steam generation with parabolic trough by inserting metal foams. *Appl Energy* 2013;102:449–60. <https://doi.org/10.1016/j.apenergy.2012.07.026>.
- [59] Reddy KS, Ravi Kumar K, Ajay CS. Experimental investigation of porous disc enhanced receiver for solar parabolic trough collector. *Renew Energy* 2015;77:308–19. <https://doi.org/10.1016/j.renene.2014.12.016>.
- [60] Dissa AO, Ouoba S, Bathiebo D, Koulidiati J. A study of a solar air collector with a mixed “porous” and “non-porous” composite absorber. *Sol Energy* 2016;129:156–74. <https://doi.org/10.1016/j.solener.2016.01.048>.
- [61] M. Pradhapraj and V. Velmurugan. Experimental Investigation of Solar Air Heater with Charcoal Porous Medium n.d.
- [62] Ebrahim Ghasemi S, Akbar Ranjbar A. Numerical thermal study on effect of porous rings on performance of solar parabolic trough collector. *Appl Therm Eng* 2017;118:807–16. <https://doi.org/10.1016/j.applthermaleng.2017.03.021>.
- [63] Jamal-Abad MT, Saedodin S, Aminy M. Experimental investigation on a solar parabolic trough collector for absorber tube filled with porous media. *Renew Energy* 2017;107:156–63. <https://doi.org/10.1016/j.renene.2017.02.004>.
- [64] Valizade M, Heyhat MM, Maerefat M. Experimental study of the thermal behavior of direct absorption parabolic trough collector by applying copper metal foam as volumetric solar absorption. *Renew Energy* 2020;145:261–9. <https://doi.org/10.1016/J.RENENE.2019.05.112>.
- [65] Reddy KS, Satyanarayana G V. Numerical Study of Porous Finned Receiver for Solar Parabolic Trough Concentrator. *Eng Appl Comput Fluid Mech* 2008;2:172–84. <https://doi.org/10.1080/19942060.2008.11015219>.
- [66] Gong X, Wang F, Wang H, Tan J, Lai Q, Han H. Heat transfer enhancement analysis of tube receiver for parabolic trough solar collector with pin fin arrays inserting. *Sol Energy* 2017;144:185–202. <https://doi.org/10.1016/J.SOLENER.2017.01.020>.
- [67] Bellos E, Tzivanidis C, Daniil I, Antonopoulos KA. The impact of internal longitudinal fins in parabolic trough collectors operating with gases. *Energy Convers Manag* 2017;135:35–54. <https://doi.org/10.1016/J.ENCONMAN.2016.12.057>.
- [68] Bellos E, Tzivanidis C. Investigation of a star flow insert in a parabolic trough solar collector. *Appl Energy* 2018;224:86–102. <https://doi.org/10.1016/j.apenergy.2018.04.099>.
- [69] Bellos E, Tzivanidis C, Tsimpoukis D. Optimum number of internal fins in parabolic trough collectors. *Appl Therm Eng* 2018;137:669–77. <https://doi.org/10.1016/J.APPLTHERMALENG.2018.04.037>.
- [70] Kurşun B. Thermal performance assessment of internal longitudinal fins with sinusoidal lateral surfaces in parabolic trough receiver tubes. *Renew Energy* 2019;140:816–27. <https://doi.org/10.1016/j.renene.2019.03.106>.
- [71] Zhao Z, Bai F, Zhang X, Wang Z. Experimental study of pin finned receiver tubes for a parabolic trough solar air collector. *Sol Energy* 2020;207:91–102. <https://doi.org/10.1016/J.SOLENER.2020.06.070>.
- [72] Bellos E, Tzivanidis C, Tsimpoukis D. Thermal enhancement of parabolic trough collector with internally finned absorbers. *Sol Energy* 2017;157:514–31. <https://doi.org/10.1016/J.SOLENER.2017.08.067>.
- [73] Mwesigye A, Bello-Ochende T, Meyer JP. Multi-objective and thermodynamic optimisation of a parabolic trough receiver with perforated plate inserts. *Appl Therm Eng* 2015;77:42–56. <https://doi.org/10.1016/j.applthermaleng.2014.12.018>.
- [74] Kalidasan B, Shankar R, Srinivas T. Absorber Tube with Internal Hinged Blades for Solar Parabolic Trough

- Collector. Energy Procedia 2016;90:463–9. <https://doi.org/10.1016/j.egypro.2016.11.213>.
- [75] Zhu X, Zhu L, Zhao J. Wavy-tape insert designed for managing highly concentrated solar energy on absorber tube of parabolic trough receiver. Energy 2017;141:1146–55. <https://doi.org/10.1016/j.energy.2017.10.010>.
- [76] Liu P, Zheng N, Liu Z, Liu W. Thermal-hydraulic performance and entropy generation analysis of a parabolic trough receiver with conical strip inserts. Energy Convers Manag 2019;179:30–45. <https://doi.org/10.1016/j.enconman.2018.10.057>.
- [77] Arshad Ahmed K, Natarajan E. Thermal performance enhancement in a parabolic trough receiver tube with internal toroidal rings: A numerical investigation. Appl Therm Eng 2019;162. <https://doi.org/10.1016/J.APPLTHERMALENG.2019.114224>.
- [78] Huang Z, Yu GL, Li ZY, Tao WQ. Numerical Study on Heat Transfer Enhancement in a Receiver Tube of Parabolic Trough Solar Collector with Dimples, Protrusions and Helical Fins. Energy Procedia, vol. 69, Elsevier Ltd; 2014, p. 1306–16. <https://doi.org/10.1016/j.egypro.2015.03.149>.
- [79] Xiao X, Zhang P, Shao DD, Li M. Experimental and numerical heat transfer analysis of a V-cavity absorber for linear parabolic trough solar collector. Energy Convers Manag 2014;86:49–59. <https://doi.org/10.1016/J.ENCONMAN.2014.05.001>.
- [80] Fuqiang W, Zhexiang T, Xiangtao G, Jianyu T, Huaizhi H, Bingxi L. Heat transfer performance enhancement and thermal strain restrain of tube receiver for parabolic trough solar collector by using asymmetric outward convex corrugated tube. Energy 2016;114:275–92. <https://doi.org/10.1016/j.energy.2016.08.013>.
- [81] Huang Z, Li ZY, Yu GL, Tao WQ. Numerical investigations on fully-developed mixed turbulent convection in dimpled parabolic trough receiver tubes. Appl Therm Eng 2017;114:1287–99. <https://doi.org/10.1016/J.APPLTHERMALENG.2016.10.012>.
- [82] Akbarzadeh S, Valipour MS. Energy and exergy analysis of a parabolic trough collector using helically corrugated absorber tube. Renew Energy 2020;155:735–47. <https://doi.org/10.1016/j.renene.2020.03.127>.
- [83] Li X, Chang H, Duan C, Zheng Y, Shu S. Thermal performance analysis of a novel linear cavity receiver for parabolic trough solar collectors. Appl Energy 2019;237:431–9. <https://doi.org/10.1016/J.APENERGY.2019.01.014>.
- [84] Saedodin S, Zaboli M, Mousavi Ajarostaghi SS. Hydrothermal analysis of heat transfer and thermal performance characteristics in a parabolic trough solar collector with Turbulence-Inducing elements. Sustain Energy Technol Assessments 2021;46. <https://doi.org/10.1016/J.SETA.2021.101266>.
- [85] Bellos E, Tzivanidis C. Parametric investigation of nanofluids utilization in parabolic trough collectors. Therm Sci Eng Prog 2017;2:71–9. <https://doi.org/10.1016/J.TSEP.2017.05.001>.
- [86] Ham J, Kim J, Cho H. Theoretical analysis of thermal performance in a plate type liquid heat exchanger using various nanofluids based on LiBr solution. Appl Therm Eng 2016;108:1020–32. <https://doi.org/10.1016/J.APPLTHERMALENG.2016.07.196>.
- [87] Waghole DR, Warkhedkar RM, Kulkarni VS, Shrivastva RK. Experimental investigations on heat transfer and friction factor of silver nanofluid in absorber/receiver of parabolic trough collector with twisted tape inserts. Energy Procedia, vol. 45, Elsevier Ltd; 2014, p. 558–67. <https://doi.org/10.1016/j.egypro.2014.01.060>.
- [88] Bellos E, Tzivanidis C, Antonopoulos KA, Gkinis G. Thermal enhancement of solar parabolic trough collectors by using nanofluids and converging-diverging absorber tube. Renew Energy 2016;94:213–22. <https://doi.org/10.1016/j.renene.2016.03.062>.
- [89] Bellos E, Tzivanidis C. Thermal analysis of parabolic trough collector operating with mono and hybrid nanofluids. Sustain Energy Technol Assessments 2018;26:105–15. <https://doi.org/10.1016/J.SETA.2017.10.005>.
- [90] Sheikholeslami M, Gorji-Bandpy M, Ganji DD. Review of heat transfer enhancement methods: Focus on passive methods using swirl flow devices. Renew Sustain Energy Rev 2015;49:444–69.

Information of the authors

Al-Aloosi Waleed, Msc., lecturer assist, Department of Medical Instruments Engineering Techniques, College of Engineering, University of Al Maarif
e-mail: waleed.muwafaq@uoa.edu.iq

Alaiwi Yaser, PhD, professor, Department of Mechanical Engineering, Altinbas Universit
e-mail: yaser.alaiwi@altinbas.edu.tr

Al-Khafaji Zainab, PhD, assistant professor, Altinbas University, Istanbul, Turkey; Universiti Kebangsaan Malaysia; Scientific Research Center, Al-Ayen University
e-mail: p123005@siswa.ukm.edu.my

Internal Surface Finish Analysis of Inconel 625 Tube Using MAF and CMAF Processes

Gurpreet Singh*, Gyanendra Singh, Harish Kumar H

Chandigarh University, Mohali (Pb.), India

*corresponding author

Abstract. Over time, numerous new alloys and materials were evolved to meet the technological demands of diverse industries. Advanced Nickel based alloys has great demands in many industrial applications such as Marine, solar power plants, Petro-chemical and aerospace due to its remarkable physical properties. Traditional methods of machining and polishing Inconel 625 alloy are difficult because to its outstanding qualities like high hardness and great strength. In present paper, both chemically assisted MAF (CMAF) and magnetic abrasive finishing (MAF) have been utilized to enhance the internal surface finish of Inconel 625 tubes. Utilizing Response Surface Methodology (RSM), experiments have been designed and conducted. The main factors influencing the internal surface finish (PISF) in MAF and CMAF processes are processing time and rotational speed. Results described that CMAF process yields better surface quality as compare to MAF process. Maximum PISF is attained in CMAF at approximately 72%, and in MAF at approximately 59%. Moreover, Surface texture of finished Inconel 625 tubes in MAF and CMAF was also analysed through Scanning electron Microscopy (SEM). Surface finished by CMAF has less scratches, waviness and scratches as compare to surface finished by MAF process.

Keywords: MAF, CMAF, Inconel 625, design expert, surface finish

Introduction

Industries are producing new metals and alloys to meet their technological demands. Inconel 625 alloy finds widespread use in solar power plants, heat exchanger tubing, nuclear power plants, and other applications of a similar nature because of its remarkable qualities [1, 2]. However, because of its greater hardness and toughness, Inconel 625 is hard to cut using conventional methods like turning, milling and grinding [3,4]. To finish hard alloys, researchers have developed some advanced finishing processes. Magnetic abrasive finishing (MAF) is a highly effective technique that is widely used in industry to obtain a precise surface finish with the minimum surface imperfections [5]. It was often used to polish rounded surfaces composed of stainless steel, brass, and aluminum. The inner surface of SUS-304 stainless steel tubes was polished using mixed-type magnetic abrasives and surface roughness descends from 0.7 to 0.2 μm [6]. To polish the inner surface, Yamaguchi and Shinmura [7] utilized MAF with the pole rotation system.

Moreover, Mulik and Pandey [8] enhanced the surface polish by combining MAF with ultrasonic vibration. Further, MAF was used to simultaneously finish the outer and inner surfaces of steel needles and surface finish enhanced around 0.01 μm [9]. Heng et al. [10] finished the SUS-316L tube (Oval shaped) using Al_2O_3 /iron-based abrasives, improving the surface polish by about 0.04 μm . Zhang et al. [11] polished the inside surface of the SS316 tube using a brand-new magnetically powered tool in MAF. Yang et al. [12] improved the surface finish from 4.1 μm to 10 nm of thin-walled tube with MAF. Wang et al. [13] suggested nanoparticle-enhanced bonded magnetic abrasive (NEBMA) to enhance the finishing performance of MAF process. Wang et al. [14] investigated MAF process for the finishing of Internal Surfaces of Waveguides fabricated by Selective Laser Melting and improved the surface quality from the roughness of the specimens decreased from Ra 2.5 μm to Ra 0.65 μm . Hence, simple MAF is less productive for hard materials instead of many advantages.

Therefore, the development of chemically assisted MAF (CMAF) aimed to improve MAF's performance with brittle and hard materials. The benefits of chemical machining as well as MAF are combined in CMAF. Initially in CMAF, chemical etching was done on the surface at a higher temperature for a predefined period of time and the workpiece surface layer get diffused due to chemical reaction. The upper surface of workpiece get weakened which is further removed using the MAF method. [15]. Singh et al. [16] used a multi-pole magnetic tool to complete the Inconel 625 tube using the MAF approach. The tungsten flat surfaces were finished using CMAF, and by utilizing ideal settings, the surface polish was increased to about 79.52% [15,17]. Furthermore, Inconel 718 flat surfaces were polished using CMAF, and the results showed that a superior surface finish was achieved at 90 minutes of finishing time, 30% abrasive weight, and 700 gm/lit. of chemical concentration [18]. CMAF was also utilized to concurrently finish the inner and outer surfaces of Inconel 625 tubes. The effects of process parameters were examined and surface finish was enhanced by 72% [19]. Additionally, the effect of CMAF input parameters was examined with regard to Inconel 625 tubes' inner and outer roundness [20, 21]. A genetic algorithm was also tried to optimize the CMAF parameters for surface finish and Material removal [22].

Prior research has documented the use of MAF and CMAF in the finishing of a variety of materials, including nickel alloys, brass, tungsten, and stainless steel. However, there hasn't been much research comparing the performance of MAF and CMAF. Both MAF and CMAF processes for finishing the inner surface of Inconel-625 tubes have been investigated in the current work. The analysis of the performance of MAF and CMAF has involved investigating the effect of input responses on PISF.

1. Materials and Methods

Figure 1 illustrates the MAF and CMAF process principle to finish the inner cylindrical surface. A cylindrical workpiece was kept between the magnet's north and south poles during the MAF process. Both silicon carbide (SiC)

particles and iron particles are mixed together as per weight% of abrasives and inserted inside the tube. As magnetic abrasives particles (MAP) align with the lines of magnetic force under magnetic field and MAPs are driven toward the inner surface of the tube. The inner surfaces of the workpiece get polished as the tube rotates and cutting edges of abrasive performs the finishing action.

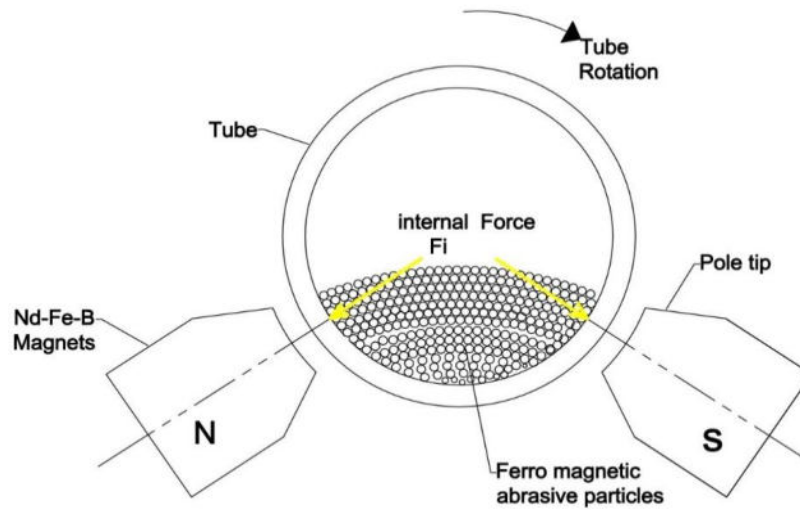


Fig. 1. - Basic finishing principle of MAF and CMAF

CMAF process involves the use of suitable chemicals on the surface of workpiece. Then chemically treated workpiece is kept in a muffle furnace for 30 minutes at a temperature between 50°C to 65°C. As a result of the etchant's reaction with the work surface, the inner surface layer of the work piece softens throughout this chemical reaction. Further basic MAF principle is used to remove the work surface's soft molecular layer formed chemical etching.

Figure 2 illustrates the finishing setup. The Inconel 625 tube ($\varnothing 25 \times 2 \times 150$ mm) inner side was polished using fabricated magnetic tool. Nd-Fe-B magnets (35x35x25 mm) are fastened with two screws on the aluminium fixture. Permanent magnets were used to maintain the constant magnetic flux density (0.5 tesla). An internal yoke composed of SS-400 steel connects the magnets' bottom N-S poles within the aluminium fixture. The outside surface of the tube is positioned parallel to the upper magnet. A multi-speed precision lathe machine was used for the experiments. The smooth rotating motion between the tube surface and the magnet poles is made possible by the PTFE tape that is used to wrap the magnet's poles. The precision lathe machine was equipped with a magnetic tool that used for the experiments.

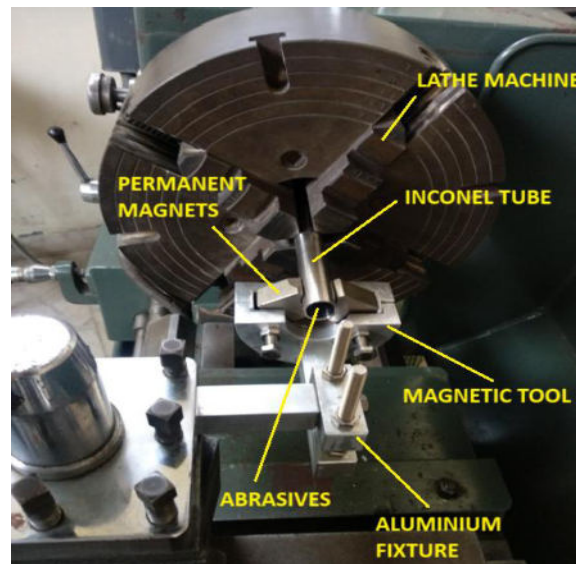


Fig. 2. - Finishing Setup

The input parameters and their range are displayed in Table 1. The range of process factors has been determined based on machine capabilities and reported literature. The three primary input parameters for the MAF and CMAF processes are processing time, abrasive weight percentage and surface rotation speed. Table 2 displays additional constant variables and chemical etching parameters. MAF did not involve any chemical treatment; however, the work surface in the CMAF process was first chemically treated using a chemical solution. The appropriate chemical concentration was taken into consideration when preparing the ethanol and ferric chloride (FeCl_3) chemical solution. The tube was placed in an

electric muffle furnace after being submerged in the chemical mixture. The temperature was kept at about 65 °C for 30 minutes in order to undergo chemical treatment. The Inconel 625 tubes' top surface diffuses as a result of a chemical reaction. The inside surface layer of tube get soften. Further, MAF is utilized to remove the diffused inner surface layer. The chemically treated tube was positioned between the permanent magnets and 3 gms. of abrasive particles were added inside the tube. The abrasive media get attracted towards the inner surface of tube due to magnetic field lines. Inside the tube, a magnetic abrasive brush was generated which carries out the cutting function. The tube's inner surface get polished as it revolves.

Table 1. - Input factors for MAF and CMAF

S.No.	Input Factors	Designation	Level-1	Level-2	Level-3
			-1	0	1
1	Processing time (Min.)	A	25	50	75
2	Tube rotational speed (RPM)	B	110	190	270
3	Weight % abrasive particles	C	25%	35%	45%

Table 2. Additional parameters

Other Constant parameters	
Specimen	Inconel 625 tubes (Ø25mm x 150mm x 2mm)
Permanent Magnet type	Nd.Fe.B SS-400 yoke Material
Abrasives	Silicon carbide (60 µm)
Iron Particle	300 µm
Chemical treatment parameters in CMAF	
Temperature	65°Celcius
Chemical Name	FeCl ₃
Chemicals Concentration	600g/lit
Etching duration	30 mins.

Final experiments were planned and executed using Response surface methodology (RSM). It minimizes the time-consuming experiment effort and produces improved correlation between output and input responses. Percentage improvement in surface finish (PISH) is regarded as output response in present work. Telesurf roughness tester was utilized to check the inner surface roughness of Inconel 625 tubes. Average of three readings were considered for the surface roughness measurement. The surface roughness of rough sample ranges from 2.18 µm to 3.88 µm and finished surface using MAF ranges from 1.19 µm to 2.52 µm and finished surface using CMAF ranges from 0.87 µm to 2.10 µm. PISH was determined using the following relation based on surface roughness values for each experiment. Table 3 shows the PISH results for MAF and CMAF under experimental settings.

$$\text{PISH} = (\text{Surface roughness of rough sample} - \text{Surface roughness of finished sample}) / \text{Surface roughness of rough sample} \times 100$$

Table 3. Experimental condition with output responses

Run	A: Processing time	B: Speed (RPM)	C: weight% of abrasives	% improvement in Surface Finish (MAF)	% improvement in Surface Finish (CMAF)
1	75	270	25	53	63
2	50	110	35	30	42
3	25	110	25	11	21
4	50	190	25	40	52
5	50	190	45	49	62
6	50	190	35	45	56
7	75	110	45	37	48
8	25	270	45	23	36
9	50	190	35	34	45
10	75	190	35	31	43
11	25	190	35	19	32
12	50	190	35	38	51
13	50	190	35	39	53
14	50	270	35	59	72
15	50	190	35	34	48

2. Results and Discussion

Results of percentage improvement in surface finish (PISH) in MAF and CMAF processes were analysed using design expert software. Significant models were created for obtained PISH in MAF and CMAF. ANNOVA analysis for PISF in MAF and CMAF are represented in Table 4 and Table 5 respectively. The model F-value for PISF in MAF and CMAF are 7.53 and 6.61 respectively. The analysis showed that predicted R^2 value is 0.9318 and 0.9225 respectively in MAF and CMAF model. The adeq. precision value is 9.4 and 9.1 in MAF and CMAF respectively. In order to examine how input factors affect PISH, 3D interaction graphs were plotted which represents the effect of process parameter on the PISF in both processes.

Table 4. ANNOVA table for PISF in MAF

Source	Sum of Squares	df	Mean Square	F-value	p-value	Value
Model	2095.14	9	232.79	7.53	0.0194	significant
A-Processing Time	72	1	72	2.33	0.1875	
B-Speed	420.5	1	420.5	13.6	0.0142	
C-Wt% of Abrasives	40.5	1	40.5	1.31	0.3042	
AB	34.98	1	34.98	1.13	0.3361	
AC	21.16	1	21.16	0.6845	0.4457	
BC	190.41	1	190.41	6.16	0.0557	
A ²	533.34	1	533.34	17.25	0.0089	
B ²	15.89	1	15.89	0.5139	0.5055	
C ²	15.89	1	15.89	0.5139	0.5055	
Residual	154.59	5	30.92			
Lack of Fit	72.59	1	72.59	3.54	0.133	not significant
Pure Error	82	4	20.5			
Cor Total	2249.73	14				

Table 5 ANNOVA table for PISF in CMAF

Source	Sum of Squares	df	Mean Square	F-value	p-value	Value
Model	2129.95	9	236.66	6.61	0.0256	significant
A-Processing Time	60.5	1	60.5	1.69	0.2503	
B-Speed	450	1	450	12.57	0.0165	
C-Wt% of Abrasives	50	1	50	1.4	0.2904	
AB	25	1	25	0.6984	0.4414	
AC	19.3	1	19.3	0.5392	0.4957	
BC	184.74	1	184.74	5.16	0.0723	
A ²	589.38	1	589.38	16.46	0.0098	
B ²	7.86	1	7.86	0.2195	0.6591	
C ²	7.86	1	7.86	0.2195	0.6591	
Residual	178.98	5	35.8			
Lack of Fit	105.78	1	105.78	5.78	0.074	not significant
Pure Error	73.2	4	18.3			
Cor Total	2308.93	14				

3.1 Processing Time and Speed's effect on PISF

The impact of processing time and speed on PISF in MAF is illustrated in Fig. 3 (a) & in CMAF in Fig. 3(b). In both processes, maximum PISF is attained at 75 min. time duration and speed 270 RPM. It has been analyzed that PISF is increasing with the increase in time duration and speed in both processes. It happens because abrasives particles strike rate on work surface is faster at higher speed and finishing duration is also longer. But, It has been observed from plots that PISF in CMAF process greater as compared MAF process. The main reason is the chemical treatment of workpiece. It makes the surface layer softer which is easily to remove using further MAF process.

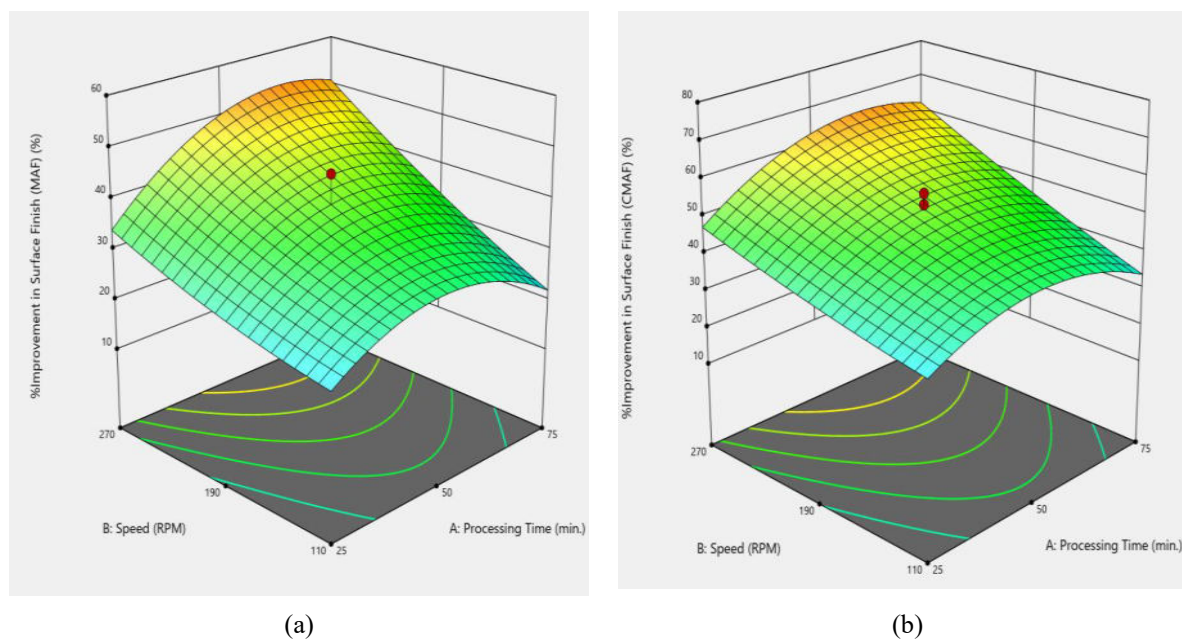


Fig.3. - Processing time and speed's effect on PISF (a) MAF; (b) CMAF

3.2 Processing Time and Weight% of abrasive's effect on PISF

The impact of time duration and weight% of abrasives in both MAF and CMAF is same as shown in Fig 4(a) and 4(b). PISH is increasing slowly with the increase in weight% of abrasives. At wt% of abrasive 35% and time duration 50 min., the better PISH is attained in both processes. It is also possible to speculate that a magnetic abrasive brush that is more effective was created when the number of cutting edges are increased using the maximum weight percentage of abrasives is 45%. More peaks were removed from surface by using effective magnetic brush for longer duration. If we compare both plots, PISH in CMAF process higher as compare to MAF process due to chemical treatment.

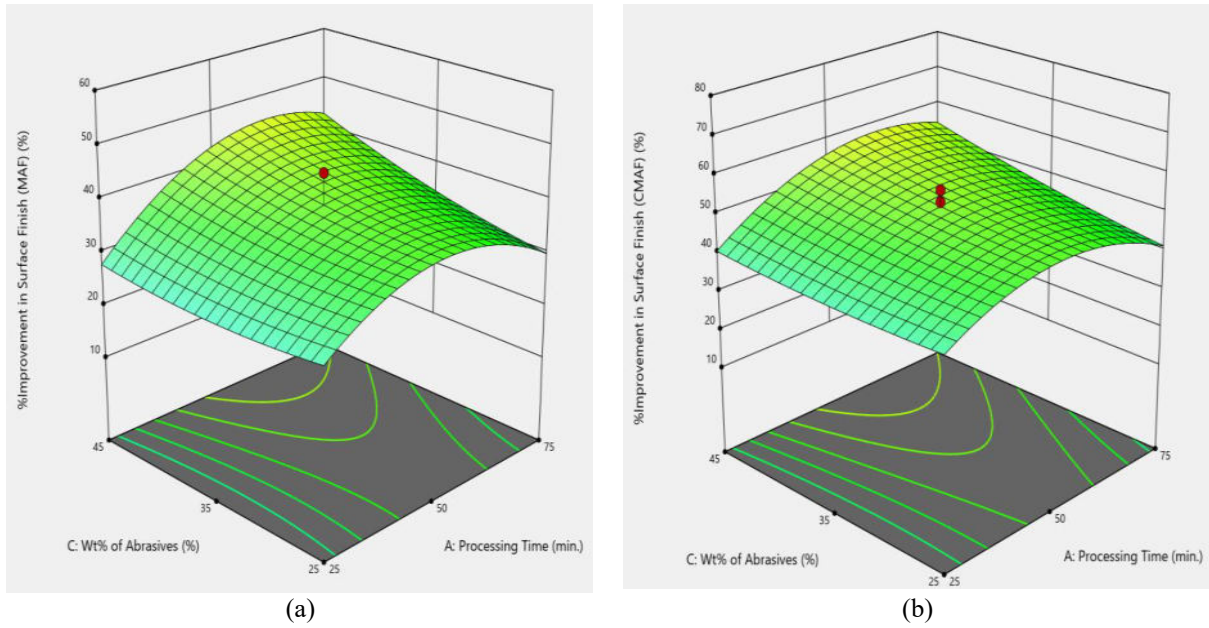


Fig. 4. - Processing time and weight% of abrasive's effect on PISF (a) MAF; (b) CMAF

3.3 Wt% of abrasives and speed's effect on PISH

The impact of speed and abrasive weight percentage on PISF in the MAF and CMAF processes is shown in Figures 5(a) and 5(b). Maximum PISF is attained in both processes at 25% weight percentage of abrasives and rotational speed of 270 RPM. This occurred as a result of employing the appropriate quantity of abrasive particles and increasing the particle strike rate on the tube surface. The 3D plot comparison also represents that around 70% PISH is achieved in CMAF and around 58% in MAF process.

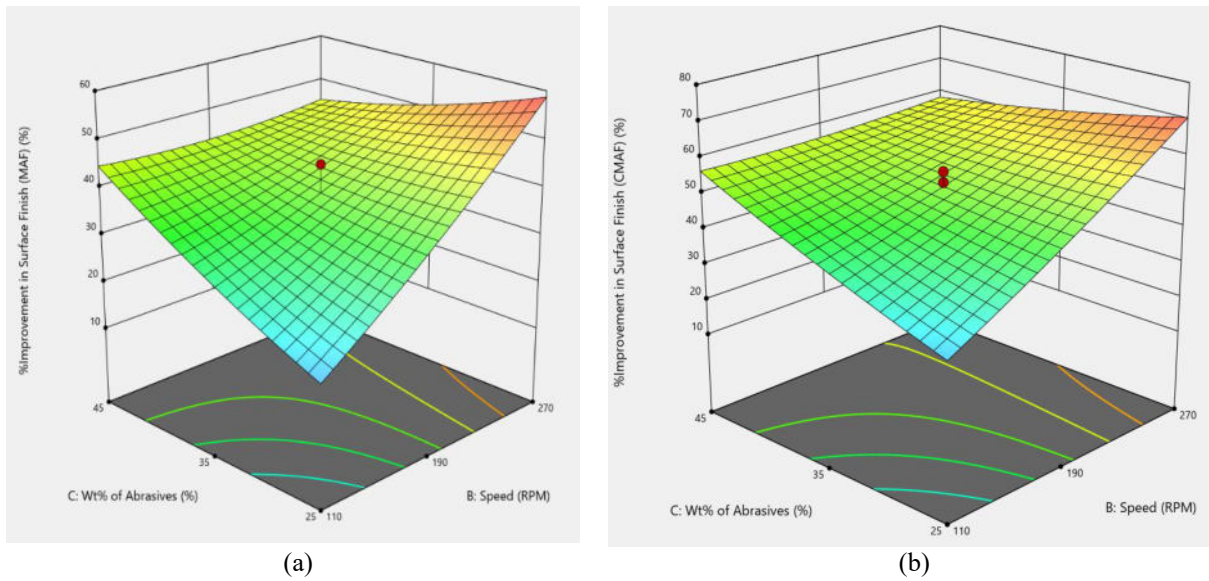


Fig. 5. - Weight% of abrasives and speed's effect on PISF (a) MAF; (b) CMAF

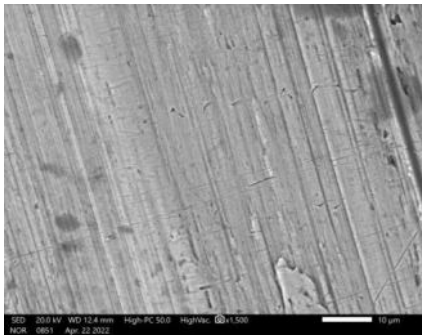
The result analysis showed that efficiency of CMAF process is better than the MAF process due to chemical treatment of workpiece. The inner surface layer of workpiece gets softer due to chemical reaction and intermolecular bonding of surface becomes weak. This weakened layer can be easily removed by MAF process. The highest processing time and speed is also responsible for improvements in internal surface finish. In CMAF and MAF process, the surface finish improvements are achieved around 72% and 59% respectively. The comparison of surface finish improvements with recently published results represents that our results are remarkable. The comparison summary is given in table 6.

Table 6. Comparison of % improvement in Surface Finish with others

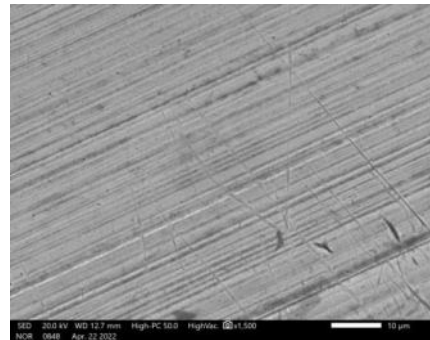
Author	Parameters	% improvement in Surface Finish
Liu and Zou [25]	Rotational speed and time	38%
Shather [23]	Rotational speed, working gap and concentration	34%
Ahmed and Shather [26]	Time, Speed, Particle size, Voltage and Gap	47%
Xie et al [24]	Speed, time and particles size	66%
Present Work	Rotation Speed, Processing Time and Weight % of abrasives	CMAF-72%, MAF-59%

3. Surface Topography

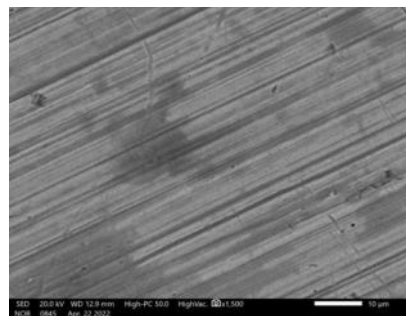
Scanning electron microscopy (SEM) has been used to investigate the surface morphology of finished surfaces by MAF and CMAF, as well as rough surfaces. The rough surface SEM picture is shown in Figure 6(a). The rough surface has imperfections like waviness, scratches, and tool marks etc. Figure 6(b) represents the SEM image of a surface that has been finished using a basic MAF technique. Analysis shows that the surface is not effectively finished using MAF because scratches and lines are visible on the surface. The surface finished by CMAF process is shown in SEM image form in Figure 6(c). It's evident that CMAF surface finishing results in fewer imperfections like scratches, waviness than standard MAF surface finishing. Therefore, it makes sense that, in comparison to the basic MAF process, CMAF offers superior surface finish. The chemical treatment makes the difference which is responsible for better surface finish in CMAF process.



(a)



(b)



(c)

Fig. 6. - SEM images (a) Rough sample; (b) Finished with MAF; (c) Finished with CMAF

4. Conclusion

Both MAF and CMAF processes have been effectively utilized to finish the inner surface of Inconel 625 tubes. Investigation points are outlined below:

- The main factors improving PISF in MAF and CMAF are Rotational speed and finishing time. It is suggested to use a 75-min. process duration and 270 RPM in order to achieve maximum PISF in both processes.
- In comparison, CMAF provides better PISF as compare to MAF and maximum PISF 72% in CMAF and 59% in MAF was achieved.
- SEM analysis also justifies that less scratches and imperfections on the CMAF finished surface as compared to MAF finished surface.
- The primary factor enhancing the CMAF process's efficacy is the chemical treatment of Inconel 625 tubes. Efficiency of CMAF is 18% greater than MAF process.

References

- [1] Fusova L., Rokicki P., Spotz Z., Saksl K., Siemers C. Tool wear mechanisms during machining of Alloy 625. *Adv Mater Res* 2011; 275:204–207.

- [2] Nath C., Brooks Z., Kurfess T.R. Machinability study and process optimization in face milling of some super alloys with indexable copy face mill inserts. *J Manuf Process* 2015; 20:88–97.
- [3] Dhanabalan S., Sivakumar K., Narayanan C.S. Analysis of form tolerances in electrical discharge machining process for Inconel 718 and 625. *Mater Manuf Process* 2014; 29:253–259.
- [4] Thakur A Gangopadhyay S. State-of-the-art in surface integrity in machining of nickel-based super alloys. *Int J Mach Tools Manuf* 2016; 100:25–54.
- [5] Kala P, Pandey P.M. Comparison of finishing characteristics of two paramagnetic materials using double disc magnetic abrasive finishing. *J Manuf Process* 2015; 17:63–77.
- [6] Shinmura T., Yamaguchi H. Study on a new internal finishing process by the application of magnetic abrasive machining: internal finishing of stainless steel tube and clean gas bomb. *JSME Int J Ser C Dyn Control Robot Des Manuf* 1995; 38:798–804.
- [7] Yamaguchi H., Shinmura T. Study of an internal magnetic abrasive finishing using a pole rotation system. Discussion of the characteristic abrasive behavior. *Precis Eng* 2000; 24:237–244.
- [8] Mulik R.S, Pandey P.M. Experimental investigations and optimization of ultrasonic assisted magnetic abrasive finishing process. *Proc Inst Mech Eng Part B J Eng Manuf* 2011; 225:1347–1362.
- [9] Nteziyaremyea V., Wang Y., Li W., Shihb A. Yamaguchi H. Surface finishing of needles for high-performance biopsy. *Procedia CIRP* 2014; 14:48–53.
- [10] Heng L., Kim J.S, Song J.H, Mun S.D. Application of Al₂O₃/iron-based composite abrasives on MAF process for inner surface finishing of oval-shaped tube: predicting results of MAF process using artificial neural network mode. *J Mater Res Technol* 2021; 15:3268-3282.
- [11] Zhang J., Wang H., Kumar A.S, Jin M. Experimental and theoretical study of internal finishing by a novel magnetically driven polishing tool // *Int J Mach Tools Manuf* 2020; 1534:103552.
- [12] Yang Y., Xue Y., Li B., Fu Y., Jiang Y., Chen R., Hang W., Sun X. A Magnetic Abrasive Finishing Process with an Auxiliary Magnetic Machining Tool for the Internal Surface Finishing of a Thick-Walled Tube // *Machines* 2022; 10:529.
- [13] Wang L., Sun Y., Zhang G., Wu P., Sun Y., Zuo D. Investigation on the preparation and finishing performance of a novel nanoparticle-enhanced bonded magnetic abrasive. *Int J Adv Manuf Technol* 2023; 129:1523.
- [14] Wang L., Sun Y., Xio Z., Yao L., Guo J., Kang S., Mao W, Zuo D. Experimental Investigation on Magnetic Abrasive Finishing for Internal Surfaces of Waveguides Produced by Selective Laser Melting. *Materials* 2024; 17(7):4631-4642.
- [15] Sihag N., Kala N.P., Pandey P.M. Chemo assisted magnetic abrasive finishing: Experimental investigations. *Procedia CIRP* 2015; 26:539–543.
- [16] Singh G., Kumar H., Kumar A. Investigations into Machining of Inconel 625 Flat Surfaces with Multi-pole // *Magnetic Tool*. *Indian J Sci Technol*, 2018, 11, 1–9.
- [17] Sihag N., Kala P., Pandey P.M. Analysis of Surface Finish Improvement during Ultrasonic Assisted Magnetic Abrasive Finishing on Chemically treated Tungsten Substrate // *Procedia Manuf* 2017, 10:136–146.
- [18] Singh G., Kumar H., Kumar A. Machining of Inconel 718 flat surfaces with chemically assisted magnetic abrasive finishing process // *Indian J Sci Technol* 2018, 11, 1-6.
- [19] Singh G., Kumar H., Kansal H.K, Srivastava A. Effects of chemically assisted magnetic abrasive finishing process parameters on material removal of inconel 625 tubes // *Procedia Manuf* 2020, 48, 466–473.
- [20] Singh G., Kumar H., Kansal H.K. Investigations into internal roundness of Inconel 625 tubes with chemically assisted magnetic abrasive finishing // *Mater Today Proc* 2019, 19,1579–1585.
- [21] Singh G., Kumar H. Influence of chemically assisted magnetic abrasive finishing process parameters on external roundness of Inconel 625 tubes // *Mater Today Proc* 2020, 37, 3283–3288.
- [22] Singh et al. Multiobjective Optimization of Chemically Assisted Magnetic Abrasive Finishing (MAF) on Inconel 625 Tubes Using Genetic Algorithm: Modeling and Microstructural Analysis // *Micromachines*, 2022,13 (8),1168.
- [23] Shather S.K. Enhancement of surface roughness and metal removal rate by using combined abrasives during magnetic abrasive finishing // *Int J Res Eng Technol*, 2019, 71–8
- [24] Xie H. and Zou Y. Investigation on finishing characteristics of magnetic abrasive finishing process using an alternating magnetic field // *Machines*, 202, 81–17
- [25] Liu J. and Zou Y. Study on elucidation of the roundness improvement mechanism of the internal magnetic abrasive finishing process using a magnetic machining tool // *J Manuf Mater Process*, 2023, 749
- [26] Ahmed A. M. S and Shather S.K. Optimizing the five magnetic abrasive finishing factors on surface quality using Taguchi-based grey relational analysis // *Eng Res Exp*, 2024, 6, 015405.

Information of the authors

Singh Gurpreet, PhD, professor, Mechanical Engineering Department, Chandigarh University
e-mail: garry.dhiman85@gmail.com

Singh Gyanendra, PhD, professor, Mechanical Engineering Department, Chandigarh University
e-mail: gyanendragoindi@gmail.com

Kumar Harish, PhD, professor, Mechanical Engineering Department, Chandigarh University
e-mail: garry.dhiman85@gmail.com

Efficient Power Voltage Management of SiC MOSFET at Low Frequencies

Ospanov B.S.^{1*}, Tatkeeva G.G.², Kelesbek N.K.³

¹Abylkas Saginov Karaganda Technical University, Karaganda, Kazakhstan

²S. Seifullin Kazakh Agrotechnical University, Astana, Kazakhstan

³E.A. Buketov Karaganda University, Karaganda, Kazakhstan

*corresponding author

Abstract. At present, the traditional power sector is undergoing significant changes. A key technology driving these transformations is power electronics, where power quality depends on the transient switching processes of power converters. Currently, commercially available switching devices include Si IGBTs and Si power MOSFETs. Unfortunately, silicon-based technologies are approaching their theoretical limits and are no longer efficient enough to meet modern requirements. This fact has drawn our attention to silicon carbide (SiC), a wide-bandgap semiconductor material. The main objective of this study is the active regulation of the gate voltage applied to the SiC MOSFET to reduce switching losses and electromagnetic interference (EMI) generation. In the conducted experiments, active gate voltage control led to a significant reduction in switching losses-by approximately 35%-compared to fixed gate drive schemes. For example, turn-off energy loss was reduced from 420 μ J to 270 μ J, while the turn-on loss decreased from 510 μ J to 340 μ J. Additionally, by optimizing the gate voltage profile (using techniques such as gate current shaping), the peak EMI voltage measured across the parasitic inductance was lowered by up to 45%, demonstrating a substantial improvement in EMI performance. Rise time was also effectively controlled, reducing from 18 ns to 11 ns, thereby enhancing overall switching speed while mitigating overshoot. These quantitative improvements confirm the effectiveness of dynamic gate control in maximizing the advantages of SiC devices, paving the way for more efficient and reliable power converter designs.

Keywords: Double-pulse test, electromagnetic interference (EMI), silicon carbide (SiC), rise time, case temperature, transistor, full modeling, electron mobility.

Introduction

The research on silicon carbide (SiC) is directly related to materials science, as it focuses on the crystalline structure, thermal and electrical properties of the material, as well as the mechanisms of crystal growth and modification. In particular, the study of SiC polytypism and the selection of the most suitable variant-4H-SiC-for power electronics applications require a deep understanding of phase transitions, crystal lattice defects, and thermal conductivity. These characteristics lie at the intersection of solid-state chemistry, materials physics, and engineering, making this field a clear example of applied materials science in the development of modern semiconductor components. Wide-bandgap semiconductors utilizing silicon carbide (SiC) have become increasingly attractive for power electronics applications due to their superior properties compared to silicon (Si), as reported in studies [1-4]. It is important to note that SiC exhibits polytypism during crystallization, meaning that a single element or compound can form multiple crystalline structures. As a result, various polytypes of SiC exist [5-7]. According to studies [5, 6, 8], the 4H-SiC polytype is the most suitable for power electronics applications. Furthermore, this specific polytype was developed specifically for power electronics applications [5]. Therefore, in this project, the term "SiC" will refer to 4H-SiC.

Three key properties of SiC make it advantageous over Si for high-temperature, high-power, and high-frequency operating conditions [6]: thermal conductivity, critical electric field strength, and bandgap energy.

Table 1. Some Characteristics of SiC & Si [6]

Parameter	Si (Silicon)	4H-SiC (Silicon Carbide)
Bandgap Energy (eV)	1.12	3.26
Critical Electric Field (MV/cm)	0.3-0.4	2.2-2.8
Thermal Conductivity (W/cm·K)	1.5	3.7-4.9
Electron Mobility (cm ² /V·s)	1350	800-1000
Saturation Drift Velocity (cm/s)	1.0×10 ⁷	2.0×10 ⁷
Dielectric Constant (ϵ_r)	11.8	9.7

This table highlights the superior properties of 4H-SiC compared to traditional silicon, making it a more suitable choice for high-temperature, high-power, and high-frequency power electronics applications.

Silicon carbide (SiC) is a semiconductor material with optoelectronic properties distinct from those of silicon (Si), making it more suitable for high-temperature, high-power, and high-frequency operating conditions. The nearly threefold greater bandgap of SiC means that more energy is required to free an electron from the valence band. Consequently, this

results in higher junction temperatures, allowing SiC-based semiconductor devices to operate at significantly higher temperatures.

Additionally, the higher thermal conductivity of silicon carbide ensures more efficient heat dissipation. In practical terms, for the same voltage and current ratings, a smaller heat sink can be used in a SiC-based semiconductor device compared to a silicon-based counterpart. Another advantage of SiC over Si is that the saturation drift velocity of electrons is nearly twice as high. This characteristic enables faster switching speeds, allowing devices to operate at higher switching frequencies.

Overall, these properties lead to reduced passive component sizes in circuit designs, making SiC-based converters more compact and efficient.

1. Methods

To evaluate the switching behavior of a SiC power MOSFET, a double-pulse test (DPT) must be conducted [4, 5, 11]. The switching dynamics can be assessed not only through a standalone double-pulse test circuit but also in the context of its use in power converters [4]. However, as stated in [4], the double-pulse test setup provides more accurate oscilloscope waveforms for current and voltage measurements.

Fundamentally, the test setup is structured as a buck converter supplying an inductive load, as illustrated in the figure below. The DPT circuit is designed to measure key switching characteristics such as turn-on and turn-off losses, voltage and current overshoot, and electromagnetic interference (EMI) generation. By analyzing the waveforms obtained from the test, important performance parameters, including switching speed and energy dissipation, can be precisely evaluated.

The double-pulse test is widely used in power electronics research and industry as a standard method for assessing transient switching performance, particularly for emerging wide-bandgap semiconductors like SiC.

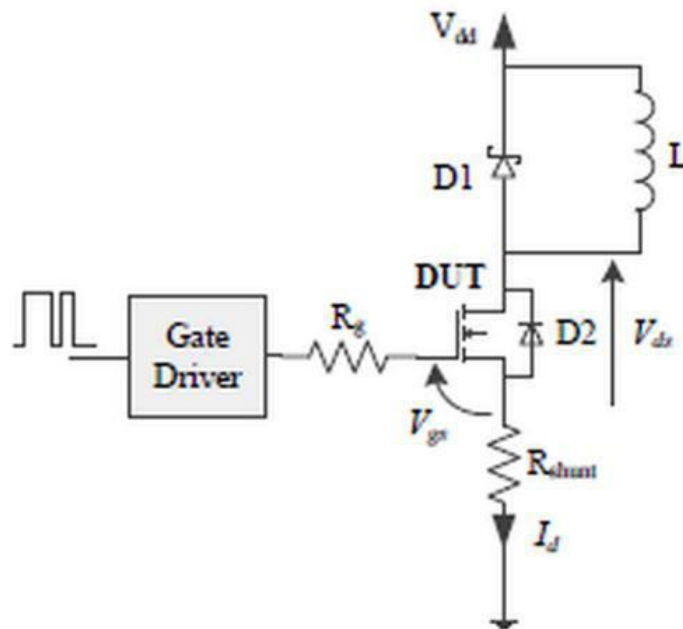


Fig. 1. Double-Pulse Test Setup [11]

In the circuit shown in Figure 1, the MOSFET serves as the Device Under Test (DUT), and its switching behavior is recorded. To generate the necessary turn-on and turn-off signals, the DUT is subjected to two consecutive pulses, where the width of the first pulse is longer than that of the second.

The idealized waveforms obtained during the double-pulse test (DPT), along with the corresponding gate drive pulses, are illustrated in Figure 2 below. These waveforms are essential for analyzing switching losses, transient voltages, and current characteristics of the SiC MOSFET, helping to evaluate its performance under realistic operating conditions.

As shown in Figure 2, the first gate drive pulse is longer than the second one. When the first pulse is initially applied, the MOSFET begins conduction, and the current increases to the desired level. The current value can be adjusted by varying the duration of this first pulse. In other words, the first pulse is modulated to test the Device Under Test (DUT) under different load conditions. Meanwhile, the voltage across the DUT drops as conduction begins.

Once the desired current level is reached, the first pulse ends, and at this moment, the turn-off characteristics of the device are recorded. Upon turn-off, the freewheeling diode enters conduction mode, allowing the inductor current to remain nearly constant at the attained level.

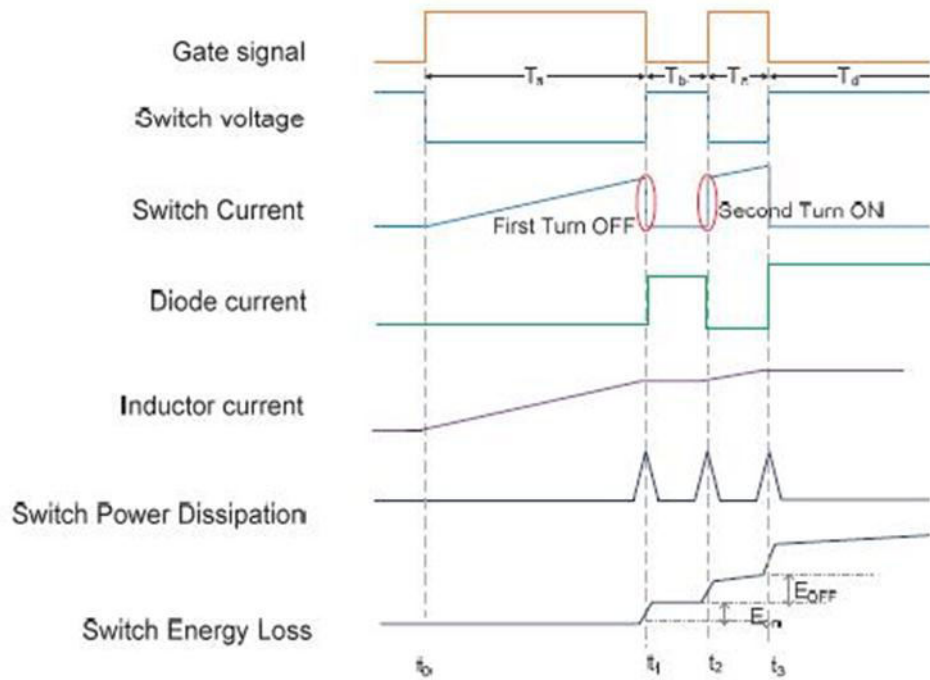


Fig. 2. - Idealized DPT Waveforms [5]

Subsequently, the second pulse is applied causing the current to rise further, while the voltage across the diode decreases at a rate determined by the dv/dt of the MOSFET. This second turn-on transition is used to capture the turn-on characteristics of the switch [9]. Finally, when the second pulse ends, the inductor current gradually decays within the loop formed by the freewheeling diode [10].

Figure 2 also illustrates that most power dissipation occurs during switching transitions (when voltage and current overlap). The switching energy losses are calculated as the integral of power dissipation over the switching transition time, providing critical insights into the efficiency and thermal performance of the MOSFET.

2. Results and discussion

The turn-off characteristics were captured during the falling edge of the gate-off signal. During turn-off, the voltage across the parasitic capacitance C_p decreases from the DC level to zero, resulting in the generation of a discharge current IC_p . Consequently, this peak causes the drain current to decrease until the MOSFET reaches the steady-state off condition. After the turn-off transition, oscillations appear in the current and voltage waveforms. These parasitic oscillations are caused by the interaction of LS, C_p and C_{oss} (the output capacitance of the MOSFET, defined as the sum of CDS and CGD as specified in the datasheet).

Switching signals for different time intervals were obtained here depending on the parasitic inductance, as shown in Table 2.

Table 2. Turn-off signal extraction times for different L_S values

LS	Extraction time when turned on
10 nH	0.3 μ s
20 nH	0.4 μ s
30 nH	0.525 μ s

Table 3 below presents similar characteristics obtained in Table 2, but this time focusing on turn-off transients.

During turn-off, the dV/dt remained relatively unchanged, while the dI/dt showed a tendency to increase, primarily due to the observed current dips. Although the frequency of parasitic oscillations decreased, the drain current settling time increased significantly.

For example, with a parasitic inductance of 10 nH, the settling time was 29.96 ns, whereas at 50 nH, the drain current settled within $\pm 5\%$ in 317.04 ns, which is **more than ten times longer**.

Overall, energy losses exhibited an increasing trend due to the prolonged oscillation period; however, these changes can be considered relatively minor.

Table 3. Turn-off transient characteristics for different parasitic inductance values

L_s	dV/dt (kV/ μ s)	dI/dt (kA/ μ s)	$f_{ringing}$ (MHz)	I_d settling time (ns)	Energy (μ J)
10 nH	117.09	4.8094	86.077	29.966	237.63
20 nH	127.32	6.5520	69.119	93.871	249.07
30 nH	125.15	7.6088	62.261	168.68	253.50

Figures 3 to 5 below illustrate the switching transient waveforms for various parasitic inductance (L_s) values using a hard-switching gate drive signal.

From these figures, it is evident that increased parasitic inductance negatively affects the voltage and current waveforms. Specifically, higher L_s leads to:

- Greater voltage overshoot;
- Higher current spikes;
- Increased parasitic oscillations in both voltage and current waveforms;
- Enhanced electromagnetic interference (EMI) generation.

These effects highlight the importance of minimizing parasitic inductance in the circuit layout to achieve efficient and reliable switching performance in SiC MOSFET-based power converters.

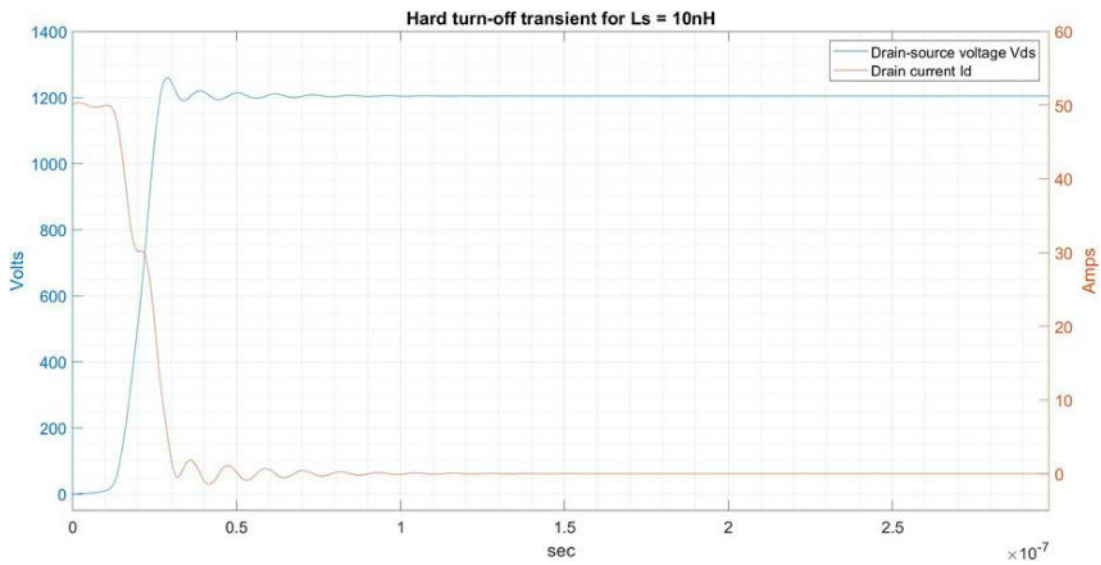


Fig. 3. – Turn-Off Transient Under Hard Switching with $L_s = 10$ nH

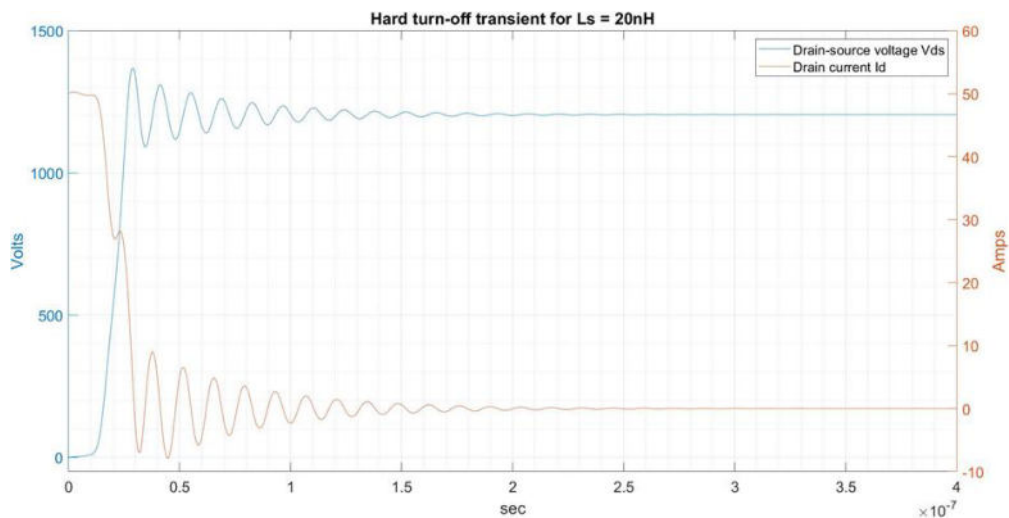


Fig. 4. – Turn-Off Transient Under Hard Switching with $L_s = 20$ nH

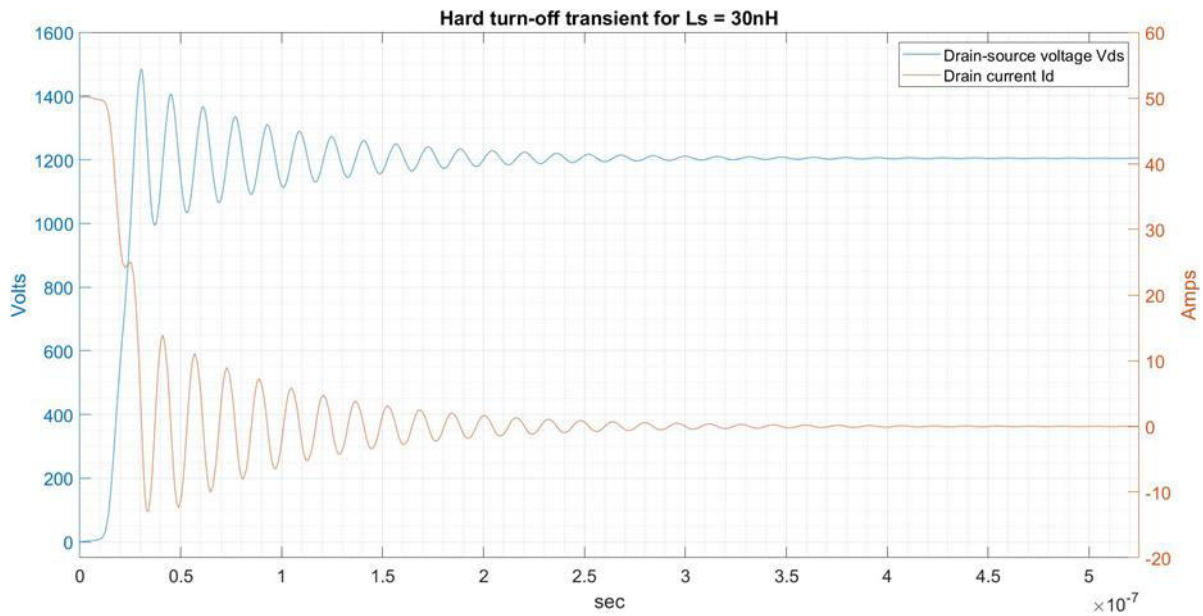


Fig. 5. – Turn-Off Transient Under Hard Switching with $L_s = 30\text{ nH}$

Conclusion

Thus, the double-pulse test (DPT) conducted within an inductance range of 10–30 nH, along with the analysis presented in the graphs, demonstrated the efficiency of SiC MOSFET transistors in power voltage management. The results confirmed that SiC devices offer superior switching performance compared to traditional silicon-based devices, particularly in terms of reduced switching losses, faster switching speeds, and lower electromagnetic interference (EMI). By actively controlling the gate voltage, it was possible to minimize energy dissipation and suppress parasitic oscillations, improving the overall performance and reliability of the system.

Moreover, the influence of parasitic elements such as inductance L_s and capacitances C_{ps} and C_{oss} on switching behavior was clearly observed, underlining the importance of precise layout design and component selection in practical applications. These findings highlight the relevance of SiC technology in modern power electronics, especially for applications that demand high efficiency, compact size, and operation under high-frequency and high-temperature conditions.

Moving forward, we will continue modeling and testing SiC MOSFETs at different switching frequencies, gate driver configurations, and load conditions to determine the most optimal operating parameters. Future work will also focus on implementing these findings in full converter systems and evaluating their real-world performance under varying thermal and electrical stress conditions.

References

- [1] Mostaghimi O., Wright N., Horsfall A. Design and performance evaluation of SiC based DC-DC converters for PV applications //IEEE Energy Conversion Congress and Exposition, 2012
- [2] McNutt T., Hefner A., Mantooth H., Berning D., Ryu S. Silicon Carbide Power MOSFET Model and Parameter Extraction Sequence //IEEE Transactions on Power Electronics, 2017, 22(2), 353-363.
- [3] Chen Z., Boroyevich D., Burgos R., Wang F. Characterization and modelling of 1.2 kV, 20 A SiC MOSFETs // Proc. IEEE ECCE, 2013, 1480-1487.
- [4] Ahmad S. S., Narayanan G. Double pulse test based switching characterization of SiC MOSFET // National Power Electronics Conference (NPEC), Pune, 2017, 319-324
- [5] Tiwari S., Abuishmais I., Undeland T., Boysen K. Silicon carbide power transistors for photovoltaic applications //IEEE Trondheim PowerTech, Trondheim, 2011, 1-6.
- [6] Tsunenobu Kimoto, 2 - SiC material properties, Editor(s): B. Jayant Baliga, In Woodhead Publishing Series in Electronic and Optical Materials, Wide Bandgap Semiconductor Power Devices, Woodhead Publishing, 2019, 21-42
- [7] Rice J., Mookken J. SiC MOSFET gate drive design considerations //IEEE International Workshop on Integrated Power Packaging (IWIPP), Chicago, IL, 2015, 24-27.
- [8] Wang J., Liu D., Dymond H. C. P., Dalton J. J. O., Stark B. H. Crosstalk suppression in a 650-V GaN FET bridgeleg converter using 6.7-GHz active gate driver //IEEE Energy Conversion Congress and Exposition (ECCE), Cincinnati, OH, 2017, 1955-1960.
- [9] Hazra S., De A., Cheng L., Palmour J., Schupbach M., Hull B. et al. High Switching Performance of 1700V, 50A SiC Power MOSFET over Si IGBT/BiMOSFET for Advanced Power Conversion Applications //IEEE Transactions on Power Electronics, 2015, 1-10.

[10] Wang L., Yang J., Ma H., Wang Z., Olanrewaju K., Kerrouche K. Analysis and Suppression of Unwanted Turn-On and Parasitic Oscillation in SiC JFET-Based Bi-Directional Switches //Electronics, 2018, 7(8), 126.

[11] Helong Li., Munk-Nielsen S. Detail study of SiC MOSFET switching characteristics // IEEE 5th International Symposium on Power Electronics for Distributed Generation Systems (PEDG), 2014.

Information of the authors

Ospanov Bektas Sekerbekovich, M.Sc., Lecturer, Abylkas Saginov Karaganda Technical University
e-mail: bektass@mail.ru

Tatkeeva Galina Galimzyanovna, D.Sc., Professor, S. Seifullin Kazakh Agrotechnical University
e-mail: tatkeeva@mail.ru

Kelesbek Nabira Kydyrbekkyzy, PhD Student, E.A. Buketov Karaganda University
e-mail: knk_93@bk.ru

Selection of Geometric Parameters of Indenters that Provide Sufficient Sensitivity to Changes in Characteristics in the Volume of Material

Tursunov T.M.¹, Tursunov N.Q.¹, Kren A.P.², Urazbaev T.T.^{1*}, Ziyamukhamedova U. A.¹

¹Tashkent State Transport University, Tashkent, Uzbekistan

²State Scientific Institution «Institute of Applied Physics of the National Academy of Sciences of Belarus», Minsk, Belarus

*corresponding author

Abstract. This study investigates the selection of geometric parameters for indenters to ensure sufficient sensitivity in assessing the physical and mechanical properties of cast iron under dynamic loads. The research focuses on optimizing indenter dimensions (diameter, shape) and impact energy to achieve measurable plastic imprints while accounting for material heterogeneity, particularly graphite inclusions. Analytical and experimental approaches were used to evaluate the relationship between indenter geometry, deformation rates, and imprint characteristics. Results indicate that a spherical indenter with a diameter of 1.2 mm, mass of 5 g, and impact velocity of 3 m/s optimally balances imprint size (450–500 μm) and depth (50–120 μm) across cast iron hardness ranges (100–500 HBW). The findings highlight the importance of maintaining complete plasticity during indentation to minimize surface preparation effects and ensure reliable non-destructive testing. This work contributes to improved methodologies for dynamic hardness testing in industrial applications, particularly for high-strength cast irons.

Keywords: high-strength cast iron, hardness, induction crucible furnace, mechanical properties, indentation, impact, imprint.

Introduction

Cast iron casting is widely used in both domestic and foreign industrial enterprises. Cast iron is one of the main structural materials and is widely used in the automotive industry (for the production of cylinder blocks and crankshafts), rail transport (brake pads) [17], machine tool industry (machine bases) and the oil industry (pipes). Due to the presence of graphite inclusions, cast iron effectively dampens vibrations and can be used at low temperatures. However, when producing various products, there are difficulties with control, since it is often necessary not only to determine the structure of the cast iron (in particular, to distinguish between gray and high-strength), but also to accurately determine its physical and mechanical properties: strength, hardness and elastic modulus. If the problem of separating cast iron types can be solved using ultrasonic methods, then determining mechanical characteristics using non-destructive testing remains an urgent problem that needs to be solved. The structure of cast iron is very sensitive to various factors, such as the composition of the feedstock [18], and the presence of components (including parasitic impurities, such as sulfur and sulfur compounds, even within the technical specifications) [11], alloying additives [24], as well as loading and mixing methods and heating conditions [13].

The situation in the field of cast iron materials science is unique: the industrial use of cast irons is ahead of the development of the theoretical foundations of their structure formation. Materials created experimentally often begin to be used before the theoretical justification for their production appears. This is especially true for new grades of cast iron, such as ADI, which have high strength (700-1450 MPa) and significant relative elongation at break.

Cast iron is a structurally heterogeneous material due to the presence of a large number of graphite inclusions, which can take various forms: lamellar (gray cast iron), spherical (high-strength), flake (malleable), there is also a vermicular form of graphite [1]. In addition to various forms of graphite, cast iron can have various bases: ferritic, ferritic-pearlite, pearlitic. White cast iron has a cementite structure. According to GOST 3443 "Cast iron castings with various forms of graphite. Methods for determining the structure" graphite inclusions can have sizes from 15 μm to 1000 μm [1]. It should be noted that large graphite inclusions sharply reduce mechanical properties and for products made of such cast iron, control of their characteristics, as a rule, is not carried out. The distribution of graphite in the cast iron structure can be both uniform and uneven, and also have a colonial, mesh and even branched distribution. The number of graphite inclusions is estimated by the average percentage of the area occupied on the microsection. For example, for lamellar graphite, the distribution density varies from 2 to 12%. Figure 1 shows the microstructure of real cast iron samples and an assessment of the distribution of characteristic sizes of various carbon inclusions.

Taking into account the above, for assessing the physical and mechanical characteristics of cast iron using the indentation method, the minimum sufficient linear size of the deformation region is about 500 μm with a hardness of about 100 HBW and 400-450 μm with a hardness of 500 HBW and more.

Cast iron is a critical structural material due to its vibration-damping properties and versatility. However, its heterogeneous structure, characterized by graphite inclusions (e.g., lamellar, spherical, vermicular), complicates non-destructive evaluation of mechanical properties like hardness, strength, and elastic modulus. While ultrasonic methods can distinguish between cast iron types (e.g., gray vs. high-strength), existing techniques fail to provide accurate, localized assessments of mechanical properties under dynamic loads, particularly for modern high-strength grades (e.g., ADI with 700–1450 MPa tensile strength). Current indentation methods lack systematic optimization of indenter geometry and loading parameters to ensure sensitivity across cast iron's hardness range (100–500 HBW). This limits their reliability in

industrial settings, where dynamic loads and material heterogeneity demand precise control of deformation regimes (elastic-plastic vs. fully plastic).

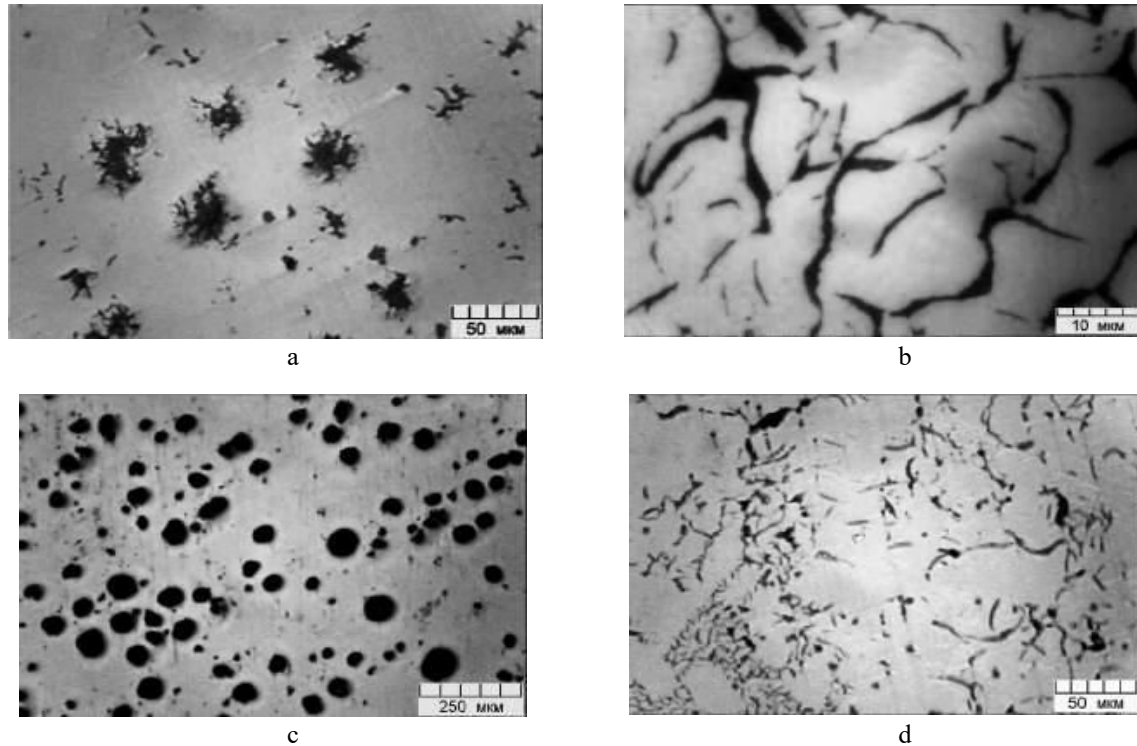


Fig.1. - Form of graphite (dark inclusions) in cast irons: a – flake-like, b – plate-like, c – spherical, d – vermicular

1. Methods

The brief analysis of the methods for determining the geometric and energy parameters of indentation shows that there is a need to solve the problem of selecting the optimal geometric and energy parameters of loading to create the required deformation of the material in order to reliably characterize its properties in a local volume and at the same time give its integral assessment.

To calculate the equivalent deformation during indentation, similar to that which will be formed during tension or compression of cast iron under uniaxial loading, and to obtain relationships linking the geometric parameters of the indenter and the created deformation value. The authors considered the process of elastic-plastic indentation. First, we will analyze the process of indentation of a sharp indenter in the form of a cone or a tetrahedral pyramid (Figure 2)

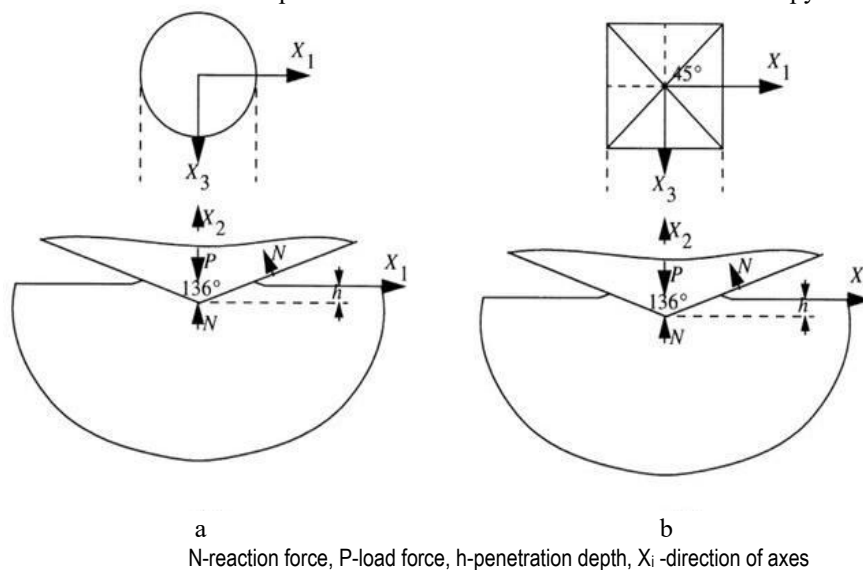


Fig. 2. - Indentation of sharp indenters: cone (a) and pyramid (b)

When the elastic limit is first exceeded, the plastic zone is small and is completely covered by the material, which is in a purely elastic state, so that the plastic deformations have the same order of magnitude as the elastic ones. In this case,

the displacement of the material by the indenter is compensated by elastic displacements of the environment. As the indentation depth increases, an increase in the pressure under the indenter is required to ensure the necessary expansion of the material. Eventually, the plastic zone reaches the free surface and the displaced material can freely flow plastically along the edges of the indenter. This becomes possible when the average pressure under the indenter P_m reaches a value determined by the theory of rigid-plastic media [2]:

$$P_m = C_k \cdot Y \tag{1}$$

where Y is the flow stress, and the value of C_k depends on the geometry of the indenter and is approximately equal to 3.0 in the state of complete plasticity.

According to [2], the flow state is achieved at pressure (1), where the constant $C_k \sim 1.1$. There is an interval of intermediate values of the average contact pressure (from Y to $3Y$), for which plastic flow is restrained by the surrounding elastic material, and deformation is carried out due to the radial expansion of the medium. From a practical point of view, three loading stages are of interest: elastic, elastic-plastic, and completely plastic. In [3], it was shown that the contact surface during indentation is covered by a hemispherical "core" of radius a (Figure 3).

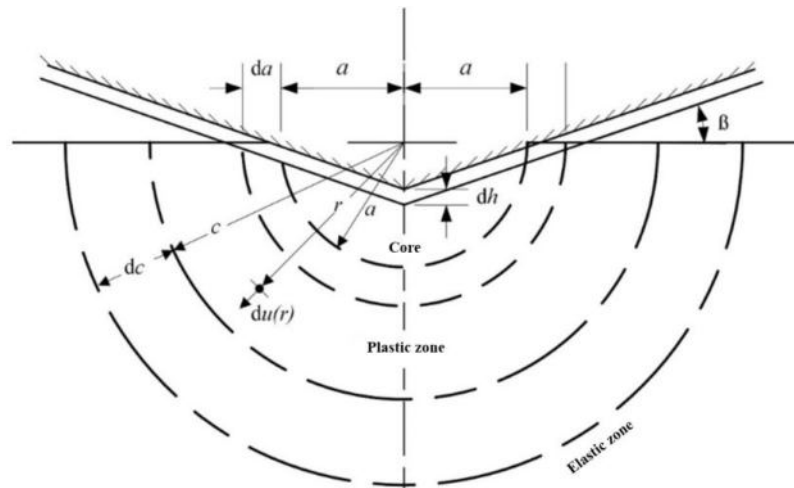


Fig.3. - Model with a spherical core for the analysis of the penetration of a cone into an elastic-plastic medium

A hydrostatic stress state of intensity \bar{p} is formed inside the core. The elastic-plastic boundary is defined by the radius c , where $c > a$. The hydrostatic pressure in the core is equal to the radial component of the stress beyond the core boundary. It can also be argued that the radial displacement of particles lying on the boundary $r=a$, with an increase in the penetration depth dh , should be compensated by the material displaced by the indenter. If we follow the work [4], then the stresses in the plastic zone $a \leq r \leq c$ are equal to:

$$\frac{\sigma_r}{Y} = -2 \ln \left(\frac{c}{r} \right) - \frac{2}{3}, \tag{2a}$$

$$\frac{\sigma_\theta}{Y} = -2 \ln \left(\frac{c}{r} \right) + \frac{1}{3}. \tag{2b}$$

In the elastic zone $r \geq c$:

$$\frac{\sigma_r}{Y} = -\frac{2}{3} \left(\frac{c}{r} \right)^3, \quad \frac{\sigma_\theta}{Y} = \frac{1}{3} \left(\frac{c}{r} \right)^3. \tag{3}$$

The pressure in the core and the radial stress at the boundary of the core are equal:

$$\frac{\bar{p}}{Y} = -\frac{\sigma_r}{Y} \Big|_{r=a} = \frac{2}{3} + 2 \ln \frac{c}{a} \tag{4}$$

Radial deformations are equal [4]:

$$\frac{du(r)}{dt} = \frac{Y}{E} \left[3(1-\nu) \left(\frac{c}{r} \right)^2 - 2(1-2\nu) \frac{r}{c} \right]. \tag{5}$$

From the condition of incompressibility of the core it follows that the expression found from this equation for c/a in (4) can be used to obtain the pressure in the core:

$$\frac{\bar{p}}{Y} = \frac{2}{3} \left[1 + \ln \left(\frac{1}{3} \frac{E \operatorname{tg} \beta}{Y} \right) \right] \quad (6)$$

where β – angle between the cone generatrix and the base surface ($\beta = \frac{\pi}{2} - \alpha$). At the same time $r=a$ and $dc/da = c/a = \text{const}$.

From expression (6) it is evident that the hydrostatic pressure under the indenter is a function of the dimensionless variable $E \operatorname{tg} \beta / Y$, which can be interpreted as the ratio of the deformation caused by the indenter ($\operatorname{tg} \beta$) to the elastic deformability of the material (Y/E). In the case of a spherical indenter, it can be assumed that $\operatorname{tg} \beta \approx \sin \beta = a/R$; the value of this ratio changes during penetration.

The penetration pressure under conditions of purely elastic, elastic-plastic and completely plastic states can be represented as a graph of the dependence of the dimensionless quantity P_m/Y on $E^* \operatorname{tg} \beta / Y$, where "β" is the angle of inclination of the indenter profile to the undeformed surface of the base at the edge of the contact area (Figure 4). This figure is based on data from [5-8].

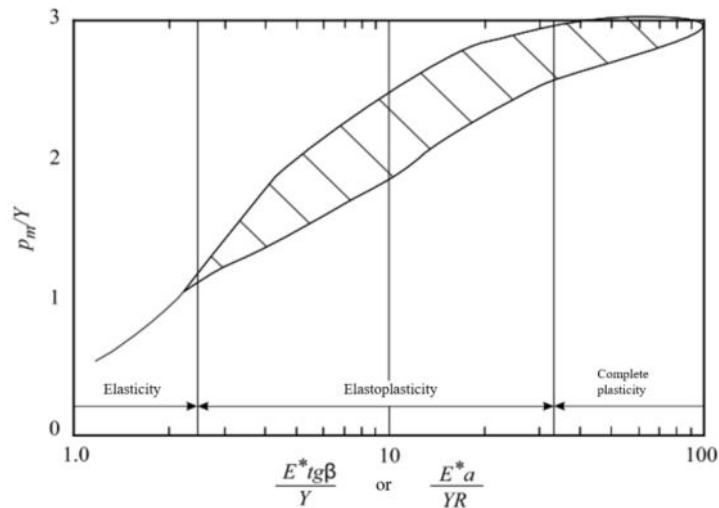


Fig.4. - Embedding of spheres and cones into an elastic-plastic half-space

The above results are valid for elastic-ideal-plastic bodies with a constant yield strength Y for uniaxial compression. Tabor [9] showed that the results for an ideal-plastic body can be applied with a good degree of approximation to bodies with hardening, for uniaxial compression upon reaching a deformation ϵ_R equal to $\epsilon_R = 0,2 \operatorname{tg} \beta$.

For the Vickers pyramid, from here we have $\epsilon_R \approx 0,07$. The theoretical calculations carried out are experimentally confirmed by the results of experiments carried out by Tabor and for a spherical indenter (Figure 5).

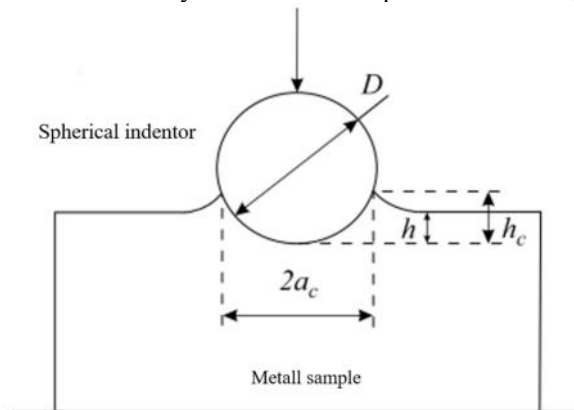


Fig.5. - Scheme of introduction of a spherical indenter

Following Meyer's work, which showed that the average contact pressure $P_m = K \left(\frac{a}{R} \right)^m$, Tabor proposed the concept of equivalent strain and stress. Based on Meyer's assumption that the index m is related to the strain hardening coefficient, Tabor assumed that the average pressure P_m in the state of full plasticity and the equivalent stress Y_r are proportional. The radius of the indentation a and the strain ϵ_r are also proportional:

$$\begin{aligned} Y_r &= \psi \frac{P}{\pi a^2}, \\ \epsilon_r &= \phi \frac{a}{R}. \end{aligned} \quad (7)$$

To test these expressions, Tabor [9] conducted experiments that confirmed their correctness and obtained the following values of the coefficients: $\psi = 2,8 - 3,2$, $\phi = 0,2$.

Thus, the obtained expressions allow us to conclude that when deforming a material with a spherical indenter, the value of the equivalent deformation is equal to $0.2 a/R$ (or $0.2 d/D$), and when indenting with a cone or pyramidal indenter, a constant deformation of about 7% will be created (when pressing in a Vickers pyramid).

2. Results

The results of calculating the pre-impact velocity of the indenter, as well as the dimensions of the imprint on materials with a hardness corresponding to the upper and lower limits of the range under consideration, are given in Tables 1 and 2.

The data in Tables 1 and 2 show that indenters with both 1 mm and 2 mm diameters are suitable for assessing the physical and mechanical properties of cast iron. For both indenter diameters, it is possible to select the impact energy that ensures the achievement of the required imprint diameter d_{\min} . It should be noted that for an indenter with a diameter of 1 mm, the required value of $d = 450 \mu\text{m}$ at a hardness of 500 HBW is ensured at an impact energy of 22 mJ. At the same time, at a hardness of 100 HBW with the same energy, the d/D ratio is 0.649. This value slightly exceeds the limits of inequality (10), but such an excess is acceptable. Therefore, it can be assumed that for an indenter with a diameter of 1 mm, the maximum indentation diameter at a hardness of 500 HBW is 450 μm . Using an indenter with a diameter of 2 mm allows increasing the indentation diameter on hard materials from 450 μm to 500 μm . However, this reduces the indentation depth by 40% (from 53.5 μm to 31.8 μm at a material hardness of 500 HBW and from 119.6 μm to 71 μm at a material hardness of 100 HBW). Since a decrease in the indentation depth will lead to an increase in the influence of the quality of the tested surface on the measurement results and, accordingly, will increase the labor intensity of preparing the product for testing, using an indenter with a diameter of 2 mm is impractical.

Table 1 - Calculation results for an indenter diameter of 1 mm

Hardness of material HBW	Diameter of the imprint $d, \mu\text{m}$	d/D	Depth of imprint $h_c, \mu\text{m}$	Impact energy, mJ	Pre-impact velocity $V_{\max}, \text{m/s}$
500	500	0,5	67,0	34,6	3,7
	450	0,45	53,5	22,0	3,0
	400	0,4	41,7	13,4	2,3
100	714	0,71	150,0	34,6	3,7
	649	0,65	119,6	22,0	3,0
	582	0,58	93,3	13,4	2,3

Table 2 - Calculation results for an indenter diameter of 2 mm

Hardness of material HBW	Diameter of the imprint $d, \mu\text{m}$	d/D	Depth of imprint $h_c, \mu\text{m}$	Impact energy, mJ	Pre-impact Velocity $V_{\max}, \text{m/s}$
500	500	0,25	31,8	15,5	2,5
	450	0,225	25,6	10,1	2,0
	400	0,2	20,2	6,3	1,6
100	740	0,37	71,0	15,5	2,5
	667	0,33	57,3	10,1	2,0
	594	0,3	45,2	6,3	1,6

At the same time, the use of indenters with a diameter in the range from 1 to 2 mm is of considerable interest. Unlike static hardness testers, this possibility is provided by portable devices implementing the dynamic indentation method: without being tied to standard diameters, it is possible to manufacture an indenter with any dimensions. Calculation of the pre-impact velocity of the indenter, as well as the dimensions of the imprint for nine variants of the indenter diameter (1.1; 1.2; ... 1.9 mm) showed that the optimal option is to use an indenter with a diameter of 1.2 mm and a pre-impact velocity of 3 m/s. The results of the corresponding calculations are given in Table 3.

Table 3 – Calculation results for indenter diameter $D=1.2 \text{ mm}$

Hardness of material HBW	Diameter of the imprint $d, \mu\text{m}$	d/D	Depth of imprint $h_c, \mu\text{m}$	Impact energy, mJ	Pre-impact Velocity $V_{\max}, \text{m/s}$
500	480	0,4	50,1	23,2	3,0
100	698	0,58	112,0		

Comparing Tables 1.1 and 1.3, we can draw the following conclusions. Increasing the indenter diameter from 1 mm to 1.2 mm allows, at the same value of the pre-impact velocity, to increase the indentation diameter on hard materials from 450 μm to 480 μm . In this case, the ratio d/D does not exceed the limits of inequality (10), and the indentation depth decreases by only 6% (from 53.5 μm to 50.1 μm for a material hardness of 500 HBW and from 119.6 μm to 112 μm for a material hardness of 100 HBW).

material hardness of 100 HBW). Thus, as a result of the analysis, it was established that the following indenter parameters are optimal for assessing the physical and mechanical properties of cast iron using the dynamic indentation method: weight - 5 g, diameter - 1.2 mm, pre-impact velocity - 3 m/s.

3. Discussion

In order to objectively characterize cast iron, one more condition must be met: the material must be in a state of complete plasticity. If this condition is met for a pyramid, then for a spherical indenter this means that the deformation must be in the range of $0.04 < \varepsilon_r < 0.12$, then the radius of the indentation must be $0.2R < a < 0.6R$. In this case, the dependence of the average contact pressure on the applied force will take on a virtually constant value (Figure 6), which will allow us to further exclude the influence of the deformation value on the measured characteristics and take into account only the influence of the loading dynamics (deformation rate).

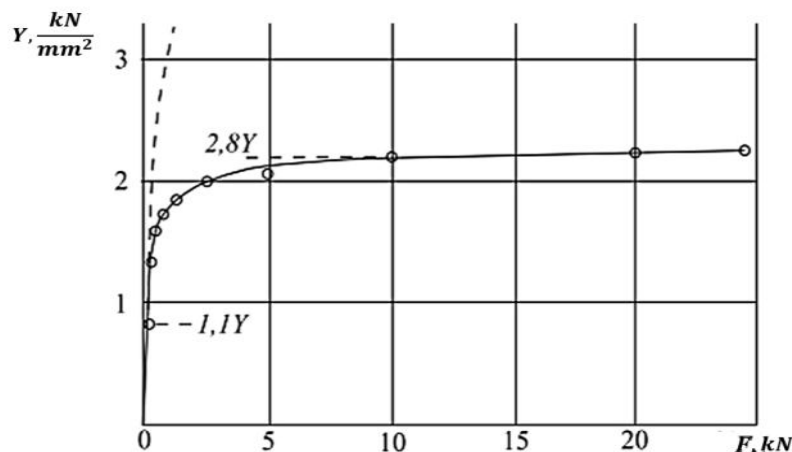


Fig. 6 - Dependence of average contact pressure on indentation force

The choice of the loading scheme for the studied cast irons with a hardness from 100 to 500 HBW consists of selecting the diameter of the spherical indenter D and the pre-impact speed of the indenter V_{\max} , upon reaching which the diameter of the imprint will correspond to the minimum sufficient size of the deformation region (let us designate this diameter of the imprint as d_{\min}). In addition, as established earlier, when measuring the physical and mechanical characteristics, the diameter of the imprint should be within the limits in the entire range of hardnesses of the tested cast irons:

$$0,2D < d < 0,6D \quad (8)$$

The value of the pre-impact velocity of the indenter V_{\max} , necessary to achieve the minimum sufficient diameter of the indentation d_{\min} , can be determined from the law of conservation of energy, equating the kinetic energy of the falling indenter W_k and the energy of deformation of the material by the indenter W_d . The kinetic energy of the indenter of mass m is calculated using the formula:

$$W_k = \frac{1}{2} m V_{\max}^2. \quad (9)$$

The energy of deformation of the material during indentation is determined by integrating the dependence of the contact force on the depth of the indentation, which can be taken as linear in the first approximation:

$$W_d = \int_0^{h_c} P dh = \frac{1}{2} P_{\max} h_c, \quad (10)$$

where h_c is the depth of the indentation, P_{\max} is the maximum contact force.

The formula for determining the pre-impact velocity of the indenter obtained from expressions (8) and (9) is as follows:

$$V_{\max} = \sqrt{\frac{P_{\max} h_c}{m}}. \quad (11)$$

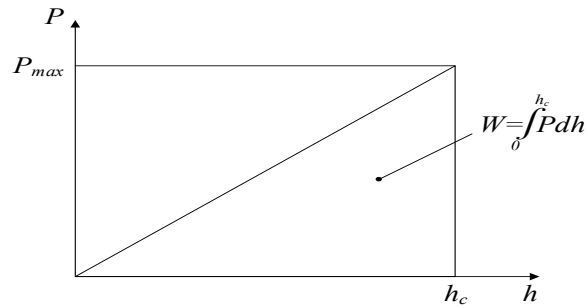


Fig.7 – Dependence of contact force on indentation depth

The depth of the indentation h_c can be determined through its diameter d from the equation obtained based on the indentation diagram (Figure 5) and given in STB ISO 6506-1-2022 “Metallic materials. Brinell hardness measurement. Part 1. Measurement method”:

$$h_c = \frac{D}{2} \left(1 - \sqrt{1 - \frac{d^2}{D^2}} \right). \quad (12)$$

STB ISO 6506-1 establishes the relationship between the hardness of the test material HBW, the applied (contact) force F and the indentation diameter d :

$$HBW = 0,102 \frac{2P}{\pi D^2 \left(1 - \sqrt{1 - \frac{d^2}{D^2}} \right)}. \quad (13)$$

Having solved this equation for the contact force, we obtain the value of the maximum contact force P at which the indentation diameter d on materials with different hardness reaches the required value (d_{\min})

$$P_{\max} = \frac{HBW \cdot \pi D^2 \left(1 - \sqrt{1 - \frac{d^2}{D^2}} \right)}{0,102 \cdot 2}. \quad (14)$$

As is known, with an increase in the hardness of the test material, the size of the imprint on its surface decreases (under the same impact conditions). Therefore, first of all, it is necessary to determine, based on the obtained equations, the impact energy and pre-impact velocity required to create a minimum sufficient imprint diameter d_{\min} on products with a hardness corresponding to the upper limit of the range under consideration (500 HBW). Then, based on the impact energy obtained for this hardness, it is necessary to calculate the actual imprint diameter d on a material with a hardness corresponding to the lower limit of the range under consideration (100 HBW), and check that this diameter corresponds to inequality (8).

Conclusions

The paper shows that sharp indenters in the form of a Vickers pyramid and a cone create a constant deformation, the value of which is determined by the angle at the apex and a constant coefficient, the determination of which is possible based on the results of comparative tensile-compression tests of the material. When indenting with a sphere, the deformation value is a variable value and depends on the ratio of the imprint diameter to the indenter diameter. It is shown that it is optimal to use an indenter with a diameter of ~ 1 mm and a mass of ~ 5 g when indenting cast iron, which allows achieving a deformation in the range of up to 0.04-0.12 and a deformation rate of 1000-3000 1/s. At the same time, sufficient sensitivity to changes in mechanical characteristics under dynamic loads is ensured based on the size of graphite inclusions of no more than 500 μm .

References

- [1] Anisovich A.G., Andrushkevich A.A. Microstructures of ferrous and non-ferrous metals. - Minsk: Belarusian Science, - 131 p. (2015)
- [2] Johnson KL. Contact Mechanics. // Cambridge: Cambridge University Press. – P. 448-452. (1985)
- [3] Boris Galanov, Sergei Ivanov, Valeriy Kartuzov. Improved core model of the indentation for the experimental determination // Mechanics of Materials, Volume 150. (November 2020, 103545)
- [4] Houlsby, Guy T., and Alexander M. Puzrin. Advanced Plasticity Theories. Springer London, 2007.
- [5] A.Kren, M. Delendik, A. Machikhin. Non-destructive evaluation of metal plasticity using a single impact microindentation // International Journal of Impact Engineering. – 2022– V.162. – P. 104141.
- [6] Kral, E. R., K. Komvopoulos, and D. B. Bogy. "Elastic-plastic finite element analysis of repeated indentation of a half-space by a rigid sphere." (1993): 829-841.
- [7] Richmond O., Morrison H. L., Devenpeck M. L. Sphere indentation with application to the Brinell hardness test. // Internat. J. Mech. Sci. № 16. – P. 75. (1974)

- [8] A.P.Kren, A.S. Machikhin, A.Y. Marchenkov Impact indentation of metals in the transition region from the elastic to plastic state // Journal of Materials Science. – 2023. – № 58. – P. 961–970.
- [9] Urazbayev, T., Tursunov, N., & Tursunov, T. (2024, March). Steel modification modes for improving the cast parts quality of the rolling stock couplers. In AIP Conference Proceedings (Vol. 3045, No. 1). AIP Publishing.
- [10] Mamaev, S., Anna, A., Tursunov, S., Nigmatova, D., & Tursunov, T. (2023). Mathematical modeling of torsional vibrations of the wheel-motor unit of mains diesel locomotive UZTE16M. In E3S Web of Conferences (Vol. 401, p. 05014). EDP Sciences.
- [11] Makhkamov, N. Y., Yusupov, G. U., Tursunov, T., & Djalilov, K. (2020, December). Properties of metal-based and nonmetal-based composite materials: A brief review. In IOP Conference Series: Earth and Environmental Science (Vol. 614, No. 1, p. 012068). IOP Publishing.
- [12] Turakulov M., Tursunov N., Yunusov S. Steeling of synthetic cast iron in induction crucible furnace taking into account consumption rate of carburizers”, E3S Web of Conferences 401, 05012 (2023). <https://doi.org/10.1051/e3sconf/202340105012>.
- [13] Tokhir Tursunov, Nodirjon Tursunov and Talgat Urazbayev, “Investigation of heat exchange processes in the lining of induction furnaces”, E3S Web of Conferences 401, 05029 (2023). <https://doi.org/10.1051/e3sconf/202340105029>.
- [14] Turakulov M., Tursunov N., Yunusov S. New concept of cast iron melting technology in induction crucible furnace, E3S Web of Conferences 401, 01060 (2023). <https://doi.org/10.1051/e3sconf/202340101060>.
- [15] Toirov O., Tursunov N. Efficiency of using heat-insulating mixtures to reduce defects of critical parts”, E3S Web of Conferences 401, 05018 (2023). <https://doi.org/10.1051/e3sconf/202340105018>.
- [16] Valieva D., Yunusov S., Tursunov N. Study of the operational properties of the bolster of a freight car bogie”, E3S Web of Conferences 401, 05017 (2023). <https://doi.org/10.1051/e3sconf/202340105017>.
- [17] Uchkun Rakhimov and Nodirjon Tursunov, “Development of technology for high-strength cast iron for manufacturing D49 head of cylinder”, E3S Web of Conferences 401, 05013 (2023). <https://doi.org/10.1051/e3sconf/202340105013>.
- [18] Suyunbayev, S., Khudayberganov, S., Jumayev, S., & Bashirova, A. (2024). Digital design trends of train and shunting operations at railway stations. In E3S Web of Conferences (Vol. 549, p. 04001). EDP Sciences. <https://doi.org/10.1051/e3sconf/202454904001>
- [19] Jumayev S., Suyunbayev S., Sultanov T., Akhmedova M., Toxtakxodjaeva M. (2024). Enhancement of local traffic management systems using information technology. In E3S Web of Conferences (Vol. 583, p. 07016). EDP Sciences. <https://doi.org/10.1051/e3sconf/202458307016>
- [20] Suyunbayev S., Khusenov U., Khudayberganov S. Sherzod Jumayev and Shokhruxh Kayumov. Improving use of shunting locomotives based on changes in infrastructure of railway station 05011 DOI: <https://doi.org/10.1051/e3sconf/202336505011>
- [21] Fayzibaev, S., Ignatenko, O., & Urazbaev, T. (2021). Development of binding based on B-N-Ti-Al system compounds for creating a composite instrumental material for a final raining of railway parts. E3S Web of Conferences, 264. <https://doi.org/10.1051/e3sconf/202126404073>
- [22] Fayzibaev S., Ignatenko O., Mamayev S., Urazbayev T., Nafasov, J. (2024). Development of a technique for the formation of Ti-Al system compounds under the influence of high pressures and temperatures. AIP Conference Proceedings, 3045(1). <https://doi.org/10.1063/5.0197358>
- [23] Fayzibaev, S., Ignatenko, O., Urazbaev, T., Mamayev, S., & Nafasov, J. (2023). Development of technology for formation of Al-B-N system joints under influence of high pressures and temperatures to create composite tool material. E3S Web of Conferences, 401. <https://doi.org/10.1051/e3sconf/202340105016>
- [24] Rakhimov U.T., Tursunov N.K., Tursunov S.E. Improvement of production technology for spheroidal graphite cast iron with increased strength”, AIP Conf. Proc. 3045, 060024 (2024). <https://doi.org/10.1063/5.0197475>.

Information of the authors

Tursunov Tokhir Muratovich, PhD, associate professor, Tashkent State Transport University
e-mail: t.tursunov87@gmail.com

Tursunov Nodirjon Kayumjonovich, DSc, professor, Tashkent State Transport University
e-mail: u_nadir@mail.ru

Kren Alexander Petrovich, DSc, professor, State Scientific Institution «Institute of Applied Physics of the National Academy of Sciences of Belarus»
e-mail: alekspk@mail.ru

Urazbaev Talgat Tileubaevich, PhD, associate professor, Tashkent State Transport University
e-mail: talgat_1988.26@mail.ru

Ziyamukhamedova Umida Alijonovna, DSc, professor, Tashkent State Transport University
e-mail: z.umida1973@yandex.ru

Investigation of Strength of Belt Conveyor Roller Bearing Shells

Yurchenko V.V., Smagulov A.S., Reshetnikova O.S., Zharkevich O.M.*, Mussayev M.M.

Abylkas Saginov Karaganda Technical University, Karaganda, Kazakhstan

*corresponding author

Abstract. The article is devoted to the study of the characteristics of a sand-polymer composite (SPC) and a comparison of its strength properties with those of a traditional structural material, St10 steel, using the example of a roller support shell for a belt conveyor. Numerical modeling using the finite element method was used to evaluate the stress-strain state of the structure. It was found that the proposed sand-polymer composite provides a sufficient level of strength, with maximum stresses in the part reaching 7.3 MPa, which does not exceed the material's yield strength of 30 MPa. The minimum safety factor for the SPC shell was 3.216, which is 3.2 times higher than the standard. The maximum displacement at the point of load application for the SPC shell was 0.1645 mm. Compared to the steel counterpart (St10), which has maximum stresses of 3.2 MPa and a safety factor of 9.6, the sand-polymer composite reduces the weight of the product by 3.5 times (the weight of the SPC shell is 1.73 kg, while that of the St10 steel shell is 6.185 kg). The results obtained confirm the feasibility of using sand-polymer material to optimize roller bearing designs, providing the required strength characteristics at a lower weight, as well as economic efficiency due to the lower cost of the material.

Keywords: shell, sand-polymer composite, stress-strain state, safety factor

Introduction

Belt conveyors are widely used in various industries for transporting bulk materials [1]. One of the key components of a conveyor is the roller support, which provides support and guides the movement of the conveyor belt [2]. The efficiency of the conveyor largely depends on the reliability and durability of the roller supports, and therefore on the strength of their main elements, in particular the shell.

The shell of the roller support absorbs significant loads arising during operation, including the weight of the transported cargo, dynamic impacts, and vibrations [2]. A violation of the strength of the shell can lead to roller failure, increased resistance to belt movement, and, as a result, to the shutdown of the entire conveyor line. The shell forms the outer surface of the roller that contacts the conveyor belt. It must be strong and rigid enough to withstand significant loads from the transported material and the weight of the belt itself, preventing deformation of the roller. This ensures even load distribution across the entire width of the belt. The shell serves as a protective cover for the bearings and roller axle. It prevents dust, dirt, moisture, and abrasive particles from entering the mechanism, which could cause premature wear and failure of the bearings.

Various materials are used to manufacture shells, such as cast iron, pressed or stamped steel, and polymer composite materials [3, 4, 5]. The use of metal shells for roller supports in conveyor systems has a number of disadvantages. First, metal shells are susceptible to corrosion under the influence of climatic factors, which reduces the service life of the product [6]. Second, metal shells are significantly heavier than similar products made of polymer materials, which can create additional loads on the structure [7]. Third, the vibration that happens when the conveyor is running leads to increased wear on both the bearings and the metal roller shafts because of friction [8, 9]. Although polymer composites have a good strength-to-weight ratio, they may be inferior to metals in terms of absolute strength and stiffness [10, 11].

The physical and mechanical properties of the roller bearing shell determine its ability to perform its intended function, taking into account its durability. Tensile strength and yield strength determine the shell's ability to withstand axial and radial loads without failure or residual deformation. The hardness of the material used is important for resistance to abrasive wear from the conveyor belt and the material being transported. High hardness contributes to increased service life. Fatigue strength determines the ability of the material to withstand repeated cyclic loads without failure. Rollers are constantly subjected to cyclic loads from the weight of the belt and cargo.

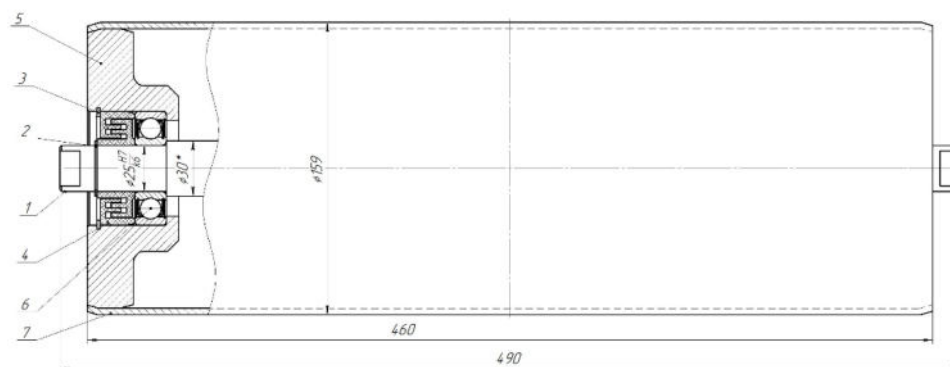
As a result, consumers, when choosing the material for roller bearings, are forced to find a balance between the advantages and disadvantages of each option, since there is no ideal solution at the moment.

Currently, there are a number of methods for assessing the strength of metal-polymer conveyor rollers based on FEM analysis [12-14]. Research is focused on creating new, more reliable and durable roller support designs that can withstand increasing loads and operate in aggressive environments. Other studies [15, 16] describe the developed mathematical models of stress-strain state based on a system of differential equations, taking into account the geometric parameters of the roller, deflection, and load pressure. Works [17-19] consider the optimization of conveyor rollers according to various criteria.

In this regard, the specific purpose of this article is to study the strength characteristics of roller support shells made of different materials, analyze the stress-strain state, and identify factors affecting its reliability. Conducting such studies allows optimizing the design of the roller support, increasing its service life, and minimizing the risk of accidents.

1. Materials and methods

The object of the study is the roller support shell of a belt conveyor (Figure 1), which bears the load from the belt and the transported material.



1 – shaft; 2,3 – retaining rings; 4 – labyrinth seal; 5 – bearing assembly housing; 6 – bearing; 7 – side plate

Fig. 1. – General view of a belt conveyor roller

The criterion for optimizing the shell when selecting material using the Davison-Fletcher-Powell method is determined by the formula [20, 21]:

$$F = \frac{m}{m_0} + V \sum_{i=1}^n \frac{1}{\varphi_i}, \tag{1}$$

where $\varphi_i = (1/(1 - g_i))$ - penalty functions;

g_i - restrictions;

V – construction volume;

m_0 - initial mass of the structure;

m - final mass of the structure.

The optimal design solution when selecting material for a belt conveyor shell is determined by criteria such as efficiency F (shell mass) and quality g_0 (shell strength). In this case, the quality function is the dependence of mass on strength: $\Phi = g_0(F)$

The shell design will be considered optimal if $F(x) \rightarrow \min$; $g(x) = g_0$.

Furthermore, $F(x)$ and $g(x)$ are given functions of the design variables. Constraints are formed on the safety factor. ($n \geq 1.6$) [22].

The materials selected for testing were St10 carbon steel, which is most commonly used in the manufacture of shells, and an experimental sand-polymer composite (SPC – 60 wt% quartz), as shown in Table 1.

Table 1. Physical and mechanical properties of bearing unit housing materials

Parametr	Sand-polymer composite (SPC – 60 wt% quartz)	Steel St10 (GOST 1050-2013)
Yield strength, MPa	30	200
Ultimate tensile strength, MPa	80	325
Modulus of elasticity, GPa	5	215
Poisson's ratio	0,25	0,3
Density, kg/m ³	2200	7800

To study the load characteristics of the roller bearing shell made of PPC [23], a static analysis was performed in APM FEM, including the following steps:

- creation of a 3D model of the roller bearing;
- assignment of physical and mechanical properties to parts (Table 1);
- selection of the fastening type. In this case, “Roller support” and “Fixed hinge” were selected for fastening (Figure 2);
- setting the load.

The pressure of bulk cargo on the horizontal section of the belt can be calculated as hydrostatic, then the normal force applied to this section is equal to [24].

$$N = 0,5 \cdot l_{on} \cdot l_p \cdot p \left[2 \cdot l_r \cdot \sin \alpha + \left(b - \frac{l_p^2}{12 \cdot b_c} \right) \cdot \operatorname{tg} \varphi_H \right], \tag{2}$$

where l_{on} – distance between roller supports;

$l_p = K_p \cdot B$ – conveyor belt width;

$K_p = 0,39$ – proportionality coefficient;

B – conveyor belt width;

φ_n – The angle of repose of the load or the angle of natural slope when moving on the belt depends on φ – the angle of natural slope for the state of rest..

Based on formula (1), a force N equal to 4000 N was set as the external load.

- creation of a mesh with the smallest elements set to 1.5 mm and 0.5 mm, respectively, on the edges at the point of load application and the point of attachment of the roller support shaft (Figure 3);

- calculation and analysis of results.

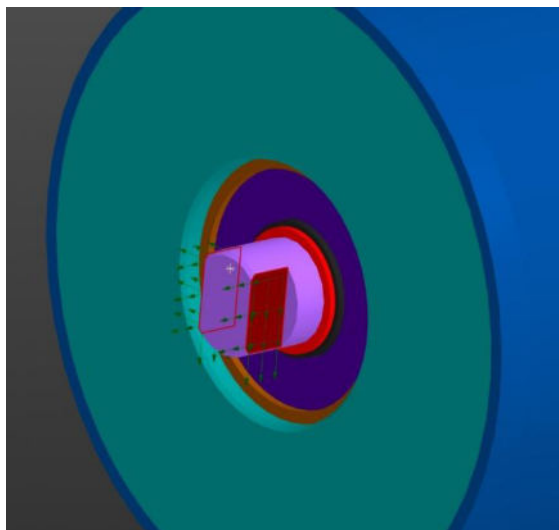


Fig. 2. – Selecting a fastener

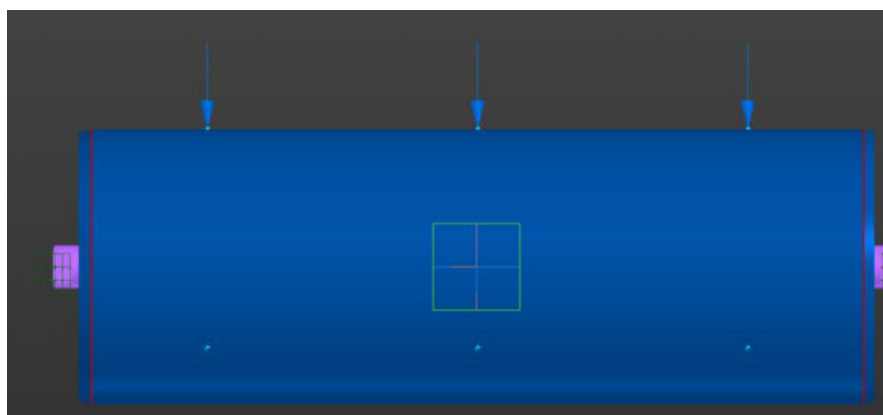


Fig. 3. – Load assignment

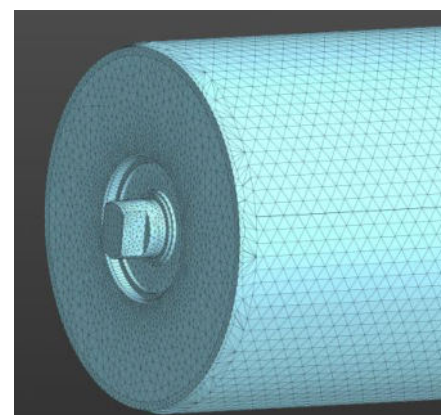


Fig. 4. – Creating a grid

2. Results and discussion

The results of the static calculation are presented in the form of diagrams in Figures 4-7.

Analysis of the figures allows us to note the following:

- the maximum displacement at the point of load application was 0.1645 mm (Figure 8);
- the stresses obtained in the part do not exceed the yield strength of the material, which is 30 MPa;
- the maximum stresses are concentrated on the shaft and amount to 7.3 MPa (Figure 5);
- the minimum safety factor of the polymer $k_s = 4.503$ (Figure 7);

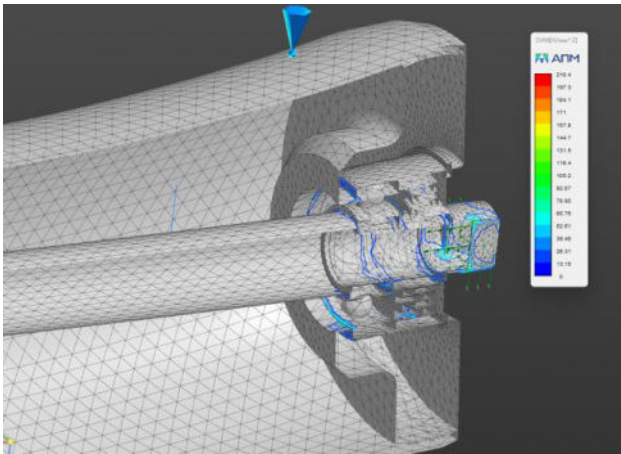


Fig. 5. – Equivalent stress according to Mises for a shell made of SPC

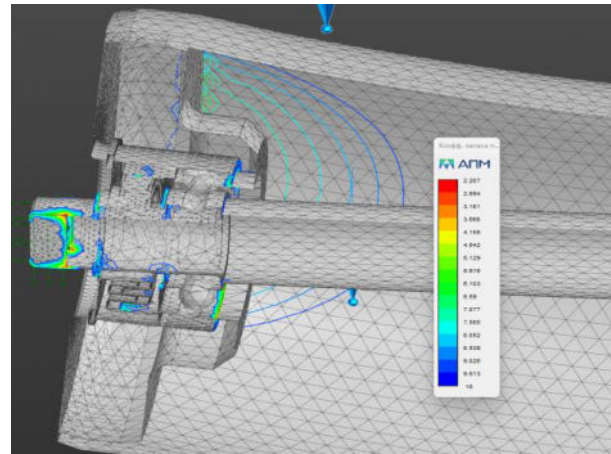


Fig. 6. – Yield strength safety factor for SPC shell

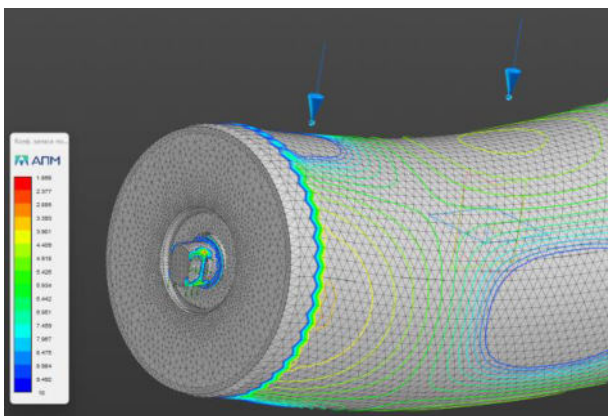


Fig. 7. – Fatigue strength safety factor for a shell made of SPC

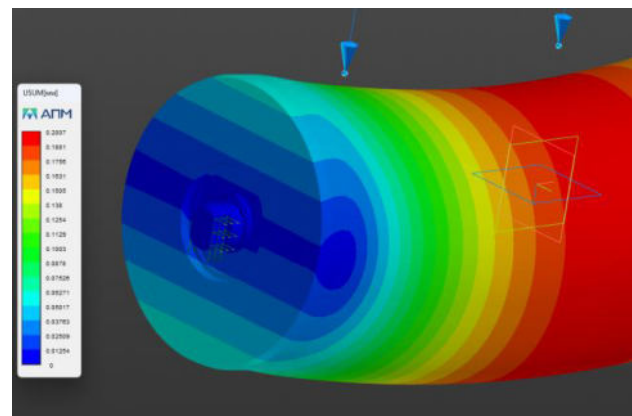


Fig. 8. – Total linear displacement for a shell made of SPC

For comparison purposes, calculations were performed for a roller bearing shell made of St10 steel. The results of the comparison of the strength characteristics and mass of the bearing assembly housing made of SPC and St10 are shown in Table 2.

Table 2. Strength characteristics of roller bearing shells made from different materials

Parametr	SPC	St10
Maximum displacement, mm	0.1645	0.01283
Maximum stresses, MPa	7.3	3.2
Safety factor	3.216	9.6
Weight, kg	1.73	6.185

Table 2 shows that the safety factor is maintained for both steel and SPC shells. At the same time, the safety factor for the sand-polymer composite shell is 3.2 times higher than the standard, and the safety factor for the steel shell is 9.6 times higher. This indicates that parts made from both materials are not overloaded. However, taking into account the efficiency F (mass) and quality g_0 (strength), as well as the cost of materials, it is recommended to use sand-polymer composites for the manufacture of shells.

Conclusions

The following results were obtained as a result of the research conducted:

1) Numerical modeling using the finite element method showed that the maximum displacements for the SPC shell were 0.1645 mm, and the maximum stresses were 7.3 MPa, which does not exceed the yield strength of the material (30 MPa). For the steel shell, the maximum displacements were 0.01283 mm, and the maximum stresses were 3.2 MPa;

2) The safety factor for the PPC shell was 3.216, which is more than 3.2 times higher than the standard value. For the steel shell, this indicator was significantly higher – 9.6. Despite the fact that steel has a higher safety factor, this indicates that the design made of both materials is not overloaded;

3) An important result of the study is the confirmation of the feasibility of using sand-polymer composite to optimize roller bearing designs. The use of SPC reduces the weight of the product by 3.5 times compared to its steel

counterpart. In addition, sand-polymer composite increases the corrosion resistance of the product, which is a significant advantage, since metal shells are susceptible to corrosion under the influence of climatic factors. The use of SPC also contributes to economic efficiency due to the lower cost of the material;

4) Both sand-polymer composite (SPC) and steel are suitable for the manufacture of belt conveyor roller bearings in terms of strength characteristics;

5) It is recommended to use sand-polymer composite (SPC) for the manufacture of belt conveyor roller shells, which, with a lower product weight, provides the required strength characteristics, as well as economic efficiency achieved due to the lower cost of SPC.

Acknowledgment

This research is funded by the Science Committee of the Ministry of Science and Higher Education of the Republic of Kazakhstan (grant AP19680121 "Development of compositions of sand-polymer composite materials and technological support for their processing into products for mechanical engineering").

References

- [1] Eshonkulov K.E., Matkasimova Sh. Design analysis of bearing units of conveyor rollers //Science and Education" Scientific Journal, 2024, Volume 5, Issue 6. – P. 87 - 95
- [2] Alharbi F., Luo S., Zhang H., Shaikat K., Yang G., Wheeler C.A., Chen Z. A Brief Review of Acoustic and Vibration Signal-Based Fault Detection for Belt Conveyor Idlers Using Machine Learning Models //Sensors 2023, 23, 1902.
- [3] Freyberger S., Benke S., Quade H., Rudnizki J. Chapter 12: Test Case Stainless Steel Bearing Housing, 15 April, 2012 <https://doi.org/10.1002/9783527646098.ch12>
- [4] Aubakirov D., Issagulov A., Kvon S., Kulikov V., Chsherbakova Y., Arinova S. Modifying Effect of a New Boron-Barium Ferroalloy on the Wear Resistance of Low-Chromium Cast Iron //Metals, 2022, 12(7), 1153
- [5] Jacques L., Dawson S., Hazotte A. Cast Iron: A Historical and Green Material Worthy of Continuous //Research International Journal of Technology 12(6), 2021, 1123-1138
- [6] Vasić M., Stojanović B., Blagojević M. Failure analysis of idler roller bearings in belt conveyors //Engineering Failure Analysis, 117, 2020, 104898. – P. 1 – 9
- [7] Nikonova T.Y., Zhetessova G.S., Zharkevich O.M., Skaskevich A.A., Ctrekal' N.D. O vozmozhnosti primeneniya peschano-polimernykh kompozitsionnykh materialov v izdeliyakh mashinostroitel'nogo naznacheniya // Vestnik YENU imeni L.N. Gumileva. Seriya tekhnicheskoye nauki i tekhnologii, 2023, 3, 89-99
- [8] Zimroz R., Król R. Failure analysis of belt conveyor systems for condition monitoring purposes //Politechnika Wroclawska, N 36, 2009. – P. 255 - 270
- [9] Rajak D.K., Pagar D.D., Menezes P.L., Linul E. Fiber-Reinforced Polymer Composites: Manufacturing, Properties, and Applications //Polymers, 2019, 11, 1667
- [10] Kamarudin S.H., Mohd Basri M.S., Rayung, M., Abu F., Ahmad S., Norizan M.N., Osman, S., Sarifuddin N., Desa M.S.Z.M., Abdullah, U.H., et al. A Review on Natural Fiber Reinforced Polymer Composites (NFRPC) for Sustainable Industrial Applications //Polymers 2022, 14, 3698.
- [12] Ceniz J.P., Martins R.S., Luersen M.A., Cousseau T. Structural Optimization of Metal and Polymer Ore Conveyor Belt Rollers //Computer Modeling in Engineering & Sciences, 2022, vol.133, no.3
- [13] Auezova A., Buzauova T., Abdugaliyeva G., Kurmangaliyeva L., Smagulova N., Zhauyt A. Investigation of the stress-strain state of the roller conveyor //Metalurgija, 59, 2020, 2, 199-202
- [14] Wei W., Peng F., Li Y., Chen B., Xu Y., Wei Y. Optimization Design of Extrusion Roller of RP1814 Roller Press Based on ANSYS Workbench //Appl. Sci. 2021, 11(20), 9584
- [15] Guo Y., Wang F. Multi Body Dynamic Equations of Belt Conveyor and the Reasonable Starting Mode //Symmetry, 2020, 12(9), 1489
- [16] Düzenli A., Gül O. Stress Analysis of Belt Conveyor Roller Tube //5th International Conference on Applied Engineering and Natural Sciences, July 10-12, 2023, 659-663
- [17] Thonte N.C., Nagure S. M. Design, development and optimization of roller conveyor // IJNRD, Volume 7, Issue 8, 2022, 740-747
- [18] Nurmatov K., Khujakhmedova Kh. Valieva D. Erkinov S. Improvement of the belt conveyor structural elements using composite materials //Universum: technicheskie nauki, №5 (122), 2024, 63-67
- [19] Zharkevich O., Nikonova T., Gierz Ł., Berg A., Berg A., Zhunuspekov D. Warguła Ł., Łykowski, W. Fryczyński, K. Parametric Optimization of a New Gear Pump Casing Based on Weight Using a Finite Element Method // Applied Sciences (Switzerland), 2023, 13, 12154
- [20] N'yunt T.Z.Ch. Optimizatsiya parametrov konstruksii stoyek metallorzhushchikh stankov metodom balansa gradiyentov pri zadannoy zhestkosti // Izvestiya vysshikh ucheb. zavedeniy //Mashinostroyeniye, 2012, №1, 3-11.
- [21] Jorga C., Desrochers A., Smeesters C. Engineering Design from a Safety Perspective //Proceedings of the 2012 Canadian Engineering Education Association (CEEA12), Winnipeg, MB, Canada, 17–20 June 2012, 1–5.
- [22] Nurzhanova O., Zharkevich O., Berg A., Zhukova A., Mussayev M., Buzauova T., Abdugaliyeva G., Shakhatova A. Evaluation of the Structural Strength of a Prefabricated Milling Cutter with Replaceable inserts During Machining //Material and Mechanical Engineering Technology, №4, 2023, 10-17

[23] Zhetessova G., Yuchenko V., Nikonova T., Zharkevich O. The development of the computer-aided design system for production processes of component part machining for single-piece production and repair conditions // Journal of Applied Engineering Science, Vol. 17, No. 4, 2019, 599 - 609

[24] Liu X., Pang Y., Lodewijks G. Theoretical and experimental determination of the pressure distribution on a loaded conveyor belt // Measurement, 2015, 77, DOI: 10.1016/j.measurement.2015.08.041

Information of the authors

Yurchenko Vassiliy Viktorovich, PhD, acting associate professor, Abylkas Saginov Technical University
e-mail: juvv76@mail.ru

Smagulov Altai Sakenovich, doctoral student, Abylkas Saginov Technical University
e-mail: smagulovaltay@gmail.com

Reshetnikova Olga Stanislavovna, PhD, acting associate professor, Abylkas Saginov Technical University
e-mail: olga.reshetnikova.80@mail.ru

Zharkevich Olga Mikhailovna, c.t.s., professor, Abylkas Saginov Technical University
e-mail: zharkevich.o.m@gmail.com

Mussayev Medgat Muratovich, PhD, associate professor, Abylkas Saginov Technical University
e-mail: m.mussayev@edu.ktu.kz

Composite Materials with Enhanced Abrasion Resistance and Certain Functional Characteristics Based on Thermoplastics

Rakhmatov M. *, Riskulov A., Nurmetov K.

Tashkent State Transport University, Tashkent, Uzbekistan

*corresponding author

Abstract. The structure and composite materials formation technology with specified indicators of functional characteristics based on organic and inorganic binders are investigated. Composite materials with increased resistance and wear, water resistance, based on thermomechanically combined polyamide-polyethylene (PA6-PET) mixtures have been developed. The dependence of the composite material characteristics on the phase structure formed during the thermomechanical interaction of the mixture components is established. The resistance to cracking under load and the abrasion resistance of composites based on mixtures of "thermoplastics-thermoplastics", thermoplastics modified with highly dispersed fillers are investigated. It is established that the introduction of nanometer dispersion of active fillers into the mixture increases the strength and tribotechnical characteristics of composite materials due to the formation of physical crosslinking nodes. Modification of the Ultrafine diamond graphite (UFDG) increases the wear resistance of high-pressure polyethylene (HPPE) by 3 times, low-pressure polyethylene (LPPE) by 2 times, polypropylene (PP) by 3 times when rubbing along a web with fine abrasive grain. Composite materials with specified functional characteristics have been developed for the manufacture of new-generation gimbals gear parts.

Keywords: thermomechanically combined mixtures, thermoplastics-thermoplastics, highly dispersed fillers, strength, tribotechnical characteristics, cardan transmission, splined joints.

Introduction

Economic indicators of sustainable development of industrial enterprises are significantly determined by the use of high-tech technologies in the development and manufacture of engineering products. Modern designs of machines and mechanisms with increased requirements for operational life, optimal material, energy costs, ergonomic and environmental aspects have been developed using functional composite materials (tribotechnical, anticorrosive, structural), special methods of hardening working surfaces, thin-film coatings and multicomponent lubricants [21-24].

The optimal gimbals transmission according to the design solution and the materials used must function satisfactorily during the entire service life due to the technical conditions. It must have a twisting strength that ensures the transmission of torque without destroying the structure. Universal hinges have a certain bearing arrangement, in which the transmission of torque is carried out at specified speeds and angles under the influence of various operational factors.

The shaft splined joints, acting as a means of axial displacement compensation, provide a predetermined transmission response to the driving conditions of the vehicle or unit. The dimensions of the gimbals transmission must have optimal proportions to reduce the adverse effects of dynamic loads resulting from the action of inertial forces and vibrations. Thus, a specific feature of cardan gears as tribotechnical systems is the need to systematically take into account the entire variety of operational factors when developing an optimal design with specified durability parameters.

Researches of hinge assemblies and spline joints of cardan gears of various machines and mechanisms used in modern automotive and agricultural machinery have allowed us to establish the characteristic features of their wear.

The prevailing type of wear in compliance with the requirements for the operation of cardan gears is corrosion-mechanical, due to the combination of operational factors characteristic of this tribosystem: the presence of high contact stresses, the alternating nature of the movement of individual parts of the structure, the impact of vibrations, shock loads, abrasive particles and corrosive environments.

The aim of this work is to develop a composition for preparing composite materials for friction-bearing parts of a cardan shaft transmission with enhanced performance characteristics.

To achieve this aim, the following tasks have been identified:

- 1) Systematic analysis of the operational features of cardan transmissions and determination of design and materials science solutions;
- 2) Development of a technology for metalpolymer materials for parts of drives with improved operational characteristics.

1. Materials and methods

Products based on vulcanized rubbers are traditionally used for the manufacture of cardan gears operated under the influence of abrasive particles. However, due to the increase in service life of modern cardan gears, the durability of such products often does not meet the technical requirements. Therefore, it became necessary to develop modern abrasive-resistant materials with an increased operational resource [1, 14]. Of particular interest in this aspect are composite materials based on thermoplastics, which have a complex of enhanced characteristics and are processed into products by a progressive injection molding method [15, 25].

Composite tribotechnical materials are processed into products by injection molding on injection molding machines with screw plasticizer under technological conditions characteristic of the basic polyamide PA6.

Thermoplastics belonging to the class of polyolefin copolymers – ethylene and vinyl acetate copolymers (CEVA) with the content of acetate groups from 8 to 30% and polyurethanes (PU) of the type "Vitur", "Desmopan", polyurethane (TPU) and its regenerated waste were selected for research. The development of abrasive-resistant materials was carried out in two directions: by introducing active dispersed modifiers into the matrix, forming a quasi-cross-linked structure, and by introducing polymer modifiers that have a complex effect on the structure and properties of matrix polymers [2, 3]. Ultrafine carbon (Ultrafine diamond graphite – UFDG), dispersed vulcanizate particles (DSE), copolymer of formaldehyde with dioxolan (CFD), acrylic butadiene styrene (ABS) copolymer and its thermomechanically combined mixture with polyvinyl chloride at the ratio ABS were used as modifiers: Polyvinyl chloride (PVC) – 40:60. Modifiers were introduced by mixing with a granular matrix with subsequent processing by injection molding.

It is established that the effect of ultrafine carbon clusters on the abrasive resistance of polyolefins is extreme and is determined by the concentration of the modifier, the composition of the matrix and the dispersion of the abrasive. The maximum effect of abrasion resistance is observed with a modifier content in the range of 0.01-0.1 wt.% [4] - [6].

2. Results and discussion

Modification of the UFDG increases the wear resistance of high-pressure polyethylene (HPPE) by 3 times, low-pressure polyethylene (LPPE) by 2 times, polypropylene (PP) by 3 times when rubbing along a web with fine abrasive grain (Figure 1). The reason for this effect is the formation of a quasi-stitched structure with increased resistance to micro-cutting and plastic displacement.

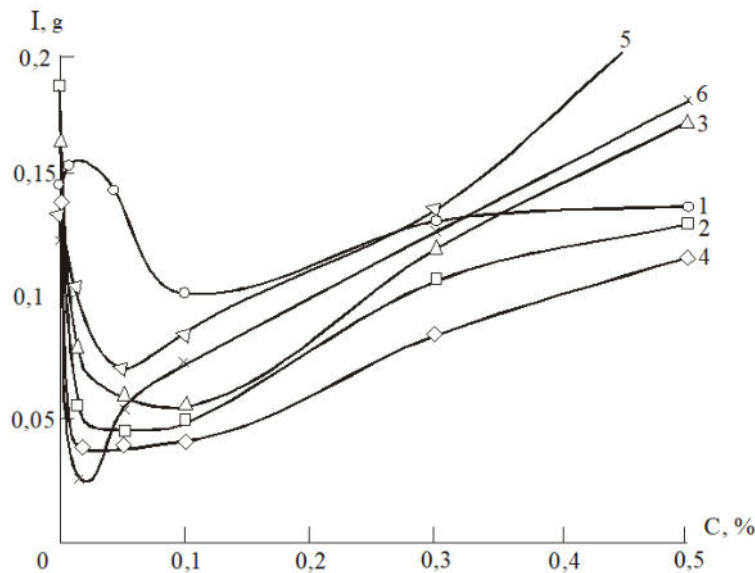


Fig. 1. - Dependence of polymers abrasive wear on the carbon charge content in the polymer binder: 1 – CEVA 11708-1250, 2 – CEVA 11306-075, 3 – CEVA 11607-040, 4 – HPPE 158, 5 – LPPE 277-03, 6 – PP 2102

The tribotechnical characteristics of the CEVA significantly depend on the content of vinyl acetate groups and the size of the abrasive particles (Figure 2). The greatest wear resistance when rubbing on a web with a fine abrasive grain has a copolymer of the CEVA 116, and when rubbing on a web with a large abrasive grain – the CEVA 113. When modifying the CEVA 117 with the UFDG, a non-monotonic dependence of the wear intensity on the filler content and the grain size of the abrasive are observed.

A composition containing 0.01-0.03% by weight of clusters has a higher wear resistance when rubbing on a fine-grained abrasive. When rubbing on coarse-grained abrasive, the amount of abrasive wear increases over the entire range of the modifier content. Obviously, the strength of the formed physical nodes of the crosslinking is insufficient to resist the processes of micro-cutting of large particles.

Compositions based on the CEVA 116 are most wear-resistant with a filler content of 0.01-0.05 wt% when rubbing on a cloth with a small grain and less wear-resistant when rubbing on a coarse-grained cloth.

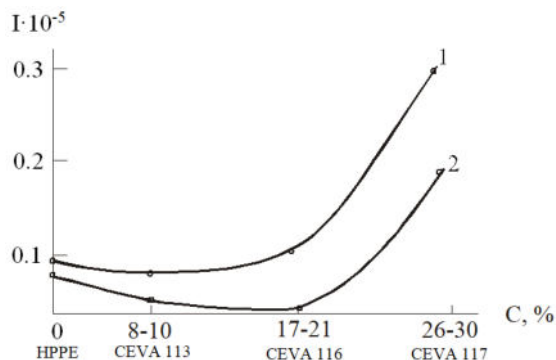


Fig. 2. - Dependence of specific wear (I) of the CEVA on the vinyl acetate groups content under abrasive friction conditions: 1 – coarse abrasive; 2 – fine-grained abrasive

Samples with a lower content of vinyl acetate groups (8-10%) have high wear resistance with a content of the UFDG in the range of 0.01-0.05 wt% when rubbing on an abrasive cloth with different grain sizes. The test results are correlated with these physical and mechanical tests.

As a result of the morphology analysis of the materials friction surfaces for researches, the features of their wear processes during friction on an abrasive cloth with a spilled size of single grains are established (Figure 3). The obtained microviews of samples of the CEVA-based thermoplastics exposed to an abrasive medium show characteristic differences between the friction surfaces of modified and raw materials.

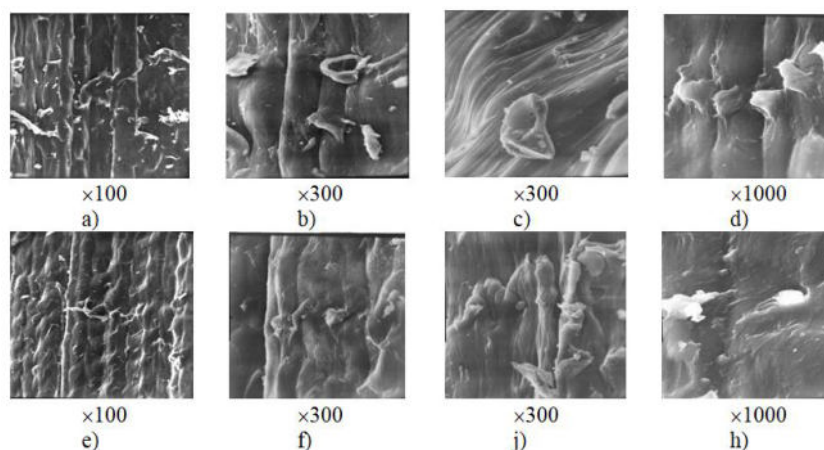


Fig. 3. - Micrographs of the original CEVA friction surface (a,b,c,d) and the modified UFDG (e,f,j,h) grades 113 (a,e), 116 (b,d,f,h) and 117 (c,j) with a modifier content of 0.01 (j,h) and 0.05 (e,f) wt.%

Thus, the friction surface of the starting materials is characterized by a more uniform arrangement of friction tracks resulting from micro-cutting and plastic deformation by abrasive particles of the surface layers of polymer materials (Figure 3). Micro-cutting tracks formed as a result of friction are characterized by a constant profile along the entire length. These features of abrasive wear are characteristic of the starting materials of all studied CEVA copolymers of all brands.

The nature of the abrasive wear processes of modified CEVA thermoplastics is determined by the filler concentration, the composition of the polymer molecule and the size of the abrasive particles. When exposed to an abrasive medium on the surface layer of CEVA-based materials containing 0.01-0.05 wt% UFDG, micro-cutting paths are formed, having an intermittent character. This is obviously due to the formation of labile physical crosslinking nodes in the volume of the polymer binder. The volumetric mesh of physical engagement nodes formed as a result of the adsorption interaction of dispersed UFDG particles with the active centers of macromolecules of the CEVA plays the role of physical obstacles to micro-cutting and plastic deformation of the surface layers of the polymer matrix during friction on the fixed abrasive, and also increases the intensity of intermolecular interaction of the matrix, as evidenced by an increase in its Shore A hardness by 2-3 units at the CEVA, 0.01-0.1 wt.% modified UFDG. An increase in the strength of the polymer matrix causes the formation of a "pile" in the friction zone of the polymer and the abrasive cloth, due to the difficult separation of abrasive wear products from the friction surface of the polymer. An increase in physical and mechanical characteristics according to [13, 19] leads to an increase in resistance to abrasive wear.

With a further increase in the content of the dispersed filler in the polymer binder (0.05 wt%), along with the formation of labile physical crosslinking nodes, agglomeration of UFDG cluster particles occurs. This causes an increase in defects and a decrease in the strength characteristics of modified thermoplastic elastomers. The data on the dependence of the abrasive wear of the CEVA modified by UFDG on the content of the modifier correlate well with the test results of the strength characteristics of these materials [9, 12].

A similar effect of increasing resistance to abrasive wear is also observed with the introduction of ultrafine modifiers in polyurethane thermoplastics such as "Desmopan", "Vitur" and PVC. Comparative tests have shown that compositions based on CEVA modified by UFDG can be used to manufacture friction parts such as seals and scrapers instead of similar products and modified vulcanizates and polyurethane (Figure 4).

It should be noted that the effect of increasing resistance to abrasive wear during modification of UFDG is observed at low filler concentrations (up to 0.05 wt%), while with the introduction of traditional fillers, a similar effect is characteristic of Al_2O_3 and TiO_2 content with particle dispersion up to 10 microns 5-25 wt%.

A high effect of increasing resistance and abrasive wear is also provided by the introduction of polymer modifiers into the polymer matrices during thermomechanical combination [16].

It is known that the doping of the polymer with polymer modifiers significantly improves the structural uniformity of the polymer, which is a continuous medium [1, 3]. If the alloying additive has a melting point higher than the matrix, its molecules, having less mobility during the formation of the structure of a continuous medium, are not able to fill in defective places, unlike additives having a melting point lower than the matrix [7, 8]. The mechanism of reinforcing action of such additives is due to the ability of molecules to be centers of crystallization of the matrix melt [11]. The excess and lack of such centers of structure formation worsens the structural uniformity of the base material. Obviously, the maximum increase in the strength characteristics of the combined mixture corresponds to the optimal concentration of the centers of structure formation. If the polymer additive has a melting point lower than the melting point of the matrix, then its more mobile molecules are displaced into the interlamellar regions, and the doping mechanism in this case is associated with filling defects in the interlamellar regions [10].

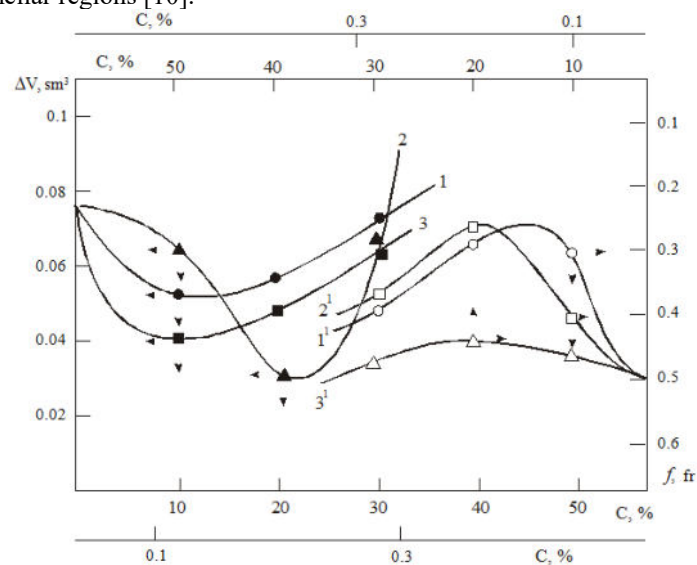


Fig. 4. - Dependence of volumetric wear and coefficient of friction on the content of Al_2O_3 (1 and 1') TiO_2 (2 and 2') and UFDG (3 and 3') in the CEVA 113 (wear and coefficient of friction values of thermoplastics "Desmopan")

A characteristic feature of thermomechanically combined polymer mixtures is their heterogeneity, the level of which depends on the quantitative ratio of the components. The melting of a pronounced alloying phase is preceded by a small (2-3 wt%) concentration interval in which the presence of an alloying additive cannot be detected by direct structural methods [17].

Analysis of the physical and mechanical characteristics of composite materials obtained by thermomechanical combination of binary mixtures of thermoplastics-thermoplastics (ABS-TPU, ABS-DST) with a mass ratio of components from 99.5:0.5 to 0.5:99.5 indicates a non-monotonic dependence of strength characteristics: tensile stress (σ_t), hardness (HB), impact strength (A) on the ratio of components in the composite material (Figures 6 and 7). The increase in strength with a low content of the modifier is a consequence of the reinforcement of the system with uniformly distributed aggregates of the dispersed phase. The effectiveness of such modification is apparently enhanced by interfacial interaction and the formation of transition layers and a copolymer phase.

The effect of strengthening polymers with small additives of thermodynamically incompatible polymer significantly depends on the sizes formed in the volume of the polymer matrix of aggregates. Thus, when aggregates are larger than 4 microns, there is no amplification effect, since aggregates with sizes larger than 4 microns do not have the ability to generate microcracks and dissipate destruction energies [19].

When modifying a relatively rigid thermoplastic polymer ABS with thermoelastoplasts DST and TPU, the thermoelastoplast aggregates are located in disordered (amorphous or defective) areas of the thermoplastic, increasing the mobility of the elements of the supramolecular structure. This leads to the acceleration of relaxation processes that contribute to the reduction of local stresses, and increase the strength and deformability of the base thermoplastics (ABS). The role of thermoelastoplast aggregates is to prevent the catastrophic spread of the resulting crack and to ensure the possibility of deformation of the thermoplastic matrix, leading to the formation of a neck. Due to the fact that the composite material contains a large number of thermoelastoplast aggregates, a large number of microcracks can be initiated

simultaneously instead of several cracks that can cause catastrophic destruction of the material [9]. Thus, in heterogeneous compositions, thermoelastoplast aggregates act as artificially created weak areas in the composition. Microcracks in such materials propagate along a broken curve from one aggregate of a dispersed particle to another. Such a specific structure of the composite leads to an improvement in the properties of the material, including strength.

The introduction of thermoplastic elastomer (TPU, DST-30) into the thermoplastic polymer ABS contributes to an increase in the impact strength of the composition (Figures 6 and 7), which is due to the occurrence of microcracks during the impact of the mesh, which differ from ordinary cracks leading to destruction generated by the thermoelastic aggregates evenly distributed in the volume of the matrix polymer. Along with this, the mechanism of the strengthening action of ABS by thermoelastoplast aggregates consists in their initiation of a larger number of localized places of plastic deformation of the matrix. This reduces the actual rate of transition of the polymer to the oriented state, reduces the power of heat generation and prevents rapid thermal destruction of the polymer [18].

The increased resistance to multiple deformations of combined composite materials "thermoplastics-thermoplastics" is explained by the ability of thermoplastics aggregates to reshape without destruction, contributing to the dissipation of deformation energy [15]. This is evidenced by a decrease in temperature in the sample volume in the inflection zone by 30-40 K compared to the base sample.

The reinforcing effect of polymer additives increases in the presence of a strong adhesive bond at the interface of the polymer matrix – modifier [19, 20].

With an increase in the content of the modifying additive – thermoplastic elastomer to 20%, its particles begin to aggregate, forming agglomerates of complex shape (Figure 5). With an increase in the content of the elastic phase, phase inversion occurs. This is evidenced by a sharp decrease in the hardness of the PA6 and CFD (Figures 6 and 7).

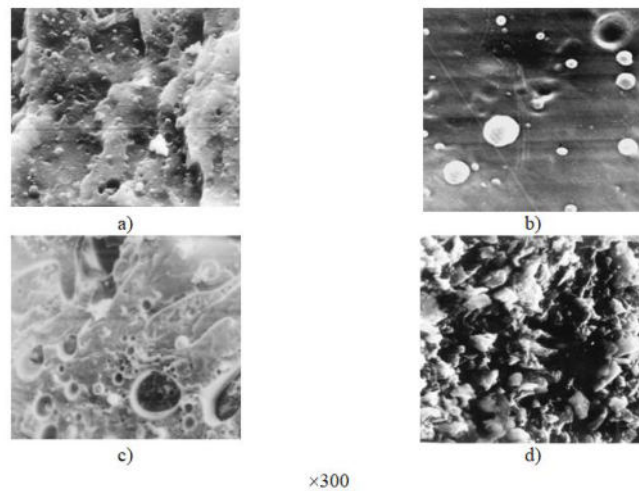


Fig. 5. - Morphology of chips in liquid nitrogen of the ABS+TPU composite materials with the TPU content of 99.5 wt.% (a), 99 wt.% (b), 50 wt.% (c) and 0.5 wt.% (d)

A similar phenomenon is observed when an appropriate amount of ABS and CFD thermoplastics is introduced into the thermoplastic (DST-30, TPU), only in this case there is an increase in the hardness and strength of the composition.

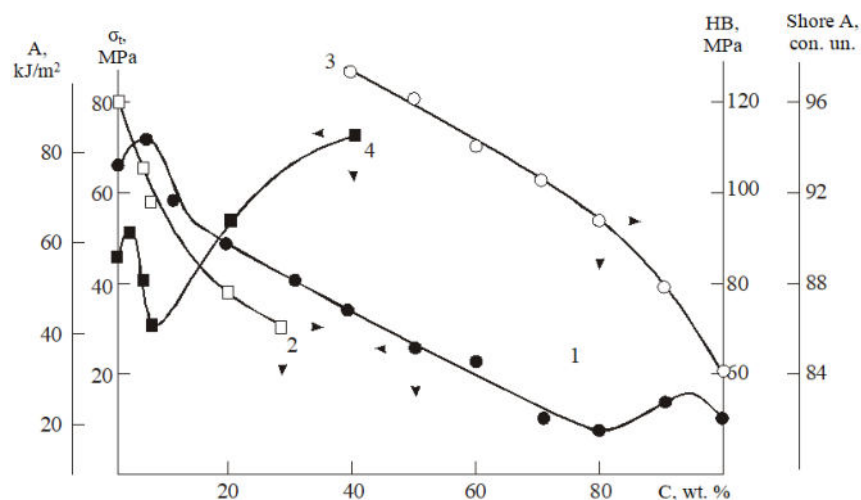


Fig. 6. - Dependence of the destructive tensile stress (1), harnesses according to Brinell (2) and Shore A (3) and impact strength (4) of the ABS on the content of the TPU

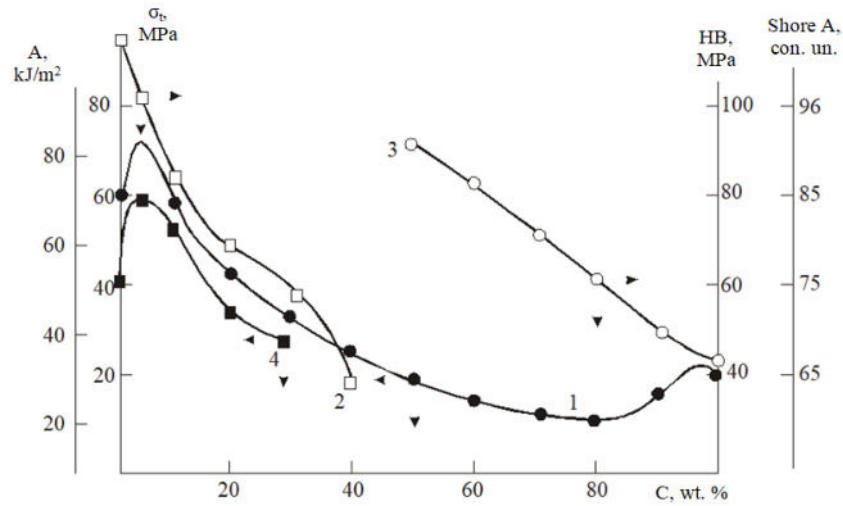


Fig. 7. - Dependence of the destructive tensile stress (1), harnesses according to Brinell (2) and Shore A (3) and impact strength (4) of the ABS on the content of the DST

Researches of the abrasion resistance of thermomechanically combined composites indicate an increase in the wear resistance of both thermoplastic and thermoplastic matrices with a small content of the alloying component (Figure 8). This is probably due to the creation of obstacles to the processes of micro-cutting and plastic displacement of the surface layer of the composite by aggregates of the alloying component [19]. This is evidenced by the nature of the wear surfaces (Figure 9). Thermomechanical combined composites based on a mixture of ABS-TPU and ABS-DST were used in the manufacture of movable seals of the spline joint of the driveshaft [12, 20].

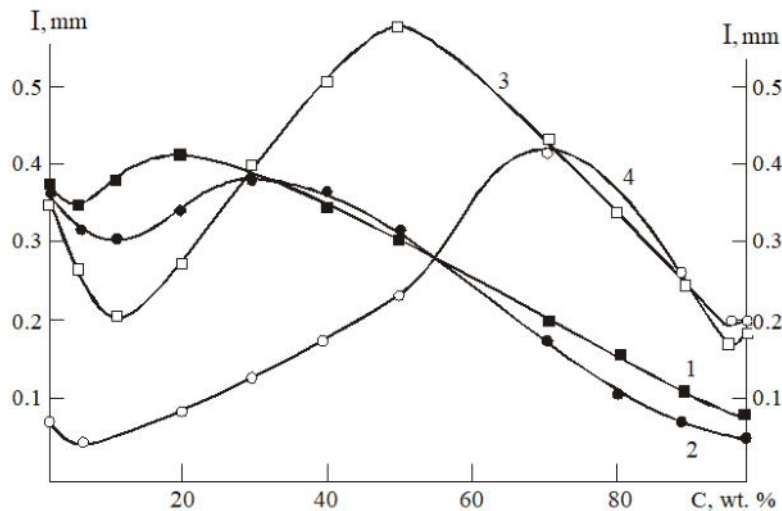


Fig. 8. - Dependence of the wear intensity of the CFD (1-3) and ABS (1) on the TPU content (1 and 2) and DST (3 and 4)

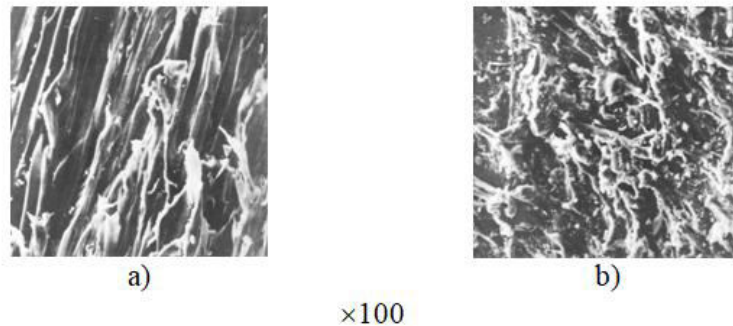


Fig. 9. - Characteristic appearance of the CFD+5 wt.% DST (1) and DST+5 wt.% CFD (2) composite materials friction surfaces

Conclusions

Based on the principle of multilevel modification, composite materials for tribotechnical and structural purposes based on aliphatic polyamides have been developed.

It is shown that the introduction of a complex modifier containing dispersed fillers with different dimensions into the matrix determines the formation of an ordered structure in the boundary layers in contact with filler particles.

As a result, the strength and tribotechnical characteristics of the filled composites are significantly increased. Combinations of fillers (charge – carbon fiber, charge – glass fiber, ultrafine metal – glass fiber, ultrafine metal – carbon fiber) have been selected to ensure optimal effect.

The additional introduction of fluorinated oligomers into the polymer matrix increases the resistance to thermo-oxidative aging and the hydrophobicity of the composite.

The thermo-oxidative combination of an acrylic butadiene styrene copolymer with a thermoplastic matrix provides the possibility of regulating service characteristics.

Composite materials with specified functional characteristics have been developed for the manufacture of new-generation gimbals gear parts.

Then, a new type of cardan transmission has been developed, in which the mechanism for changing the length of the cardan shaft is made in the form of two profiled outer and inner pipes with a lemon-type profile with a multifunctional coating applied to the working surfaces.

The use of the developed materials and technologies made it possible to increase the operating life of cardan drives to 500-800 thousand km.

Acknowledgment

The authors of this research work express sincere thanks to Professor Struk V.A. and his team for their practical supporting in conducting experimental research and obtaining results.

References

- [1] Struk V.A. Tribochemical concept of creating antifriction materials based on multi-tonnage binders: Abstract. dis. Doctor of Technical Sciences: 05.02.01 / Belarusian Polytechnic Institute. – Minsk, 1988. - 41 p.
- [2] Ziyamukhamedova U., Evlen H., Nafasov J., Jalolova Z., Turgunaliyev E., Rakhmatov E. Modeling of the process of mechano activation of filler particles in polymer composites //In E3S Web of Conferences, 2023, Vol. 401, p. 05027EDP Sciences.
- [3] Lipatov Yu.S. Physico–chemical bases of polymer filling. – M.: Chemistry, 1991. – 260 p.
- [4] Kuchkorov L., Alimukhamedov S., Tursunov N., Toirov O. Effect of different additives on the physical and mechanical properties of liquid-glass core mixtures // E3S Web of Conferences 365, 2023, 05009 <https://doi.org/10.1051/e3sconf/202336505009>
- [5] Wani M. F., Ziyamukhamedova U., Mufti T. A., Sehgal R., Saleem S. S. Design, fabrication and characterization of MoS₂ self-lubricating pure MoS₂ Coatings for space applications using PVD magnetron sputtering //E3S Web of Conferences, 2023, Vol. 401, p. 05084 EDP Sciences.
- [6] Toirov O., Tursunov N. Development of production technology of rolling stock cast parts // E3S Web of Conferences 264, 2021, 05013 <https://doi.org/10.1051/e3sconf/202126405013>
- [7] Lebedev E.V., Lipatov Yu.S., Privalko V.P. Morphological evaluation of the interaction of polyethylene with polyoxymethylene in a mixture obtained by extrusion // High-molecular compounds, 1975, Vol. A 17, No. 1., p. 148.
- [8] Lipatov Yu.S., Mamunya E.P., Lebedev E.V. Investigation of a composition based on polyethylene filled with powdered polyoxymethylene // High-molecular compounds, 1981, T. B. 23, No. 4, p. 284-287.
- [9] Ziyamukhamedova U., Bakirov L., Donaev S., Miradullaeva G., Turgunaliyev E. Study of structure formation processes in matrices of mixed components with reinforcing natural fillers. In E3S Web of Conferences, 2023, Vol. 401, p. 05074. EDP Sciences.
- [10] Lipatov Yu.S. Physical chemistry of filled polymers. – M.: Chemistry, 1977. – 304 p.
- [11] Alimov M., Riskulov A., Nurmetov K. Choosing of rational periodicity of engine crankcase oil changing taking into account energy-saving properties of oils // E3S Web of Conferences, 2023, Vol. 401. EDP Sciences. DOI: 10.1051/e3sconf/202340105021.
- [12] Struk B. A., Ovchinnikov E.V., Belyai A.S. et al. Ultrafine modifiers for thermoplastic polymers //Problems and ways of implementing the scientific and technical complex, Kiev, 2000. – pp. 170-171.
- [13] Urazbayev T., Tursunov N., Tursunov T. Steel modification modes for improving the cast parts quality of the rolling stock couplers //AIP Conf. Proc., 2024, 3045, 060015 <https://doi.org/10.1063/5.0197361>.
- [14] Thermoplastics / Edited by V.V. Moiseev. – M.: Chemistry. 1985. – 184 p.
- [15] Ethylene copolymers. – L.: Chemistry, 1983 – 224 p.
- [16] Riskulov A., Nurmetov K., Avliyokulov J. Material selection for vehicle brake chamber case with using computer methods of analysis // E3S Web of Conferences, 2023, Vol. 401 EDP Sciences. DOI: 10.1051/e3sconf/202340102061.
- [17] Lebedev E.V., Shilov V.V., Lipatov Yu.S. Structural and morphological features of binary polymer mixtures. – V.kn.: Mixtures and alloys of polymers. - Kiev.: Naukova dumka, 1978. – 148 p.
- [18] Lukovkin G.M., Volynsky A.L., Bakeev N.F. On the mechanism of increasing the impact strength of plastics by dispersions of rubbers// High-molecular compounds,1983,Vol.25, No.4, p. 845-855.

- [19] Tenenbaum M.M. Wear resistance of structural materials and machine parts. – M.: Mechanical Engineering, 1966. – 331 p.
- [20] Avdeychik S.V., Avdeychik O.V., Kravchenko V.I., Kostyukovich G.A. Composite materials based on regenerated binders for friction units of cardan gears // Second International Congress on Waste Management "WAYSTEK – 2001", p. 202-203.
- [21] Toirov O., Tursunov N. Efficiency of using heat-insulating mixtures to reduce defects of critical parts. In *E3S Web of Conferences*, 2023, Vol. 401. EDP Sciences. DOI: 10.1051/e3sconf/202340105018.
- [22] Alimov M., Riskulov A., Nurmetov K. Choosing of rational periodicity of engine crankcase oil changing taking into account energy-saving properties of oils // *E3S Web of Conferences*, 2023, Vol. 401. EDP Sciences. DOI: 10.1051/e3sconf/202340105021.
- [23] Rakhimov U., Tursunov N. Development of technology for high-strength cast iron for manufacturing D49 head of cylinder. // *E3S Web of Conferences*, 2023, Vol. 401 EDP Sciences. DOI: 10.1051/e3sconf/202340105013.
- [24] Rutkovskiy A. L., Salikhov Z. G., Kovaleva M. A., Bakhteev E. M. An optimized process of drying titanium pellets in a tunnel kiln // *Tsvetnye Metally*, 2021, (5), 89-94. 10.17580/tsm.2021.05.12.
- [25] Şahin N., Işikgöl A., Ziyamukhamedova U., Ahlatci H., Acarer M., Sevim, M. Investigation of corrosion properties of box boring din 20MnCr5 steel bars. In *E3S Web of Conferences*, 2023, Vol. 401, p. 05035. EDP Sciences.
- [26] Ziyamukhamedova U., Wasil S., Kumar S., Sehgal R., Wani M. F., Singh C. S., Gupta H. S. Investigating Friction and Antiwear Characteristics of Organic and Synthetic Oils Using h-BN Nanoparticle Additives: A Tribological Study // *Lubricants*, 2024, 12(1) <https://doi.org/10.3390/lubricants12010027>.
- [27] Taranova E. S., Komissarov V. V. Regularities of influence of operating factors on friction and wear characteristics at rolling // *Journal of Friction and Wear*, 2013, 34(2), 142-146. <https://doi: 10.3103/S106836661302013X>
- [28] Rakhimov U.T., Tursunov N.K., Tursunov S.E. Improvement of production technology for spheroidal graphite cast iron with increased strength // *AIP Conf. Proc.*, 2024, 3045, 060024 (). <https://doi.org/10.1063/5.0197475>.
- [29] Seydametov S.R., Tursunov N.K., Alimukhamedov S.P. Development of out-of-furnace steel treatment technology for the manufacture of railroad transport parts // *AIP Conf. Proc.*, 2024, 3045, 060022. <https://doi.org/10.1063/5.0197429>.

Information of the authors

Rakhmatov Murodjon Iskandarovich, Senior Lecturer, Tashkent State Transport University

e-mail: behbudbek@gmail.com

Riskulov Alimjon Akhmadjanovich, DSc, professor professor, Tashkent State Transport University

e-mail: behbudbek@gmail.com

Nurmetov Khurshidbek Ikromovich, PhD, associate professor, associate professor, Tashkent State Transport University

e-mail: behbudbek@gmail.com

Overview of Monitoring Methods for Metalworking Fluids

Kim A.S.* , Mateshov A.K., Savchenko N.K, Shakirova Y.K.

Abylkas Saginov Karaganda Technical University, Karaganda, Kazakhstan

*corresponding author

Abstract

The article presents a comprehensive review of current methodologies for monitoring the condition of metalworking fluids (MWFs) employed in machining operations. Emphasis is placed on physico-chemical, biological, and electrochemical assessment techniques, including the measurement of pH levels, concentration, contamination, microbial activity, electrical conductivity, and optical characteristics. Particular attention is devoted to the integration of automated and sensor-based monitoring systems capable of real-time data acquisition and analysis. The advantages, limitations, and applicability of these methods within the framework of modern digital and automated manufacturing environments are critically examined. The findings underscore the importance of adopting a multidisciplinary and systematic approach to MWF quality control in order to enhance process efficiency, ensure production stability, and extend the service life of fluids.

Keywords: metalworking fluids (mwfs); condition monitoring; cutting fluid quality; ph measurement; contamination detection; bacterial contamination; sensor technologies; real-time diagnostics; machining processes; smart manufacturing.

Introduction

Metalworking fluids (MWFs) are indispensable to modern machining and metal-forming operations. Their multi-component formulations provide rapid heat dissipation, reduce friction coefficients, suppress corrosion on freshly machined surfaces, and facilitate chip evacuation from the cutting zone. Yet the harsh service environment-characterised by elevated temperatures, pressures, and continuous exposure to air and workpiece debris-accelerates the physical, chemical, and biological degradation of MWFs. Undetected shifts in concentration, pH, particulate load, or microbial activity can quickly erode surface integrity, shorten tool life, increase unplanned downtime, and exacerbate environmental risks.

As industry embraces the paradigms of smart and zero-defect manufacturing [1], [2], the demand for reliable, highly sensitive, and preferably real-time monitoring of coolant condition has intensified. Over the past two decades, researchers have proposed a broad spectrum of approaches, ranging from classical titrimetric and refractometric assays to integrated cyber-physical platforms that blend spectroscopy, electrochemistry, ultrasonics, and machine-learning analytics. Despite promising laboratory results, widespread industrial adoption still faces hurdles such as sensor fouling, frequent recalibration, lack of harmonised standards, and significant capital investment.

This article aims to systematise existing methods for monitoring metalworking-fluid quality, critically evaluate their advantages and limitations within digital-manufacturing environments, and outline future directions for sensor technologies and data-analysis frameworks capable of enabling predictive maintenance and extended coolant life cycles.

1. Classification and functions of metalworking fluids (MWFs)

Metalworking fluids (MWFs) are an indispensable element of most metal cutting and forming technologies. Their multi-component formulations simultaneously address several critical tasks: efficient dissipation of heat from the cutting zone, reduction of friction between the tool and the workpiece, removal of chips, prevention of surface corrosion, and enhancement of dimensional stability in machined parts. As cutting speeds increase, surface-quality requirements tighten, and the range of difficult-to-machine materials expands, the performance demands placed on MWFs have risen correspondingly. Modern fluids must exhibit high thermo-oxidative stability, resistance to microbial growth, compatibility with automated delivery systems, and full compliance with environmental and occupational-safety regulations.

Given the diversity of functions they perform and the variety of operating conditions they face, several fundamentally different classes of MWFs have emerged-from neat mineral and synthetic oils to aqueous solutions and hybrid cryogenic systems. Each group has its own advantages and limitations that define its optimal field of application. The following section provides a structured classification of contemporary metalworking fluids, outlining their typical compositions, key characteristics, and characteristic areas of use, followed by a consolidated list of the core functions they fulfil in industrial machining processes.

Table 1. The classification of metalworking fluids

Main Group	Typical Sub-groups	Key Features	Typical Applications
Neat oils	<ul style="list-style-type: none"> • Mineral • Refined paraffinic • Vegetable / bio-based oils 	<ul style="list-style-type: none"> • 100 % oil, non-miscible with water • Maximum film strength • High viscosity & thermal conductivity 	Slow cutting, deep drilling, threading
Soluble oils (macro-emulsions)	<ul style="list-style-type: none"> • Mineral emulsions 50–80 % oil + surfactants • Bio-emulsions 	<ul style="list-style-type: none"> • Milky macro-emulsion at 5–10 % in water • Balanced cooling and lubrication 	General turning/milling, sawing
Semi-synthetic (micro-emulsions)	<ul style="list-style-type: none"> • 5–30 % oil dispersed in synthetic matrix 	<ul style="list-style-type: none"> • Transparent micro-emulsion • Enhanced cooling, less foam/odor 	High-speed milling, grinding
Synthetic aqueous solutions	<ul style="list-style-type: none"> • Poly-glycols, borates, phosphates • HWCF 	<ul style="list-style-type: none"> • Clear, oil-free solutions • Maximum heat removal, fire-safe 	High-speed grinding, high-pressure die casting
Special / hybrid	<ul style="list-style-type: none"> • Pastes & gels, MQL mists • Cryogenic (N₂, CO₂) • Ionic liquids 	<ul style="list-style-type: none"> • Minimal consumption • Eco-friendly, localized cooling 	Micro-machining, aerospace, hard-to-cut alloys

In summary, the spectrum of metalworking fluids spans from oil-rich neat formulations to fully synthetic, water-based, and even cryogenic systems—each engineered to balance lubrication, cooling, cleanliness, and environmental performance under specific machining scenarios. Selecting the most appropriate fluid therefore requires a holistic evaluation of work-piece material, cutting parameters, tool metallurgy, downstream surface requirements, and regulatory constraints. Continuous advances in additive chemistry, bio-derived base stocks, and minimal-quantity lubrication (MQL) are further widening the toolbox available to process engineers, enabling both higher productivity and lower ecological impact.

Yet, as fluid chemistries become more sophisticated, so too does the need for rigorous monitoring and maintenance practices. Real-time sensing of concentration, pH, microbial activity, and wear metals is rapidly moving from laboratory settings onto the shop floor, supporting predictive maintenance strategies and extending fluid life cycles. Looking ahead, the convergence of smart sensors, data analytics, and environmentally benign formulations is expected to reshape the role of metalworking fluids—from a consumable production aid to an integral, digitally managed component of advanced manufacturing systems.

2. Methods of monitoring metalworking fluids

Main Approaches to Monitoring Metalworking Fluids (MWFs):

1) Comprehensive Analysis of MWF Composition:

Chemical control involves determining the concentration of active components (surfactants, corrosion inhibitors, and biocides), pH levels, as well as quantifying the presence of organic and inorganic contaminants.

Physical control includes measurements of viscosity, density, surface tension, and other parameters that influence the lubricating and cooling performance of the fluid.

2) Assessment of Fluid Contamination:

Control of mechanical impurities is performed using filtration systems and includes the detection and removal of solid particles, metal chips, and abrasive residues.

Microbiological control is carried out using bacteriological methods to determine the quantity of microorganisms (bacteria, molds, etc.) that may cause biodegradation of the fluid. These procedures are regulated by relevant industrial standards and methodologies.

3) Adjustment of Emulsion Concentration

Adjustment of the fluid composition is based on continuous monitoring data, enabling the maintenance of optimal ratios between concentrate and water, depending on material properties, machining conditions, and processing parameters.

To ensure a systematic control approach, it is advisable to implement a regulated monitoring schedule:

Daily monitoring includes visual assessment of the emulsion (color, transparency, foaming) and temperature measurement.

Weekly monitoring includes pH measurement, concentration determination (using refractometric methods), and analysis of mechanical impurities.

Monthly monitoring includes a complete chemical analysis, microbiological testing (in accordance with GOST 9.060–75), and diagnostics of filtration equipment.

A systematic approach to monitoring the operational characteristics of MWFs significantly improves the quality of machined parts, reduces maintenance costs, extends the service life of working emulsions, and minimizes environmental risks associated with their disposal.

Effective MWF monitoring contributes to prolonged equipment lifespan, improved machining quality, and reduced operational expenses at the enterprise level.

One of the most widely used and accessible techniques for MWF condition monitoring is refractometry, performed using refractometers. This method is based on the measurement of the refractive index and its derivative parameters. It is widely used in industrial settings for chemical identification, quantitative and structural analysis, and the determination of physicochemical properties of substances.

A refractometer measures the refraction of light in a fluid, typically expressed in degrees Brix ($^{\circ}\text{Bx}$), which represents the mass fraction of dissolved solids in a liquid.

The term "refractometer" originates from the Latin word *refractus* ("bent"), introduced into scientific use by Isaac Newton in the early 18th century. The device evaluates the deviation of light from a straight path when it passes between substances with different optical densities. The ratio of the angle of incidence to the angle of refraction is referred to as the refractive index.



Fig.1. – Refractometer

This value increases proportionally with the fluid's density. The refractometer measures this relative to distilled water, which is used for calibration.

Refractometry (from Latin *refractus* - 'bent' and Ancient Greek *μετρέω* - 'to measure') is an analytical method based on the determination of the refractive index (coefficient of refraction) and its related functions. The refractometric method is widely used for the identification of chemical compounds, quantitative and structural analysis, and the determination of the physicochemical properties of substances.

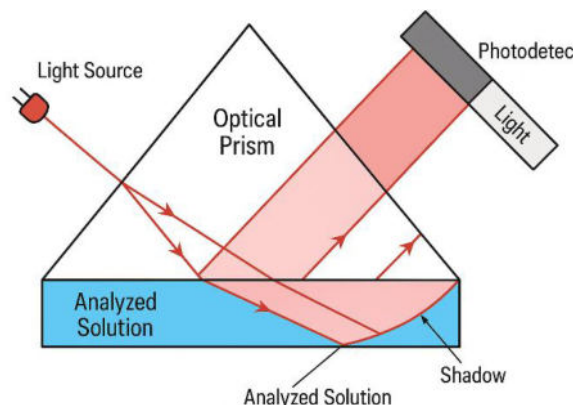


Fig.2. – The operating principle of a refractometer

The relative refractive index n is defined as the ratio of the speed of light in two adjoining media. For liquids and solids, n is typically measured relative to air, while for gases, it is measured relative to vacuum (absolute refractive index).

The value of n depends on the wavelength λ of light and temperature, which are indicated in the subscript and superscript, respectively. For example, the refractive index at 20°C for the D-line of the sodium spectrum ($\lambda = 589\text{ nm}$) is written as n_{D}^{20} . Other commonly used spectral lines include the hydrogen H-line ($\lambda = 656\text{ nm}$) and F-line ($\lambda = 486\text{ nm}$).

In the case of gases, the dependence of n on pressure must also be considered, with values either specified or normalized to standard pressure conditions.

In ideal systems (formed without changes in volume or polarizability of components), the dependence of the refractive index on composition is approximately linear when composition is expressed in volume fractions (percentages):

$$n = n_1V_1 + n_2V_2, \quad (1)$$

where n - is the refractive index of the mixture,

n_1 and n_2 - are the refractive indices of the individual components,

V_1 and V_2 - are their respective volume fractions ($V_1 + V_2 = 1$).

The refractometer analyzes the degree to which a light beam deviates from a straight-line path when transitioning from one substance to another. The ratio between the angle of incidence and the angle of refraction at the boundary between two media is referred to as the refractive index. This index increases proportionally with the density of the substance. The relative “weight” of a sample is determined by the refractometer in comparison with distilled water, which is used for preliminary calibration of the instrument.

Refractometry, performed using refractometers, is one of the most widely used methods for the identification of chemical compounds, quantitative and structural analysis, and the determination of physicochemical properties of substances.

The condition of metalworking fluids (MWFs) is also monitored by assessing their acidity levels. Over time, the pH value of the emulsion may decrease due to microbiological activity, such as the growth of fungi and bacteria, which leads to the formation of acids. A pH drop below acceptable limits indicates significant bacterial contamination and necessitates either fluid replacement or the implementation of regeneration measures. Under standard operating conditions, the pH level should remain within the range of 8.5 to 9.5.

To assess the degree of microbiological contamination in MWFs, dip slides are widely used—special indicator devices that allow for visual determination of fungal and bacterial concentrations in the fluid. To obtain reliable results, it is essential to strictly follow the application procedure provided in the manufacturer's instructions.

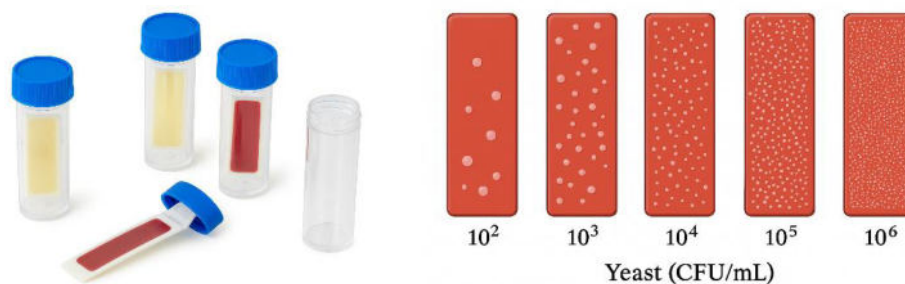


Fig.3. – The dip slides

This issue is also relevant at the global level, and several modern methods for monitoring the quality of metalworking fluids (MWFs) have been proposed to date.

3. Review of the latest metalworking fluid monitoring systems

Many articles on this topic have been analyzed, and we will consider the main scientific directions. Over the last two decades the scientific community has proposed a rich palette of monitoring concepts – from classical titration and refractometry to advanced multi-sensor cyber-physical platforms.

1. Spectroscopic techniques

Optical spectroscopy has evolved into a versatile tool for rapid, non-destructive assessment of MWF quality. Kiefer et al. employed visible and near-infrared (NIR) absorbance signatures to quantify oil concentration and detect emulsion ageing in commercial fluids [3]. Their calibration models ($R^2 > 0.95$) demonstrated that multispectral data outperform single-wavelength refractometry when tramp oils or hard-water salts interfere with refractive index. Other researchers expanded this concept by integrating fibre-optic probes directly into machine-tool sumps, enabling continuous spectral acquisition at 1-minute intervals [4]. The authors reported a detection limit of 0.1 % (v/v) for mineral-oil fraction and proposed a rule-based algorithm for coolant make-up control.

Long-path transmission spectroscopy was adopted by another group of researchers to monitor droplet coalescence during accelerated thermal ageing tests [5]. A broadening of the 600 nm peak served as an early indicator (48 h advance) of phase separation. In a complementary study, Schandl et al. embedded a USB-based miniature spectrometer inside a machining centre and successfully tracked concentration fluctuations caused by high-pressure coolant delivery [6]. A fluorescence-based variant was proposed by another study, who exploited native fluorophores (long-chain amides, antimicrobial dyes) for contamination detection; the spectral shift at 350 nm correlated logarithmically with bacterial count [7].

Recent study demonstrated that inline NIR spectroscopy can close the loop in automatic dosing systems; when concentration deviated by $\pm 0.5\%$ the pump response time was < 30 s, maintaining surface finish within Ra 0.8 μm [8]. a group of authors introduced an indirect spectro-thermographic approach: by capturing infrared thermograms of a falling film they reconstructed apparent viscosity maps which agreed with rotational-rheometer data within 6 % [9]. research conducted miniaturised the optical path in a microfluidic chip (total volume 30 μL) suitable for point-of-use analysis on shop-floor carts [10].

Collectively, these works underscore the sensitivity of optical observables – absorbance, fluorescence, NIR overtones and mid-IR fingerprints – to multiple degradation modes (oil depletion, emulsifier breakdown, microbial metabolites). Remaining challenges include light-scattering by swarf, temperature compensation, and standardisation across fluid chemistries.

2. Electrochemical and impedance methods

Electrochemical impedance spectroscopy (EIS) has gained momentum as a multi-parameter probe. Investigators established a three-electrode flow-cell that simultaneously predicts droplet size, pH and concentration through radial basis function regression of magnitude-phase spectra [11]. Their root-mean-square error for pH was 0.08 over the industrial range 7–10. Riaz et al. designed thick-film RuO₂ transducers whose open-circuit potential varies quasi-Nernstian with hydrogen ion activity, enabling affordable in-situ pH tracking under high ionic strength [12].

Researchers advanced the concept by fabricating an interdigitated micro-electrode printed on ceramic; the 1 kHz impedance modulus increased linearly with emulsifier depletion ($R^2 = 0.93$) and was robust against tramp-oil fouling [13]. A study tackled chemical by-products: they quantified nitrite accumulation (a corrosion indicator) via square-wave voltammetry with a detection limit of 0.3 mg L⁻¹ [14]. The study recommends a 500 mg L⁻¹ alarm threshold to mitigate ferritic pitting of machine beds.

Recent investigation merged EIS hardware with machine-learning analytics. Using a dataset of 14 000 spectra they trained a gradient-boosting model that classified coolant age into four maintenance states with 95 % accuracy [15]. The authors emphasise that data-driven techniques compensate for fluid-to-fluid variability and sensor drift. Ultrasonic monitoring, though not electrochemical, also relies on propagation impedance: authors related attenuation coefficients at 5 MHz to solid particle loading (1–50 g L⁻¹) with a 3 g L⁻¹ standard error [16].

3. Microbiological assessment

Metalworking fluids have a negative impact on human health [17], [18]; therefore, special attention is given to the control of biological contamination. Unchecked microbial proliferation degrades lubricant efficacy and poses occupational hazards. Early studies pioneered culture-based field surveys linking sump colony counts ($>10^6$ CFU mL⁻¹) to aerosol mist exposure [19]. Authors synthesised 60 years of microbiology literature and identified *Pseudomonas*, *Mycobacterium* and *Candida* as dominant taxa in semi-synthetic emulsions [20]. Their review recommends dip-slide screening every 72 h, corroborating earlier ATP bioluminescence work by previous research; the latter reduced test time from 48 h incubation to 5 min swab-to-result [21].

An investigation introduced optical coherence tomography (OCT) to visualise biofilm formation on transparent coupons immersed in coolant; OCT intensity contrasted biofilm thickness with 2 μm depth resolution, triggering sanitisation before biomass exceeded 100 μm [22]. Shen et al. combined fluorescence excitation-emission matrices (EEM) with HPLC to fingerprint dissolved organic matter produced by bacteria, isolating tryptophan-like signals as early spoilage markers [23]. Valuated a novel heterocyclic biocide in 12 industrial sites; microbial counts dropped by three orders of magnitude within 24 h and remained suppressed for four weeks [24].

Researchers broadened the scope to environmental risk, reviewing ISO 14852 and OECD 301 protocols for assessing biodegradability and eco-toxicity of new coolant chemistries [25]. Documented metal leaching (Zn, Fe, Cr) into fresh and used fluids, underscoring the complex interaction between microbiology, corrosion inhibitors and worker dermatitis [26].

4. Physical stability and functional performance

The physical integrity of oil-in-water emulsions is a prerequisite for chip evacuation and thermoregulation. Glasse et al. utilised turbidity spectra (400–900 nm) to determine creaming index; phase inversion was predicted when absorbance at 750 nm exceeded 1.2 AU [27]. Earlier researchers provided a macroscopic perspective, coupling tribometer tests with frictional power analysis to link lubricant depletion to tool flank wear, thereby translating laboratory metrics into production economics [28].

Scientists (spectroscopic sensor) and other researchers (automatic titration) both investigated the impact of replenishment strategies on kinematic viscosity and surface tension, whereas research findings demonstrated that inline refractometer feedback prevents under-dilution events that would raise cutting temperature by 40 °C [29]. Infrared thermography by a group of authors further revealed that a 10 % viscosity rise elevated the thermal boundary layer thickness, reducing convective heat transfer coefficients by 12 % [9].

5. Cyber-physical and IIoT integration

Also an Arduino-based prototype was described, combining refractometer, temperature, flow and conductivity sensors; MQTT messaging transmitted data to a cloud dashboard for rule-based alerts [30]. Scientists expanded the architecture to OPC-UA and edge analytics for latency-critical tasks such as pump actuation [31]. Their pilot reduced fluid consumption by 18 % over eight months. Research in manufacturing framed coolant monitoring within a zero-defect manufacturing roadmap: sensor fusion, cyber-twins and predictive maintenance loops enabled a 25 % scrap reduction in automotive cylinder-head machining [32].

A recent study as well as a recent investigation (machine learning) illustrate convergence between process control and chemical diagnostics, while research conducted highlight the trend toward miniaturisation for decentralised sampling. Collectively, sources [6], [15], [8], [10] and [32] emphasise the need for open ontologies and standard data models to ensure interoperability.

6. Ultrasonic monitoring

Ultrasound is also employed for monitoring the quality of metalworking fluids, and several up-to-date techniques have been identified. Recent literature highlights three complementary ultrasonic-based strategies for assessing and maintaining metalworking-fluid quality.

Attenuation-based ultrasonic monitoring employs a broadband 5 MHz transducer placed in a flow-through cell; the amplitude decay of the acoustic signal increases quasi-linearly with the volumetric concentration of solid debris between 1 and 50 g L⁻¹, enabling continuous estimation of particle loading without sampling [33]. The method is attractive for its in-line configuration, immunity to oil-content fluctuations and low capital cost, yet its accuracy deteriorates below ≈ 5 g L⁻¹, sensor faces are prone to fouling and the reading must be temperature-compensated.

A second line of research couples fluorescence spectroscopy with ultrasonic stirring to monitor organic contamination. Here, ultrasound is used only to homogenise the coolant and stabilise the optical signal, while the diagnostic variable is the fluorescence intensity of native dye or biocide molecules that correlates with bacterial proliferation and tramp-oil ingress [34]. The approach offers sub-second response and multi-parameter calibration for pH and concentration, but it relies on the presence of a stable fluorophore, is sensitive to light-absorbing impurities and generally involves higher instrument costs than purely acoustic probes.

Ultrasonic cleaning with concurrent turbidity sensing combines high-power cavitation (20–40 kHz) to detach metallic fines from the recirculating coolant with real-time monitoring of the resulting turbidity change as an index of cleaning efficiency [35]. Integrating regeneration and diagnosis in a single loop prolongs fluid life and reduces manual filtration; however, sustained cavitation increases power consumption, may destabilise emulsifiers if over-driven, and requires cavitation-resistant tank materials.

Collectively, the attenuation approach [33] is best suited for tracking solid particulate levels, fluorescence monitoring [34] excels at detecting organic and microbiological spoilage, whereas the cavitation-based system [35] provides a holistic “clean-and-measure” solution. Selection among these techniques should therefore be guided by the dominant failure mode of the coolant, permissible energy budget and instrumentation constraints of the target manufacturing environment. Besides monitoring the quality of metalworking fluids, ultrasound is widely applied in many other fields, where it has proven highly effective [36 - 38].

Conclusions

The reviewed literature evidences a vibrant research landscape moving from periodic laboratory tests toward real-time, in-machine intelligence. Spectroscopic methods dominate due to versatility, but electrochemical and acoustic probes provide complementary selectivity, especially for chemical by-products and particulate fouling. Microbiological diagnostics have benefited from optical and biochemical accelerations, yet incubation-free quantitation remains an open frontier.

Despite promising prototypes, industrial uptake lags behind. Key barriers include sensor fouling, fluid-specific calibration, proprietary communication protocols and unclear cost-benefit justification. Future work should prioritise: harmonised performance benchmarks, adaptive machine-learning models transferable across fluid chemistries, self-cleaning or disposable sensor architectures, and cybersecurity of cloud-connected monitoring platforms. Cross-disciplinary collaboration between mechanical engineers, analytical chemists, microbiologists and data scientists will be essential to unlock the full potential of smart metalworking fluids management.

Pilot trials under real production conditions will be crucial to demonstrate sensor durability and data fidelity over extended machining cycles. Robust economic models that link continuous monitoring data to tangible savings—through reduced fluid consumption, lower tool wear and minimized downtime - can help solidify management buy-in. Standardisation bodies and industry consortia should work together to define clear protocols for sensor interoperability, data encryption and quality assurance. Advances in bio-inspired coatings and novel miniaturised electronics offer promising routes toward self-healing, auto-calibrating probes that require minimal maintenance. Finally, building open-source software platforms and shared data repositories will accelerate innovation, lower entry barriers for small and medium-sized enterprises, and drive widespread adoption of smart MWF monitoring systems.

Acknowledgments

This research is funded by the Science Committee of the Ministry of Education and Science of the Republic of Kazakhstan (Grant No. AP25794035)

References

- [1] Kadyrov A.S., Kunaev V.A., Georgiadi I.V. Prospects for Processing of Ferrous Metallurgical Waste Based on Arcelormittal Temirtau Experience // *Metallurgist*, Vol. 62, Issue 1-2, p. 22–28. <https://doi.org/10.1007/s11015-018-0684-5>
- [2] Kumar V., Putra Z. A. Zero-waste manufacturing strategies for metal removal processes: A systematic review // *Journal of Manufacturing Processes*, 2023, 92, 556-572. <https://doi.org/10.1016/j.jmapro.2023.05.021>
- [3] Kiefer J., Seidel B., Meyer D. Optical Spectroscopy for Analysis and Monitoring of Metalworking Fluids // *Applied Spectroscopy*, 2018, 72(12), 1790–1797. <https://doi.org/10.1177/0003702818789700>
- [4] Grossi M., Riccò B. Oil Concentration Measurement in Metalworking Fluids by Optical Spectroscopy // *Measurement*, 2017, 97, 8–14. <https://doi.org/10.1016/j.measurement.2016.11.044>

- [5] Pott T., Fritsching U., Trägner S. Long-Term Monitoring of Metalworking Fluid Emulsion Aging Using a Spectroscopic Sensor //Canadian Journal of Chemical Engineering, 2017, 95, 1363–1371. <https://doi.org/10.1002/cjce.22931>
- [6] Schandl M., et al. System for Real-Time Monitoring of Metalworking Fluids //Proceedings of the 30th DAAAM International Symposium, 2019, 104–109. <https://doi.org/10.2507/30th.daaam.proceedings.104>
- [7] Tork J., Ali M. Online Monitoring of Cutting Fluid Contamination Using Fluorescence Spectroscopy //Journal of Manufacturing Processes, 2019, 38, 493–500. <https://doi.org/10.1016/j.jmapro.2019.01.045>
- [8] Yoon S., Lee D. Real-Time Control of Coolant Concentration with Inline NIR Spectroscopy //Procedia CIRP, 2021, 104, 1123–1128. <https://doi.org/10.1016/j.procir.2021.11.189>
- [9] Zhang M., Wang L. Infrared Thermography-Based Viscosity Estimation of Machining Coolant //Measurement Science and Technology, 2019, 30(9), 095601. <https://doi.org/10.1088/1361-6501/ab1f33>
- [10] Pasquale A., Rossi G. Development of a Microfluidic Device for On-Site Analysis of Coolant Emulsions //Microchemical Journal, 2020, 154, 104593. <https://doi.org/10.1016/j.microc.2019.104593>
- [11] Budilyan A., Schramm M., Kiefer J. Simultaneous Determination of Droplet Size, pH Value and Concentration of Metalworking Fluid Emulsions Using Electrochemical Impedance Spectroscopy //Sensors, 2021, 21(24), 8299. <https://doi.org/10.3390/s21248299>
- [12] Riaz M., Bashir F., Khan R. Electrochemical Impedance Spectroscopic Analysis of RuO₂-Based Conductimetric pH Sensors for Metalworking Fluids Monitoring //Electrochimica Acta, 2015, 182, 895–903. <https://doi.org/10.1016/j.electacta.2015.10.017>
- [13] Cavdar M., Delibas B. Development of an Impedance-Based Sensor for Metalworking Fluid Quality Assessment //Sensors and Actuators B: Chemical, 2020, 309, 127752. <https://doi.org/10.1016/j.snb.2020.127752>
- [14] Sharma P., Verma S. Electrochemical Sensing of Nitrite Buildup in Cutting Fluids //Electroanalysis, 2018, 30(12), 2762–2769. <https://doi.org/10.1002/elan.201800228>
- [15] Heisel U., Meier H. Machine Learning Approach for Predicting Aging of Metalworking Emulsions from Sensor Data //Journal of Manufacturing Science and Engineering, 2022, 144(6), 061002. <https://doi.org/10.1115/1.4052789>
- [16] Sadeghi M., Mahdavejad R., Ramazanifar M. Ultrasonic Monitoring of Particle Contamination in Metalworking Fluids. //Ultrasonics, 2017, 81, 96–103 <https://doi.org/10.1016/j.ultras.2017.05.009>
- [17] Mindubayeva F., Niyazova Y., Nigmatullina R., Sadykova D., Akhmaltdinova L., Salikhova Y., Kadyrova I., Akhmetova M., Sabirova D. Membrane serotonin transporter as a Biomarker of Pulmonary arterial hypertension in children with Congenital Heart Defect //Research Journal of Pharmacy and Technology. Vol. 13, Issue 5, 2020. – p.2435-2438. doi: <http://dx.doi.org/10.5958/0974-360X.2020.00436.9>
- [18] Akhmaltdinova L., Kolesnichenko S., Lavrinenko A., Kadyrova I., Avdienko O., Panibratov L. Influence of Pathogen Type on Neonatal Sepsis Biomarkers. Wiley //International Journal of Inflammation. Vol. 2021, Issue 2. – p.1 - 7. doi: <http://dx.doi.org/10.1155/2021/1009231>
- [19] Beardsall D., Wetton P. Occupational Exposure to Metalworking Fluid Mist and Sump Fluid Microbiology //Annals of Occupational Hygiene, 2003, 47(1), 17–27. <https://doi.org/10.1093/annhyg/mef005>
- [20] Jadhav R., Khajuria B. The Microbiology of Metalworking Fluids: A Review //Applied Microbiology and Biotechnology, 2013, 97, 5843–5857. <https://doi.org/10.1007/s00253-012-4055-7>
- [21] Liu X., Yang C. A Rapid Technique for Determining Microbial Loads in Metalworking Fluids Using ATP Bioluminescence. //Tribology International, 1981, 14(1), 33–40. [https://doi.org/10.1016/0301-679X\(81\)90021-9](https://doi.org/10.1016/0301-679X(81)90021-9)
- [22] Kim J., Park H. Optical Coherence Tomography for Detecting Microbial Growth in Metalworking Fluids //Optics & Laser Technology, 2023, 161, 109234. <https://doi.org/10.1016/j.optlastec.2022.109234>
- [23] Shen J., Liu B., Wu J. Characterization of Fluorescent Dissolved Organic Matter in Metalworking Fluid by Fluorescence Excitation-Emission Matrix and HPLC //Chemosphere, 2020, 239, 124703. <https://doi.org/10.1016/j.chemosphere.2019.124703>
- [24] Passman F. J., Summerfield J., Sweeney J. Field Evaluation of a Newly Registered Metalworking Fluid Biocide //Lubrication Engineering, 2000, 56(3), 26–32.
- [25] Masoudi S., et al. A Review on Testing Methods of Metalworking Fluids for Biodegradability and Eco-toxicity //Materials Today: Proceedings, 2020, 33, 1018–1025. <https://doi.org/10.1016/j.matpr.2020.04.708>
- [26] Nichols M. N., et al. Metals in Used and Unused Metalworking Fluids: X-Ray Fluorescence Analysis //Contact Dermatitis, 2020, 82(6), 397–405. <https://doi.org/10.1111/cod.13533>
- [27] Glasse B., Guardani R., Fritsching U. Analysis of the Stability of Metalworking Fluid Emulsions by Turbidity Spectra //Chemical Engineering & Technology, 2013, 36(7), 1202–1208. <https://doi.org/10.1002/ceat.201200590>
- [28] Norrby T., Hartig C. Metalworking Fluids—Mechanisms and Performance //Tribology International, 2016, 94, 582–597. <https://doi.org/10.1016/j.triboint.2015.10.014>

- [29] Kumar R., Patel K. Online Monitoring of Cutting Fluid Concentration Using Inline Refractometer //Procedia Manufacturing, 2018, 26, 1352–1358. <https://doi.org/10.1016/j.promfg.2018.07.156>
- [30] Rozza O., Kavka J., Samek D. Design of Real-Time Monitoring System for Cutting Fluids //Inventions, 2022, 7(2), 43. <https://doi.org/10.3390/inventions7020043>
- [31] Saini R., Kumar V., Singh P. Comprehensive Approach toward IIoT-Based Condition Monitoring of Machining Operations //Measurement, 2023, 218, 113112. <https://doi.org/10.1016/j.measurement.2023.113112>
- [32] Gomes P., Silva R. Toward Zero-Defect Manufacturing: Integrated Coolant Quality Monitoring in Cyber-Physical Production Systems //Journal of Cleaner Production, 2023, 409, 137385. <https://doi.org/10.1016/j.jclepro.2023.137385>
- [33] Sadeghi M., Mahdavejad R., Ramazanifar M. Ultrasonic Monitoring of Particle Contamination in Metalworking Fluids //Ultrasonics, Vol. 81, 2017, pp. 96 – 103. <https://doi.org/10.1016/j.ultras.2017.05.009>
- [34] Tork J., Ali M. Online monitoring of cutting-fluid contamination using fluorescence spectroscopy //Journal of Manufacturing Processes, 2019, 38, 493-500. <https://doi.org/10.1016/j.jmapro.2019.01.045>
- [35] Sadeghi M., Mahdavejad R., Ramazanifar M. Ultrasonic cleaning of recirculating coolants containing metal debris //Ultrasonics Sonochemistry, 2021, 70, 105328. <https://doi.org/10.1016/j.ultsonch.2020.105328>
- [36] Kadyrov A., Bembenek M., Sarsembekov B., Kukeshva A., Nurkusheva S. The Influence of the Frequency of Ultrasound on the Exhaust Gas Purification Process in a Diesel Car Muffler //Appl. Sci. Vol.14, Issue 12, 2024. – p. 2 - 19
- [37] Kukeshva A., Kadyrov A., Kryuchkov Y. Establishing the parameters of the operation mode of the electric pulse automobile muffler //Journal of Applied Engineering Science, Vol. 22, Issue 1, 2024. – p. 89–99. <https://doi.org/10.5937/jaes0-45196>
- [38] Ibatov M.K., Kadyrov A.S., Pak I.A., Kadyrova I.A., Askarov B.Sh. Results of experimental studies of the operation of capacitive equipment for ultrasonic cleaning of exhaust gases of motor vehicles //Ugol, Vol. 2, Issue 1127, 2020. - p. 73-78. <https://doi.org/10.18796/0041-5790-2020-2-73-78>

Information of the authors

Kim Anna Stanislavovna, master of engineering sciences, lecturer, Abylkas Saginov Karaganda Technical University
e-mail: a.kim@ktu.edu.kz

Mateshov Arman Karievich, master of engineering sciences, senior lecturer, Abylkas Saginov Karaganda Technical University
e-mail: a.mateshov@ktu.edu.kz

Savchenko Natalya Karimovna, master, senior tutor, Abylkas Saginov Karaganda Technical University
e-mail: sav_nata@mail.ru

Shakirova Yuliya Karimovna, master, senior tutor, Abylkas Saginov Karaganda Technical University
e-mail: uliya_sch@mail.ru

Designing a Robot-Manipulator of the Structure of a Human Upper Limb

Zhumasheva Zh.^{1*}, B. Nurakhmetov B.²

¹Al-Farabi Kazakh National university, Kazakhstan

²Almaty Technological University, Kazakhstan

* corresponding author

Abstract. Today, robotics is one of the key areas of creating new "smart" technology. The peculiarity of such robotic devices is a wide variety of movements of their executive bodies, including the ability to construct so-called "anthropomorphic" movements that imitate to some extent the movements of a person and his limbs. One of the important qualities of any anthropomorphic device is the kinematic similarity of its working movements to similar human movements. However, the movements of most existing robots are formed according to traditional machine control schemes, which leads to the "machine" kinematics of these movements, which is sharply different from the "living" kinematics of a person, although the intended purpose of the movements is almost the same. Therefore, when developing anthropomorphic manipulators, it is extremely important to ensure not only the kinematic similarity of their movements to the movements of human arms and legs, but also to give them smoothness. The issue of creating a natural-looking human hand is of great relevance for modern science and technology. This is primarily dictated by the need to create universal manipulators for flexible production, solving the problem of prosthetics of the upper limbs and developing anthropomorphic robots to assist a person in various areas of his activity. The article discusses the possibilities of creating a robot manipulator in the form of a human upper limb, in the sense that the robot will be able to repeat the basic movements of the hand: shoulder, elbow and hand. Available low-cost means were used in the design, which helps to reduce the cost of the final product in order to make it accessible to all segments of society. The goal is achieved using 3D modeling and additive printing technology. The work of the hand gripper, that is, bending and unbending the fingers, is not considered in the work. As a result, we will receive a ready-to-use prototype of the hand for the operator, who will remotely move his hand "transfer" the movement to the robot manipulator.

Keywords: robot, manipulator, human upper limb, prototype, movement, 3D modeling.

Introduction

One of the main areas of modern science and technology is robotics, which is a mechatronic system that combines fundamental and applied research in the field of mechanics (including machine mechanics), electronics and information technology [1, 2, 3, 4].

A striking illustration of the mutual penetration of information technology and industry is robotics, which is a classic example of a mechatronic system that combines the principles of mechanics and electronics (control).

Currently, more and more attention is being paid to the creation of humanoid robots, both those that are similar in appearance and those that imitate all human movements [5, 6, 7].

Possession of skills in computer-aided design systems [8, 9] is a prerequisite in the engineering profession, thanks to which productivity and quality of work achieves better results, and the drawing board and pencil are a thing of the past.

Due to the presence of multi-link kinematic chains, mostly open during movement, a person has a large number of degrees of freedom.

Thus, the mobility of the fingertips relative to the chest is determined by 12 degrees of freedom; the wrist relative to the shoulder blade - 7; and the total number of degrees of freedom of the entire body is a three-digit number.

The kinematic diagram of the arm skeleton shows the movable links of the skeleton and the types of hinge joints (two ball joints and one cylindrical joint).

The skeleton model has seven degrees of freedom: three degrees of freedom in the shoulder girdle, one degree of freedom in the elbow joint and three degrees of freedom in the hand [10, 11, 12].

The basic movements (Fig. 1) are illustrated using a rotational pair, so it can be said that the shoulder movements are characterized by a spherical kinematic pair. In this work, a prototype with 3 degrees of freedom is designed: 1 degree at the elbow, and 2 degrees at the hand.

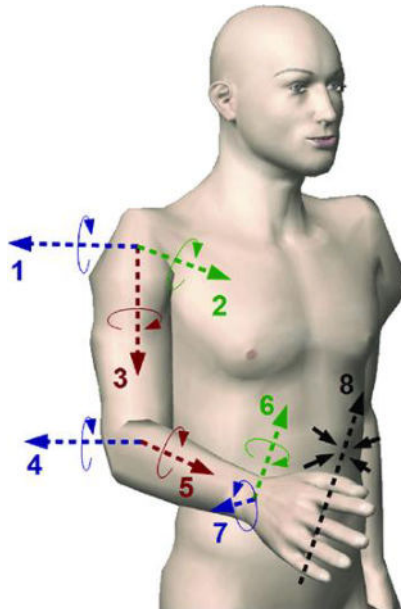


Fig. 1 - Basic movements (degrees of freedom) of the human upper limb: 1 - flexion and extension at the shoulder joint; 2 - adduction and abduction at the shoulder joint; 3 - internal and external rotation at the shoulder joint; 4 - flexion and extension at the elbow joint; 5 - pronation and supination at the radioulnar joint; 6 - flexion and extension at the wrist joint; 7 - abduction and adduction at the wrist joint; 8: grasping and releasing with the hand

1. Materials and methods

1.1 Materials

The development of modern electrical engineering and microelectronics has made it possible to simultaneously reduce the weight and dimensions of mechanical systems through the use of electronic components and increase the efficiency and durability of operation.

Selecting the Basic Hardware for a Structural Prototype:

- The hardware part of the system is the Arduino UNO microcontroller (Fig. 2). Arduino boards are a line of electronic devices equipped with a microcontroller, their own memory, a set of digital and analog contacts, an ADC module, and a port for connecting to a computer. Arduino Uno is a controller based on the ATmega328P-AU processor. In addition to the processor, it includes: 16 digital contacts, 6 analog contacts, a 16 MHz quartz resonator, a USB connector, a power connector, an ICSP connector for in-circuit programming, and a reset button. The ATmega16U2 microcontroller is used as a USB-UART converter [13].

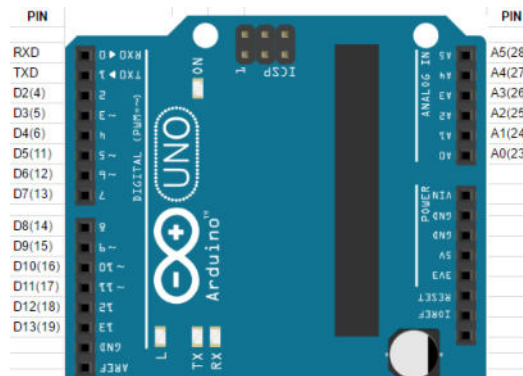


Fig. 2 – Digital and analog controller contacts

- **Electromechanical actuators for robotic arm:** In our work, we used the MG996R servo drive to rotate the links. MG996R (Fig. 3) high torque digital servo drive features a metal gear train that delivers a very high torque of 10 kg in a tiny package.

1.2 Methods

Design of a structural prototype:

Design of prototype blocks: The design of the structural prototype was based on an open-source project by user Bitluni on the “electromaker.io” platform [14]. The design of the structural prototype of the robot-manipulator was performed in the SolidWorks solid modeling software tool.

Fig. 7, 8, 9, 10, 11, 12, 13 show the structural elements of the prototype in sequential order.

Servos are extremely useful in robotics and automation. Robots use servo motors because of their smooth switching and precise positioning. Servo Motors are DC motors equipped with a servo mechanism for precise angular position control.

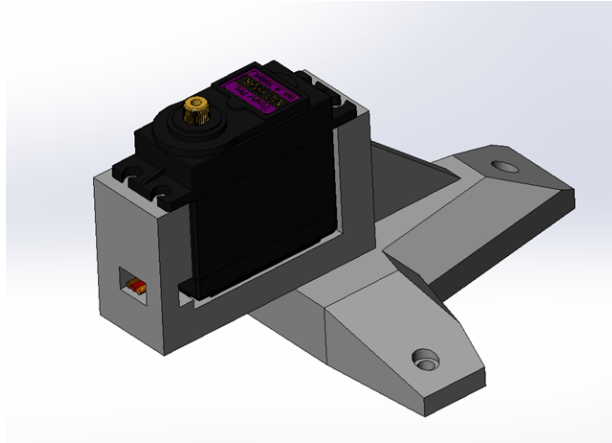


Fig. 7 – Structural element of the prototype



Fig. 8 - Structural element of the prototype

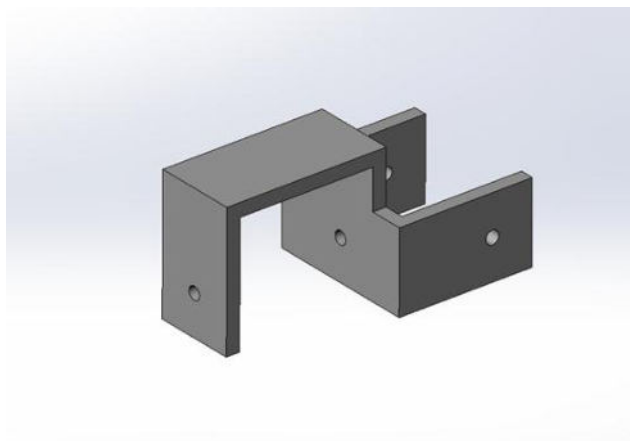


Fig. 9 - Structural element of the prototype



Fig. 10 - Structural element of the prototype

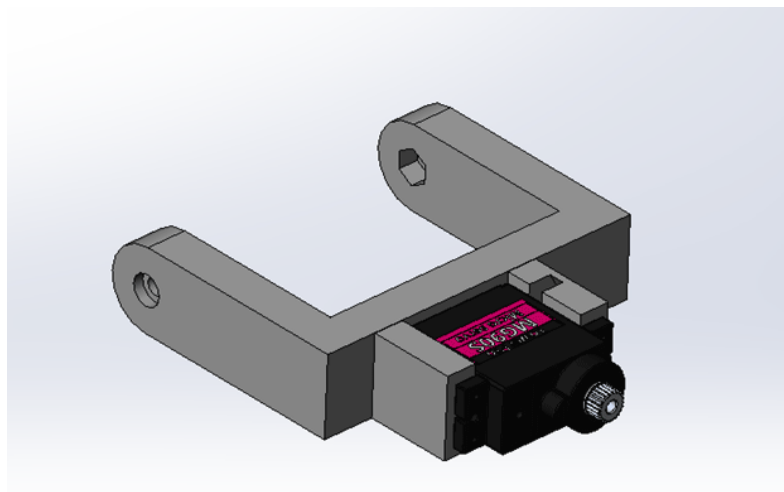


Fig. 11 - Link for pronation and supination in the radioulnar joint

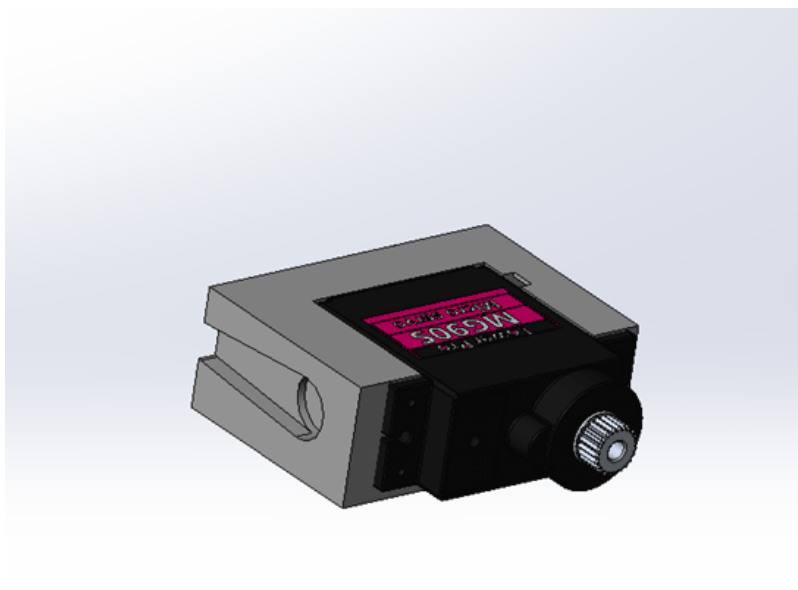


Fig. 12 - Wrist flexion and extension link

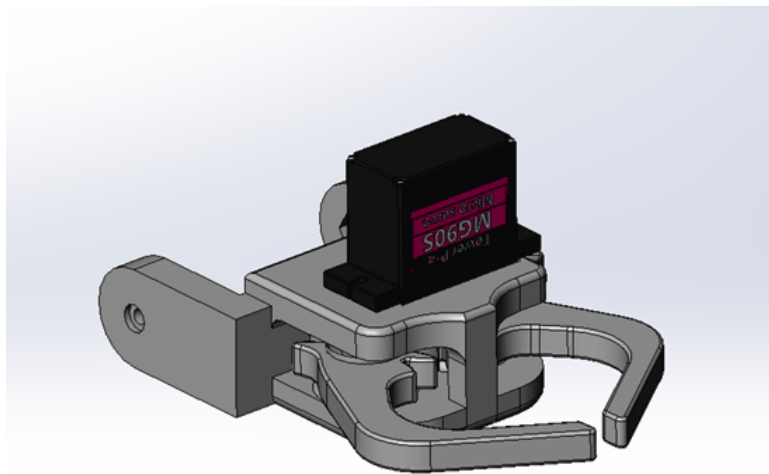


Fig. 13 - Gripper device

The complete assembly (Fig. 14) represents a structural prototype of a robotic manipulator for simulating human upper limb movement.

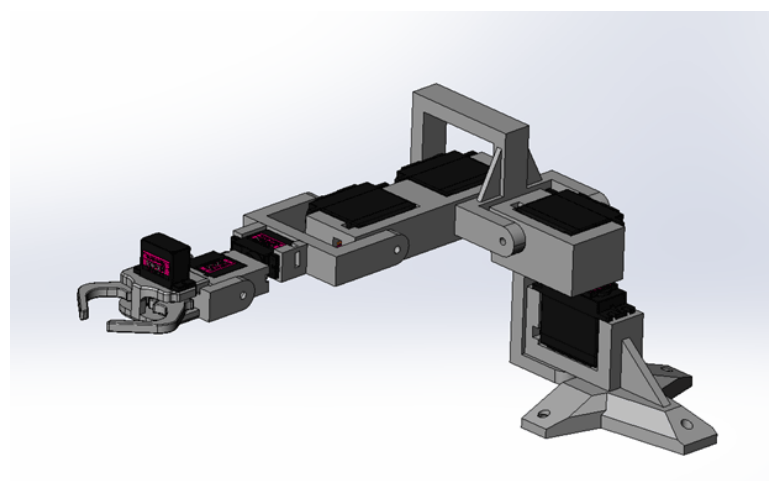


Fig. 14 - Structural prototype of a robotic manipulator for simulating the movement of the human upper limb

2. Results

Assembly of all structural elements of the prototype

During the process of 3D printing and assembly of the prototype itself, there were some mismatches and the elements of the parts were improved.



Fig. 15 - 3D Printing Process



Fig. 16 - Fasteners and bearings



Fig. 17 - Bearing location

Bearings are used to better rotate kinematic pairs to ensure frictionless movement, which affects the final moment of force in the link.



Fig. 18 – Installing bearings to the manipulator links

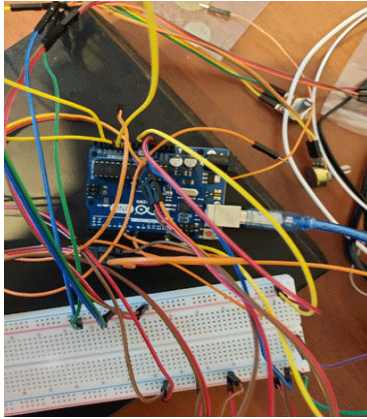


Fig. 19 – The process of connecting to Arduino and testing

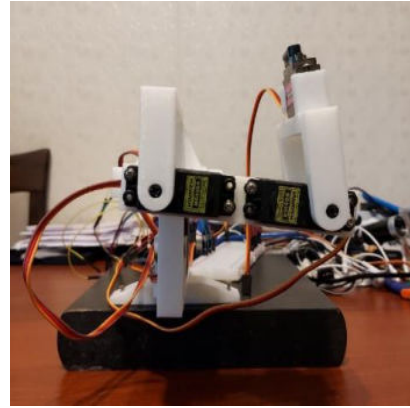


Fig. 20 – Assembling the manipulator links



Fig. 21 – Assembling the manipulator

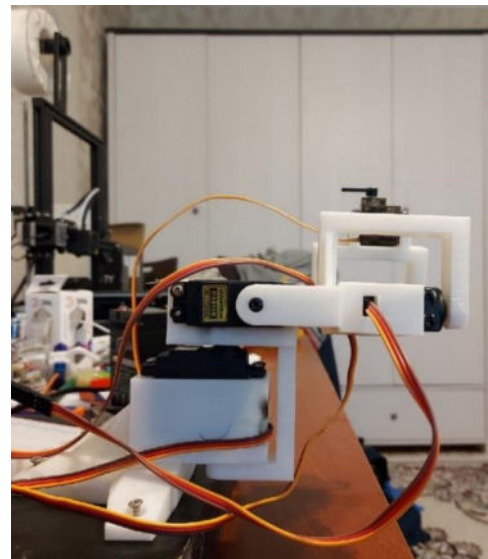


Fig. 22 – Designed prototype of a robotic manipulator

Conclusion

The digitalization process today affects almost all countries in the world. Currently, robotics is becoming one of the key areas of development of science, technology and engineering, which in the 21st century will determine the scientific, technical, industrial and defense potential of the state.

In recent years, various robotic devices have been increasingly introduced into the medical field [15, 16, 17]. One of the promising areas of medical robotics is the development of hardware and software for prosthetics of limbs and their individual parts. This allows to a significant extent to restore the quality of life of a person, his physical (movement, taking, carrying objects, etc.) and sociological needs, reduce the social burden on his relatives, nursing services, etc. As a result, practical skills were obtained during the process of performing the work. The human upper limb, its mobility and features were considered. The hardware and technical component was selected for designing a prototype of a robot-manipulator. A prototype of a robot-manipulator was designed that replicates the structure of the joints and the movement of the human upper limb. The article shows the general assembly and various elements involved in the layout. The scheme and methods of connecting electronics to the entire hardware platform are considered.

References

- [1] Gulletta G., Erlhagen W., Bicho E. Human-Like Arm Motion Generation: A Review //Robotics 2020, 9, 102. <https://doi.org/10.3390/robotics9040102>.
- [2] Winfield, Robotics: A very short introduction, OUP Oxford, 2012
- [3] W. H. Organization, World report on ageing and health, WorldHealth Organization, 2015
- [4] Khosravi P., Rezvani A., Wiewiora A. The impact of technology on older adults' social isolation //Computers in Human Behavior, 2016, 63, 594–603
- [5] Feil-Seifer D., Mataric M. J. Defining socially assistive robotics// 9th International Conference on Rehabilitation Robotics(ICORR 2005), IEEE, 2005, 465–468
- [6] Graaf M. M., Allouch S. B., Dijk J. van What makes robots social?: A user's perspective on characteristics for social human-robot interaction, In: International Conference on Social Robotics, Springer, 2015, 184–193

- [7] Social robot, https://en.wikipedia.org/wiki/Social_robot
- [8] CAD SOLIDWORKS, <https://www.hitechcaddservices.com/news/why-solidworks-over-other-cad-tools/>
- [9] CAD and manual drawing, <https://www.pivotint.com/blog/7-reasons-why-you-should-be-using-cad-instead-of-manual-drafting/>
- [10] Anderson B.W., Ekblad J., Bordoni B. StatPearls [Internet]. StatPearls Publishing; Treasure Island (FL): Aug 10, 2020. Anatomy, Appendicular Skeleton. [PubMed]
- [11] McCausland C., Sawyer E., Eovaldi B.J., Varacallo M. StatPearls [Internet]. StatPearls Publishing; Treasure Island (FL): Aug 10, 2020. Anatomy, Shoulder and Upper Limb, Shoulder Muscles. [PubMed]
- [12] McGhee D.E., Coltman K.A., Riddiford-Harland D.L., Steele J.R. Upper torso pain and musculoskeletal structure and function in women with and without large breasts: A cross sectional study. *Clin Biomech (Bristol, Avon)*. 2018 Jan; 51:99-104.
- [13] What is an Arduino?, <https://opensource.com/resources/what-arduino>
- [14] Robot Arm That Mimics Your Arm Movements, <https://www.electromaker.io/project/view/robot-arm>
- [15] Ren H., Liu T., Wang J. Design and Analysis of an Upper Limb Rehabilitation Robot Based on Multimodal Control // *Sensors* 2023, 23, 8801. <https://doi.org/10.3390/s23218801>.
- [16] Pang Z., Wang T., Wang Z., Yu J., Sun, Z., Liu S. Design and Analysis of a Wearable Upper Limb Rehabilitation Robot with Characteristics of Tension Mechanism // *Appl. Sci.* **2020**, *10*, 2101. <https://doi.org/10.3390/app10062101>.

Information of the authors

Zhumasheva Zhadyra, PhD, associate professor, Al-Farabi Kazakh National University

e-mail: Zhadyra_14@mail.ru

Nurakhmetov Baurzhan, d.t.s, professor, Almaty Technological University

e-mail: b.nurakhmetov@mail.ru